UNIVERSITY OF CALIFORNIA

Los Angeles

The Non-Newtonian Heat and Mass Transport of He II in Porous Media Used for Vapor-Liquid Phase Separation

A dissertation submitted in partial satisfaction of the requirements for the degree Doctor of Philosophy in Engineering

by

Sidney W.K. Yuan

1985

The dissertation of Sidney W.K. Yuan is approved.

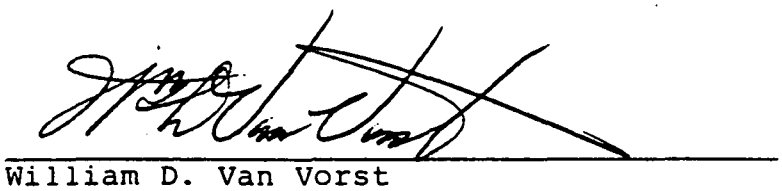

William D. Van Vorst

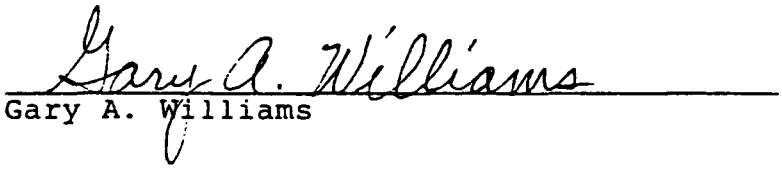

Gary A. Williams

Traugott H.K. Frederking, Committee Chair

University of California, Los Angeles

1985

To My Parents

And My Wife Katherine

TABLE OF CONTENTS

LIST OF SYMBOLS

A	Area, constant
A_c	Cross-sectional area
A_{GM}	Gorter-Mellink coefficient
A_w	Wall area
a_r	Area ratio
B	Vinen parameter, constant
C_B	Boundary layer coefficient
C_F	Friction coefficient
c	Velocity of sound
c_p	Heat capacity
D	Diameter
D_E	Equivalent Ergun diameter
D_p	Particle diameter
E	Energy of liquid helium
E_o	Energy of the phonons
F	Friction force, proportionality constant of Petrac
F_{sn}	Mutual friction force
f	Friction factor
f_M	Friction factor used by Murakami
G	Gibbs free energy
g	Gravitation force
h	Planck's constant
j	Mass flux density
K	Thermal conductivity

K_{GM}	Gorter-Mellink constant of bulk liquid helium
K^{*}_{GM}	Gorter-Mellink constant in porous media
K_p	Permeability
K_{pn}	Normal fluid permeability
K_x	Horizontal wave vector of periodic disturbance
L	Length
L_c	Characteristic length
L_v	Vortex line density
L_{vo}	Vortex line density at equilibrium
m	mass
N	Number of channels in the capillary model
N_q	Dimensionless heat flux number
N_{VT}	Dimensionless driving force number
P	Pressure
P_g	Hydrostatic pressure
P_v	Vapor pressure
P_T	Thermo-Osmotic pressure
P_σ	Surface tension pressure
Pr	Prandtl number
p	Momentum
Q	Heat
q	Heat flux density
R	Radius, electrical resistance, fluid flow resistance factor
R_N	Reference fluid flow resistance factor
Re	Reynolds number

Re_k	Modified Reynolds number
Re_M	Modified Reynolds number used by Murakami
r	Radial direction
S	Entropy
S_o	Nominal pore size
T	Temperature
t	Time
t_Θ	Time constant for the diffusion of vorticity
t_v	Relaxation time due to damping of motion by shear viscosity
U	Internal energy
u	Drift velocity in liquid helium
V	Volume
v	Velocity
W	Work
w	Relative velocity between normal and superfluid
x	X - direction
y	Y - direction
Z	Liquid level
z	Z - direction

Greek Symbols

β	Vertical temperature gradient =-dT/dz in the thermal convection model
χ_1	Vinen parameter for vortex line generation
χ_2	Vinen parameter for vortex line annilhilation at wall
δ	Boundary layer thickness

ε	Porosity
γ	Vinen parameter for vortex decay
η	Viscosity
θ	Temperature fluctuation in horizontal direction
$\varkappa_c$	Critical constant
λ	Latent heat of vaporization
μ	Chemical potential
π_{ik}	Momentum flow density tensor
π_{osm}	Mass osmotic pressure
ρ	Density
σ	Surface tension
τ	Shear stress
Ω	Growth number in the linear stability analysis
ω	Error
ξ	Vortex line length
ζ_o	Throughput factor in the London-Zilsel equation

Superscripts

$-$	Average value
$\rightarrow$	Vector quantity
$\cdot$	Derivative, rate

Subscripts

b	Bath
d	Downstream
GM	Gorter-Mellink
i	Inside
max	Maximum

n	Normal fluid
o	Outside
room	Room temperature
s	Superfluid
T	Thermo-Osmotic
u	Upstream
VLPS	Vapor-Liquid Phase Separation mode
v	Vapor
ZNMF	Zero Net Mass Flow mode
λ	Lambda temperature

LIST OF TABLES

LIST OF FIGURES

ACKNOWLEDGEMENTS

The author wishes to express his deep appreciation to his faculty advisor and doctoral committee chairman, Professor Traugott H.K. Frederking for his guidance and wisdom, and for his invaluable assistance whenever it was needed.

The author's gratitude is also extended to the other members of the doctoral committee: Professor Kyle D. Bayes, Professor Walter J. Karplus, Professor William D. Van Vorst and Professor Gary A. Williams for their helpful comments and suggestions.

Special thanks go to Mr. William A. Hepler, for his help in every phase of this work.

The cooperation of Romeo Carandang, Mr. W.F. Feng, Mrs. Frederking, Tuan Le and Chau Nguyen in the experimental work is deeply appreciated.

Finally, the author would like to thank his family for their patience and encouragements throughout his study.

This work was supported in part by the National Aeronautics and Space Administration.

VITA

[redacted] -- Born, [redacted]

1980 -- B.S., University of California, Los Angeles

1980-1981--Research Assistant, University of California, Los Angeles

1981 -- M.S., University of California, Los Angeles

1982-1985--Post Graduate Research Engineer, University of California, Los Angeles

1984-1985--Teaching Assistant, University of California, Los Angeles

PUBLICATIONS

"Fountain Effect Pump Phenomena for Liquid Helium Transfer: Thermodynamic System Studies", Space Workshop, Boulder, Colorado, August 1985 (with T.H.K. Frederking and R.M. Carandang).

"Determination of the Darcy Permeability of Porous Media Below 4 K", Cryogenic Engineering Conference, Boston, Massachusetts, August 1985 (with T.H.K. Frederking, W.A. Hepler and W.F. Feng).

"Equations for Heat and Mass Flow of Non-Newtonian Fluid Through Porous Media: Liquid Helium II - Helium-4 Vapor Separation", National Heat Transfer Conference, Denver, Colorado, August 1985 (with Jeffrey M. Lee, W.A. Hepler and T.H.K. Frederking).

"Simplified Thermodynamic Functions for Vapor-Liquid Phase Separation and Fountain Effect Pumps", Proc. Cryog. Process and Equipment, ASME, New Orleans, Louisiana, Dec. 1984, p. 169 (with W.A. Hepler and T.H.K. Frederking).

"Comparison of Flow Through Porous Plugs: Is the Darcy Permeability a Useful Measure of Throughput?", Proc. Space Cryogenic Workshop, Berlin, W. Germany, August 1984, p. 83 (with J.M. Lee, W.A. Hepler and T.H.K. Frederking).

"Thermodynamic Performance Evaluation of Liquid Pumps Based on the Fountain Effect of Superfluid Liquid Helium II", Proc. 10th International Cryogenic Engineering Conference, Helsinki, Finland, August 1984, p. 301 (with T.H.K. Frederking and R.M. Carandang).

"Sintered Plug Flow Modulation of a Vapor-Liquid Phase Separator for a Helium II Vessel", Proc. Advances in Cryogenic Engineering, Colorado Springs, August 1984, p. 687 (with T.H.K. Frederking, C. Chuang, Y. Kamioka and J.M. Lee).

"Plug Flow Comparison", Proc. Space Helium Dewar Conference and Workshop, Huntsville, Alabama, August 1983, p. 149 (with J.M. Lee, Y. Kamioka and T.H.K. Frederking).

"Darcy Law of Thermo-Osmosis for Zero Net Mass Flow at Low Temperatures", ASME-JSME Thermal Eng. Joint Conference, Honolulu, Hawaii, March 1983, vol. 2, p. 191 (with T.H.K. Frederking).

FIELDS OF STUDY

Major Field: Chemical Engineering Thermodynamics

Minor Fields: 1) Chemical Engineering Processes

2) Computer Methodology

ABSTRACT OF THE DISSERTATION

The Non-Newtonian Heat and Mass Transport of He II
in Porous Media
Used for Vapor-Liquid Phase Separation

by

Sidney W.K. Yuan
Doctor of Philosophy in Engineering
University of California, Los Angeles, 1985
Professor Traugott H.K. Frederking, Chair

The present investigation of vapor-liquid phase separation (VLPS) of He II is related to long-term storage of cryogenic liquid. This VLPS system utilizes porous plugs in order to generate a thermomechanical (thermo-osmotic) force which in turn prevents liquid from flowing out of the cryo-vessel (e.g. Infrared Astronomical Satellite).

In part, VLPS research reported in the literature has produced apparently contradictory results. Therefore, an apparatus was built and VLPS data were collected for a 2 μm and a 10 μm sintered stainless steel plug (1/2 inch diameter and 1/8 inch thick) and a 5-15 μm sintered bronze plug (1/2 inch diameter and 1/2 inch thick).

The VLPS data obtained at high temperature (close to T_λ) were in the non-linear turbulent regime. At low temperature, the Stokes regime was approached.

A turbulent flow model was developed, which provides a phenomenological description of the VLPS data of the present experiment and of other laboratories. According to the model, most of the phase separation data in the literature and the present work are in the turbulent regime. The model is based on concepts of the Gorter-Mellink transport involving the mutual friction known from the zero net mass flow (ZNMF) studies. The latter had to be modified to obtain agreement with the present experimental VLPS evidence. In contrast to the well-known ZNMF mode, the VLPS results require a geometry dependent constant. This parameter K^*_{GM} ("Gorter-Mellink constant") to first order, is independent of temperature and is found to be proportional to $K_p^{1/2}$ within data scatter (K_p = room temperature permeability).

A theoretical interpretation of the phenomenological equation for the VLPS data obtained, is based on modelling of the dynamics of quantized vortices proposed by Vinen. In extending Vinen's model to the VLPS transport of He II in porous media, a correlation between the K^*_{GM} and K_p was obtained which permits an interpretation of the present findings.

As K_p is crucial, various methods have been introduced in the present work to measure the permeability of the porous media at low temperatures. Good agreement (within 10%) was found between the room temperature and the low temperature K_p-value of the plugs.

Chapter I

INTRODUCTION

1.1 GENERAL

Space vessels like the Infrared Astronomical Satellite (IRAS) make use of liquid helium (He II) for cooling purposes. In the case of IRAS, He II was used to keep the telescope sensors at low temperature (around 1.8 K). At this temperature, the telescope has a better resolution of the outer space regions emitting low intensity radiation in the far infrared spectrum. The duration of such a mission usually depends on how long the cryogen can last. When all the He II on IRAS evaporated, the telescope was out of operation. Therefore, it is crucial to keep the cryogen in the cryostat as long as possible. To confine liquid helium in the container by conventional means for very long times, e.g. 10 years, is difficult. Vent lines are necessary for the vapor to be ejected from the cryostat due to the heat input. Since the pressure inside the cryostat is always higher than that of the outer space, any liquid in the container will tend to escape through the vent line. It was proposed by Professor William Fairbank to utilize the fountain effect of He II to confine the liquid in the cryostat (Selzer et al. 1970).

A porous medium is mounted between the container and the vent line (Figure 1.1). The porous plug is in contact with liquid helium on one side, and on the other side it is open to the vapor in the vent line. That is why the system is called the vapor-liquid phase separator. Any heat that is carried into the cryostat liquid is transported by one of the two fluids, called normal fluid (Fig 1.2). The other fluid is superfluid responsible for the fountain effect pressure. The normal fluid seeps slowly through the pores of the separator. Once it has penetrated the plug at the vapor-liquid interface on the downstream side, the liquid is vaporized immediately. The latent heat of vaporization is taken away which results in a lower temperature on the downstream side. This is how the heat absorbed by the cryostat is rejected. In doing so, a temperature gradient is set up across the plug with higher temperature at the helium bath side.

1.2 PREVIOUS WORKS

A number of investigators have studied the vapor-liquid phase separator (VLPS). One of the earliest models was the one suggested by Professor Fairbank (Selzer et al. 1970). By assuming that the normal fluid of He II is clamped and that only superfluid can penetrate the porous plug, Fairbank was able to come up with a simple solution of the VLPS system. Such a model assumes that the only way heat can be

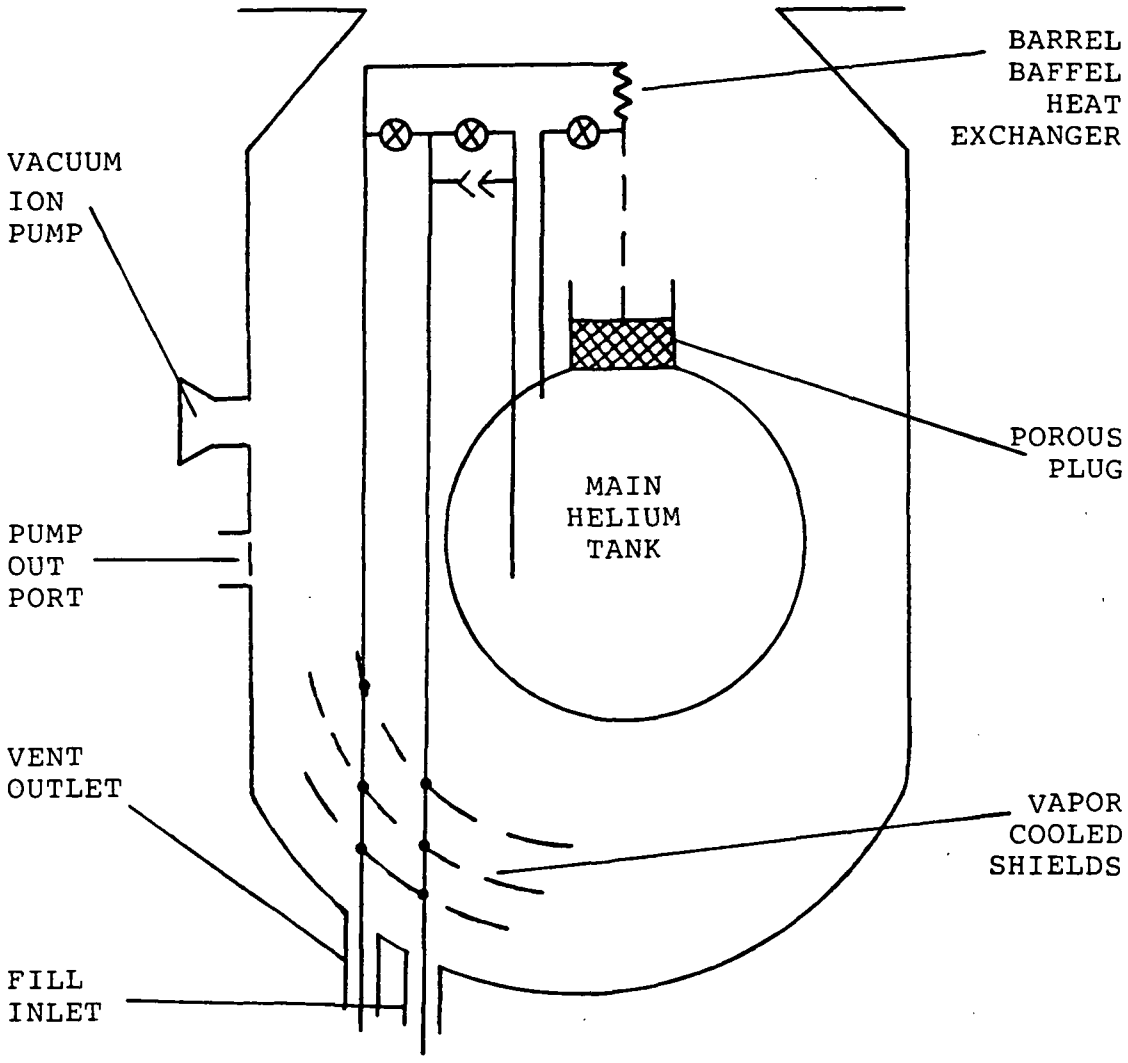

Figure 1.1. Schematic diagram of the main cryogen dewar on IRAS.

THE
VAPOR-LIQUID PHASE SEPARATOR

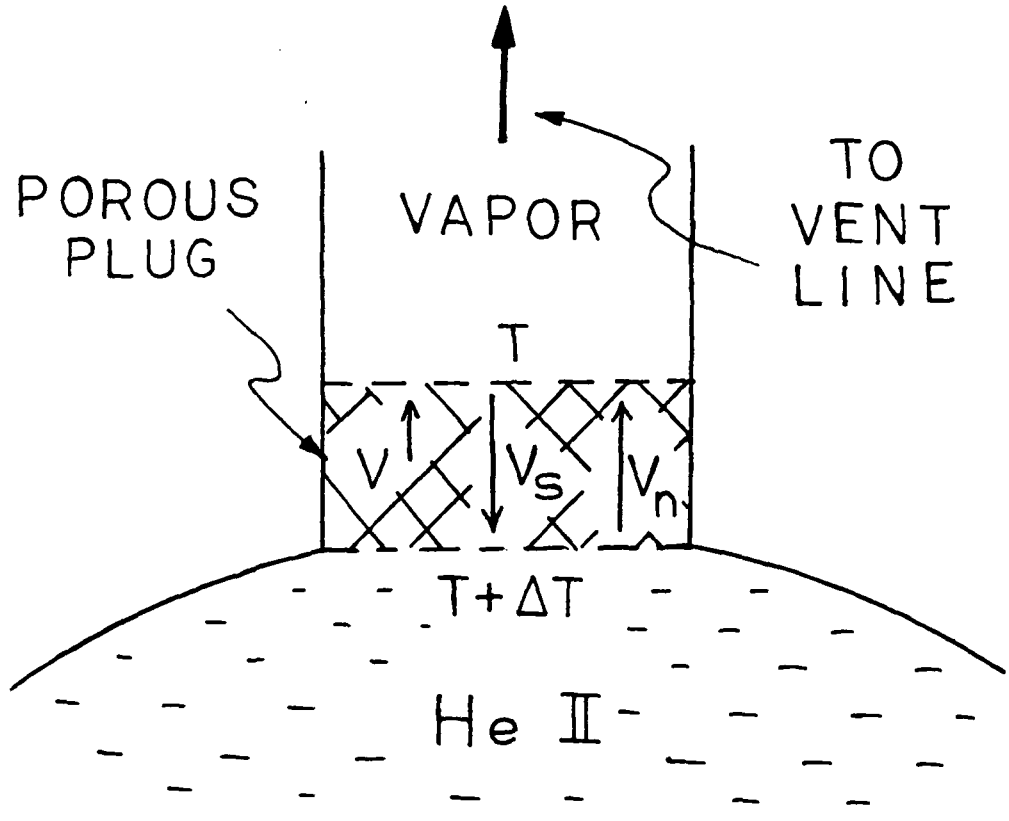

Figure 1.2. Schematic diagram of a vapor-liquid phase separator.

transported across the porous medium is by conduction through the solid portion of the plug. The solution is in a quadratic form

$$\dot{m} = \frac{\rho SL\lambda/K \pm \sqrt{(\rho SL\lambda)^2/K^2 - \Delta P/A^2\rho_s}}{1 \,/\, A^2\rho_s} \qquad (1.1)$$

where ρ, S and λ are the density, entropy and latent heat of He II respectively, ρ_s is the superfluid density, ΔP_v is the vapor pressure difference. A and L are the cross sectional area and thickness of the porous media ,and K is the thermal conductivity of the plug.

It was found that the second term under the radical is much smaller than the first. By expanding to a first order approximation, Fairbank got

$$\dot{m} \simeq \Delta PK \,/\, \rho SL\lambda \qquad (1.2)$$

and

$$\dot{m} \simeq \frac{2\rho_s \rho SLA^2\lambda}{K} - \frac{\Delta PK}{\rho SL\lambda} \qquad (1.3)$$

Since Equation 1.3 yields flow rates that greatly exceed the superfluid critical velocity, it is rejected, and Equation 1.2 is the physically meaningful solution of Fairbank's model.

Figure 1.3 is a plot of mass flow rate versus the bath temperature for the VLPS data of Klipping. (Denner et al. 1977). The data were obtained by using a 1 μm ceramic porous medium. Also included in Figure 1.3 is Fairbank's model for an aluminum plug. Klipping's (1 μm ceramic) sintered plug is one of the smallest (in pore size) in the literature, and yet Fairbank's model lies below the data. For a sintered plug of very small pore size made of highly conductive metals, this model is very useful.

Among all the investigators, Murakami (Murakami 1984 and Murakami et al. 1984) probably has the largest amount of data reported so far. He has tested both stainless steel and ceramic plugs. In his apparatus, a heater was mounted at the downstream side of the porous plug to control the flow rate. Murakami measured the temperature distribution across the porous media by positioning thermometers along the thickness of the plugs. A large temperature drop was found across a thin layer of his plugs close to the downstream side. He suggested that the vapor-liquid interface might have withdrawn into the porous medium and the presence of a thin layer of vapor was responsible for the large ΔT observed. By measuring the ΔT close to the upstream and the

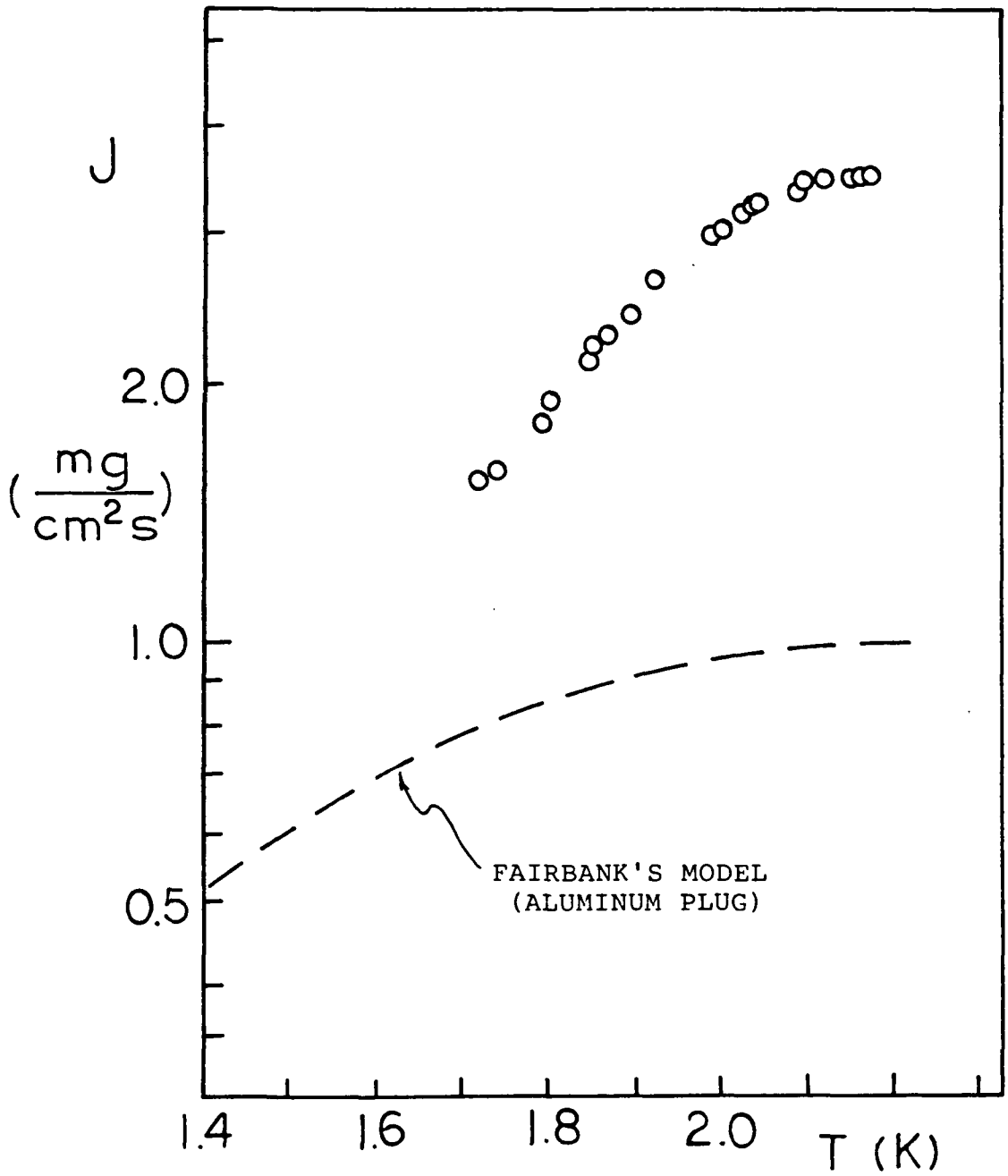

Figure 1.3. Comparison of Fairbank's model to vapor-liquid phase separation data of Klipping et al.(1 μm ceramic plug).

middle portion of the plugs (and ignoring the ΔT drop of the thin vapor layer at the downstream side), Murakami was able to fit his data by the Blake-Kozeny equation (Murakami 1984). Murakami thus concluded that under normal operating condition of VLPS, the transport of normal fluid in the porous media is in the laminar regime. Figure 1.4 is a plot of friction factor as a function of Reynolds number of Murakami's data.

Hendricks and Karr (Hendricks and Karr 1982) have proposed a two fluid modification based on the Poiseuille flow in straight channels of diameter D. The authors assume that the total throughput area in a porous medium is equal to

$$A = N\pi D^2 / 4 \qquad (1.4)$$

where N is the number of channels. Hendricks and Karr obtained the following equation

$$\dot{m} = \frac{N\pi D^4}{128} \frac{ST}{\lambda} \frac{\rho}{\eta_n} \frac{\Delta P}{L} \qquad (1.5)$$

where η_n is the normal fluid viscosity.

Petrac and Mason suggested that the mass flow rate in a VLPS system below 1.9 K is given approximately by

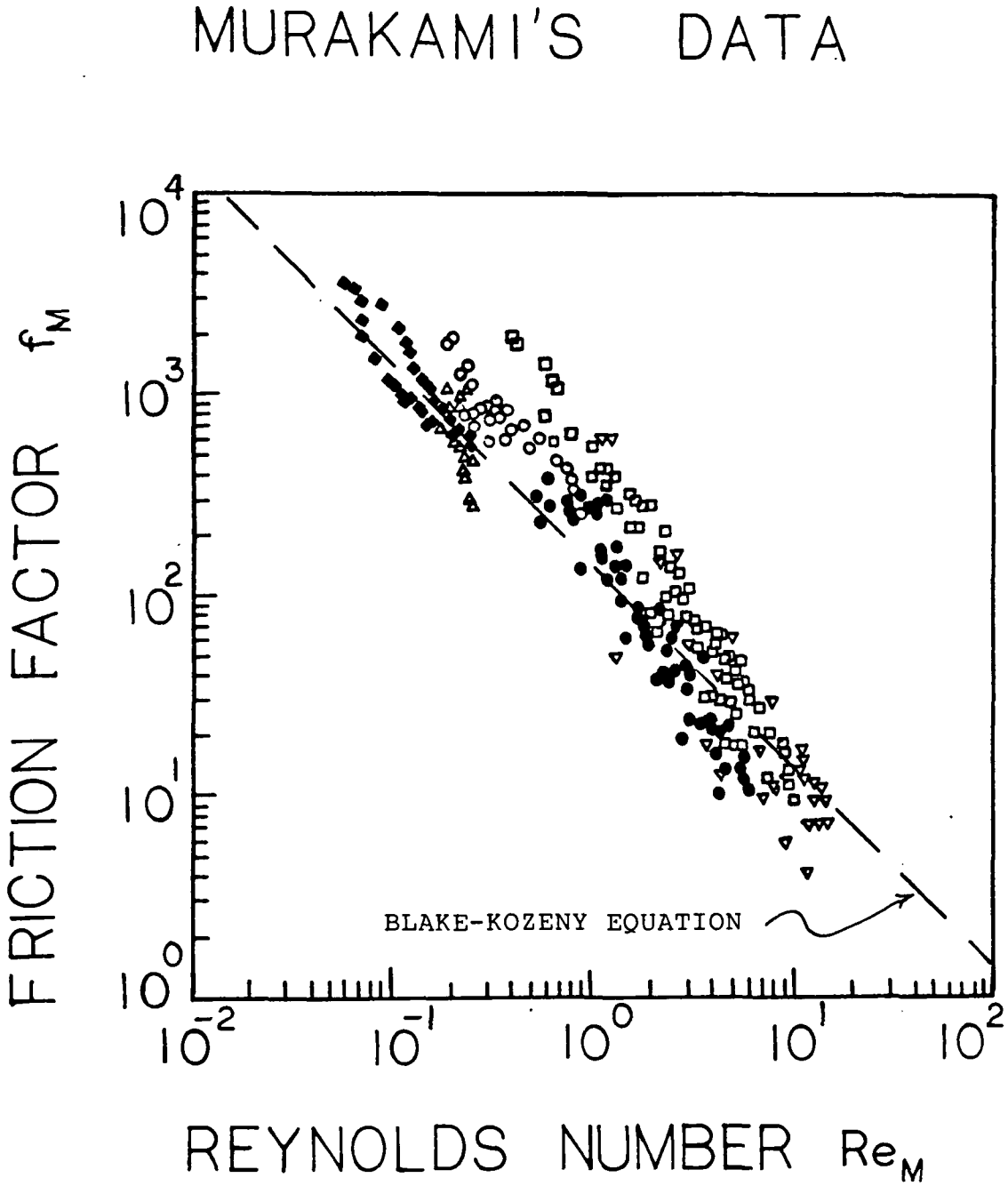

Figure 1.4. A plot of friction factor versus Reynolds number (Re_M) for Murakami's data.

$$\dot{m} = FA\Delta P \qquad (1.6)$$

where F is a proportionality constant which depends on pore size, porosity, plug length and structure. They have measured the F value for ceramic, glass and stainless steel plugs (Petrac and Mason 1978).

Concerning secondary effects, Dipirro (1983) has stressed the importance of surface tension effects (for "2 μm" plugs and below the 1 micron range).

Hendricks and Karr have studied the importance of the recession of liquid into the plug interior. In the recent Boulder worshop (1985), these authors mention the possibility of a constant temperature gradient in the turbulent regime described by the Allen and Reekie rule. Any "dry-out" length would cause a smaller liquid path, i.e. a larger pressure gradient. Apparently, the authors do not assign a large emphasis on this dry-out effect in their recent work.

Instead of using porous media as vapor-liquid phase separator, Schotte and Denner (Schotte and Denner 1981, Schotte 1982) have studied the so called active phase separator (APS). The APS consists of a pin which can be moved in and out of an orifice bushing as shown in Figure 1.5. A typical diameter of the annulus is 20 mm, and the gap length L varies from 0 to 15 mm. The gap size is of the order of 10 μm. By varying the gap length one can control the flow rate, that's why it is called the active phase separator.

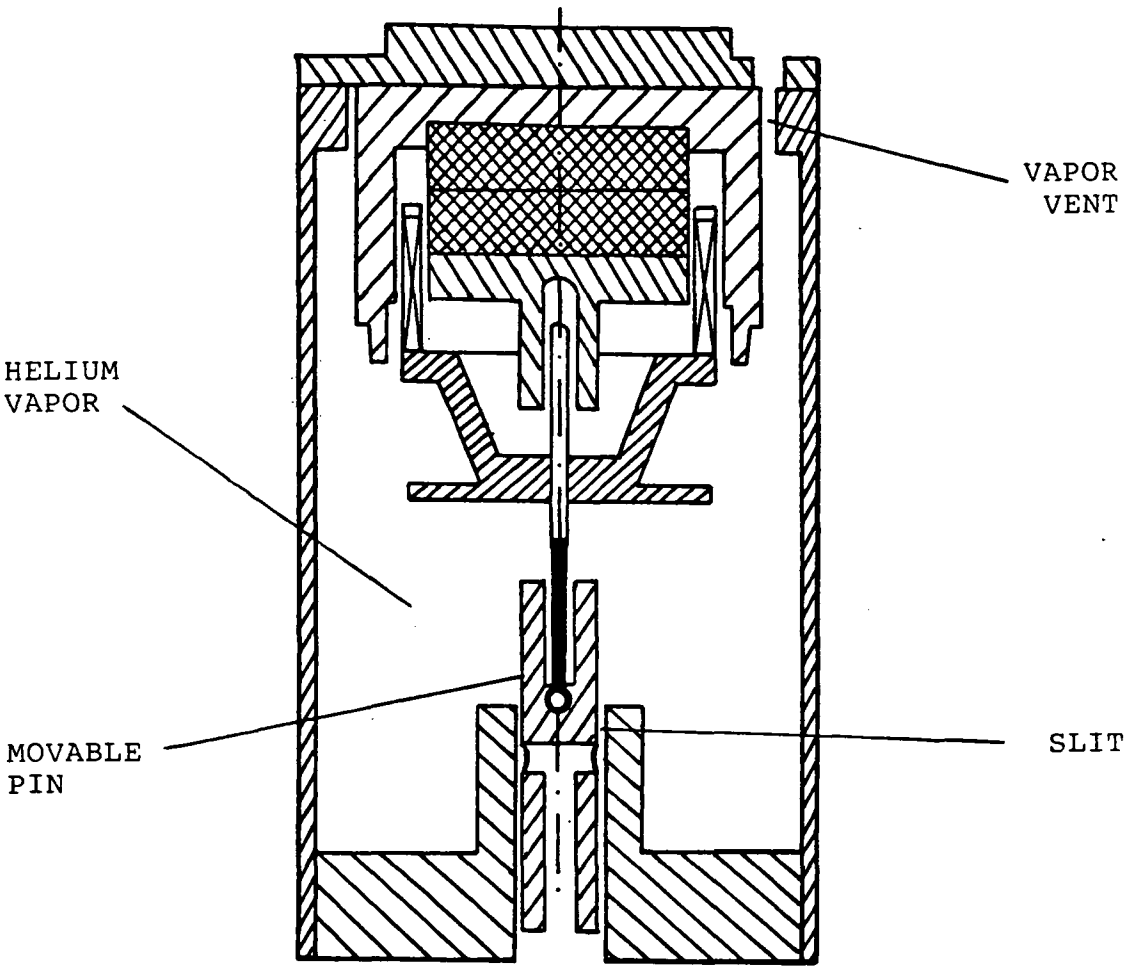

Figure 1.5. Schematic diagram of an active phase separator.

1.3 SCOPE

Vapor-Liquid phase separation research in the literature has produced partially contradictory results. As mentioned in the previous section, different investigators have stressed the role of various secondary effects in the VLPS, namely the thermal conductivity of plug metarial, the surface tension effects and the recession of liquid. Additional confusion may have arisen from the introduction of the idea of a third "Gorter-Mellink regime", e.g. Schotte et al. (1980). Historically, the original Gorter-Mellink (GM) regime has been for the zero net mass flow (ZNMF) mode. The second use of GM has been for one particular region of the resistance transition from the Landau regime to the "classical Newtonian flow" (Rorschach 1957 and Vote et al. 1971). The third case is the case mentioned above. It has been used for the transition from the onset to the completion of liquid breakthrough in the active VLPS system. As this uses a gap size of the order of 10 μm, no linear regime could be detected easily in that work.

Therefore, the present thesis research has been directed towards the resolution of the heat and mass transport of He II with emphasis on the non-linear regime of the VLPS systems. An apparatus has been built, and data have been taken with porous plugs of nominal pore size of 2 to 10 micrometer. At low temperatures, the linear (laminar) regime has become accessible. Most of the data however, have been tak-

en in the non-linear regime of quantum fluid turbulence. For the data description, various modes of the two-fluid model have been calculated, in particular the zero net mass flow mode, and the phase separation mode.

The theoretical description has a simple solution of laminar normal fluid flow as a basic solution. Starting from this simple case, a turbulent flow model has been developed resulting in a phenomenological description of various phase separator data of the present experiments and of other laboratories. The latter have not always been given in terms of suitable plug parameters. The present research has emphasized a common frame of reference for the throughput. Using this basis for well-documented data, there appears to be consistency between the present data and other results.

Chapter II

LIQUID HELIUM

2.1 BASIC PROPERTIES OF LIQUID HELIUM

Helium was first liquefied by Kamerlingh Onnes in 1908. Its normal boiling point is 4.2 K at atmospheric pressure. Liquid helium remains in the liquid phase under its own vapor pressure and would apparently do so right down to absolute zero temperature (Figure 2.1). Due to the small mass and extremely weak forces between the He atoms, pressure is required to produce solid helium (25 atm or more).

When liquid helium is cooled to 2.172 K it undergoes a transition (Figure 2.1). Because of the characteristic profile of the heat capacity curve, the temperature at which the transition takes place is called the lambda temperature (T_λ). There is no specific volume change or latent heat involved in the lambda transition. Keesom and Wolfke (1927) used the terms He I and He II to distinguish the liquid above and below T_λ respectively. He I behaves like a Newtonian liquid, however He II owing to its quantum effects has remarkably strange properties. In 1938, Kapitza and independently Allen and Misener reported that there is no measurable resistance to the flow of He II through small capil-

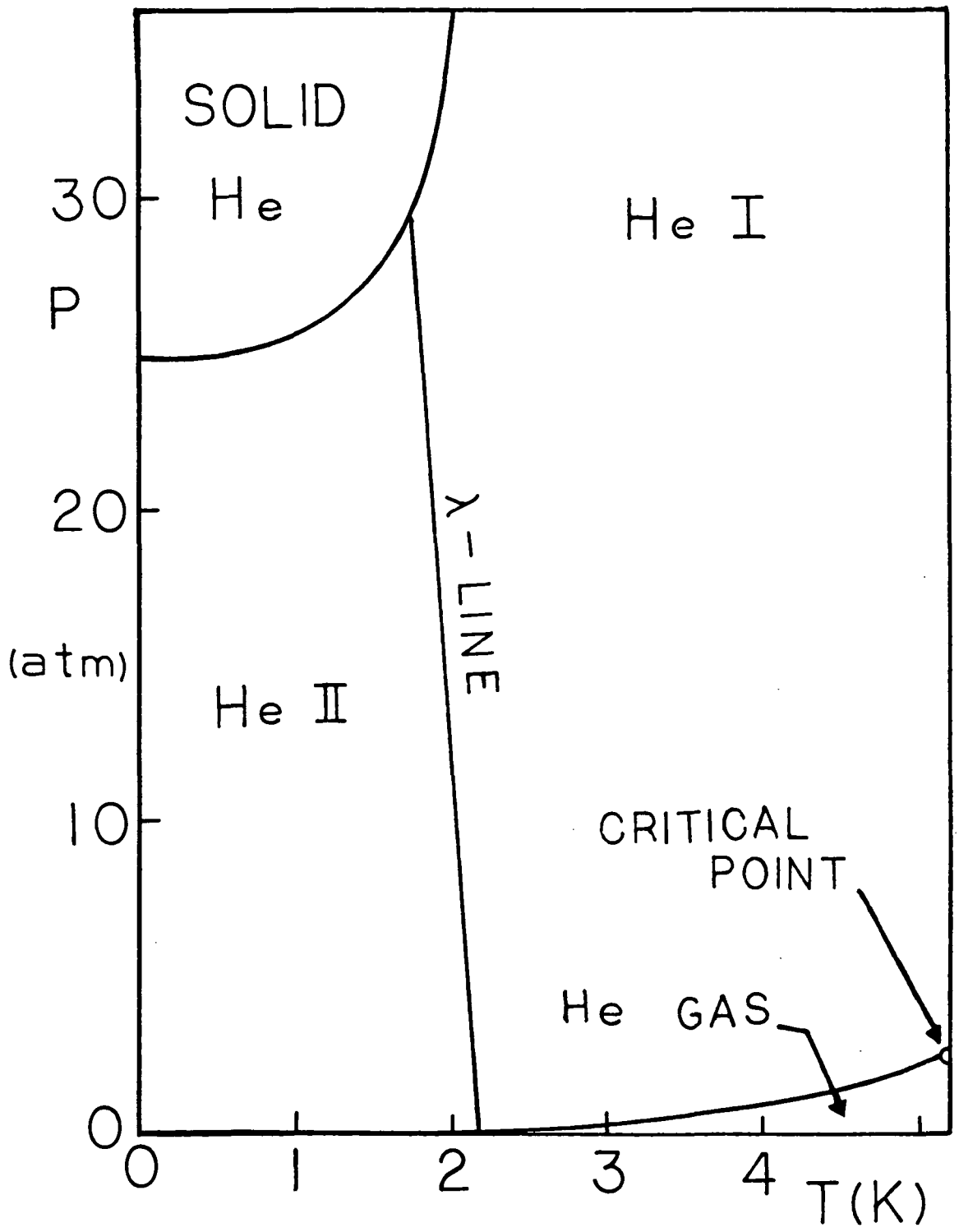

Figure 2.1. Phase diagram of liquid helium.

laries with diameter of the order of 10^{-4} cm (Kapitza 1938, Allen & Misener 1938). Kapitza referred to He II as the "superfluid". On the other hand, experiments using oscillating disks by Keesom and MacWood (1938) demonstrated the existence of a viscous drag, consistent with a viscosity coefficient not much less than that of helium gas. It seems that He II is capable of being both viscous and non-viscous at the same time. This has led to the formulation of the two fluid model by Tisza and Landau. In addition to superfluidity, some of the remarkable properties of He II include extremely high thermal conductivity, the fountain effect, the mechano-caloric effect and the Rollin film.

2.2 THE TWO FLUID MODEL

The two fluid model proposed by Tisza (Tisza 1940) and Landau (Landau 1941) independently postulates that He II is made of two fluids, namely the normal fluid and superfluid (Figure 2.2). Further, the sum of the normal fluid density and the superfluid density is equal to the bulk fluid density

$$\rho = \rho_n + \rho_s \tag{2.1}$$

where ρ is the density of He II, ρ_n and ρ_s are the density of the normal and superfluid respectively.

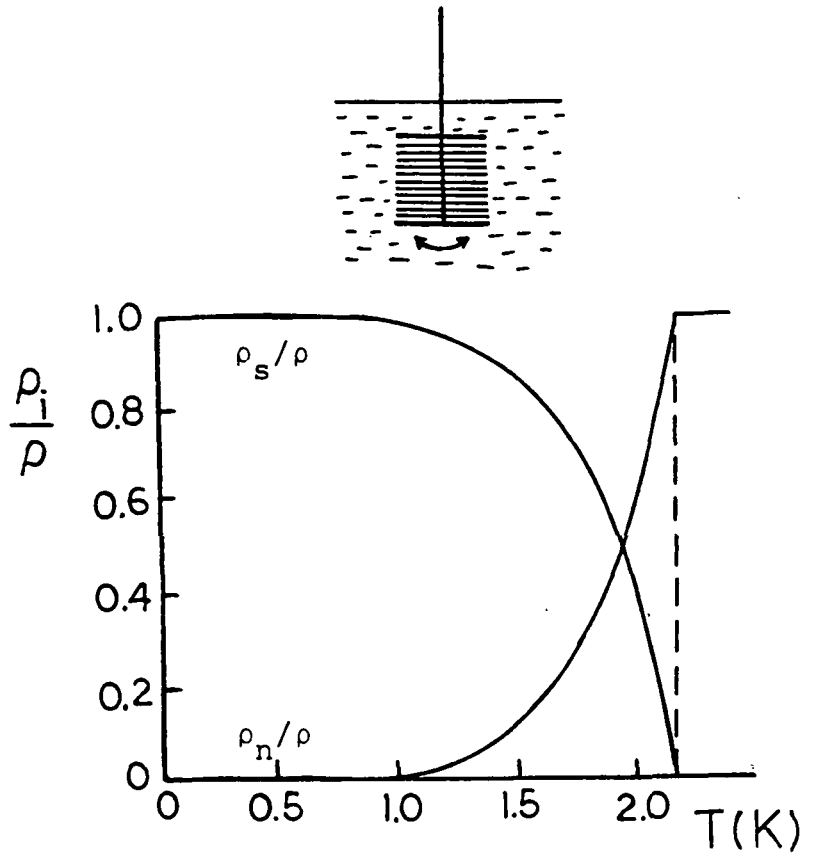

Figure 2.2. Andronikashvili's experiment.

Table 2.1. Essential parameters for the two fluid model.

	DENSITY	MASS FLUX	ENTROPY	VISCOSITY
BULK He II	ρ	J	S	η
NORMAL FLUID	ρ_n	J_n	S	η_n
SUPER-FLUID	ρ_s	J_s	0	0

At T_λ, only normal fluid is present in He II. As the temperature is decreased, more and more normal fluid is transformed into superfluid. Finally, at absolute zero temperature, He II consists of superfluid only. The essential parameters of the two fluid model are summarized in Table 2.1. The normal fluid behaves like a Newtonian fluid. It has finite viscosity and is the only entropy carrying component in the system. Superfluid on the other hand has no viscosity and does not carry any heat.

The total mass flux density of He II is equal to the sum of the two components (Appendix A)

$$\vec{j} = \rho\vec{v} = \rho_n\vec{v}_n + \rho_s\vec{v}_s \qquad (2.2)$$

The subscript n represents the normal fluid component and subscript s represents the superfluid component.

According to Landau (Landau 1941), the simplified equations of motion for the normal fluid and the superfluid can be written as (see Appendix A)

$$\rho_n\frac{\partial\vec{v}_n}{\partial t} + \rho_n(\vec{v}_n\cdot\nabla)\vec{v}_n = -\frac{\rho_n}{\rho}\nabla P - \rho_s S\nabla T + \eta_n\nabla^2\vec{v}_n \qquad (2.3)$$

$$\rho_s \frac{\partial \vec{v}_s}{\partial t} + \rho_s (\vec{v}_s \cdot \nabla) \vec{v}_s = \nabla \mu = - \frac{\rho_s}{\rho} \nabla P + \rho_s S \nabla T \qquad (2.4)$$

where ∇P and ∇T are the pressure and temperature gradient and η_n is the viscosity of the normal fluid. The chemical potential is denoted by μ.

2.2.1 The Fountain Effect

For demonstration, a glass container is packed with fine particles (of the order of 1 μm). One end of the container is connected to a fine capillary tube (as shown in Figure 2.3), and on the other end it is open to the He II bath. Now if a light is shone onto the particles, the liquid inside the packing will be excited. This results in a higher concentration of normal fluid inside the container. According to the two fluid model, superfluid will tend to rush into the packing to equilibrate the concentration. Normal fluid on the other hand tries to carry the entropy away from the heat source. However, due to its finite viscosity, normal fluid cannot penetrate the fine particles easily whereas the superfluid with no viscosity can enter the packing with ease. Thus a net pressure (the fountain pressure) is set up by the motion of the superfluid, forming the He fountain.

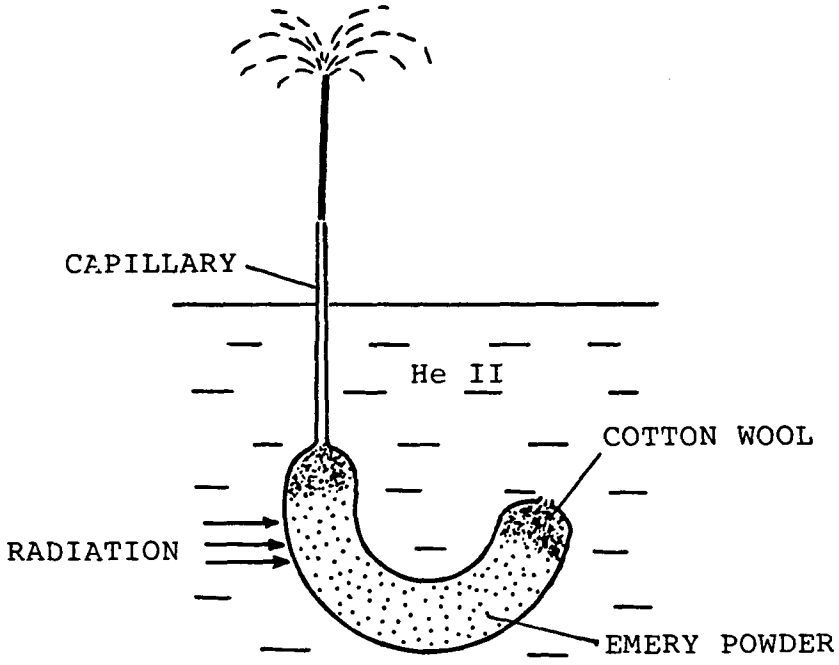

Figure 2.3. The helium fountain.

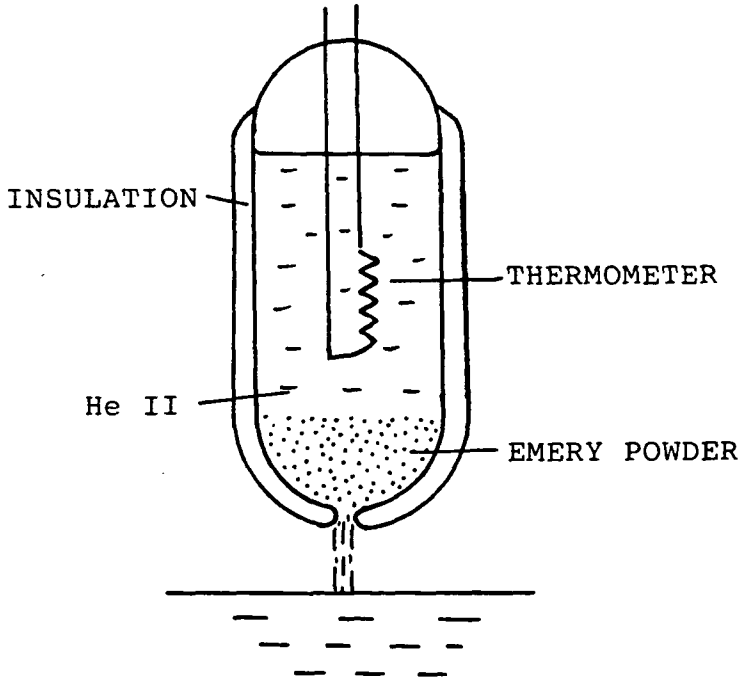

Figure 2.4. The mechano-caloric effect.

2.2.2 The Mechano-Caloric Effect

For the apparatus shown in Figure 2.4, a small hole is drilled in the bottom of an insulated container. The hole is then plugged by very fine particles (emery powders). The apparatus is set up such that it can be raised from or lowered into a bath of He II. It was found (Daunt and Mendelssohn 1939) that when liquid flowed into the container, the temperature dropped about 10^{-2} K, and when liquid flowed out, the temperature rose by the same amount. According to the two fluid model, only superfluid can penetrate the powder easily. So when more superfluid flows into the container the temperature should drop, and when liquid exits, the increase in normal fluid concentration will increase the temperature.

2.3 THE THERMO-OSMOTIC PRESSURE

Since the driving force for the fountain effect is the temperature difference, the fountain pressure is also known as the thermo-osmotic pressure. The thermo-osmotic pressure can be derived following Zemansky's approach (Zemansky 1968).

Consider two vessels of He II connected by a fine porous media (superleak) as shown in Figure 2.5. According to Putterman's definition a superleak is made of fine packings with particle diameter less than 10^{-4} cm (Putterman 1974).

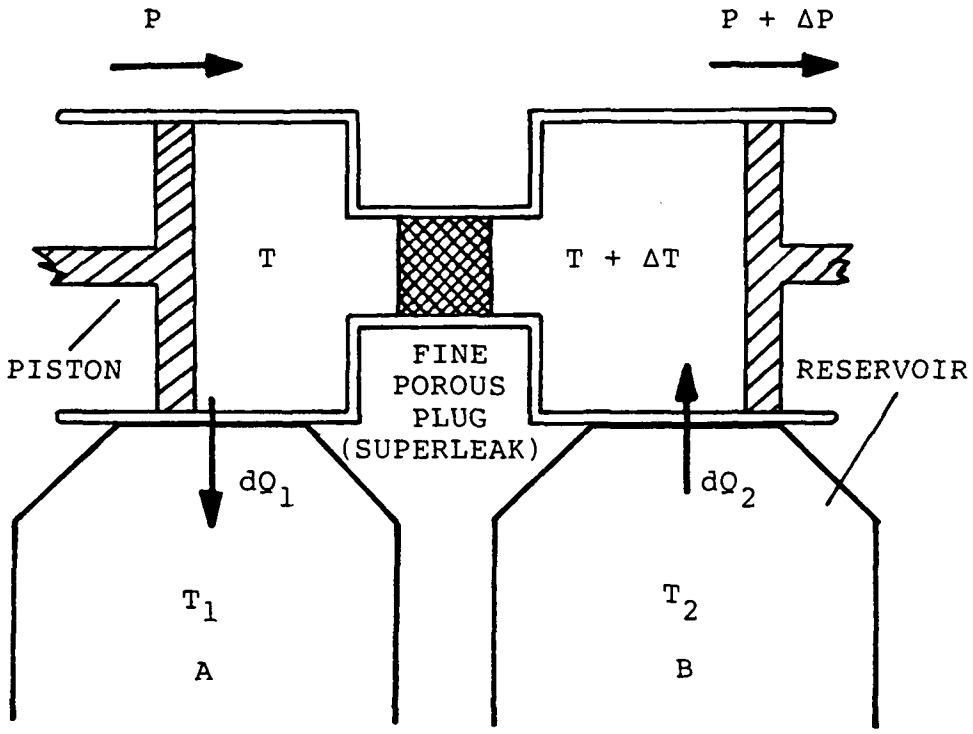

Figure 2.5. Demonstration of fountain effect set up by a fine porous medium (superleak).

The vessels are in thermal equilibrium with reservoir A and B at T_1 and T_2 respectively. The frictionless, non-leaking pistons are moved slowly and reversibly from left to right, so that an amount of liquid equal to dm is transferred from vessel A to B. If we assume that only superfluid can penetrate the porous medium and that there is no friction or heat conduction across the plug, the liquid helium at each side should undergo an isothermal and isobaric change of state.

The temperature in vessel A tends to rise, due to the accumulation of normal fluid, unless heat is removed. On the other hand, the temperature in vessel B tends to drop, unless heat is supplied. Maintaining thermal equilibrium with the reservoirs, dQ_1 is removed from vessel A (to the reservoir at T_1), and dQ_2 is added to vessel B (from the reservoir at T_2). The entropy loss from vessel A is

$$S_1(m_1 - dm) - S_1 m_1 = -S_1 dm \tag{2.5}$$

For a reversible process entropy is conserved

$$\frac{dQ_1}{T_1} - S_1 dm = 0 \tag{2.6}$$

or

$$dQ_1 = T_1 S_1 dm \tag{2.7}$$

Similarly, the amount of heat added to vessel B is

$$dQ_2 = T_2 S_2 dm \tag{2.8}$$

Therefore, the net heat supply to the present ideal superleak system is

$$dQ_{net} = dQ_2 - dQ_1 = (T_2 S_2 - T_1 S_1) dm \tag{2.9}$$

From the first law of thermodynamics

$$\begin{aligned} dU &= dW + dQ \\ &= (-P_2 V_2 + P_1 V_1) dm + (T_2 S_2 - T_1 S_1) dm \end{aligned} \tag{2.10}$$

or

$$(U_2 + P_2 V_2 - T_2 S_2) = (U_1 + P_1 V_1 - T_1 S_1) \tag{2.11}$$

$$G_1 = G_2 \tag{2.12}$$

This means that the Gibbs free energy difference across the plug is equal to zero. Usually the low temperature literature uses the symbol μ (- Gibbs free energy per unit mass) called "chemical potential". Thus we have $d\mu = 0$, or

$$\mu_1 = \mu_2 \tag{2.13}$$

According to the first and second law of thermodynamics, we have

$$d\mu = -SdT + dP/\rho \tag{2.14}$$

From Equation 2.13 and 2.14 one gets

$$\Delta P = \rho S \Delta T = \Delta P_T \tag{2.15}$$

The above equation is H. London's fountain pressure prediction. The subscript T is used to distinguish the thermo-osmotic pressure.

The ideal superleak system discussed so far does not include dissipative processes, as only the superfluid is transported. Any realistic fluid flow description ought to include both the fountain pressure difference (Equation

2.15) and viscous dissipation. The two fluid equations of Landau appear to be appropriate in this respect. It is noted that for steady state and parallel flow, Equation 2.4 reduces to Equation 2.15.

The present thermo-osmosis is conveniently understood as an analog of mass osmosis. In the case of mass osmosis, (Figure 2.6a) a semi-permeable membrane is used to separate salt solutions of different concentration. Water will penetrate the membrane to get to the high concentration side and equilibrate the concentration on both sides. Since the membrane only allows the water molecules to pass through (but not the salt), a mass osmotic pressure is set up. The liquid level on the high salt concentration side will rise until the mass osmotic pressure is equal to the hydrostatic pressure (Figure 2.6b). If an external pressure is applied at the high salt concentration side, one can separate the water from the salt solution (Figure 2.6c). This is known as reverse-osmosis.

In the case of thermo-osmosis (Figure 2.7a), a porous medium is used to separate a He II bath. A light or heat source is being applied to the bath on the right hand side to induce a temperature difference. According to the two fluid model, there is a higher concentration of normal fluid in the "hot" container. By analogy to mass osmosis, superfluid penetrates the porous plug, flowing to the high temperature side and equilibrating the concentration. Since the

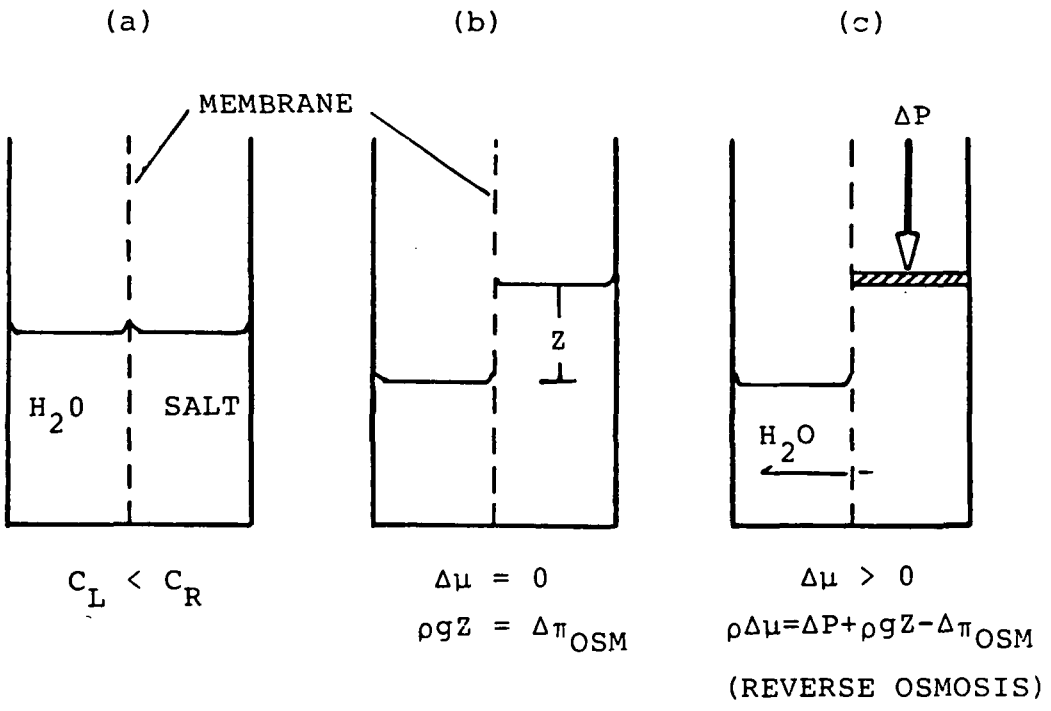

Figure 2.6. Mass osmosis.

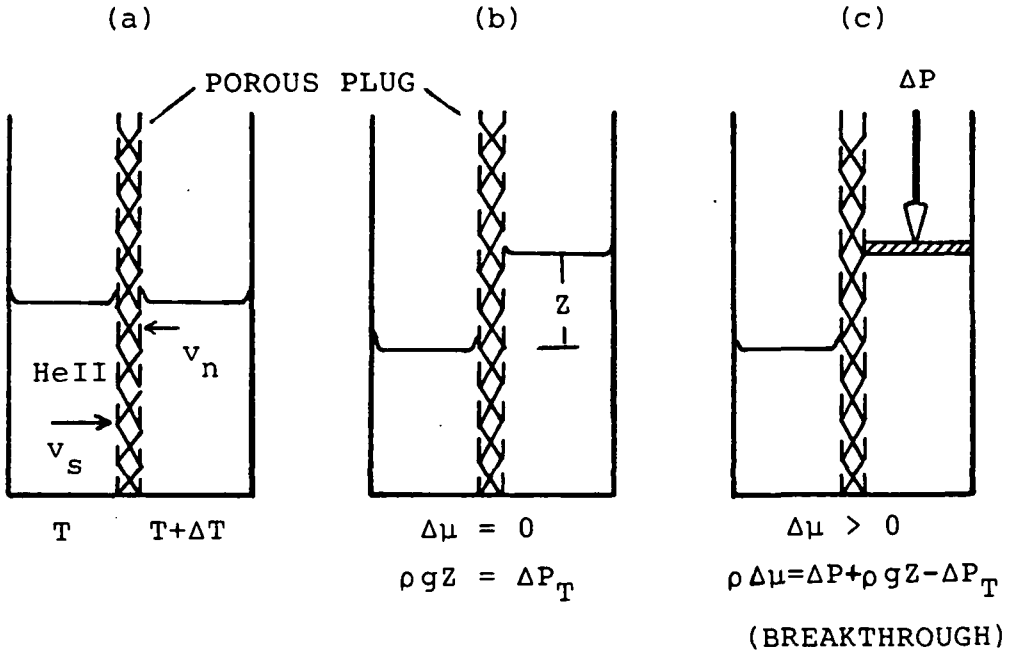

Figure 2.7. Thermo-Osmosis.

superfluid can pass through the porous medium much easier than the normal fluid, a thermo-osmotic pressure is set up. Similarly, the liquid level on the high temperature side will rise until the hydrostatic pressure is equal to the fountain pressure (Figure 2.7b). If an external pressure is applied to the bath on the right hand side, superfluid can be forced back into the low temperature side (Figure 2.7c). This is known as breakthrough. In the discussion of thermo-osmosis so far, the dissipation effect has been neglected. For the non-ideal case, please refer to Section 3.2.1..

Chapter III

TRANSPORT OF HE II IN POROUS MEDIA

As it was mentioned earlier, the normal fluid behaves like a Newtonian fluid. With the assumption of parallel flow, one can add Equation 2.3 and 2.4 including Equation 2.1 to get

$$\rho_n \frac{\partial \vec{v}_n}{\partial t} + \rho_s \frac{\partial \vec{v}_s}{\partial t} = -\nabla P + \eta_n \nabla^2 \vec{v}_n \qquad (3.1)$$

If we introduce a relative velocity defined by

$$\vec{w} = \vec{v}_n - \vec{v}_s \qquad (3.2)$$

Equation 3.1 can be rewritten as

$$\rho \frac{\partial \vec{v}_n}{\partial t} - \rho_s \frac{\partial \vec{w}}{\partial t} = -\nabla P + \eta_n \nabla^2 \vec{v}_n \qquad (3.3)$$

For small relative velocity $(\vec{v}_n - \vec{v}_s)$

$$\rho \frac{\partial \vec{v}_n}{\partial t} = -\nabla P + \eta_n \nabla^2 \vec{v}_n \qquad (3.4)$$

The preceeding equation is the Navier-Stokes equation for the normal fluid, with the pressure gradient ∇P. For steady state conditions, Equation 3.4 reduces to

$$\nabla P = \eta_n \nabla^2 \vec{v}_n \tag{3.5}$$

Therefore at steady state, the normal fluid satisfies the Navier-Stokes equation apparently, regardless of the magnitude of the relative velocity $\vec{w}$. This shows that the normal component of He II is indeed Newtonian for the conditions assumed.

3.1 ZERO NET MASS FLOW MODE

Zero net mass flow (ZNMF) means that the total mass flux density of normal fluid is counter balanced by the mass flux density of the superfluid. There is no net flow of the bulk helium liquid in one direction or the other. From Equation 2.2,

$$0 = \rho_n \vec{v}_n + \rho_s \vec{v}_s \tag{3.6}$$

3.1.1 Laminar ZNMF

Figures 3.1a and b show the zero net mass flow of He II in a capillary and a porous medium respectively. There is no net driving force for bulk liquid motion as a whole and the chemical potential across the capillary (or porous plug) is zero. From the superfluid equation of motion (Equation 2.4) one gets London's fountain pressure for steady and fully developed flow

$$\Delta P_T = \Delta P = \rho S \Delta T \tag{3.7}$$

Substituting Equation 3.7 into Equation 3.5 for the normal fluid ,we get

$$\nabla P_T = \eta_n \nabla^2 \vec{v}_n \tag{3.8}$$

Thus the driving force for the normal fluid is the thermo-osmotic pressure produced by the superfluid.

Let's look at the ZNMF of He II in a capillary first.

3.1.1.1 Capillaries

For a circular capillary, the axial component of the Navier-Stokes equation in the cylindrical coordinate can be simplified to

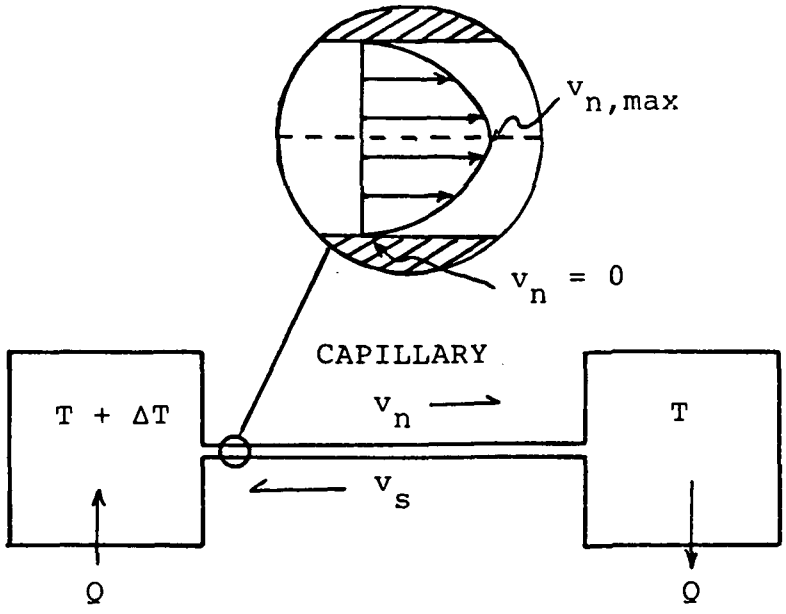

Figure 3.1a. Zero net mass flow of He II in a capillary.

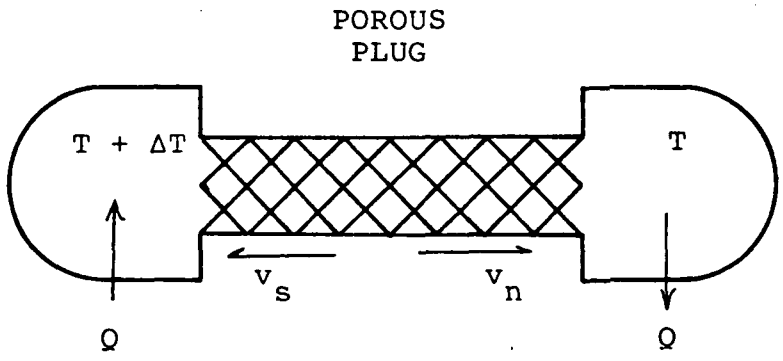

Figure 3.1b. Zero net mass flow of He II in a porous medium.

$$\nabla P_T = \eta_n \left(\frac{\partial^2 \vec{v}_n}{\partial r^2} + \frac{1}{r} \frac{\partial \vec{v}_n}{\partial r} \right) \tag{3.9}$$

where ∇P_T and $\vec{v}_n$ are the thermo-osmotic pressure gradient and normal fluid velocity along the capillary axis and r is the radial direction.

For no slip boundary condition of the normal fluid ($\vec{v}_n$ = 0, at r=R), the solution for the above equation gives

$$\vec{v}_n = - \frac{\nabla P_T}{\eta_n} (R^2 - r^2) \tag{3.10}$$

Equation 3.10 is an exact solution to Equation 3.9. The maximum velocity on the axis is

$$\vec{v}_{n,max} = - \frac{R^2}{4} \frac{\nabla P_T}{\eta_n} \tag{3.11}$$

It can be shown that the average velocity can be expressed as

$$\bar{v}_n = \frac{1}{2} \vec{v}_{n,max} = \frac{D^2}{32} \frac{|\nabla P_T|}{\eta_n} \tag{3.12}$$

The preceeding equation is the Hagen-Poiseuille law for the laminar transport of normal fluid in a capillary.

For ZNMF, the heat flux density is related to $\vec{v}_n$ by the following equation

$$\vec{q}_{ZNMF} = \vec{v}_n \rho S T \tag{3.13}$$

By substituting Equation 3.13 into 3.12, one can express the heat flux density as a function of the temperature gradient,

$$\bar{q}_{ZNMF} = \frac{D^2}{32} \frac{\rho^2 S^2 T |\nabla T|}{\eta_n} \tag{3.14}$$

3.1.1.2 Porous Media

By analogy to the Hagen-Poiseuille law for laminar flow of He II in capillaries, Darcy's law was found to be valid in the case of porous media (Yuan et al. 1983).

$$\bar{v}_n = K_{pn} \frac{|\nabla P_T|}{\eta_n} \tag{3.15}$$

where K_{pn} is the normal fluid permeability. The above equation is called the thermo-osmotic Darcy equation in this research. In terms of the heat flux density,

$$\bar{q}_{ZNMF} = K_{pn} \frac{\rho^2 S^2 T |\nabla T|}{\eta_n} \tag{3.16}$$

Equations 3.14 and 3.16 can be rewritten in dimensionless form (see Appendix B).

$$N_q = N_{\nabla T} \tag{3.17}$$

where N_q and $N_{\nabla T}$ are defined as,

$$N_q = \frac{\bar{q}_{ZNMF} L_c}{\eta_n S T} = \frac{\rho \bar{v}_n L_c}{\eta_n} \tag{3.18}$$

$$N_{\nabla T} = \frac{\rho^2 S \nabla T L_c^3}{\eta_n^2} \tag{3.19}$$

N_q is a dimensionless heat flux number and $N_{\nabla T}$ is a dimensionless driving force number. For capillaries the characteristic length L_c is equal to $(D^2/32)^{\frac{1}{2}}$, for porous media $L_c = K_p^{\frac{1}{2}}$ (K_p = permeability).

If the thermo-osmotic Darcy equation is indeed valid for the ZNMF of He II in porous media, then a plot of N_q versus

$N_{\nabla T}$ should yield a linear curve with a slope of unity. Figure 3.2 is a plot of the dimensionless numbers for the ZNMF of He II in packed materials. Data include that of Heijden et al. (1972), fiber packing of Frederking et al. (1981) and packings with different particle diameter (Schmidt et al. 1979), and column thickness (Forstat 1958). One can see that all the data fall on the theoretical line, proving that the thermo-osmotic Darcy equation does describe the flow of normal fluid in porous media (Yuan et al. 1983).

In Figure 3.3, the normal fluid permeability is plotted as a function of temperature for the same data presented in Figure 3.2. It is seen that every packing has a well defined normal fluid permeability.

3.1.2 Turbulent ZNMF

For turbulent flow, it has been found experimentally that the heat flux density is proportional to the cube root of the temperature gradient. It is observed that there is another friction force larger than the one associated with the viscosity of the normal fluid. Gorter and Mellink (1949) attempted to account for this by assuming a mutual friction force between the normal fluid and the superfluid. In order to obtain the correct proportionality between $\vec{q}_{ZNMF}$ and ΔT, they assumed a mutual friction force proportional to the cube of the relative velocity $(\vec{v}_s - \vec{v}_n)$.

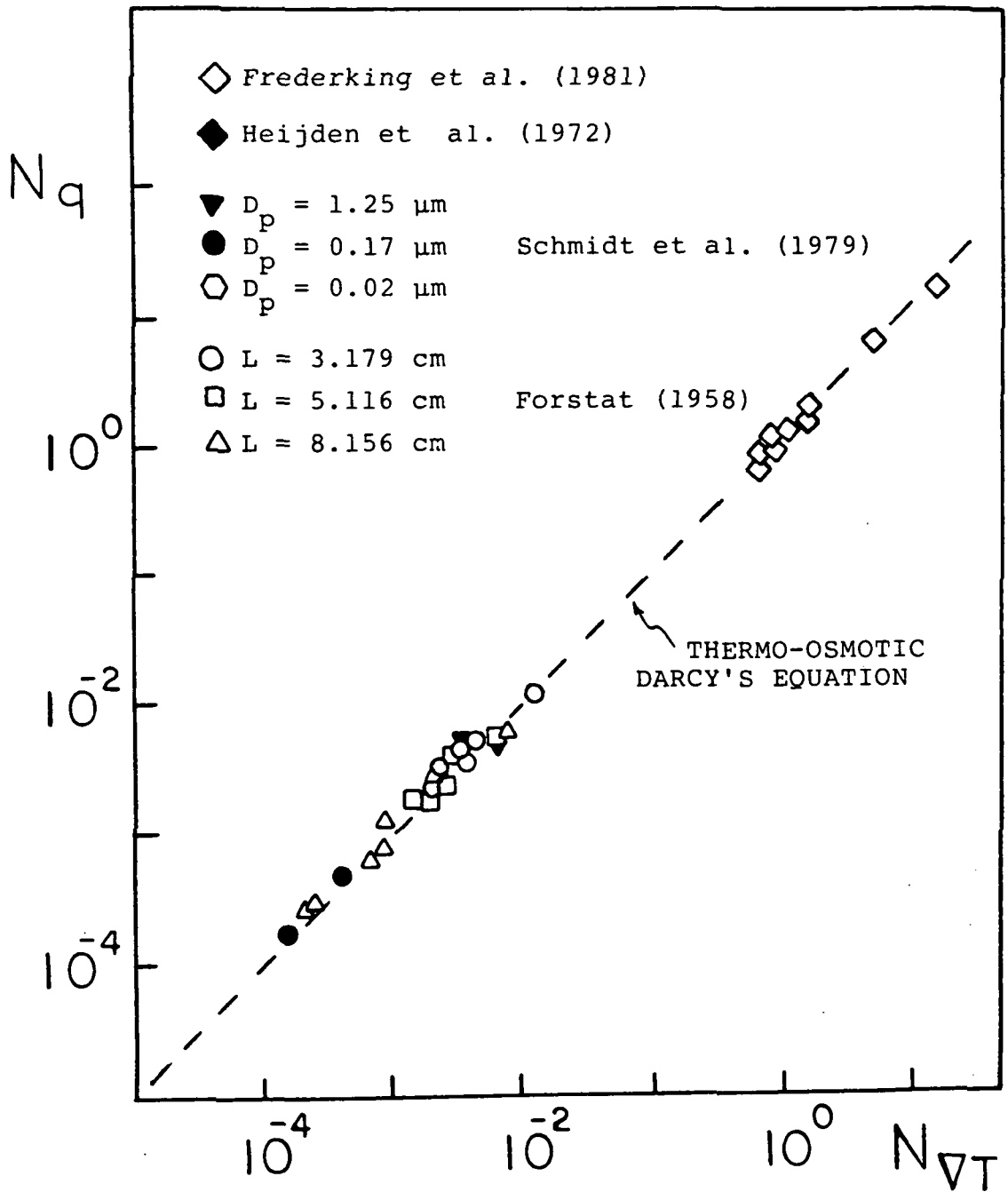

Figure 3.2. Dimensionless heat flux number versus dimensionless driving force number.

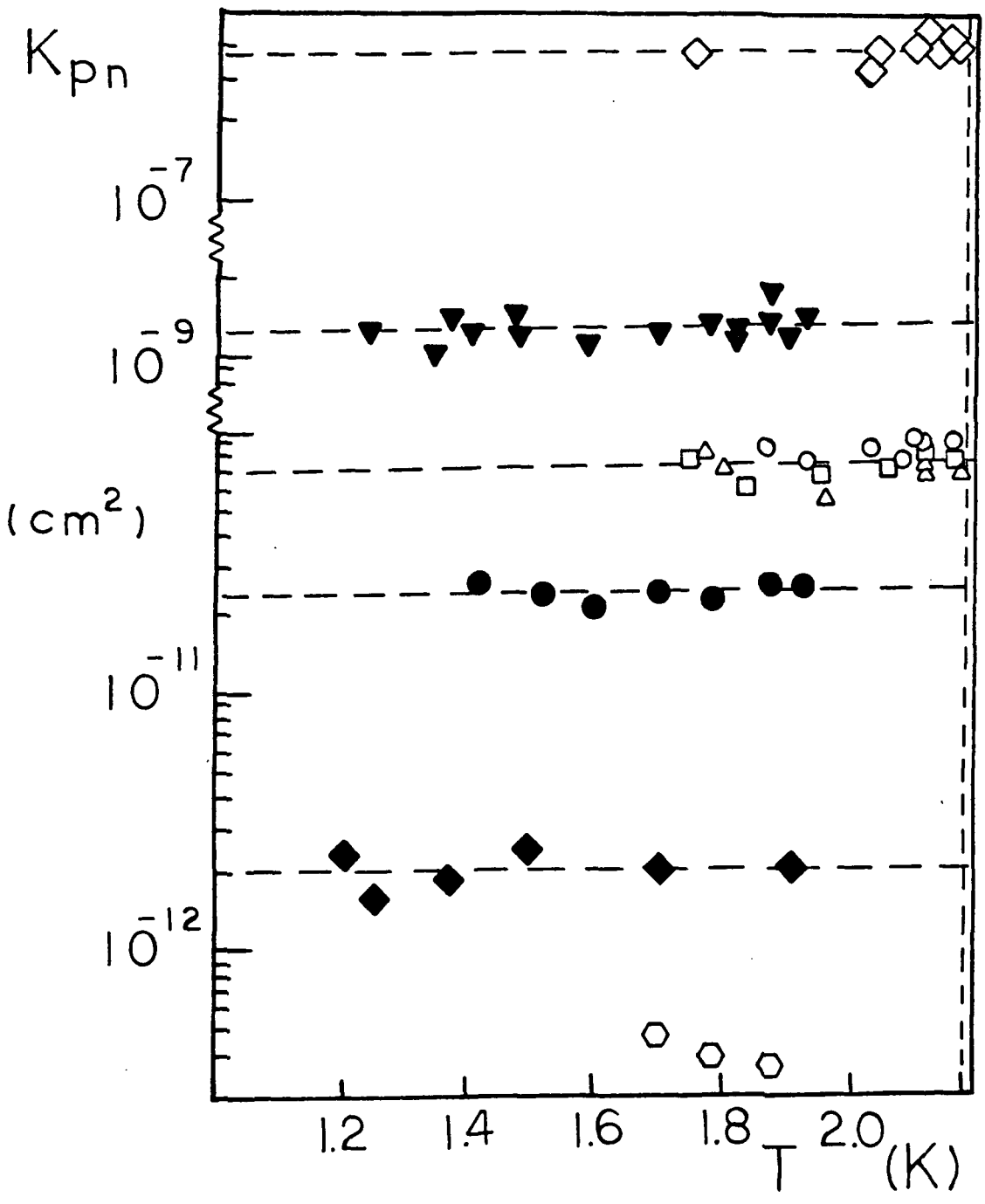

Figure 3.3. Permeability of normal fluid flow in various packing systems; ◇ Frederking et al. (1981); ◆ Heijden et al. (1972); ▼ ● ○ Schmidt et al. (1979); ○ □ △ Forstat (1958).

Gorter and Mellink modified Landau's two fluid equations to include the mutual friction term. According to Gorter and Mellink, the equations of motion for the normal fluid and superfluid are

$$\rho_n \frac{\partial \vec{v}_n}{\partial t} + \rho_n (\vec{v}_n \cdot \nabla) \vec{v}_n = - \frac{\rho_n}{\rho} \nabla P - \rho_s S \nabla T + \eta_n \nabla^2 \vec{v}_n - \vec{F}_{sn} \tag{3.20}$$

$$\rho_s \frac{\partial \vec{v}_s}{\partial t} + \rho_s (\vec{v}_s \cdot \nabla) \vec{v}_s = - \frac{\rho_s}{\rho} \nabla P + \rho_s S \nabla T + \vec{F}_{sn} \tag{3.21}$$

where

$$\vec{F}_{sn} = \rho_s \rho_n A_{GM} (\vec{v}_s - \vec{v}_n)^3 \tag{3.22}$$

with A_{GM} being the Gorter-Mellink coefficient for mutual friction. For steady, parallel flow and small ΔP, Equation 3.21 becomes

$$\rho_s S \nabla T = \rho_s \rho_n A_{GM} (\vec{v}_n - \vec{v}_s)^3 \tag{3.23}$$

Rearranging the preceeding equation and substituting Equation 2.1 and 3.2 ,one gets

$$\vec{v}_n = \frac{\rho_s}{\rho}\vec{w} = \frac{\rho_s}{\rho}\left(\frac{\rho_s S\nabla T}{A_{GM}\rho_s\rho_n}\right)^{1/3} \tag{3.24}$$

or

$$\vec{q}_{ZNMF} = \rho_s ST\left(\frac{\rho_s S\nabla T}{A_{GM}\rho_s\rho_n}\right)^{1/3} \tag{3.25}$$

Equation 3.25, is the Gorter-Mellink equation. Soloski (1977) modified the above equation by introducing a Gorter-Mellink constant

$$K_{GM} = (\rho/\rho_s A_{GM}\eta_n)^{1/3} \tag{3.26}$$

where K_{GM} is equal to 11.3 for wide ducts and is not a function of temperature. Substituting Equation 3.26 into 3.24 and 3.25 ,we get

$$\vec{v}_n = K_{GM}\frac{\eta_n\rho_s}{\rho^2}(\rho^2\rho_s S\nabla T/\rho_n\eta_n^2)^{1/3} \tag{3.27}$$

and

$$\vec{q}_{ZNMF} = K_{GM}\eta_n ST\frac{\rho_s}{\rho}(\rho^2\rho_s S\nabla T/\rho_n\eta_n^2)^{1/3} \qquad (3.28)$$

Note that for turbulent flow of He II, $\vec{v}_n$ or $\vec{q}_{ZNMF}$ does not depend on the characteristic length ($L_c = (D^2/32)^{\frac{1}{2}}$ for capillaries & $L_c = K_p^{\frac{1}{2}}$ for porous media). Therefore Equations 3.27 and 3.28 are applicable to the transport of He II in ducts or porous plugs.

One can arrange Equation 3.28 into dimensionless form (Appendix B) as below

$$\frac{\rho}{\rho_s}N_q = K_{GM}(\frac{\rho_s}{\rho_n}N_{\nabla T})^{1/3} \qquad (3.29)$$

Turbulent ZNMF transport data of He II in porous media are limited in the literature. Figure 3.4 represents the result of Frederking et al. (1981) for ZNMF of He II in fiber packing. If we plot N_q versus $N_{\nabla T}$, then all the data in the laminar regime will fall on the thermo-osmotic Darcy equation with the slope of unity (Figure 3.5). In the turbulent region, the data start to deviate from the thermo-osmotic Darcy equation into the Gorter-Mellink regime. From Figure 3.5, we can see that the transition between the laminar and turbulent regime is broad compared to the sharp transition in ducts. If the Gorter-Mellink equation is also valid for

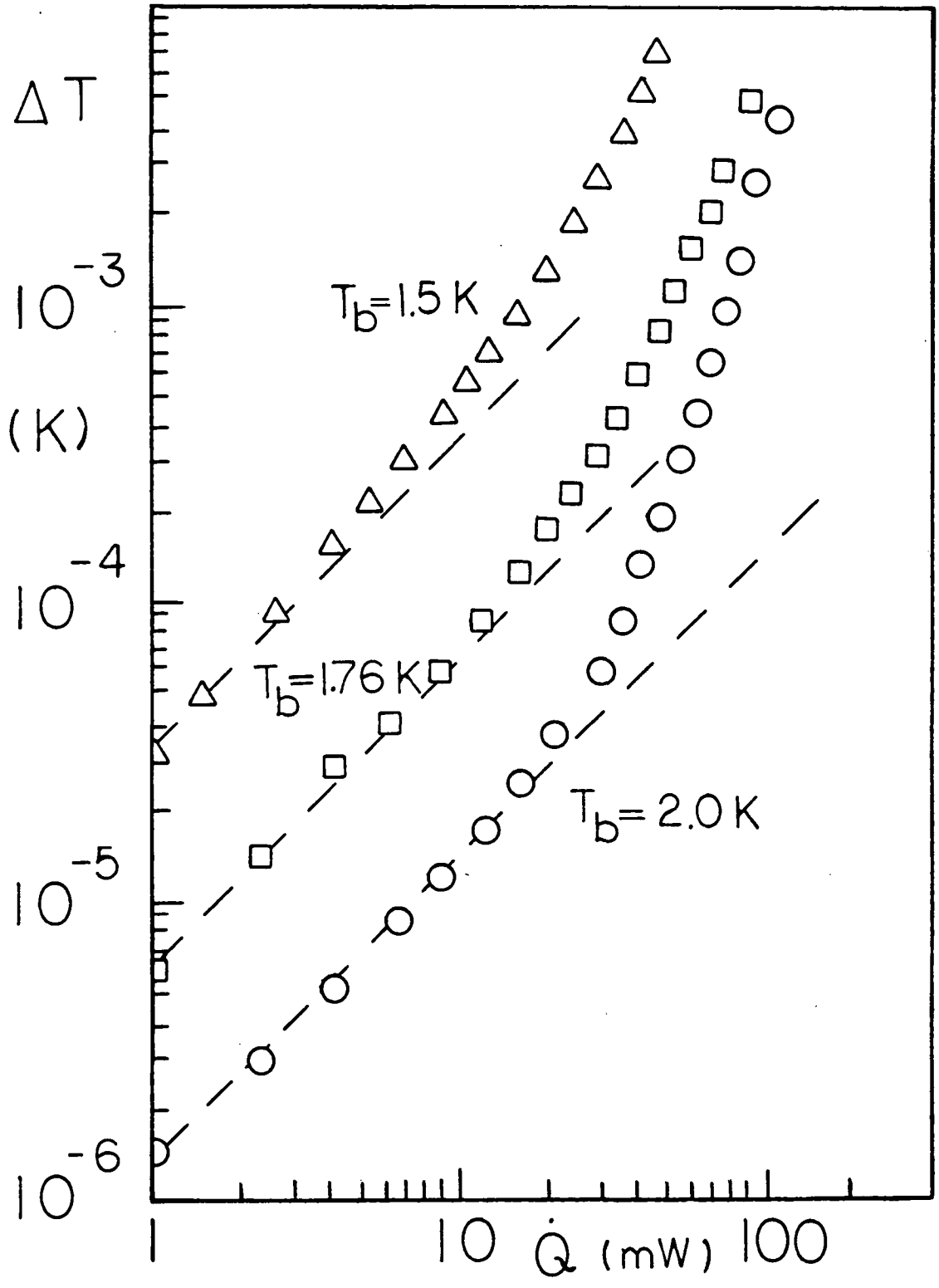

Figure 3.4. Data of turbulent zero net mass flow of He II in packings; Frederking et al. (1981).

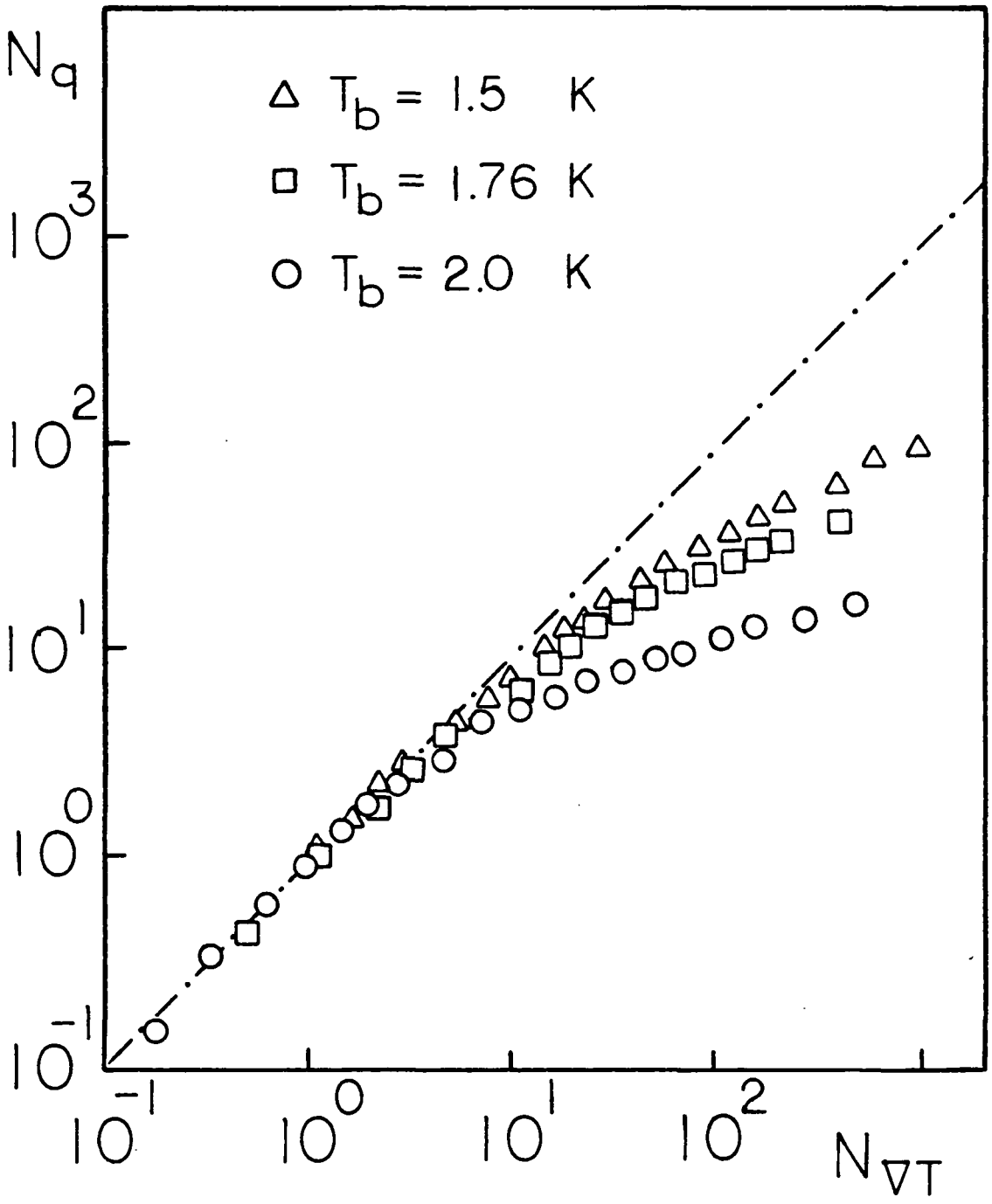

Figure 3.5. Data of Frederking et al.(1981) in dimensionless coordinate of N_q vs. $N_{\nabla T}$.

the ZNMF of He II in porous media, then a plot of $\log(\rho/\rho_s)N_q$ versus $\log(\rho_s/\rho_n)N_{\nabla T}$ should result in a straight line with a slope of 1/3. The y-axis interception is log K_{GM}. Lee (1982) has transformed the data of Figure 3.4 into the dimensionless coordinate for turbulent flow (Figure 3.6). He found that for fully developed turbulent ZNMF of He II in packing systems, the data are described by the Gorter-Mellink equation. The solid line represents the Gorter-Mellink equation for wide ducts with K_{GM} equals to 11.3. From Figure 3.6 one can see that all the data for porous media are below the Gorter-Mellink equation indicating a lower K_{GM}.

Knowing the ZNMF transport equations in both laminar and turbulent regime, one can interpolate between Equation 3.16 and 3.28 and come up with the following equation

$$\vec{q} = (\vec{q}^3_{Laminar} + \vec{q}^3_{Turbulent})^{1/3} \qquad (3.30)$$

In Figure 3.7, the above equation is used to fit the data of Frederking et al. (1981). The dashed lines represent Equation 3.30. A good fit of the data was found with K_{GM} equal to 7.5.

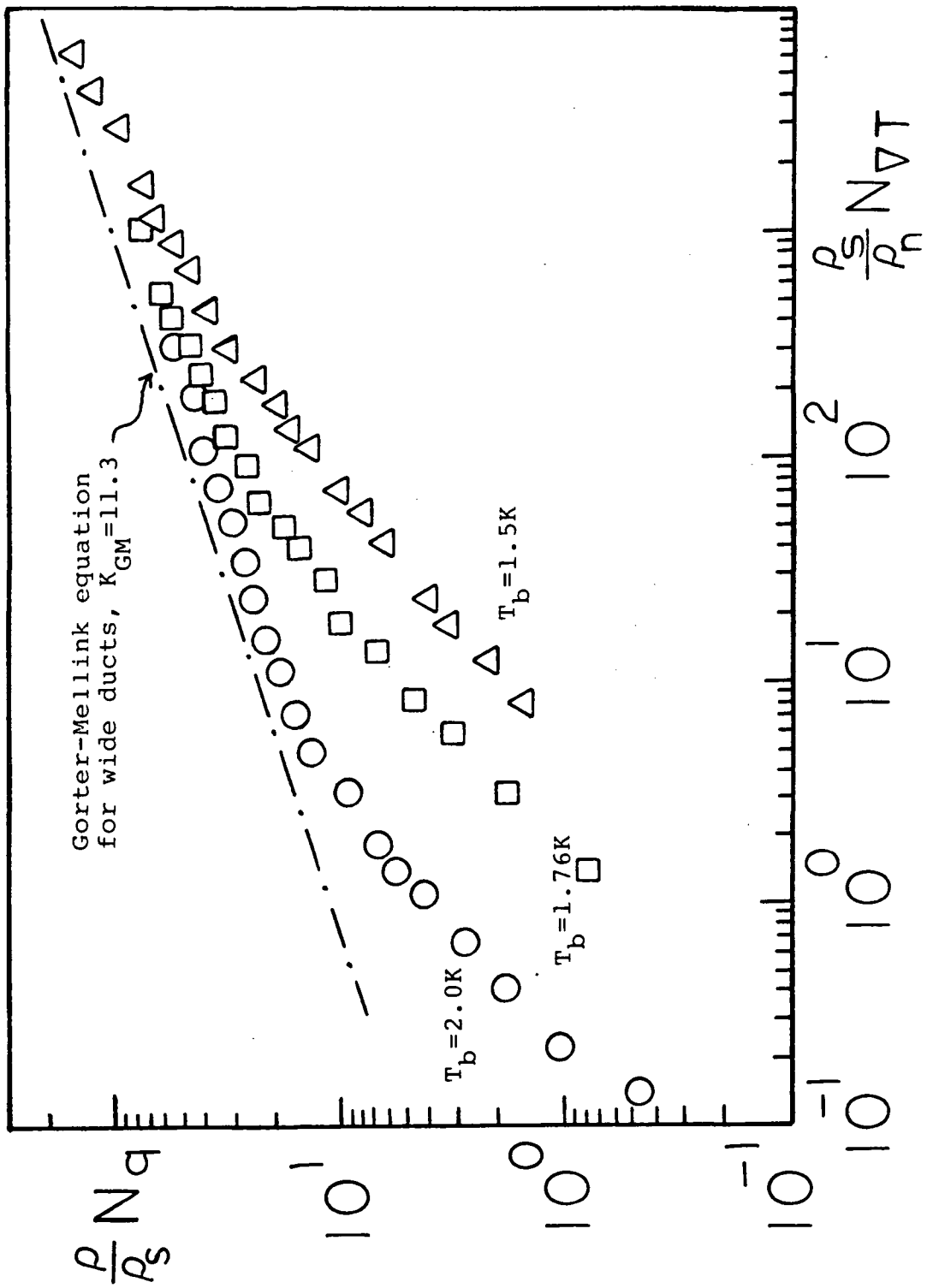

Figure 3.6. $(\rho/\rho_s)N_q$ versus $(\rho_s/\rho_n)N_{\nabla T}$ for data of Frederking et al. (1981).

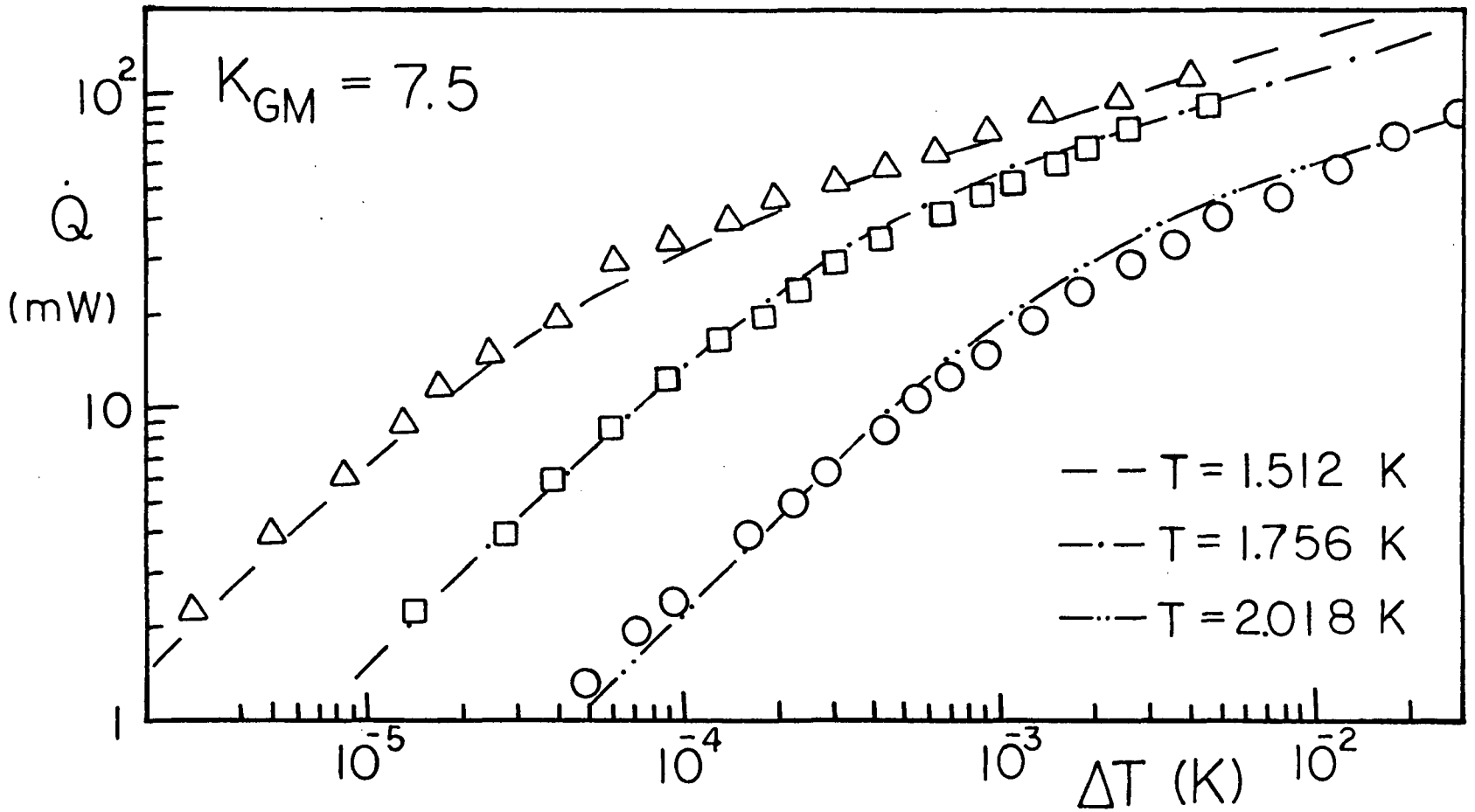

Figure 3.7. Fitting the data of Frederking et al. (1981) by the interpolation equation (Equation 3.30).

3.1.2.1 Vinen's Vortex Model

The mutual friction term in Equation 3.20 and 3.21 are thought to arise from the collision of normal fluid and the vortex lines. Vinen (1957 and 1958) has developed a model based on the growth and decay of vortex tangle maintained in equilibrium. For unbound He II,

$$\frac{dL_v}{dt} = \frac{\chi_1 B \rho_n}{2\rho} \vec{w} L_v^{3/2} - \frac{\chi_2 h}{2\pi m} L_v^2 \qquad (3.31)$$

The first term of the above equation represents the generation of vortex lines due to the interaction of normal fluid and the vortex lines. The second term is the annihilation of vortex lines through line-line collision of the vortex. L_v is the length of the vortex line per unit volume, $h/2\pi m$ is the quantum of circulation and B is a known parameter describing the interaction between the line and normal fluid. χ_1 and χ_2 are unknown functions that can be fitted by experimental data.

It was shown (Vinen 1957 and 1958) that the Gorter-Mellink coefficient equals

$$A_{GM} = \frac{\pi B^3}{6} \frac{\rho_n^2}{\rho^3} \frac{2\pi m}{h} \left(\frac{\chi_1}{\chi_2}\right)^2 \qquad (3.32)$$

In a later paper, Vinen further proposed the effect of walls on the turbulence in channels. It was assumed that the vortex generation mechanism is inactive within a characteristic distance = $L_v^{\frac{1}{2}}$ from the wall. Thus for turbulence in channels with diameter = D

$$\frac{dL_v}{dt} = \frac{\chi_1 B}{2\rho} \vec{w} L_v^{3/2} \left(1 - \frac{\gamma}{L_v^{\frac{1}{2}} D}\right) - \frac{\chi_2 h}{2\pi m} L_v^2 \qquad (3.33)$$

where γ is a parameter of the order of unity.

Childers and Tough (1976) have interpreted the ZNMF data in terms of Vinen's idea. Recently, Barenghi et al. (1983) have studied further details of this model.

3.1.3 Thermal Convection of He II in Porous Media

Classical thermal convections in porous media due to buoyancy force or surface tension have been studied extensively. Similarly, the counter flow of normal and superfluid results in the internal convection of He II. A linear stability analysis approach will be attempted in this section.

The equation of motion for the normal fluid and the equation of energy are

$$\frac{\partial \vec{v}_n}{\partial t} = -\nabla P/\rho - \frac{\rho_s}{\rho} S\nabla T + \frac{\eta_n}{\rho_n}\nabla^2 \vec{v}_n \qquad (3.34)$$

$$\frac{\partial T}{\partial t} - \beta v_n \vec{z} = \frac{K}{\rho c_p}\nabla^2 T \qquad (3.35)$$

where $\beta = -dT/dz$ and c_p is the heat capacity of liquid helium.

For convection of He II between two parallel plates heated from below, lets consider one-dimensional variation along the X-axis (Figure 3.8). Guyon and Pieranski (1974) found that the effect of the distance between the plates, L, can be expressed in the horizontal wave vector of the periodic disturbance K_x, with

$$K_x \approx \pi/L \qquad (3.36)$$

Retaining only the dominant contributions in the horizontal direction, Equation 3.34 and 3.35 can be written as

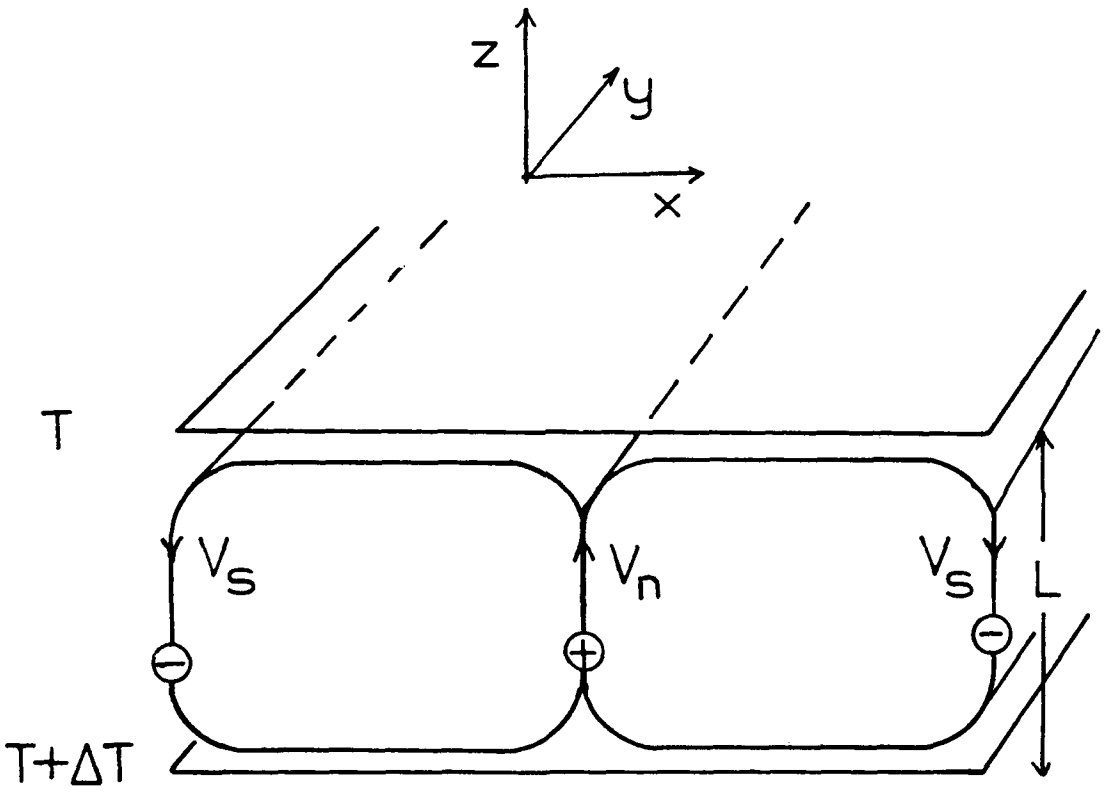

Figure 3.8. Schematic diagram showing the formation of convection cells in He II, between two parallel plates.

$$\dot{v}_n = - \frac{\rho_s}{\rho_n} \frac{S\theta}{L} + \frac{\rho}{\rho_n} \frac{v_n}{t_v} \tag{3.37}$$

$$\dot{\theta} = \beta v_n + \theta / t_\theta \tag{3.38}$$

where θ is the temperature distribution in the horizontal axis.

$$t_v = [\frac{\eta_n}{\rho} (\frac{2\pi}{L})^2]^{-1} \tag{3.39}$$

is the relaxation time due to damping of motion by shear viscosity, and

$$t_\theta = [\frac{K}{\rho c_p} (\frac{2\pi}{L})^2]^{-1} \tag{3.40}$$

is the time constant for the diffusion of vorticity.

Substituting Equation 3.38 into 3.37, we get

$$\frac{\ddot{\theta}}{\beta} - \frac{\dot{\theta}}{\beta t_\theta} = \frac{\rho_s}{\rho_n}\frac{S\theta}{\rho} + \frac{\rho}{\rho_n}\frac{\dot{\theta}}{\beta t_v} - \frac{\rho}{\rho_n}\frac{\theta}{\beta t_v t_\theta} \tag{3.41}$$

The useful concepts of stability investigation can be applied by stating that at threshold, v_n and θ are proportional to $e^{\Omega t}$ with the real quantity $\Omega = 0$

$$\frac{\rho_s}{\rho_n}\frac{S}{L} = -\frac{\rho}{\rho_n}\frac{1}{\beta t_v t_\theta} \tag{3.42}$$

Substituting for t_v and t_θ, we have

$$\frac{\rho_s}{\rho}\frac{\rho^2 S\nabla T L^3}{K\eta_n/c_p} = 16\pi^4 \tag{3.43}$$

For a pseudo-classical model with Pr = 1, the above equation becomes

$$\frac{\rho_s}{\rho}\frac{\rho^2 S\nabla T L^3}{\eta_n^2} = \frac{\rho_s}{\rho} N_{\nabla T} = 1704 \tag{3.44}$$

From this, the critical driving force number (or Rayleigh number) is found.

3.2 THE VAPOR-LIQUID PHASE SEPARATION MODE (VLPS)

3.2.1 The Thermodynamics Of VLPS

The thermodynamics of various VLPS systems is discussed in this section, namely,

1) Ideal VLPS at linear range with terrestrial gravity force

2) VLPS at linear range including surface energy effects and gravity

3) Dynamic operation

4) VLPS at zero gravity

The discussion of the above systems will be based on the condition of local thermodynamic equilibrium.

3.2.1.1 Ideal VLPS At Linear Range With Terrestrial Gravity Force

In this case, both the interfacial vapor-liquid contribution (surface tension) and the kinetic energy are neglected. The thermomechanical (thermo-osmotic) pressure gradient is providing for the liquid retention in the vessel (Figure 3.9b). The thermomechanical pressure difference is opposed by the vapor pressure difference and the hydrostatic pressure.

$$\Delta P_T = \rho S \Delta T = g \rho \Delta Z + \Delta P_v \qquad (3.45)$$

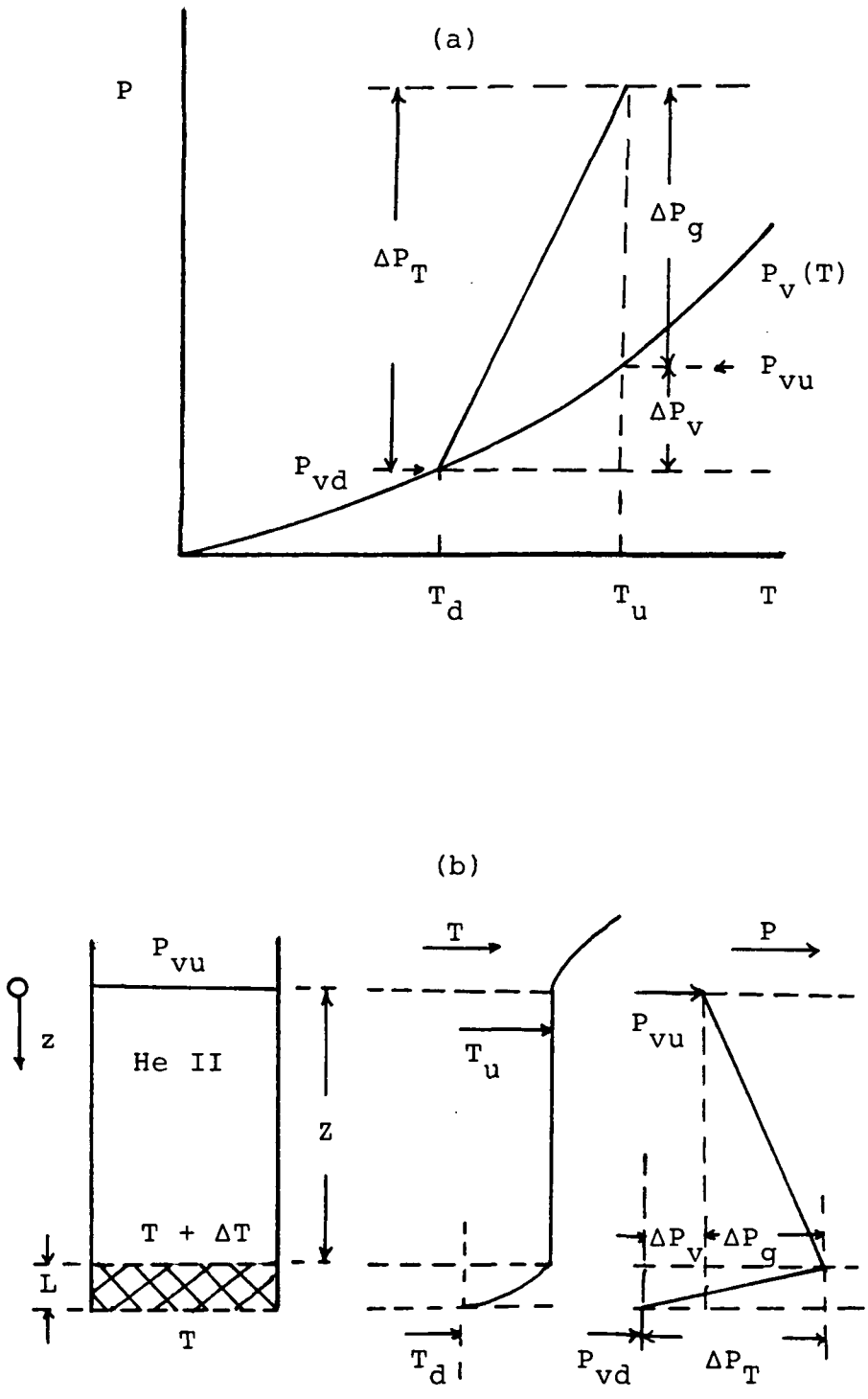

Figure 3.9. Ideal VLPS system at laminar range with terrestrial gravity force (schematic diagram).

In the P-T diagram, this case is depicted readily in graphical form as in Figure 3.9a.

The spatial distribution sketched in Figure 3.9b cannot be maintained indefinitely. At the critical velocity, the quantized vortices generated from the superfluid require kinetic energy. Thus, for a given ΔT, a portion of the energy supplied is converted into kinetic energy at the expense of the thermostatic energy. For the present ideal case, it is considered sufficient to rely on the "critical temperature gradient". In recent time, it has been found for tubes (Dimotakis 1974) and porous media (Frederking et al. 1981) that the dimensionless T-gradient is proportional to (ρ_s/ρ_n). From this criterion, we obtain a limit on the spatial condition T(z).

$$N_{\nabla T_c} = (\nabla T)_c \rho S \frac{\rho L_c^3}{\eta_n^2} \propto (\rho_s/\rho_n) \qquad (3.46)$$

or

$$|\nabla T|_c = \kappa_c (\rho_s/\rho_n) \ \eta_n^2 \ / \ \rho^2 S L_c^3 \qquad (3.47)$$

For small $\Delta T << T$, we have an inequality

$$|\Delta T| \; / \; L < |\nabla T|_c \tag{3.48}$$

This implies that

$$\frac{\Delta P_T}{L} < \varkappa_c (\rho_s/\rho_n) \; \eta_n^2 \; / \; \rho L_c^3 \tag{3.49}$$

Further, with $\Delta P_v = \Delta T \rho_v \lambda / T$

$$\frac{\Delta P_v}{L} < |\nabla P_T| / \; (\frac{\rho S T}{\rho_v \lambda}) \tag{3.50}$$

or

$$\frac{\Delta P_v}{L} < (\frac{\rho_v \lambda}{\rho S T}) \varkappa_c (\rho_s/\rho_n) \; \frac{\eta_n^2}{\rho L_c^3} \tag{3.51}$$

For a critical temperature difference $\Delta T = 10^{-4}$ K at 2 K, ΔP_v is less than 10 microbar (for a plug of 1 cm thick).

3.2.1.2 VLPS At Linear Range Including Surface Energy Effect And Gravity

Consider the grains of a phase separator (porous plug) at the vapor-liquid interface (Figure 3.10a). At the "top" with a small radius of curvature, there is a pressure gradient towards the "bulk". At the "bottom", there might be a tendency towards a lower pressure than the vapor pressure. However, the "bottom" is expected to tend towards a "flat" interface. This effect ought to make the pressure rise at the "top" the dominant effect, such that there is a net ΔP. Thus, for a given ΔT the static contribution of the previous case cannot be maintained. Therefore ΔP_g $(=\rho g Z)$ becomes less than before, as shown in Figure 3.10b. Thus,

$$\Delta P_T = \rho g \Delta Z + \Delta P_v + \Delta P_\sigma \qquad (3.52)$$

However, the surface tension effect is very small. For a 10 μm plug, the pressure difference due to surface tension, ΔP_σ, is only of the order of 1 mbar.

3.2.1.3 Dynamic Operation

First an ideal system is considered, such as a capillary with smooth inlet and exit geometry giving rise to Onsager-Freynman vortex ring shedding. The energy is proportional to $\rho v^2/2$. For instance (for an exaggerated schematic view)

(a)

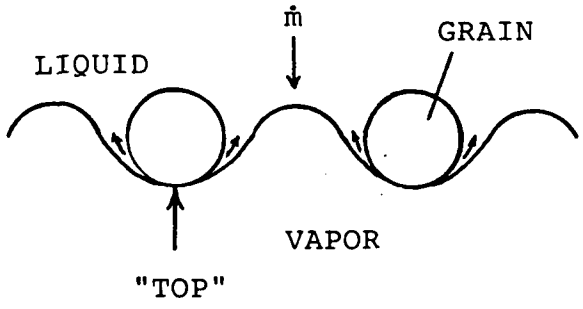

(b)

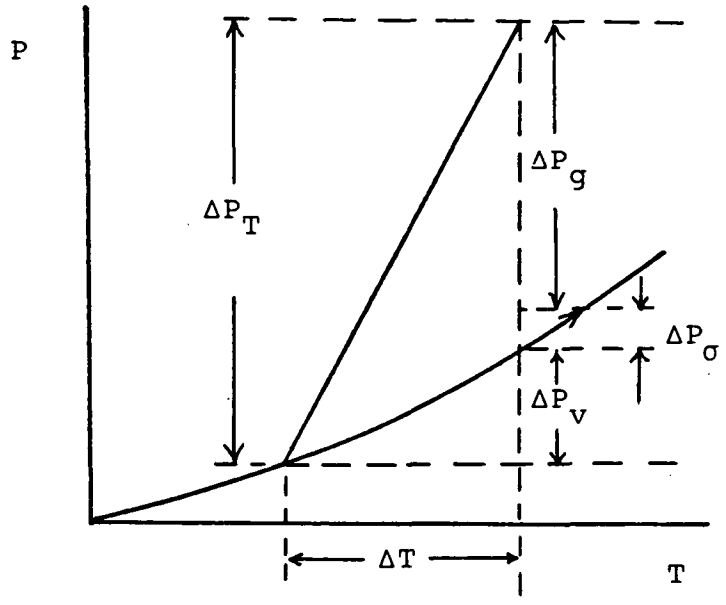

Figure 3.10. Linear VLPS system with gravity force and surface energy effects included (schematic diagram).

with velocity of order 100 cm/s, there is a dynamic pressure difference of the order 1 millibar. This is indicated schematically in the P-T-diagram in Figure 3.11a.

Second, a real plug system is considered with $\rho v^2/2$ reductions at various grains and narrow flow passages respectively. The apparent path is expected to involve fluctuations in pressure related to the local velocity fluctuations. Similarly, the state functions of pressure and temperature versus position coordinate show these effects (Figure 3.11b). Thus,

$$\Delta P_T = \rho g \Delta Z + \Delta P_v + \Delta P_\sigma + \Delta P_{dissipation} \qquad (3.53)$$

where $\Delta P_{dissipation}$ is used to denote to kinetic terms.

3.2.1.4 VLPS At Zero Gravity

For the zero gravity case there is no hydrostatic pressure. Therefore the initial P-T-diagram is changed significantly. The absence of gravity "pushes" the "inlet" condition to a point quite close to the vapor pressure curve (Figure 3.12). Thus, kinetic energy terms appear to be important. Because of this, it does not appear to be possible to operate in the linear regime, and the above non-linear operation with liquid accelerations (normal fluid accelerations) has to be considered.

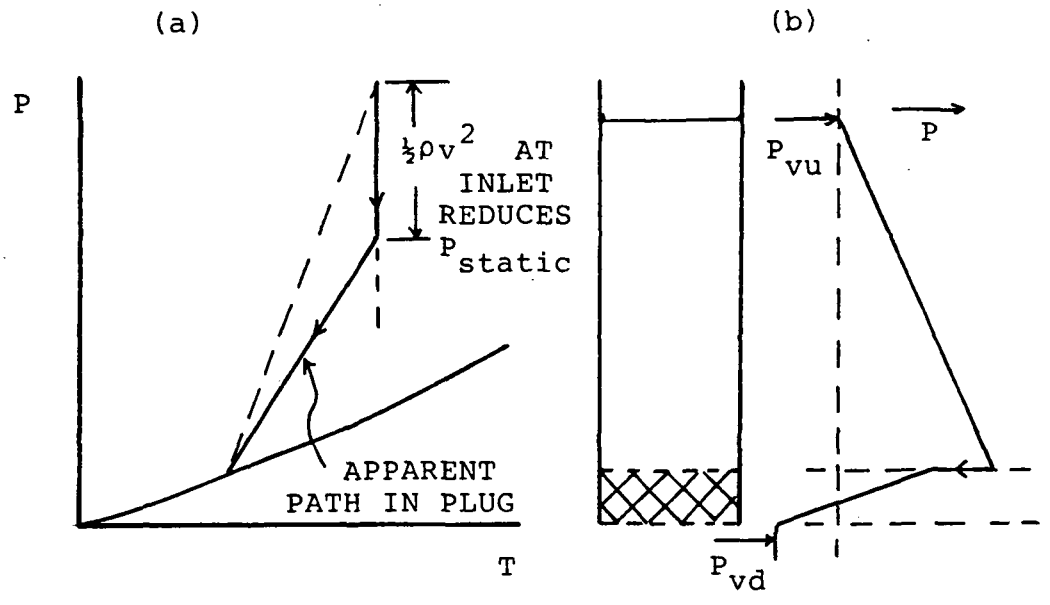

Figure 3.11. Dynamic operation (including kinetic energy) of VLPS (schematic diagram).

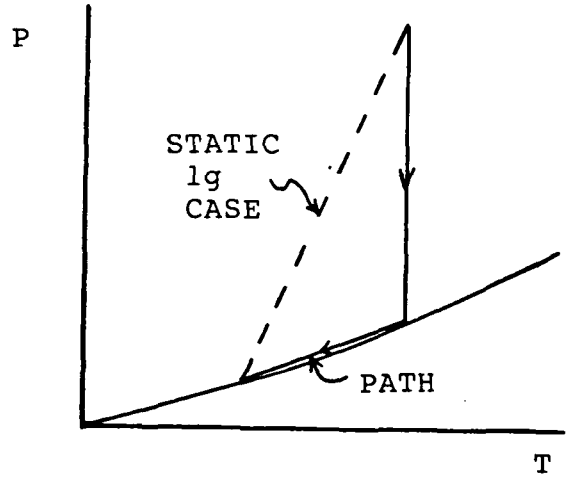

Figure 3.12. VLPS operation at zero gravity (schematic diagram).

$$\Delta P_T = \Delta P_v + \Delta P_\sigma + \Delta P_{dissipation} \qquad (3.54)$$

3.2.2 Heat And Mass Transport In VLPS

The vapor-liquid phase separation mode belongs to the case of finite mass flow. By introducing a relative velocity $\vec{w}$, one can eliminate the superfluid velocity $\vec{v}_s$ in Equation 2.2 and get

$$\vec{j} = \rho\vec{v} = \rho\,\vec{v}_n - \rho_s\vec{w} \qquad (3.55)$$

where

$$\vec{w} = \vec{v}_n - \vec{v}_s \qquad (3.56)$$

For finite mass flow, the heat flux density is usually written as

$$\vec{q} = \rho_s\vec{w}ST \qquad (3.57)$$

Substituting Equation 3.57 into 3.55 and eliminate $\vec{w}$, one gets

$$\rho\vec{v} = \rho\vec{v}_n - \vec{q}/ST \tag{3.58}$$

With the liquid helium being evaporated at the downstream, one can eliminate $\rho\vec{v}$ by

$$\vec{q} = \lambda\vec{j} = \lambda\rho\vec{v} \tag{3.59}$$

and rearrange to get

$$\vec{j} = [ST/(\lambda+ST)]\rho\vec{v}_n \tag{3.60}$$

or

$$\vec{q}_{VLPS} = [\lambda/(\lambda+ST)]\rho ST\vec{v}_n \tag{3.61}$$

Note that on the right hand side of the above equation, $\rho ST\vec{v}_n$ is equal to the heat flux density in the zero net mass flow ($\vec{q}_{ZNMF}$), therefore

$$\vec{q}_{VLPS} = [\lambda/(\lambda+ST)]\vec{q}_{ZNMF} \tag{3.62}$$

One can further substitute Equation 3.16 and 3.28 into Equation 3.62 to get the laminar and turbulent transport equation in a VLPS,

$$\vec{q}_{VLPS}=K_p[\lambda/(\lambda+ST)]\rho^2 S^2|\nabla T|/\eta_n \quad \text{(Laminar)} \tag{3.63}$$

$$\vec{q}_{VLPS}=K^*_{GM}\eta_n ST[\lambda/(\lambda+ST)]\frac{\rho_s}{\rho}(\rho^2\rho_s S|\nabla T|/\rho_n\eta_n^2)^{1/3} \quad \text{(Turbulent)} \tag{3.64}$$

where K^*_{GM} is used to denote the Gorter-Mellink constant in porous media. The term $\lambda/(\lambda+ST)$ in the above equation is quite close to unity because $\lambda<<ST$. It ranges from ~0.999 (at 1 K) to ~0.872 (at T_λ). Therefore it is not unreasonable to assume that the VLPS mode is pretty close to the ZNMF situation. Especially at low temperature, the ZNMF condition should be reached asymptotically.

Figures 3.13 and 3.14 show the property functions in Equations 3.63 and 3.64 (for property data of He II, please

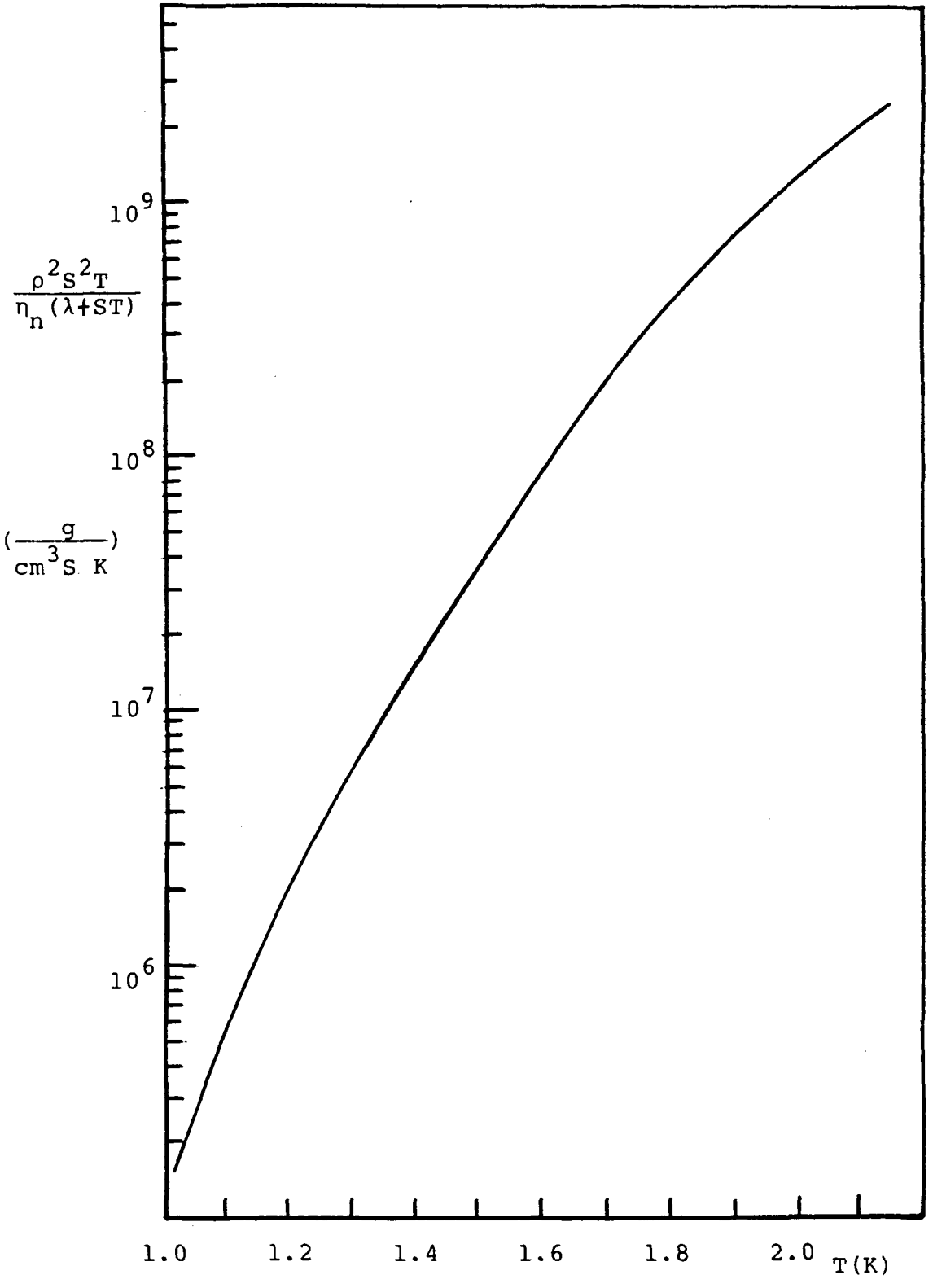

Figure 3.13. Property function in Equation 3.63 versus temperature.

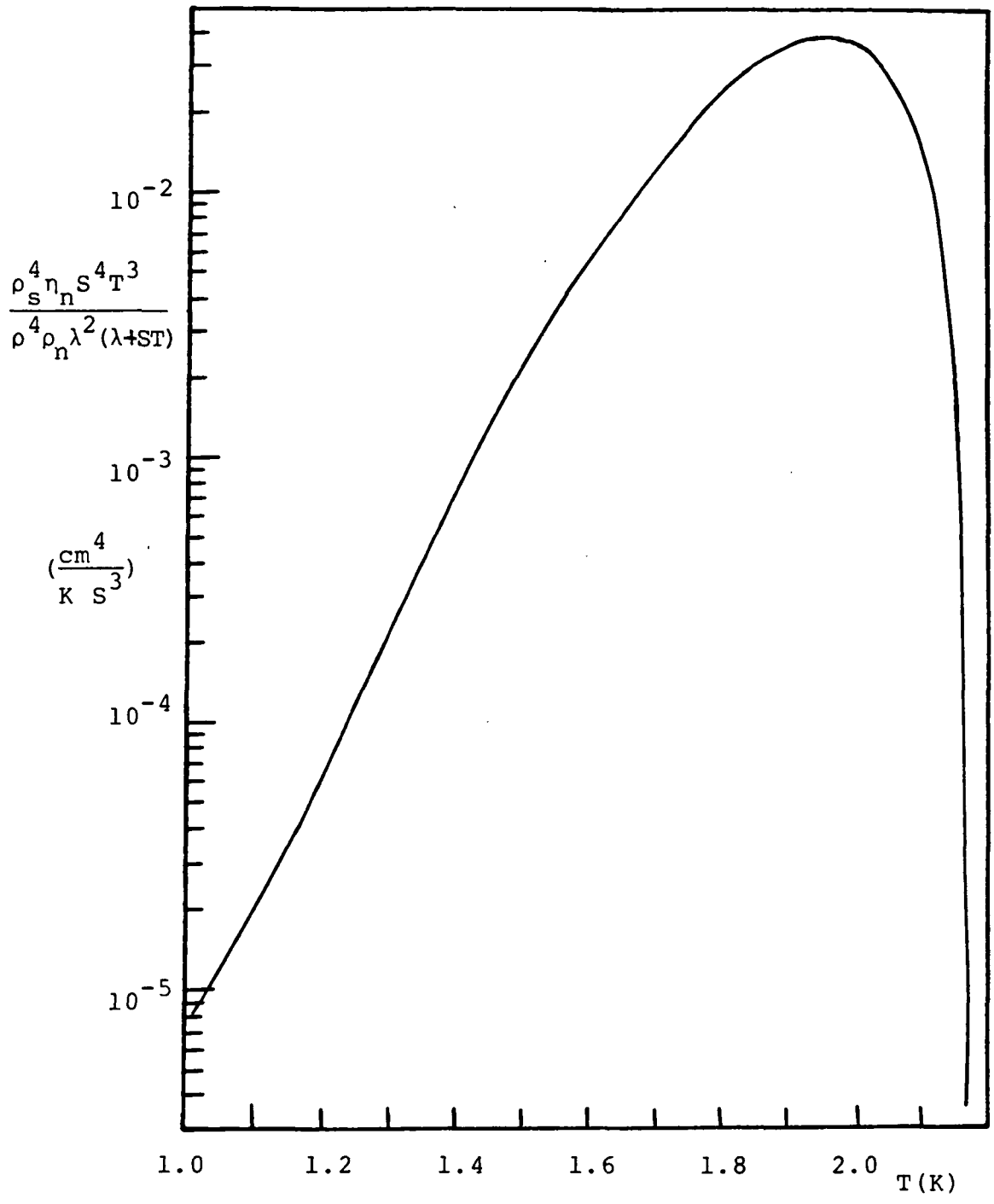

Figure 3.14. Property function in Equation 3.64 versus temperature.

refer to Appendix H). One can see that the heat flux density is a strong function of the thermal properties of He II. Therefore, a small change in temperature will result in a drastic change of the heat flux density $\vec{q}$. Thus in using the preceeding equations, it is recomended to integrate the equations from the downstream temperature T_d to the upstream temperature T_u rather than simply using the arithmetic mean temperature.

Figures 3.15 and 3.16 represent the integrated function for the laminar equation (Eq. 3.63). In Figure 3.15, the downstream temperature is held constant with T_u being varied, where as T_u is held constant as T_d is lowered in Figure 3.16. Similarly, Figures 3.17 and 3.18 show the integrated turbulent equation (Eq. 3.64), with constant T_d in Figure 3.17 and constant T_u in Figure 3.18 (see Appendix C).

3.3 BOUNDARY LAYER MODEL FOR THE TRANSITION INTO TURBULENT FLOW

Consider the flow of He II in a pipe with a boundary layer thickness of δ (Figure 3.19). Outside this layer, He II flows with a relative velocity of $\vec{w}$. Inside the boundary layer, vortex cells are formed due to the shear stress. Lets say that the cells are separated by distances of L_c.

According to the momentum theorem, the effective shear force $\vec{F}$ acting across a mean stream line is equal to the rate of momentum transfer.

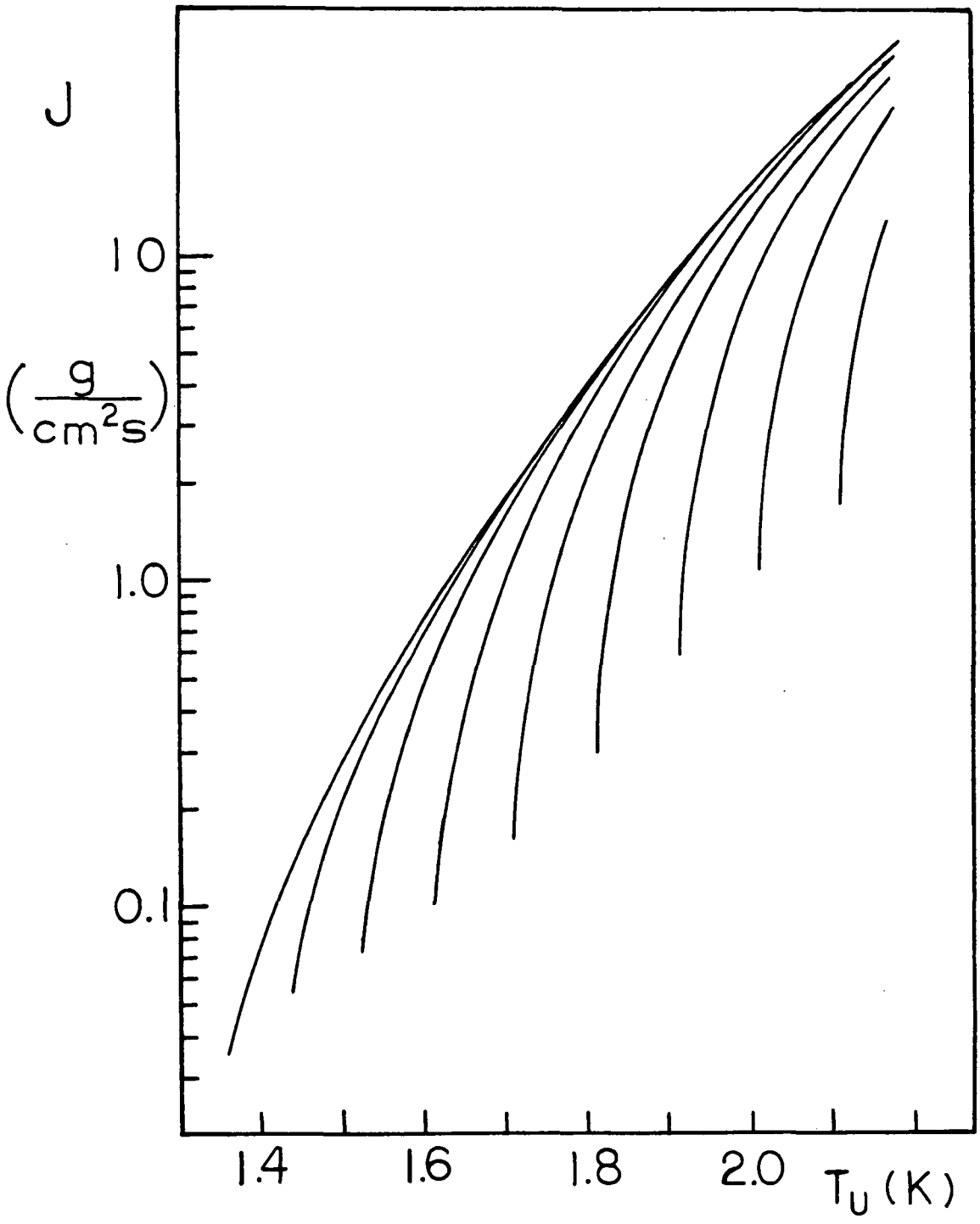

Figure 3.15. Integration of the laminar VLPS equation (Equation 3.63) from constant T_d to various T_u.

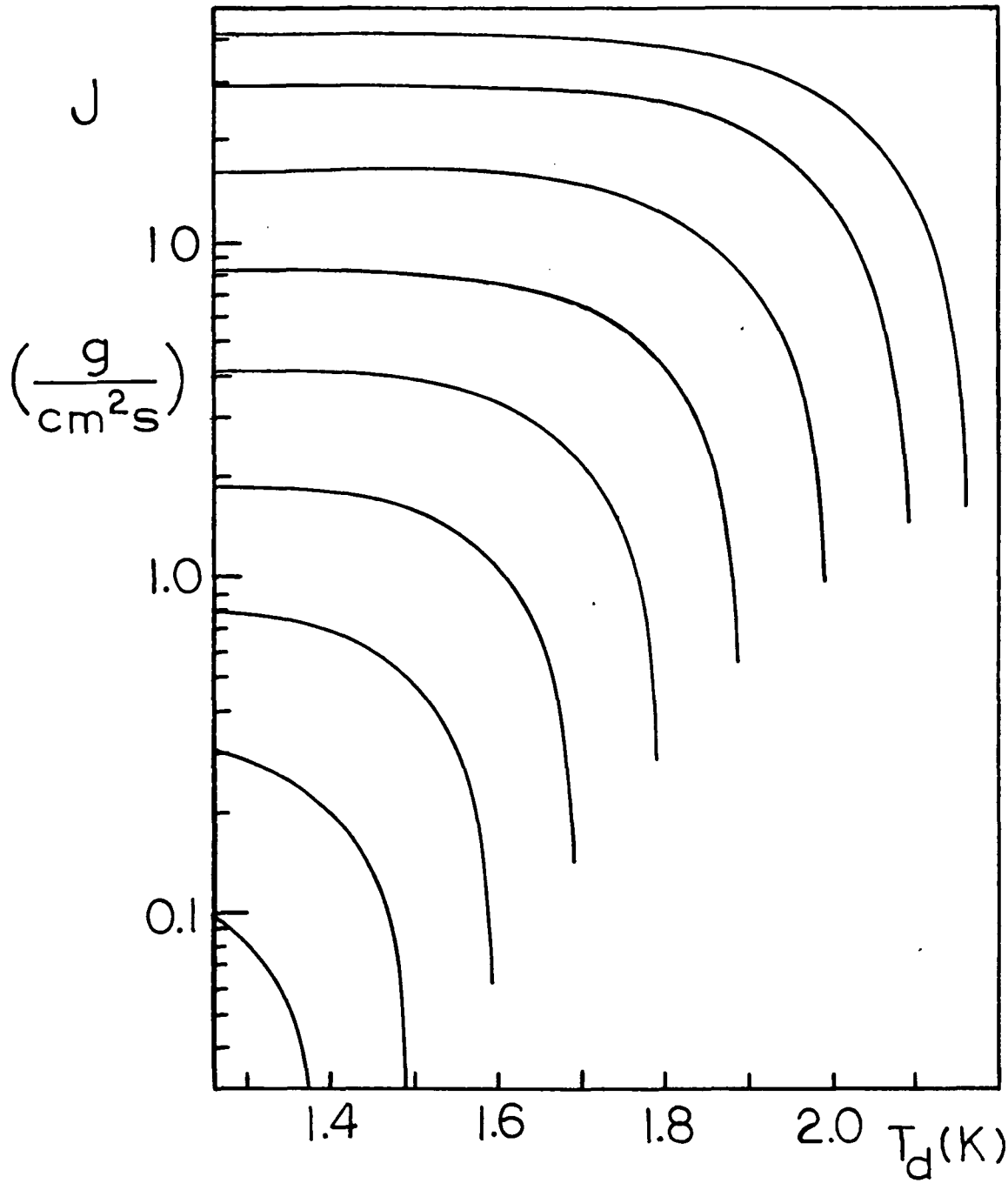

Figure 3.16. Integration of the laminar VLPS equation (Equation 3.63) from various T_d to constant T_u.

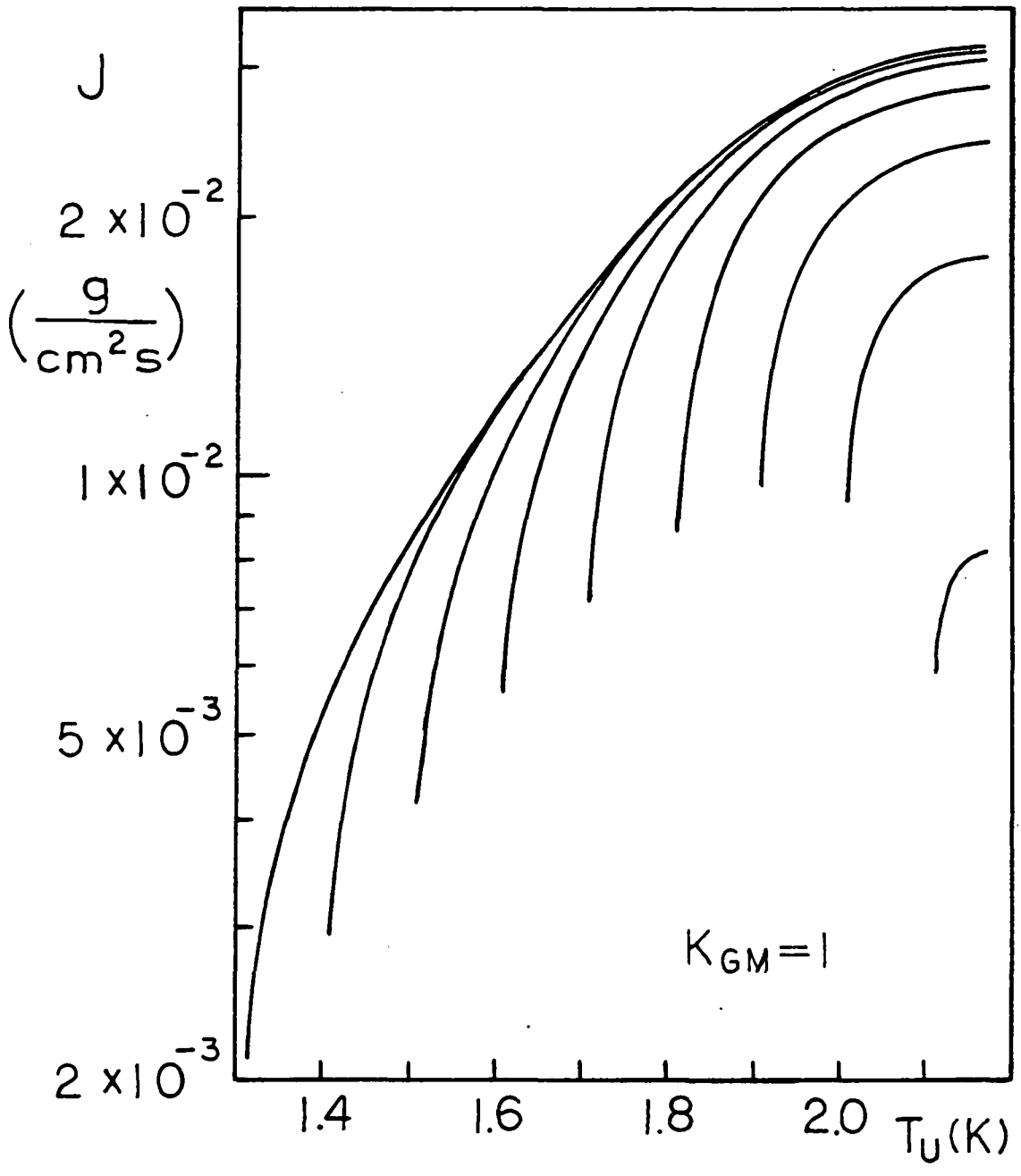

Figure 3.17. Integration of the turbulent VLPS equation (Equation 3.64) from constant T_d to various T_u.

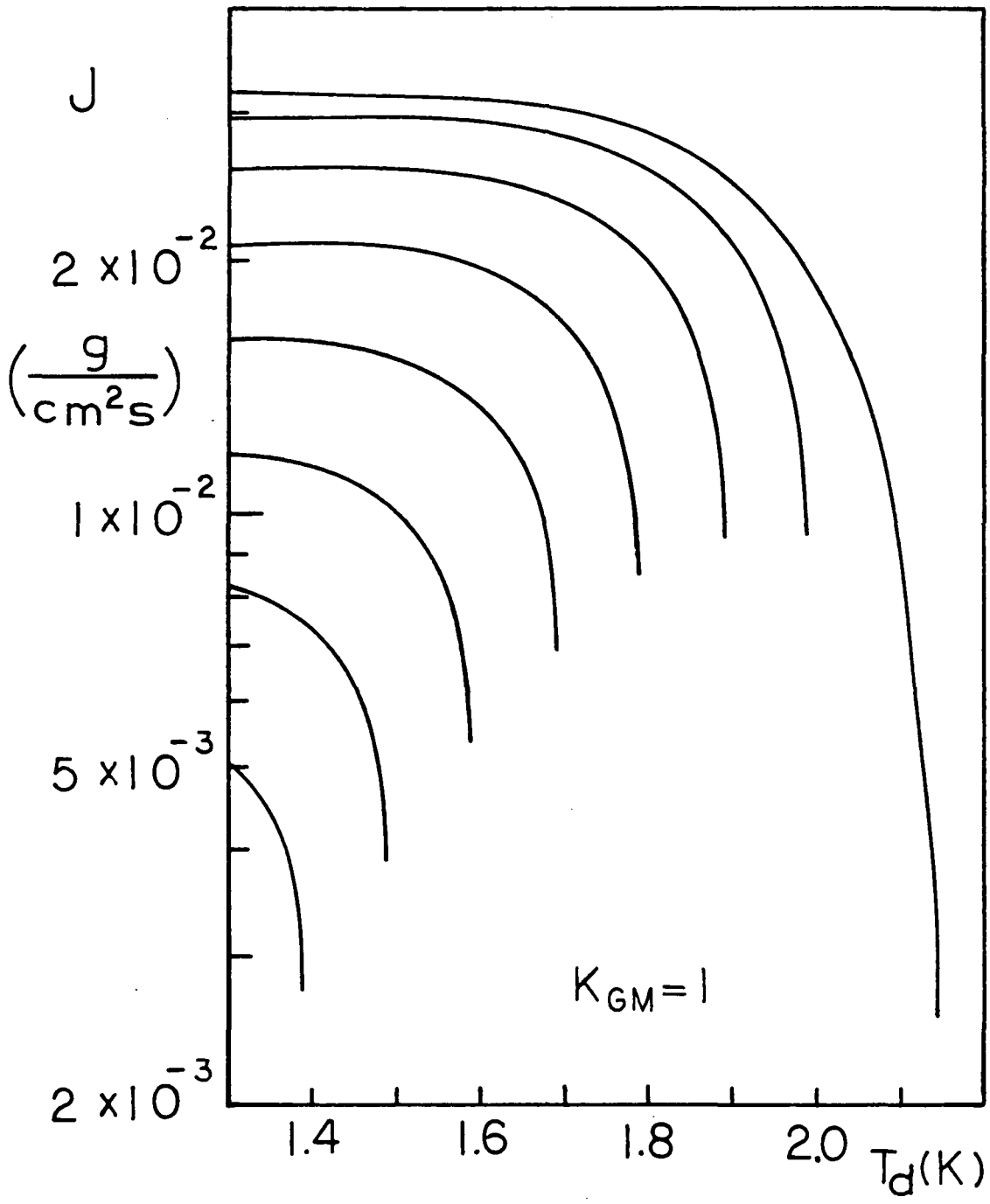

Figure 3.18. Integration of the turbulent VLPS equation (Equation 3.64) from various T_d to constant T_u.

$$\vec{F} = A_w \vec{\tau} = d(m\vec{w}/dt) \tag{3.65}$$

where A_w is the wall area. $\vec{\tau}$ is the shear stress and m is the mass of the fluid.

The rate of change of momentum transfer can be written as

$$\frac{d(m\vec{w})}{dt} = m\vec{\dot{w}} + \vec{w}\dot{m} \tag{3.66}$$

Combining Equation 3.65 and 3.66, for steady state ($\vec{\dot{w}} = 0$)

$$A_w \vec{\tau} = \vec{w}\dot{m} = A_c \vec{w}^2 \rho \tag{3.67}$$

where A_c is the cross sectional area. For unit width $A_c = \delta x 1$ and $A_w = L_c x 1$, the above equation becomes

$$L_c \vec{\tau} = \delta \vec{w}^2 \rho \tag{3.68}$$

By definition

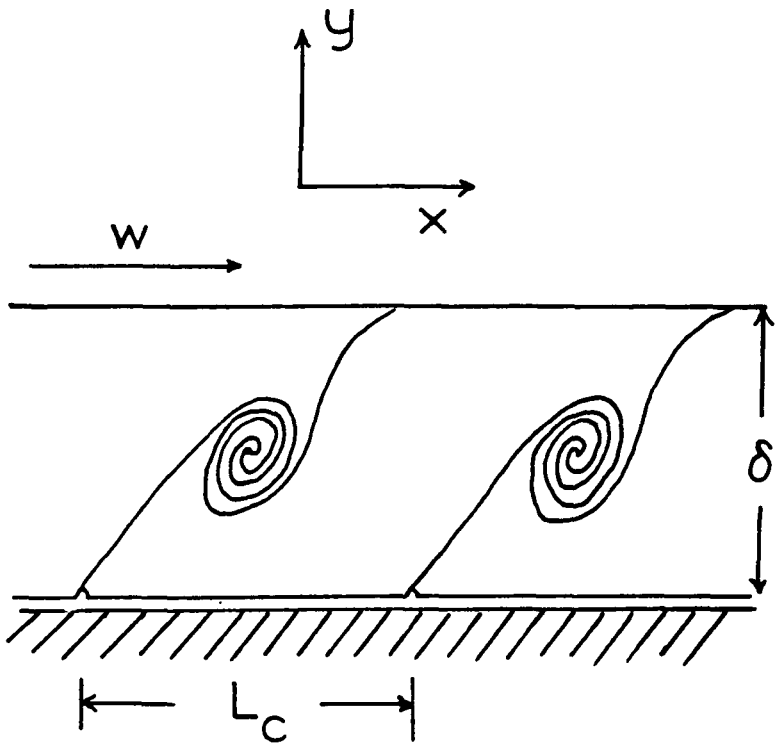

Figure 3.19. Schematic diagram showing the formation of vortex lines within the hydrodynamic boundary layer.

$$\vec{\tau} = \eta_n \left(\frac{\partial \vec{w}}{\partial y}\right) = \eta_n \frac{\vec{w}}{\delta} \tag{3.69}$$

Substituting Equation 3.69 into 3.68, we get

$$\vec{w} = \frac{L_c \eta_n}{\rho \delta^2} \tag{3.70}$$

For pipe flow, the transport of He II is described by the London-Zilsel equation

$$\vec{w} \sim \vec{v}_n = \zeta_o \frac{|\nabla P_T|}{\eta_n} \delta^2 \tag{3.71}$$

with $\zeta_o = 1/8$. Equating Equation 3.70 and 3.71, the boundary layer thickness is found to be

$$\delta = (L_c \eta_n / \zeta_o \rho |\nabla P_T|)^{\frac{1}{4}} \tag{3.72}$$

Substituting Equation 3.69 for δ and multiplying both sides by L_c ,we have

C-2

$$\frac{L_c \tau}{w \eta_n} \sim (\rho \zeta_o |\nabla P_T| L_c^3 \; / \; \eta_n^2)^{\frac{1}{4}} \tag{3.73}$$

If we now define a local friction coefficient

$$C_f = 2\vec{\tau} \; / \; \rho \vec{w}^2 \tag{3.74}$$

then Equation 3.73 can be written as

$$\frac{C_f}{2} \frac{\rho \vec{w} L_c}{\eta_n} = (\zeta_o \rho |\nabla P_T| L_c^3 \; / \; \eta_n^2)^{\frac{1}{4}} \tag{3.75}$$

or

$$\frac{C_f}{2} \frac{\rho}{\rho_s} \frac{\vec{q} L_c}{\eta_{nST}} = (\zeta_o \rho |\nabla P_T| L_c^3 \; / \; \eta_n^2)^{\frac{1}{4}} \tag{3.76}$$

In dimensionless form the preceeding equation becomes

$$\frac{\rho}{\rho_s} N_q = C_B \; (N_{\nabla T})^{\frac{1}{4}} \tag{3.77}$$

where $C_B = 2\zeta_o^{1/4}/C_f$. According to this model, the heat flux density of He II is proportional to the fourth root of temperature gradient instead of the cube root found experimentally in the Gorter-Mellink case.

Chapter IV

APPARATUS AND EXPERIMENTS

The experiments in this research can be divided into two main categories, namely the vapor-liquid phase separation and the permeability measurement experiment.

4.1 VAPOR-LIQUID PHASE SEPARATION EXPERIMENT

4.1.1 Apparatus of VLPS

The apparatus for vapor-liquid phase separation (VLPS) is depicted in Figure 4.1. The plug holder (with porous media) was soldered onto the stainless steel pipe (grade 304, 2.54 cm I.D., 0.051 cm wall thickness) of the main apparatus (as shown in Figure 4.2). For the preparation of the plug holder and the mounting of the porous media please refer to section 4.2.1.3. An outer vacuum jacket (304 stainless steel, 3.2 cm O.D. with 0.051 cm wall thickness) thermally insulated the inner vented helium vapor from the He II bath.

For easy control and reading of the He II liquid level, a Kovar beaker was attached to the apparatus surrounding the outer vacuum jacket

A fountain effect pump was used to replenish liquid helium into the Kovar beaker. A schematic diagram of the fountain effect pump is presented in Figure 4.3. Figure 4.4

THE VLPS APPARATUS

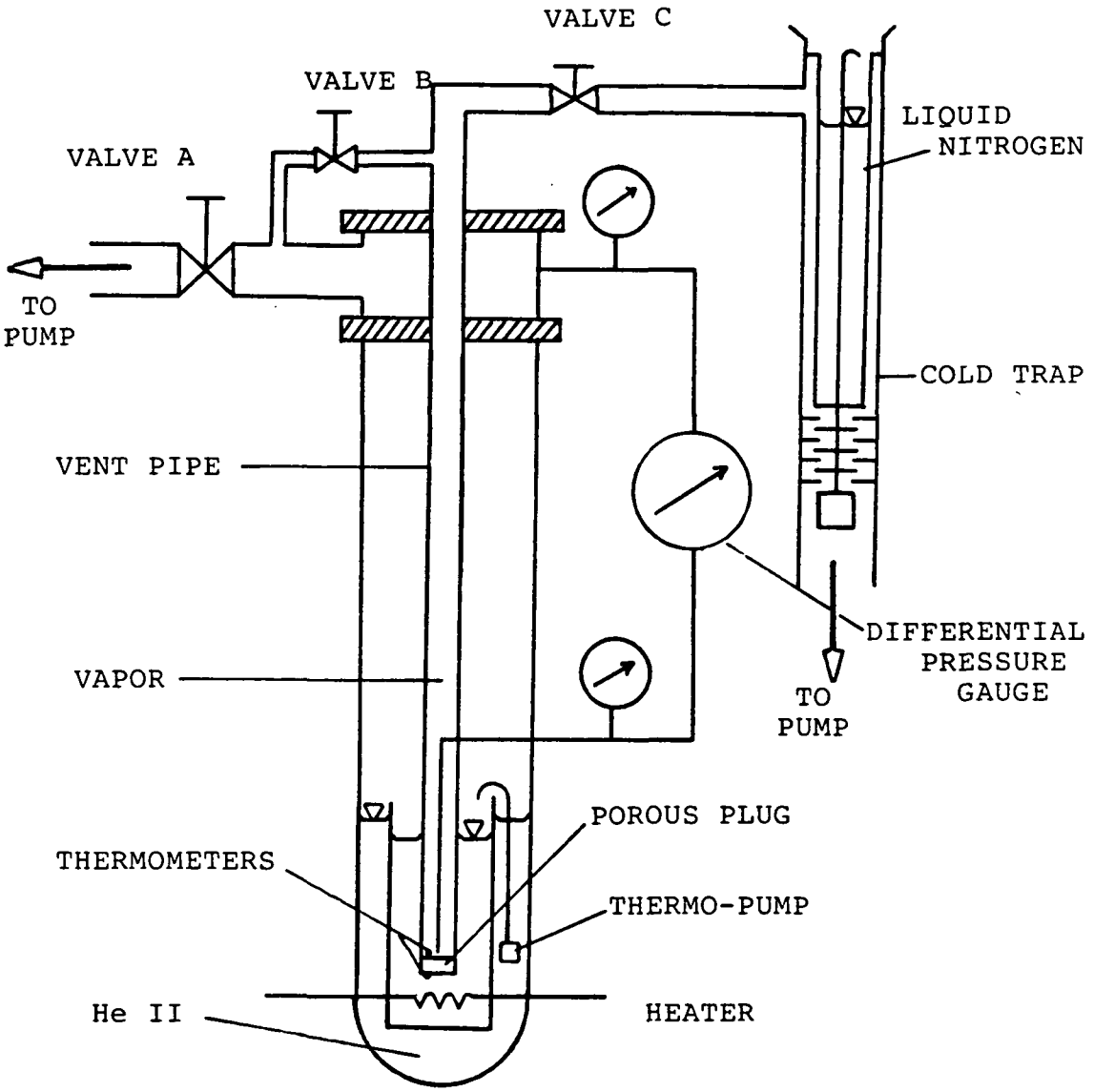

Figure 4.1. Schematic diagram of the VLPS apparatus.

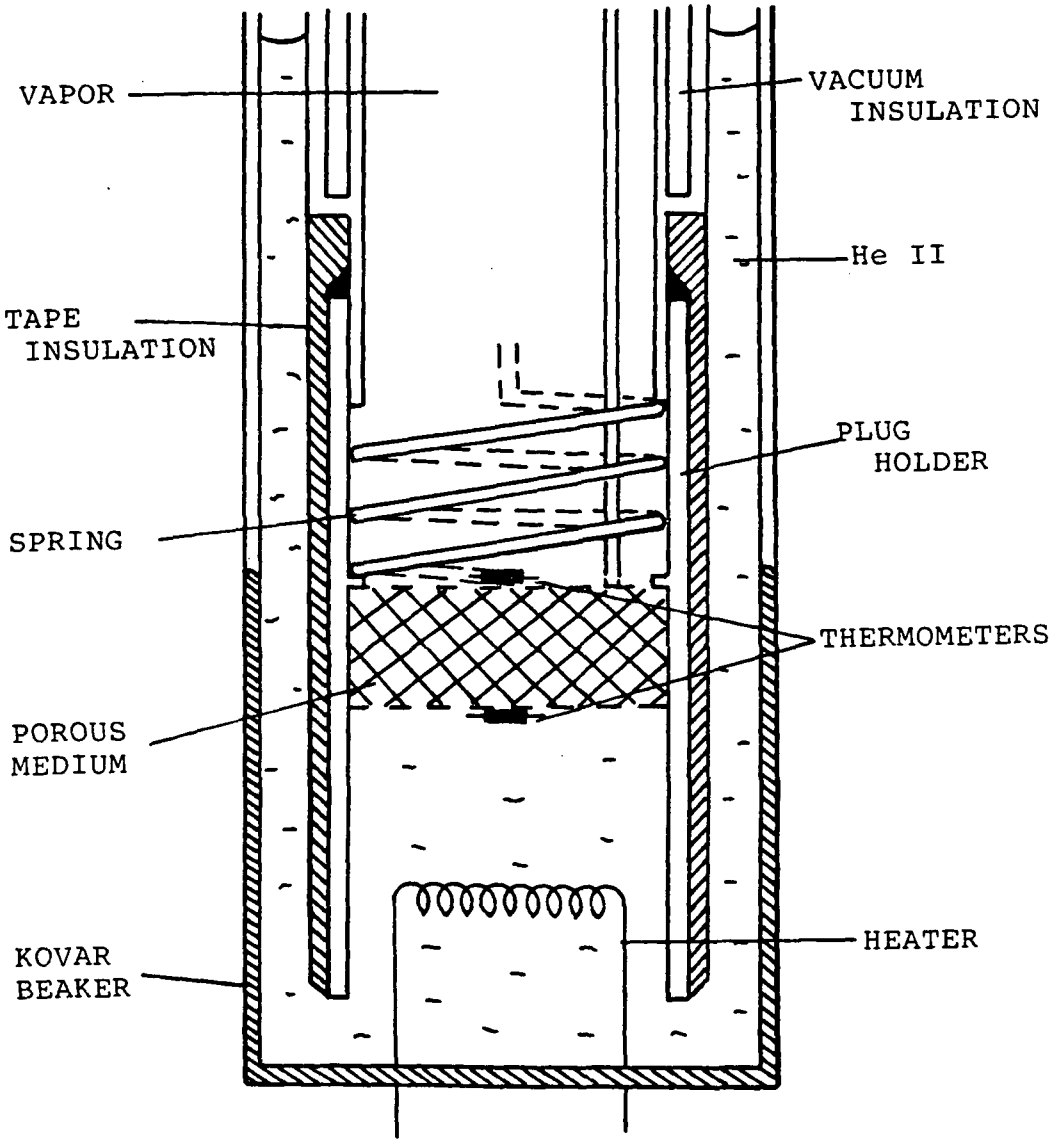

Figure 4.2. Schematic diagram of the vapor-liquid phase separator.

shows the typical results of the fountain effect pump (Yuan et al. 1984). A heater was installed at the bottom of the Kovar beaker to simulate external heat input from the instruments on board of a satellite. The vapor at the downstream vent pipe was pumped away by a Kinney mechanical pump (model KC-46). Between the Kinney pump and the apparatus, a cold trap was installed to prevent any backflow of impurities to the apparatus and thus contaminate the porous media. Figure 4.5 is a schematic diagram of the liquid nitrogen trap.

The temperature difference across the plug was measured by carbon resistor thermometers. A spring made of a thin stainless steel tubing was used to press the downstream thermometer on the porous plug to make sure that it was measuring the temperature right at the vapor-liquid interface (Figure 4.2). Pressure taps were present on both the upstream and downstream of the system. Once again, a spring device was used to press the pressure tap onto the plug at the downstream side.

4.1.2 Thermometry and Heater

The temperatures in the VLPS experiment were measured by carbon resistor thermometers (1/8 watt Allen-Bradley, 39 ohms). The insulation layer of the resistor was removed by sanding the resistor into a thin slab. Teflon-coated copper

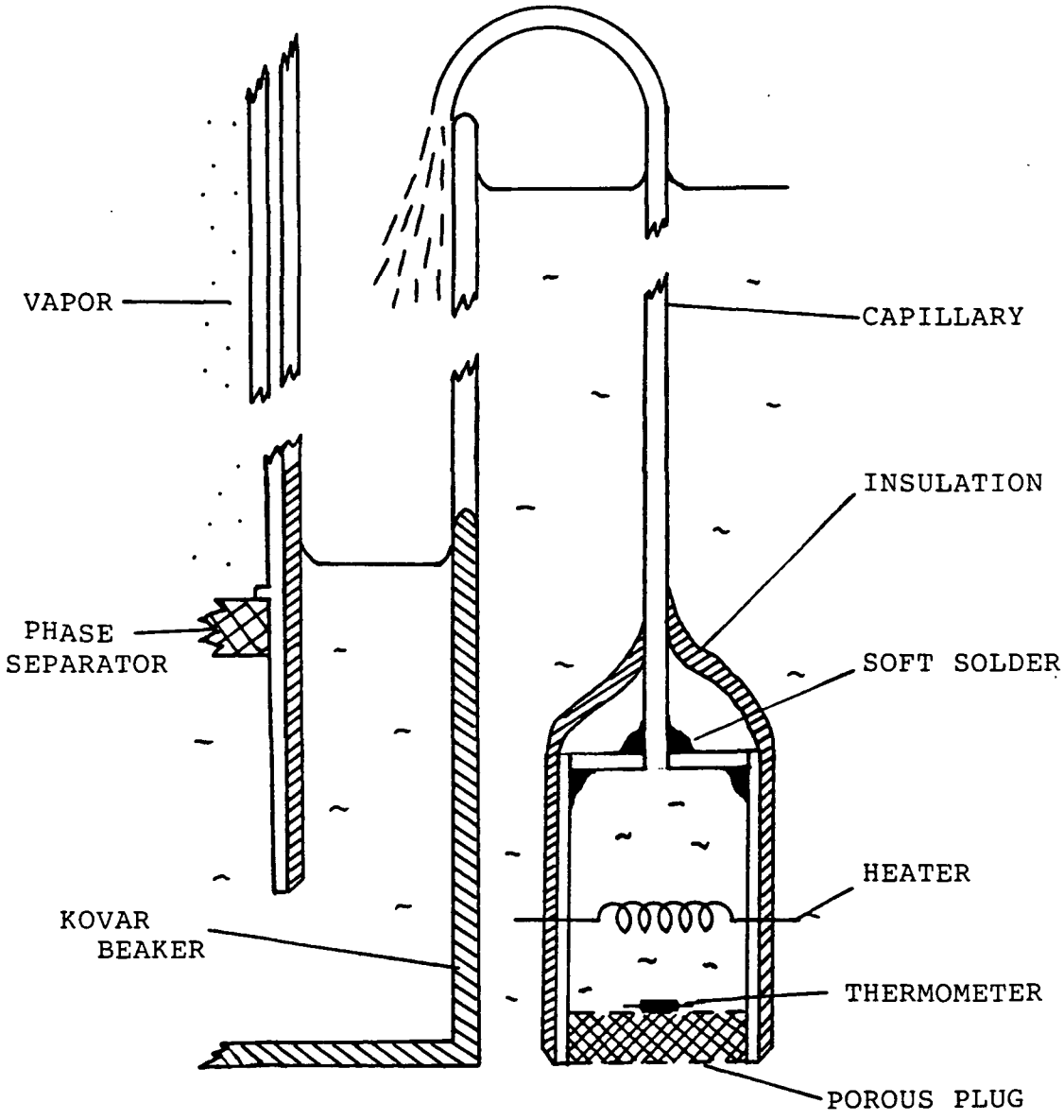

Figure 4.3. Schematic diagram of the thermo-pump used in the VLPS experiments to refill liquid helium.

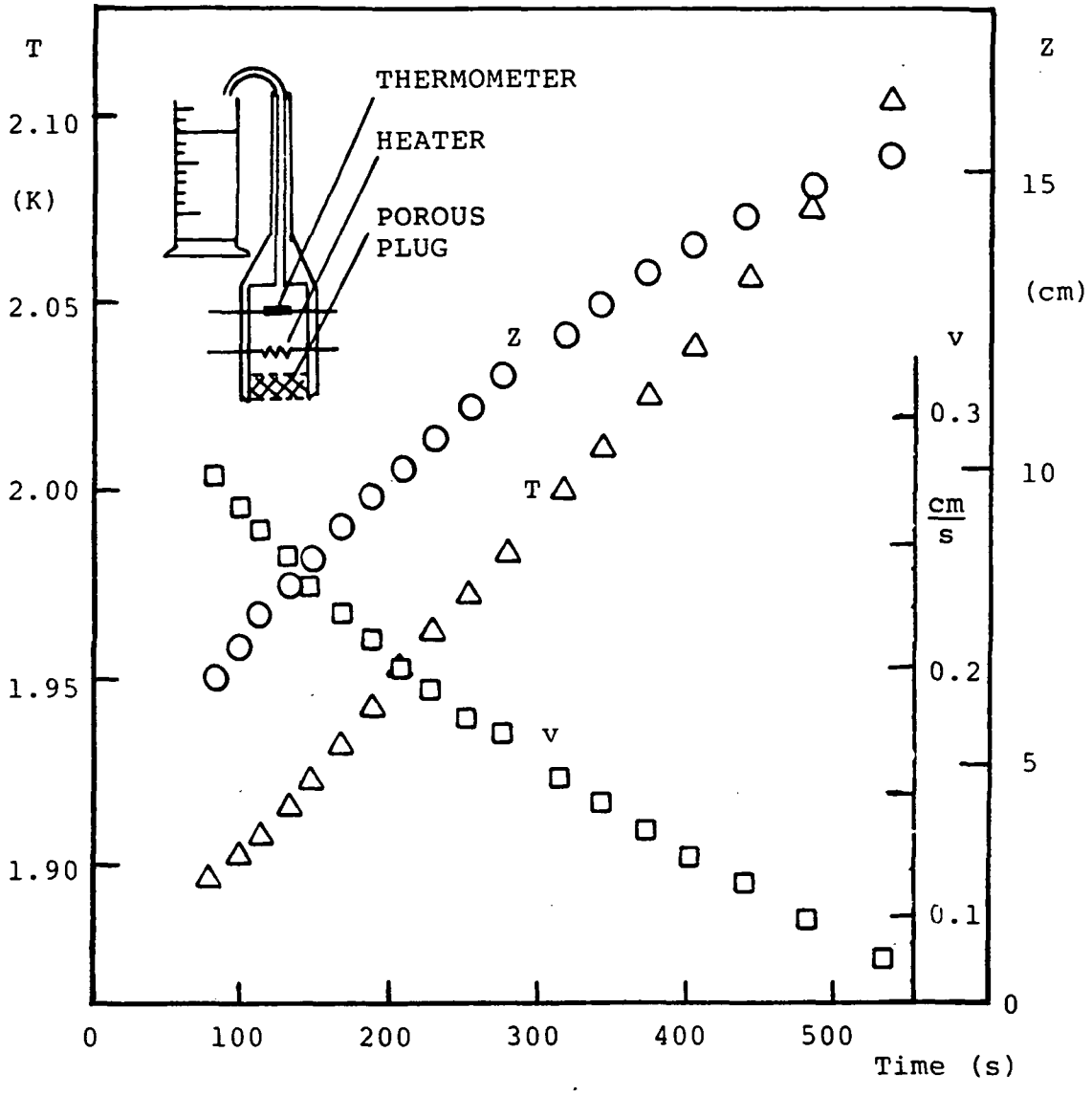

Figure 4.4. Typical results of the fountain effect pump.

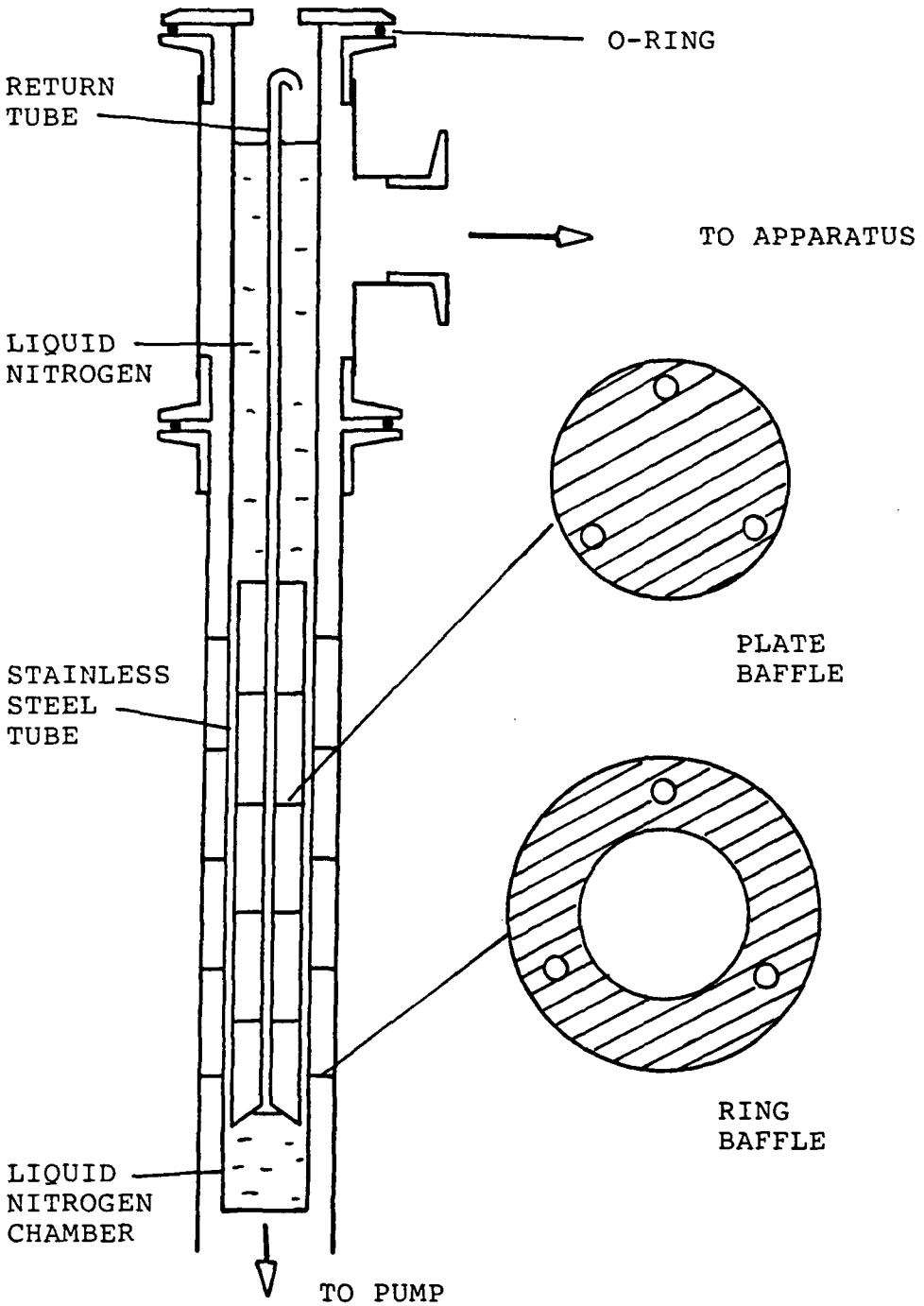

Figure 4.5. Schematic diagram of the liquid nitrogen cold trap.

wires (5 mils diameter) were soldered onto each side of the thermometer. The thermometer was then coated with a thin layer of varnish. Both the upstream and downstream thermometer used in this experiment had a resistance of 93 ohms at room temperature. The resistance measured by the carbon resistor thermometers were calibrated against the Wallace & Tiernan pressure gauges (model FA 145, FA 160). A least squares program was used to fit the resistance and the pressure data by the following equation

$$\log R = A + B \log P \qquad (4.1)$$

where A and B are experimentally determined constants. One can obtain temperature readings from the vapor pressure by using the T-58 scale (Brickwedde et al. 1960). The uncertainty in temperature measurements are discussed in Appendix D.

The heater in the VLPS experiment was made of teflon insulated constantan wire (0.0076 cm, 3 mil in diameter). The wire was wrapped around a short copper tube to increase the heat flux surface area. The heater was then coated with a thin layer of varnish to prevent any short circuit. The heater used had a room temperature resistance of 50 ohms.

4.1.3 Instrumentation

Figures 4.6 and 4.7 depict the circuitry for the heater and the thermometers. Current to the carbon resistors was supplied by a Keithley current source (model 225). Two Houston Instruments X-Y plotters (model 2000) were used to record the resistance across the upstream and downstream thermometers. The heater current was supplied by a Kepco current source (model ABC 40-0.5). A Hewlett Packard Moseley X-Y plotter (model 7035A) was used to record voltage drop across the heater. The vapor pressure across the porous plug was measured by a Pennwalt differential pressure gauge (model 62D-4C-0040D) and a Validyne pressure transducer (model DP 15-20) with a Validyne digital readout (model CD 23). The mass flow rate ($\dot{m}$) of liquid helium through the 5-15 μm bronze plug was measured by a 'pressure mass flow meter'. The pressure difference from the downstream pipe to the vacuum pump (Kinney, model KC-46) was measured by a Wallace & Tiernan absolute pressure gauge (model FA 160). A calibration curve of $\dot{m}$ versus pressure difference is shown in Appendix E. The bath temperature of liquid helium above and below T_λ were recorded by Wallace & Tiernan pressure gauges FA 145 and FA 160 respectively, on the basis of vapor pressure thermometry.

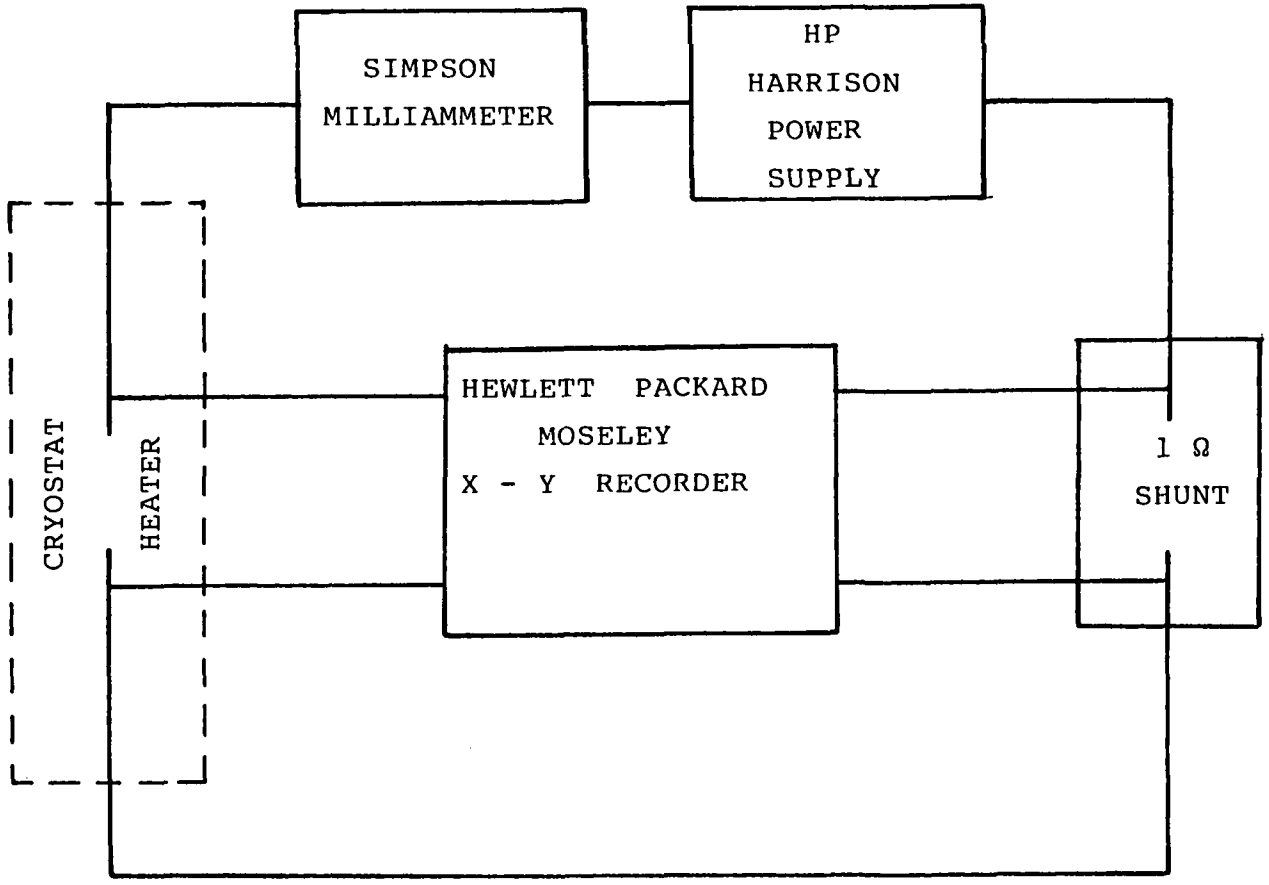

Figure 4.6. Circuitry for the heater of the VLPS experiments.

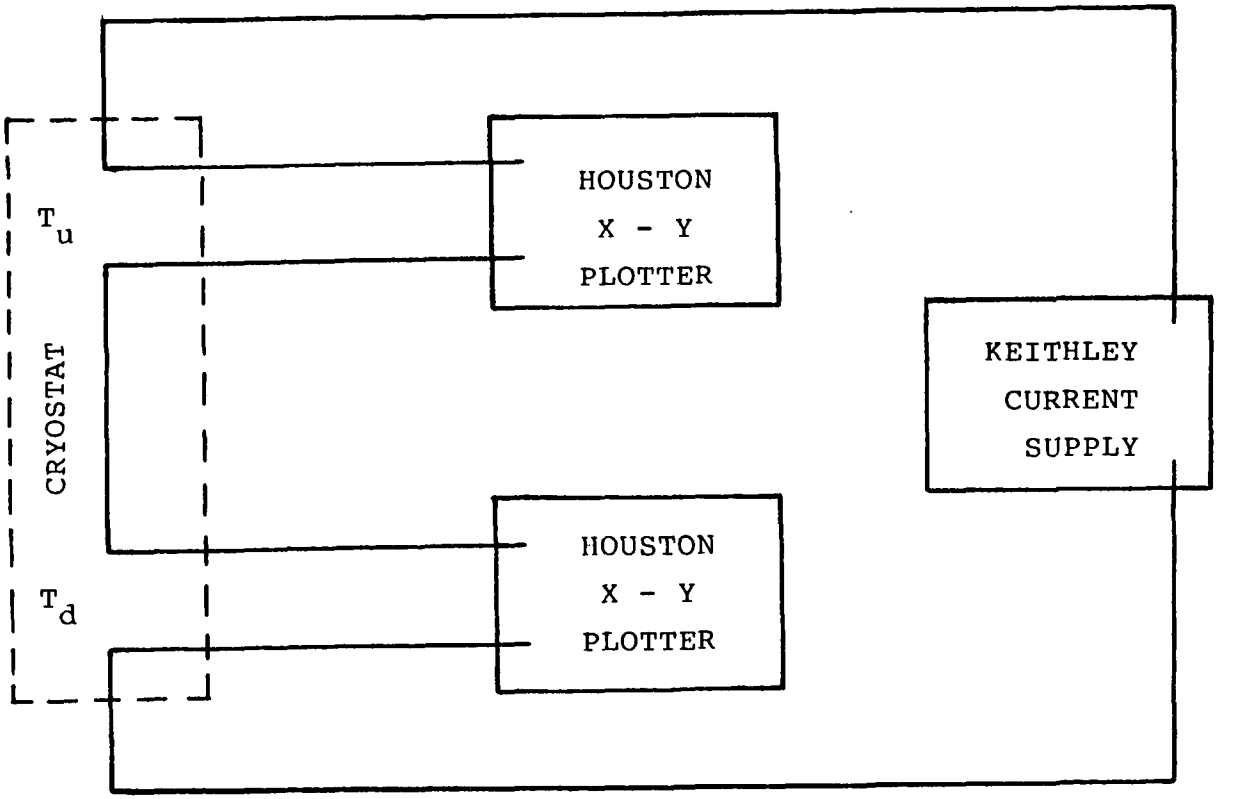

Figure 4.7. Circuitry for the thermometers in the VLPS experiments.

4.1.4 Procedures for the VLPS Experiment

The VLPS experiment was carried out in an existing cryostat. A schematic diagram of the entire system is presented in Figure 4.8.

Prior to the experiment, liquid nitrogen was transferred into the outer jacket. The by-pass valve (valve B) was opened to equilibrate the pressure between the upstream and downstream of the plug. The dewar was then evacuated overnight by opening the main valve A with valve C closed. The apparatus was purged with helium gas, and the evacuation was repeated for at least two times. Liquid helium was then transferred into the inner dewar. In order to cool the system down to He II temperature, the vapor pressure on top of the liquid helium was reduced. Latent heat of vaporization was taken away and the system was cooled down following the vapor pressure curve. During the cool down process, the thermometers were calibrated by recording the bath temperature and the resistance readings of the carbon resistor thermometers. The cold trap was filled with liquid nitrogen and the apparatus was ready for the experiment.

The system was operated in three different methods:

4.1.4.1 The Transient Cool Down Experiment

In this experiment, the by-pass valve (B) was closed and the downstream helium vapor was pumped away by opening valve C. Data were taken as soon as the VLPS mode was reached.

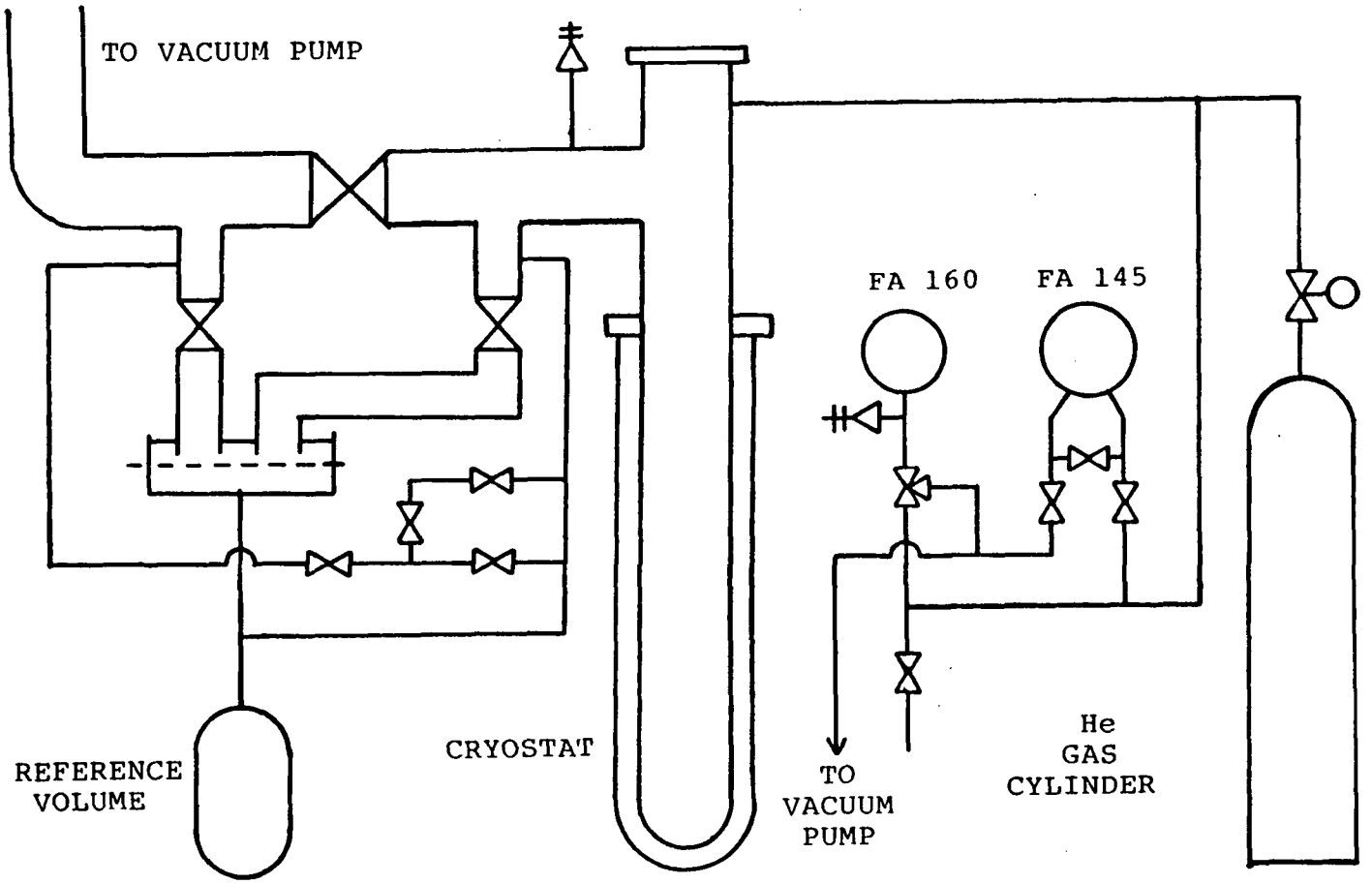

Figure 4.8. Schematic diagram of the cryostat system.

Since the vapor at the downstream was continuously being pumped away, the bath temperature got lower and lower until steady state was reached (Figure 4.9). The experiment was repeated with different heater power input ($\dot{Q}$=0 mW, 50 mW, 100 mW, 150 mW, 200 mW etc.).

4.1.4.2 The Transient Warm Up Experiment

The heater power was increased mechanically by using a potentiometer. Starting with no heater input, the system was ramped up to 1000 mW. The speed of the ramping was pre-programmed. Data were collected as the heater power increased (Figure 4.10).

4.1.4.3 The Steady State Experiment

For the steady state runs, the heater power was stepped up (or down) in increments of 50 or 100 mW. Data were recorded when the upstream and downstream temperatures reached steady state. After recording the data, the heater power was stepped up (or down) to the next value (Figure 4.11).

In each of the above experiments, the upstream and downstream temperatures, vapor pressure differences, mass flow rates and bath temperatures were recorded.

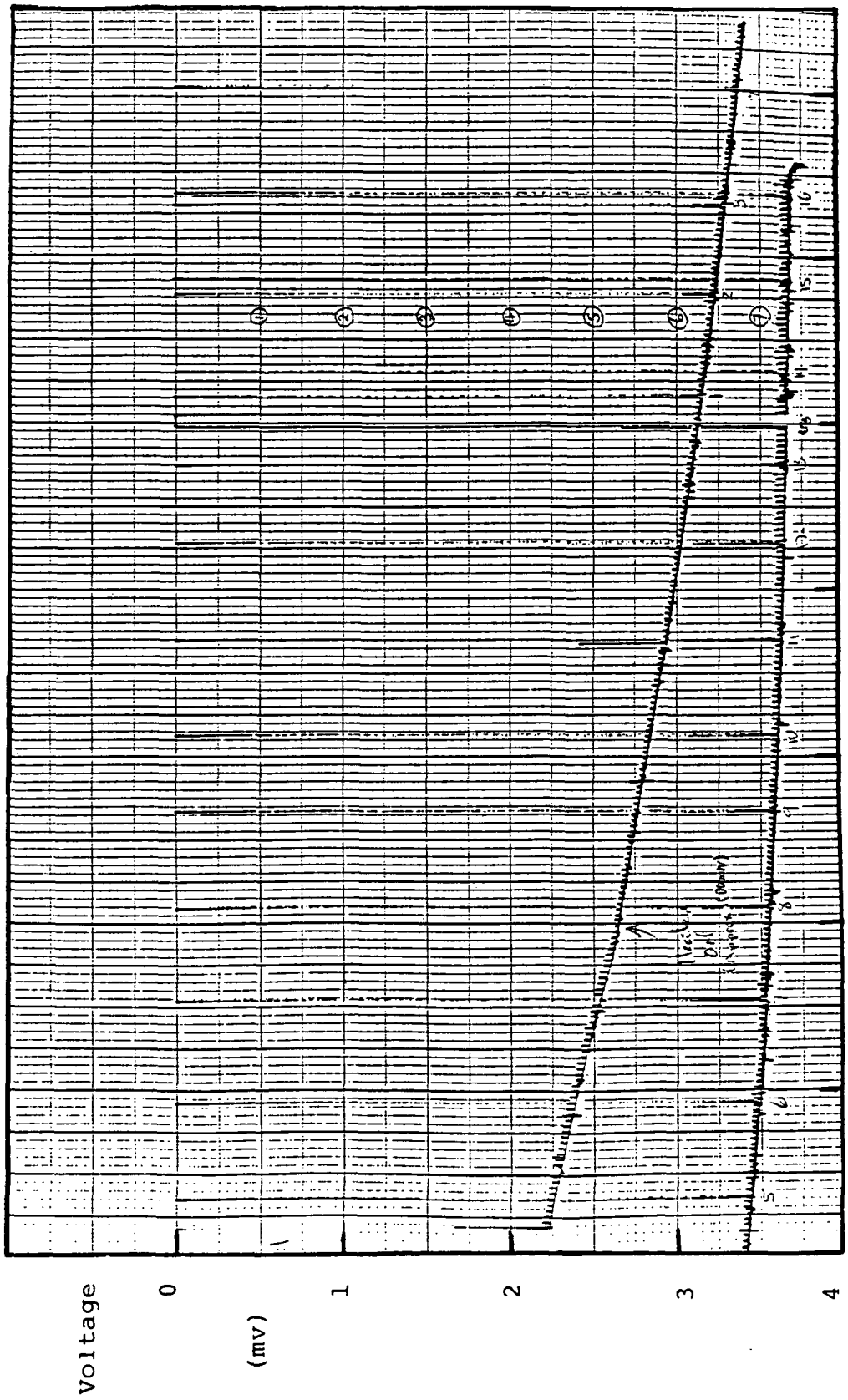

Figure 4.9. Typical run of VLPS, data collected by the transient cool down technique.

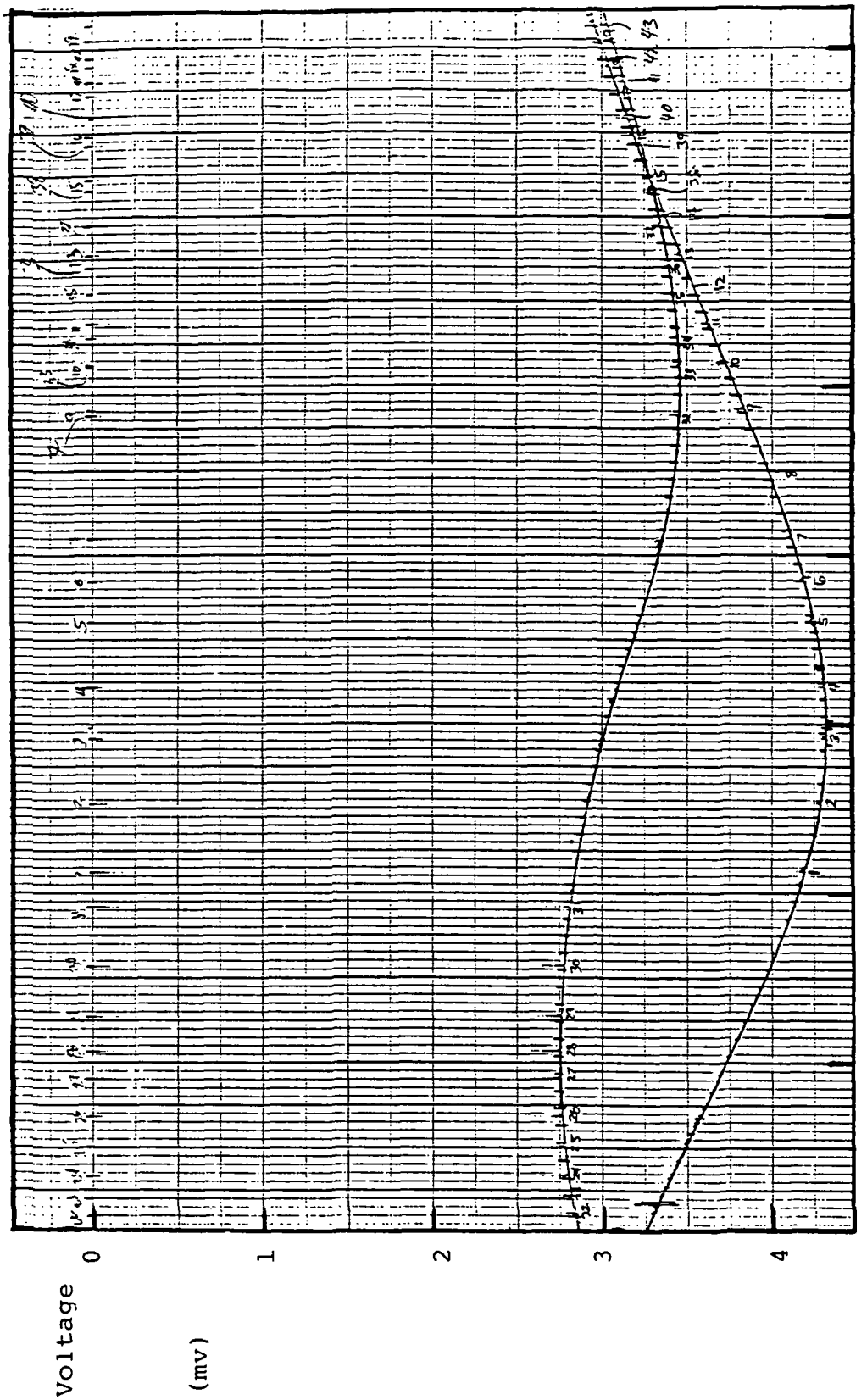

Figure 4.10. Typical run of VLPS, data collected by the transient warm up technique.

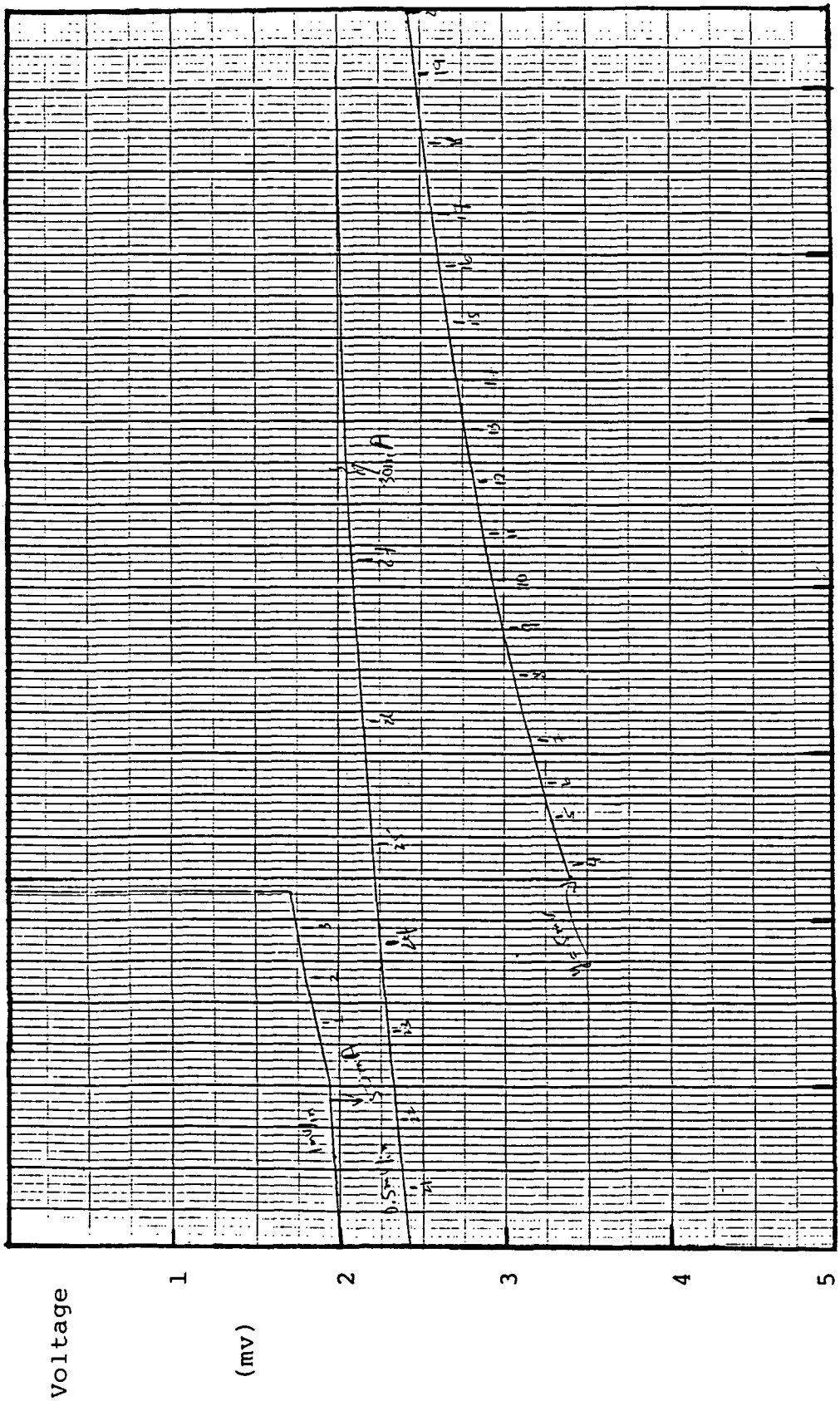

Figure 4.11. Typical run of VLPS, data collected by the steady state technique and quasi-steady approaches respectively.

4.2 PERMEABILITY MEASSUEMENT EXPERIMENTS

There are a number of ways one can measure the permeability of porous media. In this section, the pressurized helium gas permeability determination, the liquid outflow experiment of He I and the cold vapor permeability measurement at below 4.2 K will be discussed.

4.2.1 Pressurized Helium Gas Permeability

In this experiment, the permeability K_p was measured by passing helium gas through the porous plugs. The K_p's were calculated from Darcy's law. Figure 4.12 is a schematic diagram of the apparatus. The main part of the apparatus consists of a plug chamber made of stainless steel (grade 304, O.D.=2.54 cm, wall thickness = 0.065 cm), Figure 4.13. The end caps of the plug holders were machined out of brass. Incorporated within both end caps were provisions for helium gas throughput tubings, thermocouple leads and pressure taps. Rectifying tubes were installed at the upstream end cap. Copper mesh was stuffed between the end cap and the rectifying plate to trap and absorb any impurities in the helium gas. A heat exchanger (made of copper tubing with O.D.=3.18 cm wound into a spiral coil) was installed between the plug chamber and the helium gas cylinder. Such a heat exchanger acted as a cold trap for permeability tests below room temperature. Without the cold trap, impurities would condense in the porous media and reduce the K_p. The porous

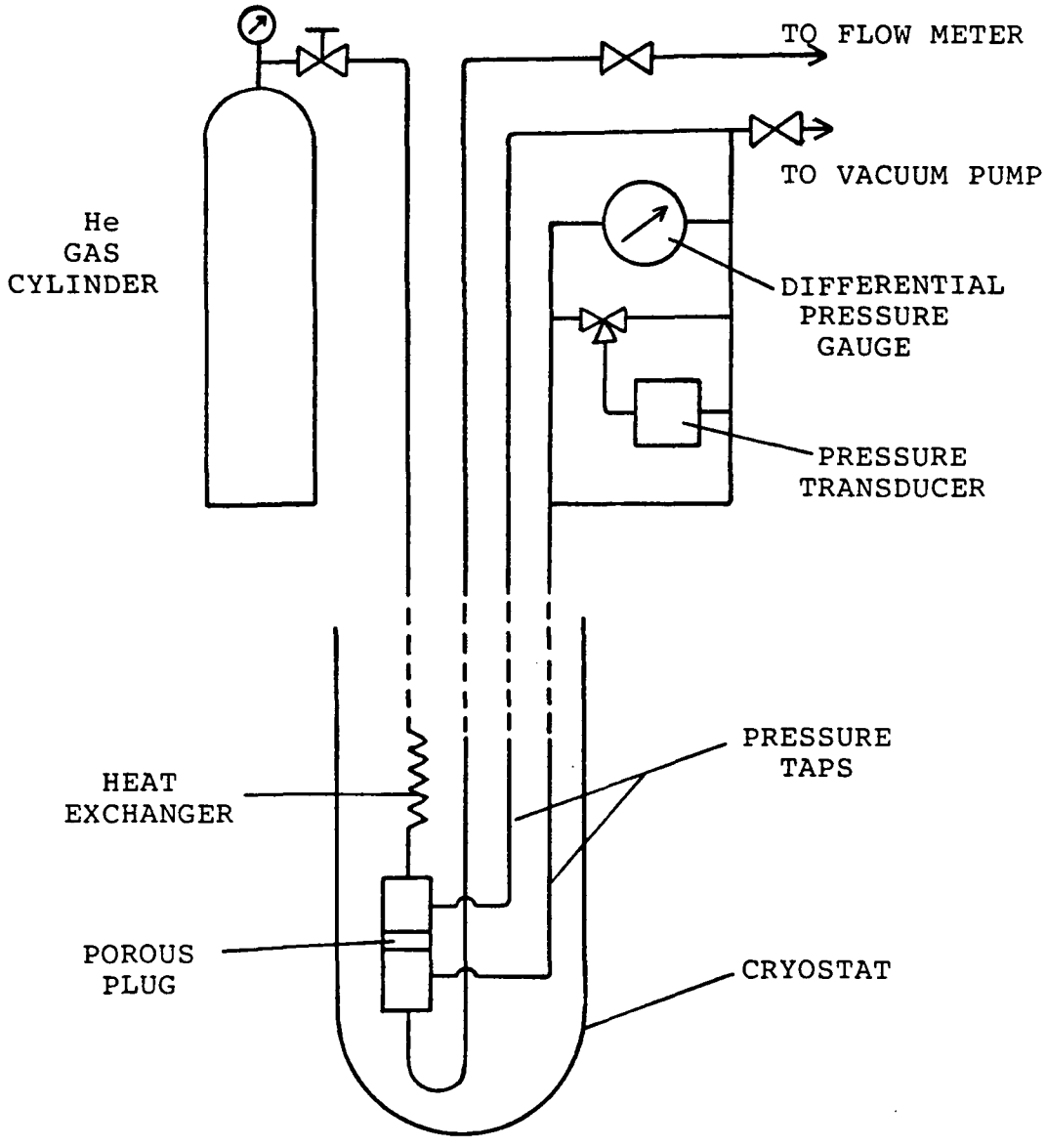

Figure 4.12. Schematic diagram of the permeability measurement apparatus.

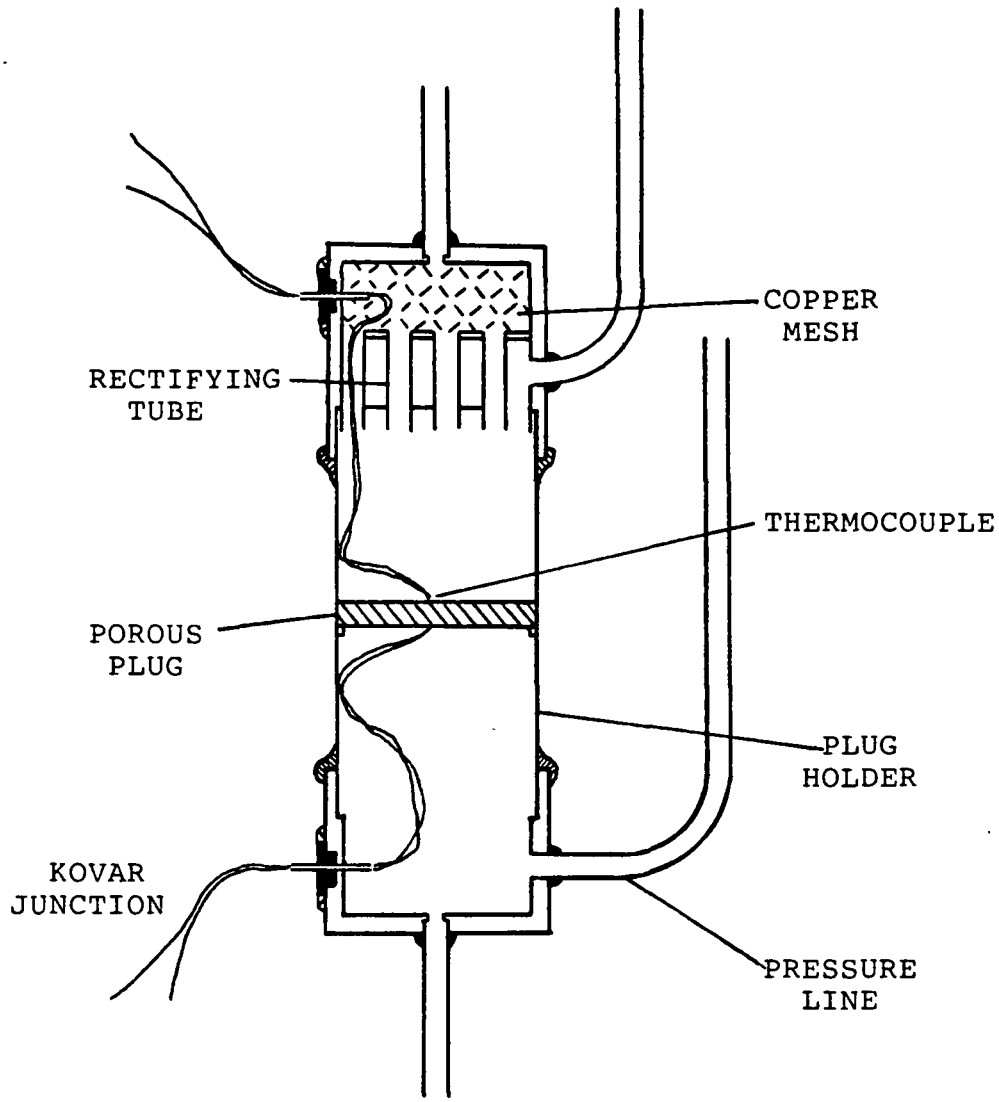

Figure 4.13. Schematic diagram of the permeability measurement chamber.

plugs were mounted onto the plug holders by Stycast (1266). Pressure taps were present at both the upstream and downstream side of the plug to measure the differential pressure. Thermocouples were used to sense temperature within the plug chamber, Figure 4.13.

4.2.1.1 Thermometry

In this experiment, the temperatures within the plug chamber were measured by thermocouples made of Chromel-Constantan wires (0.0076 cm, 3 mils in diameter). The thermocouples were positioned on both the upstream and downstream side of the plug. The constantan wires ran from the reference temperature bath to the inside of the plug chamber through a Kovar lead (as shown in Figure 4.13). Stycast (1266) was used to seal the gap between the wires and the Kovar leads. The thermocouples had been calibrated against temperature at three fixed points (as shown in Appendix E) and was found to agree within 2 K with the data of NBS Circular 561 (1955) and Omega Engineering Manual (1979).

4.2.1.2 Instrumentation

The helium gas flow rate was measured by a Precision Scientific wet-test flow meter (model 63118) and a Brooks Instruments rotameter (model P-72-H-RO). The differential pressure across the plug was recorded by a Pennwalt differential pressure gauge (model 62D-4C-0040D) and a Validyne

pressure transducer (model DP 15-20) with a Validyne digital readout (model CD 23). The voltage across the thermocouples were recorded by two Houston X-Y plotters (model 2000) as shown in Figure 4.14.

4.2.1.3 Procedures for Pressurized Helium Gas Permeability Tests

Before the experiments, the porous plugs to be tested had to be mounted onto the plug holders. The plug holders were machined out of stainless steel pipes and their dimensions are presented in Figure 4.15. After weighing the plugs on a beam balance (to determine their porosity ε) they were glued onto the plug holders by Stycast (1266). Precaution has to be taken such that the viscosity of the Stycast was not too low that it would be soaked into the pores of the plugs. The end caps were then soldered onto the plug holder. For room temperature permeability measurements the procedures were simple. Helium gas was passed from the gas cylinder to the test chamber, Figure 4.12. The gas flow rate was controlled by a Matheson regulator (model 3104 A). Flow rate and differential pressure readings were then recorded. To test another porous medium, simply unsolder the end caps and put in a new holder with the plug to be tested.

For permeability measurements below room temperature (say at liquid nitrogen temperature, 77 K), the procedures were slightly modified. The cryostat in Figure 4.12 was filled with liquid nitrogen. Besides recording the flow rate and

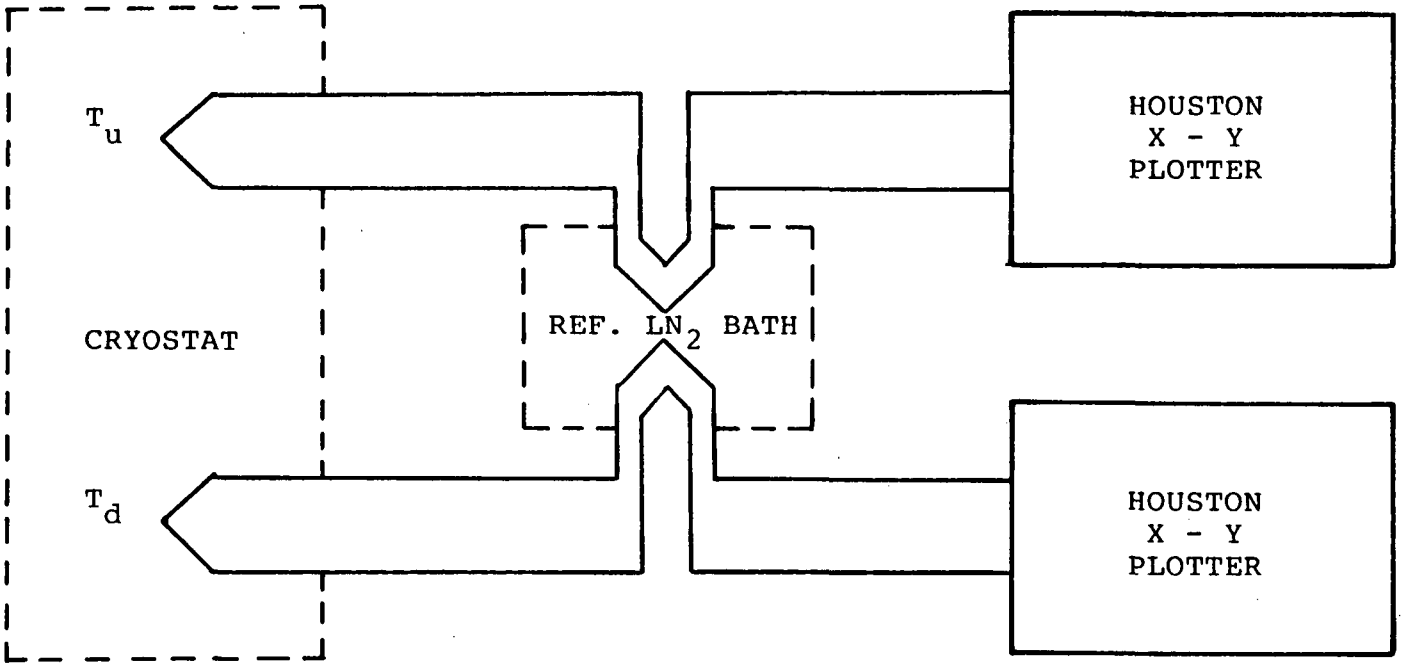

Figure 4.14. Circuitry for the permeability measurement experiments.

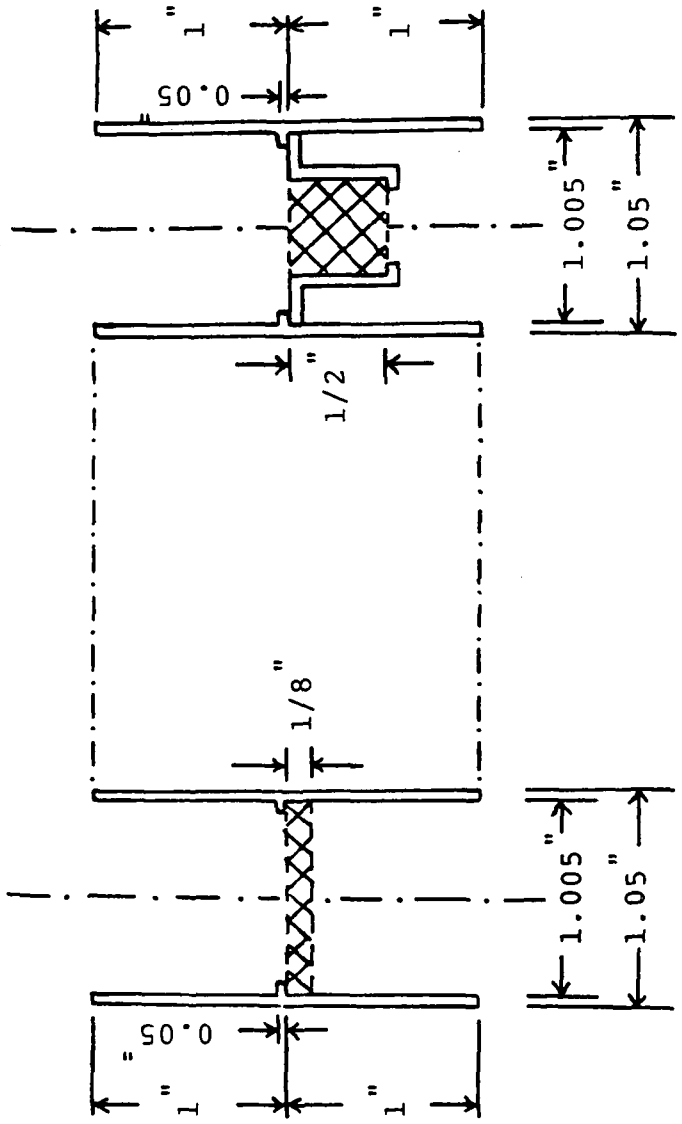

Figure 4.15. Dimensions of the porous plug holder for a 1 inch and a 1/2 inch diameter porous plug.

the differential pressure, both the upstream and the downstream temperatures were measured. A Union Carbide molecular sieve (part# SG 6140) was also installed between the gas cylinder and the apparatus to remove any impurities that might be condensed in the porous plugs.

4.2.2 Liquid Outflow Permeability of Helium I

For the liquid outflow tests, the experiment was conducted using the VLPS apparatus. Therefore both the instrumentation and thermometry & heater description will be same as section 4.1. The only difference was the procedures of operation. The experiment was performed at temperature above the T_λ. Referring to Figure 4.1, the by-pass valve (B) was closed and the downstream pressure was reduced by opening valve C. Liquid He I was forced through the porous plug and accumulated at the downstream vent pipe. The by-pass valve was then opened with valve C closed allowing the liquid to flow back into the upstream beaker under gravitation force. The liquid level, temperature and time were recorded. Permealility was calculated by the Darcy limit of Ergun's equation. Figure 4.16 is a schematic diagram of the He I outflow experiment.

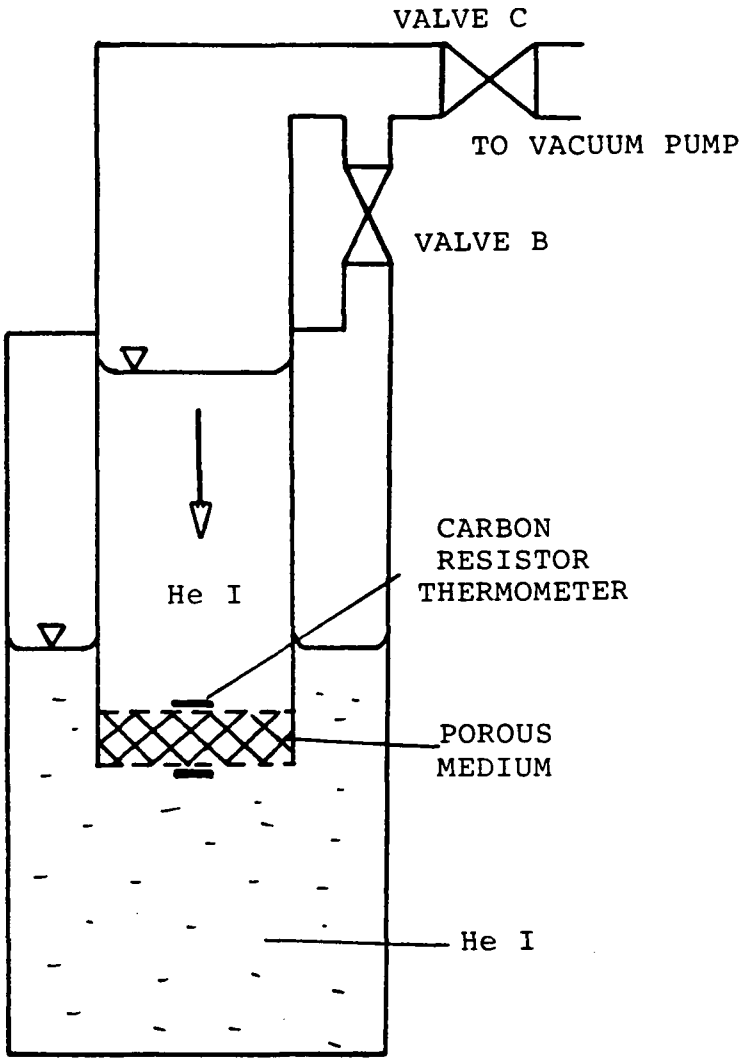

Figure 4.16. Schematic diagram of the liquid He I outflow experiment.

4.2.3 Cold Vapor Helium Gas Permeability

This experiment was also performed in the VLPS apparatus. Data were collected when the liquid level was below the porous plug. The vapor at the vent line was pumped away by the Kinney pump with valve C open. The upstream and downstream of the system was isolated with valve B close. The gas flow rate was controlled by liquid boil-off using the heater, see Figure 4.17. Data were collected at temperatures below 4.2 K. The mass flow rate was measured at the downstream side by using a line section as 'pressure mass flow meter' (for the calibration of the mass flow meter, see Appendix E). Both the vapor pressure difference and the temperature across the plug were recorded. The cold vapor permeability was calculated by the Darcy limit of the Ergun equation.

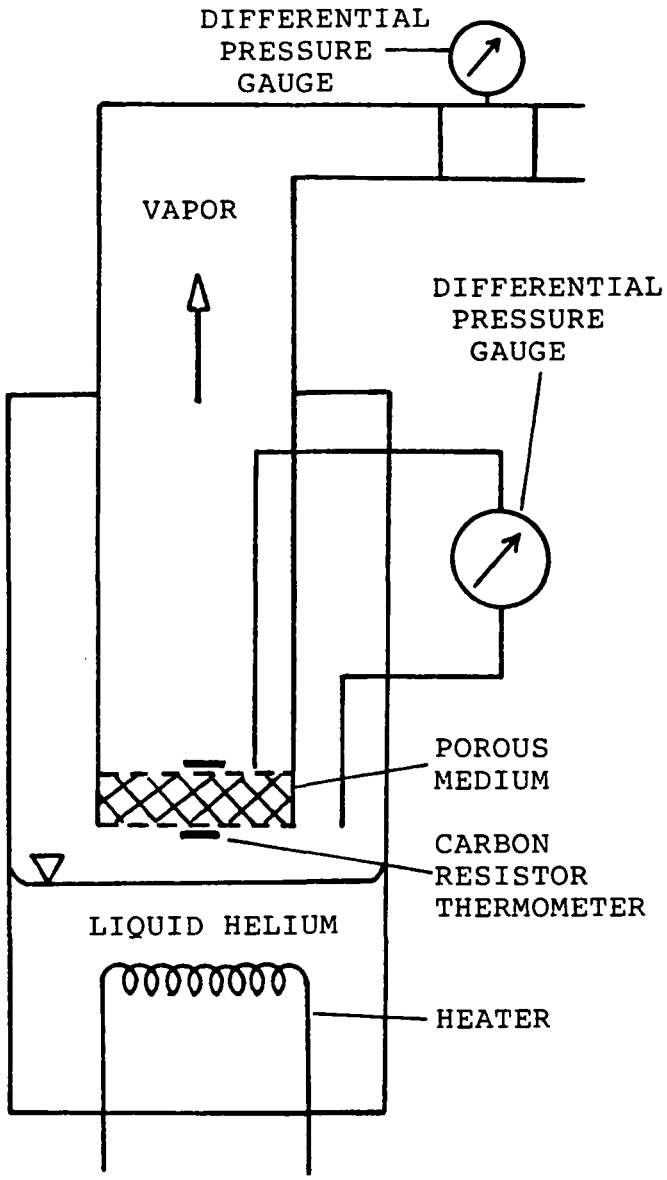

Figure 4.17. Schematic diagram of the cold vapor permeability measurement apparatus.

Chapter V

RESULTS AND DISCUSSION

The permeability (K_p) is very important in characterizing porous media used for vapor-liquid phase separation (VLPS) in the present model. It is crucial to measure the K_p accurately. Once the room temperature K_p of the plugs is known, the VLPS data can be analyzed with considerable confidence. Therefore, the results of VLPS experiments will be discussed following the permeability measurement results in this chapter.

5.1 PERMEABILITY MEASUREMENT RESULTS

Four different methods of K_p measurements were performed.

5.1.1 Room Temperature Permeability

The porous media being tested were purchased from two different manufacturers. They consisted of 0.5, 2, 5 and 10 μm filtration grade stainless steel plugs from Mott Metallurgical Corporation, also 2 μm (stainless steel) and 5-15 μm (bronze) particle removal size plugs from Pacific Sintered Metals Company (PSM). The permeability was calculated by using Darcy's law.

$$v = K_p \Delta P / \eta L \qquad (5.1)$$

In Figure 5.1, the square root of permeability is plotted as a function of the particle removal size (or filtration grade), S_o. From such a plot, one can see the range of permeability for each pore size. The dash-solid lines are drawn to guide the eye. It is seen that the range of K_p increases with the decrease in pore size. This is expected, because as the particle diameter becomes smaller the possible configuration inside the plug becomes more unpredictable. The manufacturing of these very small plugs leads to a more compressed top and bottom domain of the porous media.

Various characteristic lengths are plotted versus permeability in Figure 5.2. The figure includes particle removal size or filtration grade (S_o), $K_p^{\frac{1}{2}}$ and equivalent Ergun diameter. The characteristic length = $K_p^{\frac{1}{2}}$ is used in the calculation of dimensionless numbers, e.g. N_q, $N_{\nabla T}$ and the Reynolds number. Note that the L_c versus K_p function is completely linear because of the definition of L_c. The equivalent Ergun diameter (D_E) is obtained from the analogy between Darcy's law and Ergun's equation

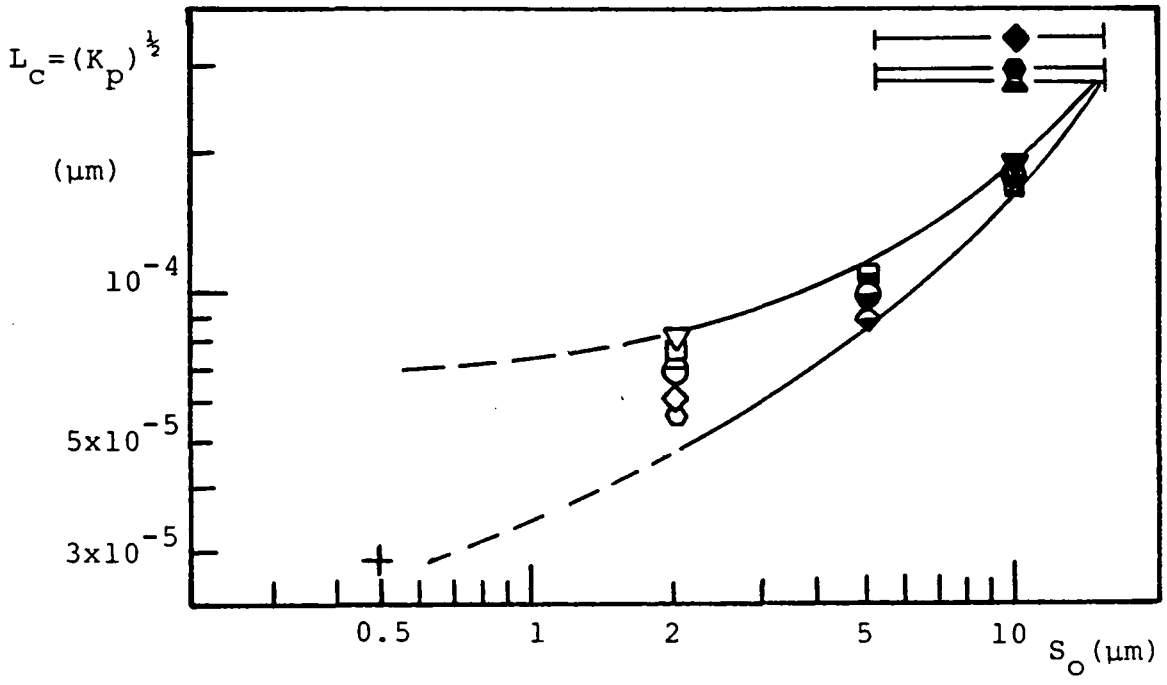

Figure 5.1. Nominal pore size versus square root of permeability (see Table I.6 for detail).

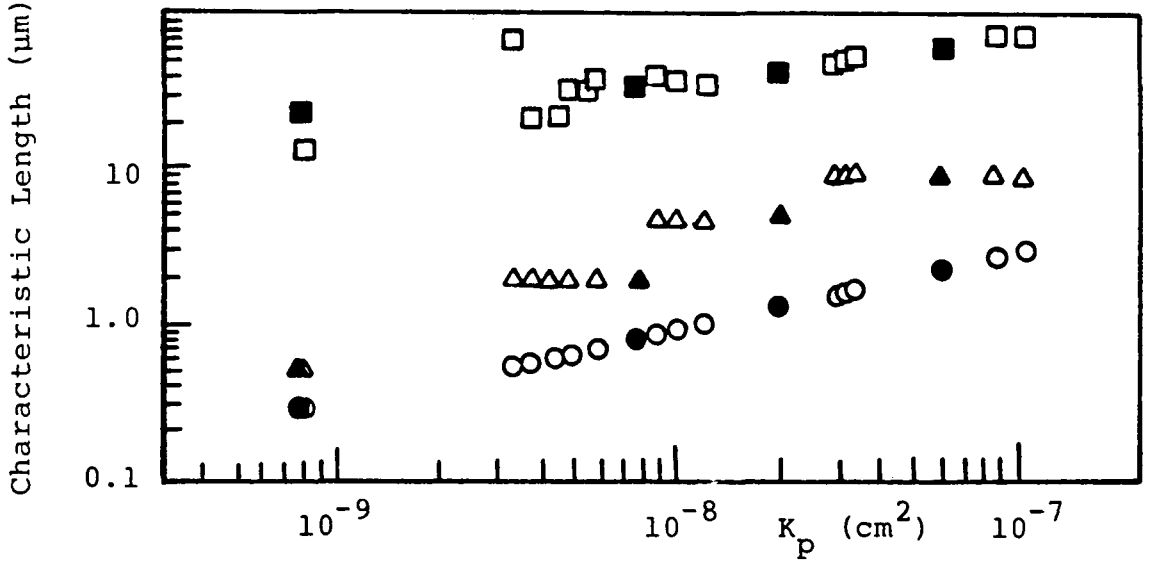

Figure 5.2. Various characteristic lengths versus permeability (German's data are represented by full symbols).

$$D_E = K_p^{\frac{1}{2}} (1 - \varepsilon)(150 / \varepsilon^3)^{\frac{1}{2}} \qquad (5.2)$$

The plug results of German (1981) are also included in Figure 5.2. Good agreement is found between the present experiments and German's data.

The K_p's measured for various plugs are very reproducible. One question remains whether the room temperature permeability will be retained at low temperatures (say below 4.2 K). In the following sections, the K_p measurement at low temperatures will be discussed.

5.1.2 Cold Vapor Permeability Measurement

The passage of pure vapor through porous media is one of the simplest and cleanest methods of measuring permeability at low temperatures. The K_p's can be obtained by Darcy's law (Equation 5.1) for the laminar flow of vapor through the plugs. One can also calculate the permeability by the Darcy limit of Ergun's equation. By substituting Equation 5.2 into Ergun's equation one gets

$$\nabla P = \frac{v\eta}{K_p} + 1.75 \frac{\rho v^2}{\eta(150\varepsilon^3 K_p)^{\frac{1}{2}}} \qquad (5.3)$$

In Figure 5.3, K_p calculated by Equation 5.3 is shown as a function of the vapor temperature for a 5-15 μm PSM bronze plug. Excellent agreement (within 10 %) is found between the room temperature K_p and the low temperature vapor permeability measured at 1.5 - 2.4 K. A similar result for Klipping's 1 μm ceramic plug is presented in Figure 5.4. Again, the room temperature permeabilities appear to be recovered at low temperatures.

5.1.3 Liquid Outflow Permeability of He I

From the procedures described in Section 4.2.2, the flow rate of He I can be measured from the change of liquid level in the Kovar beaker. For little or no vapor pressure difference across the plug, the only driving force in the experiment was the hydrostatic pressure. Therefore, one can express both the pressure gradient and the velocity term in the modified Ergun equation (Equation 5.3) by the rate of change of liquid level

$$1.75a_r^2\rho(150K_p\varepsilon^3)^{-\frac{1}{2}}(dZ/dt)^2 + a_r(\eta/K_p)(dZ/dt) - (g\rho/L)Z = 0 \qquad (5.4)$$

where a_r is the area ratio. A Runge-Kutta-Fehlberg algorithm was used to integrate the above equation (see Appendix

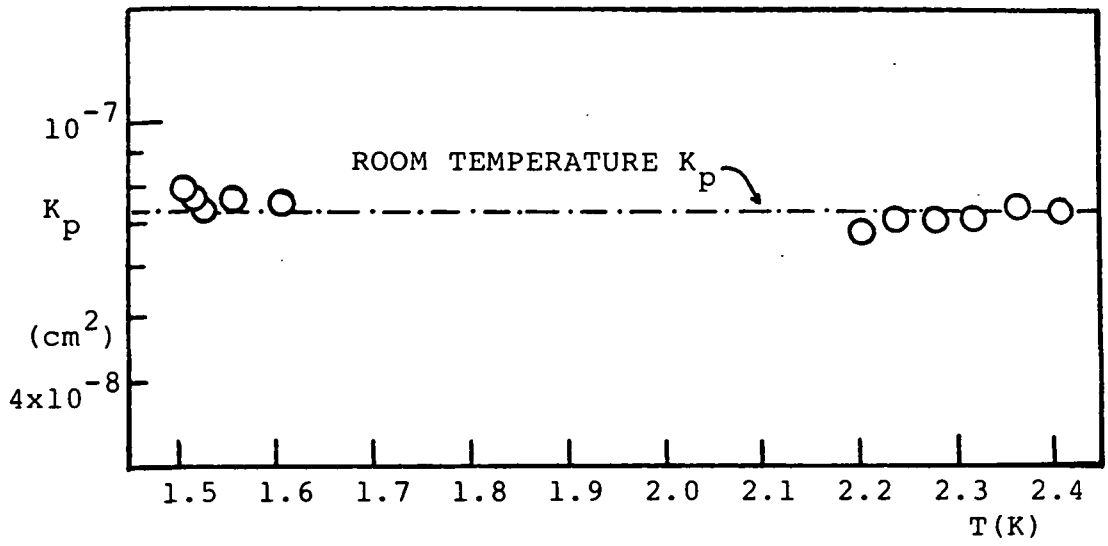

Figure 5.3. Cold vapor permeability of a 5-15 μm bronze PSM plug (P5-15B2-4x4).

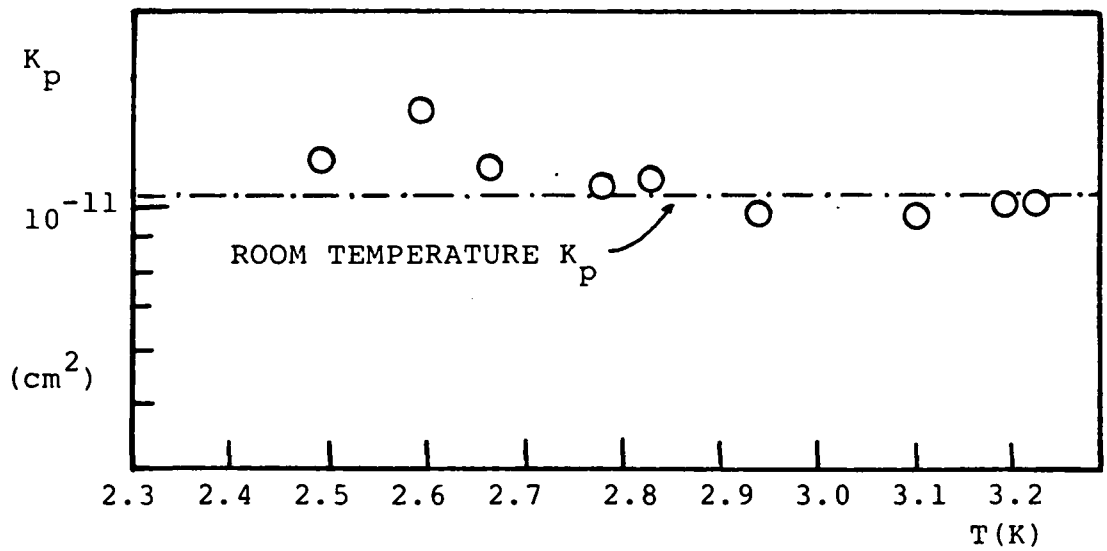

Figure 5.4. Cold vapor permeability of a 1 μm ceramic plug (Denner et al. 1977).

F).

Figures 5.5 to 5.8 show experimental results of He I outflow through the same plug used in the cold vapor test with different initial liquid level. The dashed line represents Equation 5.4 with viscosity η = 30 μP and $K_p = K_{p,room}$ = 7.364×10^{-8} cm^2. The data show good agreement with the theoretical curve indicating that the room temperature permeability is indeed retained at such low temperatures.

5.2 THE VAPOR-LIQUID PHASE SEPARATION RESULTS

In order to achieve true vapor-liquid phase separation (VLPS) mode, the downstream of the porous plug tested must be dry. Following the procedures outlined in section 4.1, the VLPS mode could not be reached instantaneously. Figures 5.9 and 5.10 represent the results of a 10 μm Mott plug (M10S1-4x1) at the beginning of a typical run. The bath temperature and mass flow rate are plotted in Figure 5.9 and the temperature difference and vapor pressure difference are presented in Figure 5.10.

As the valve to the downstream pump was opened during the experiment, the bath temperature decreased monotonically. For $\dot{m}$ in Figure 5.9, a negative mass flow rate indicates that the liquid was flowing from upstream to downstream (from the Kovar beaker to the downstream vent pipe), whereas a positive value shows that the liquid was traveling in the opposite direction. At the start of the experiment (region

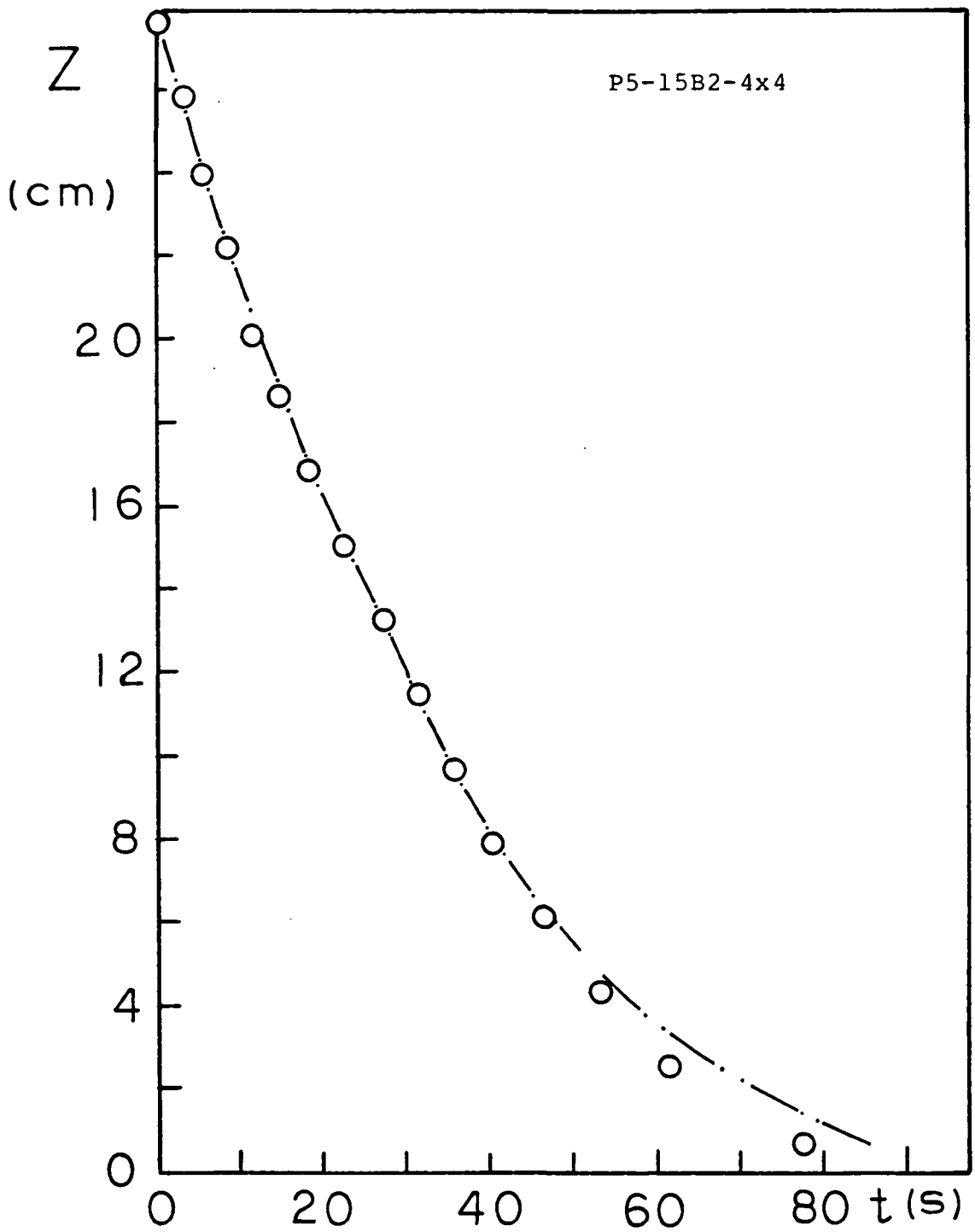

Figure 5.5. Rusults of the liquid He I outflow experiment, run # 1.

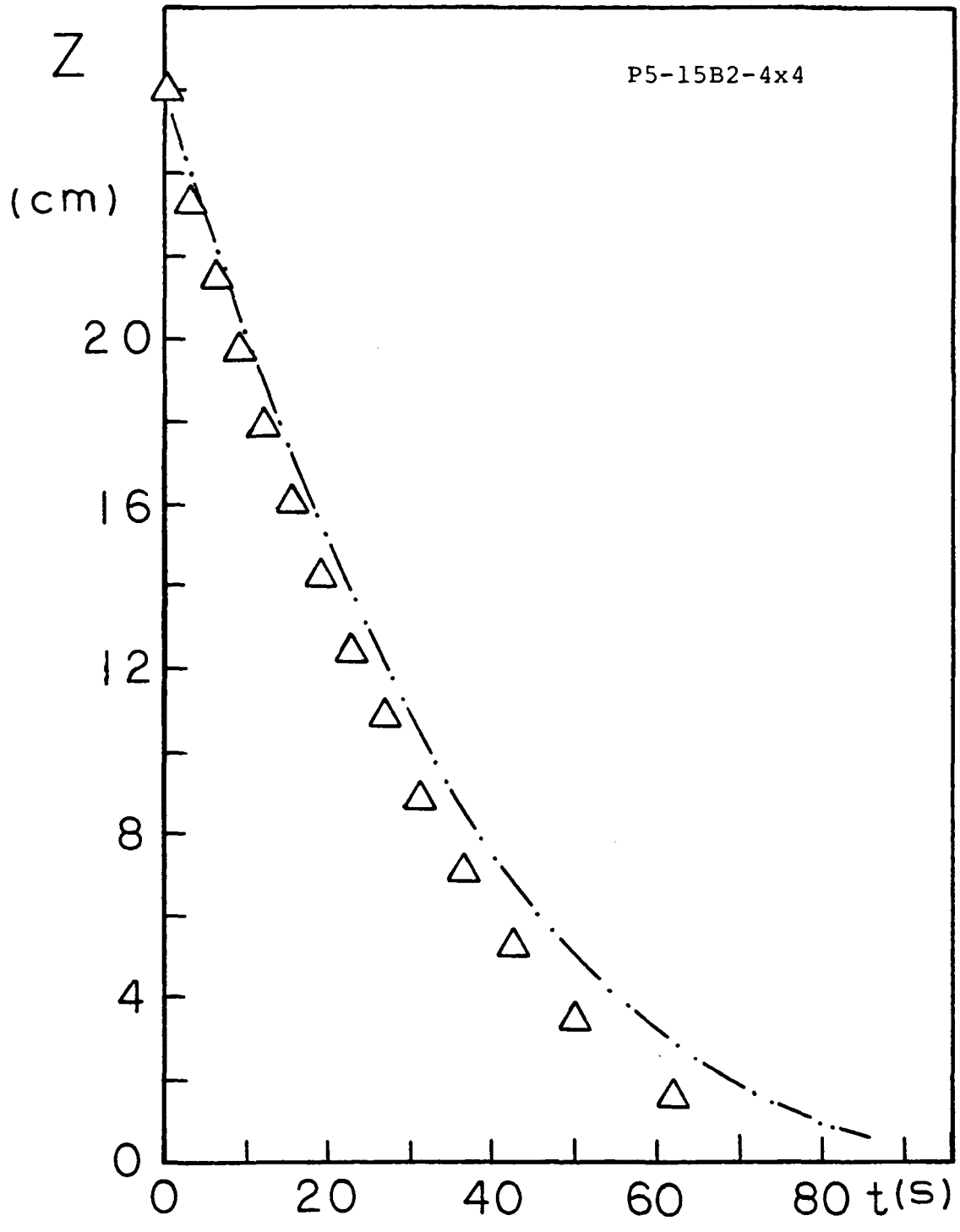

Figure 5.6. Results of the liquid He I outflow experiment, run # 2.

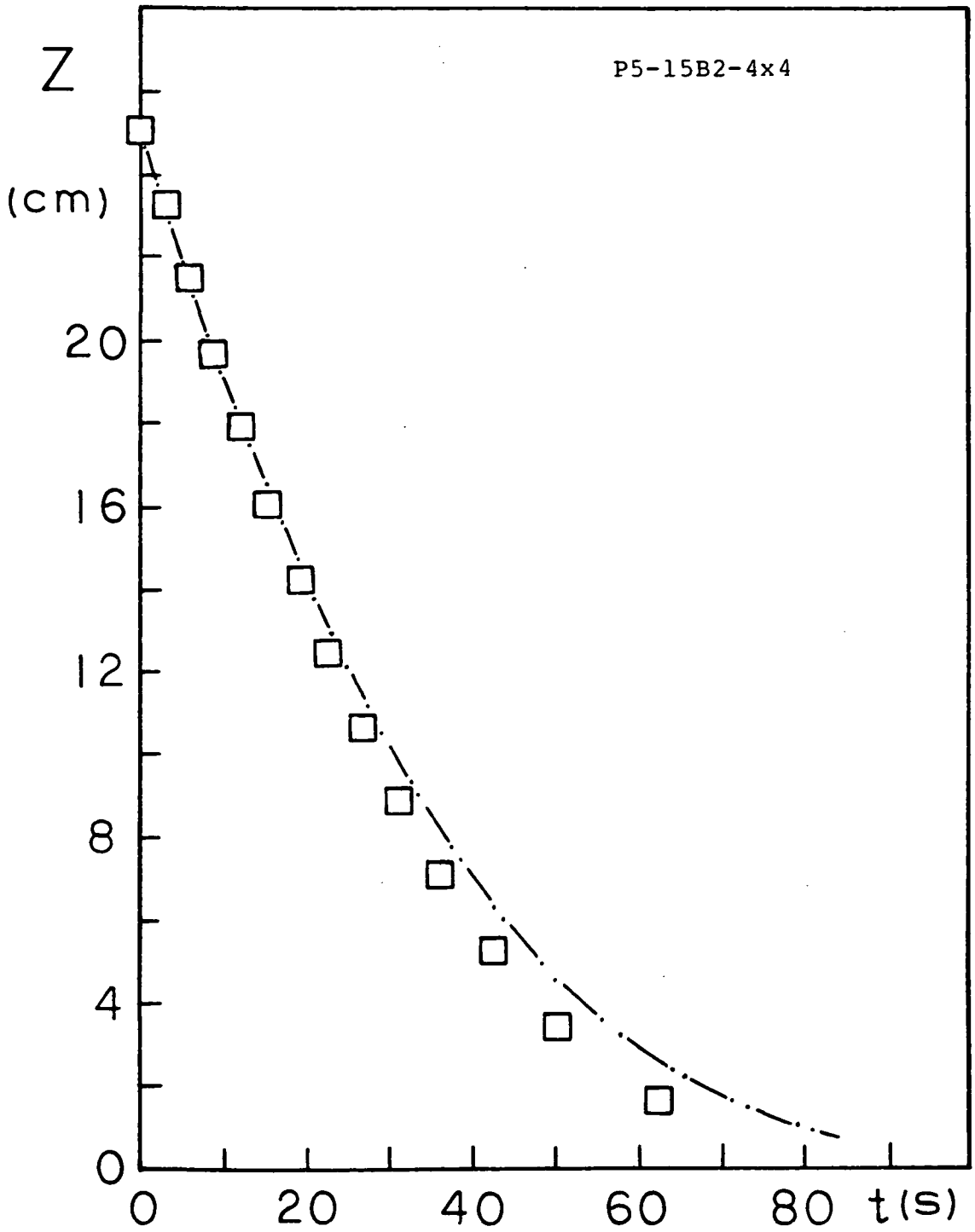

Figure 5.7. Results of the liquid He I outflow experiment, run # 3.

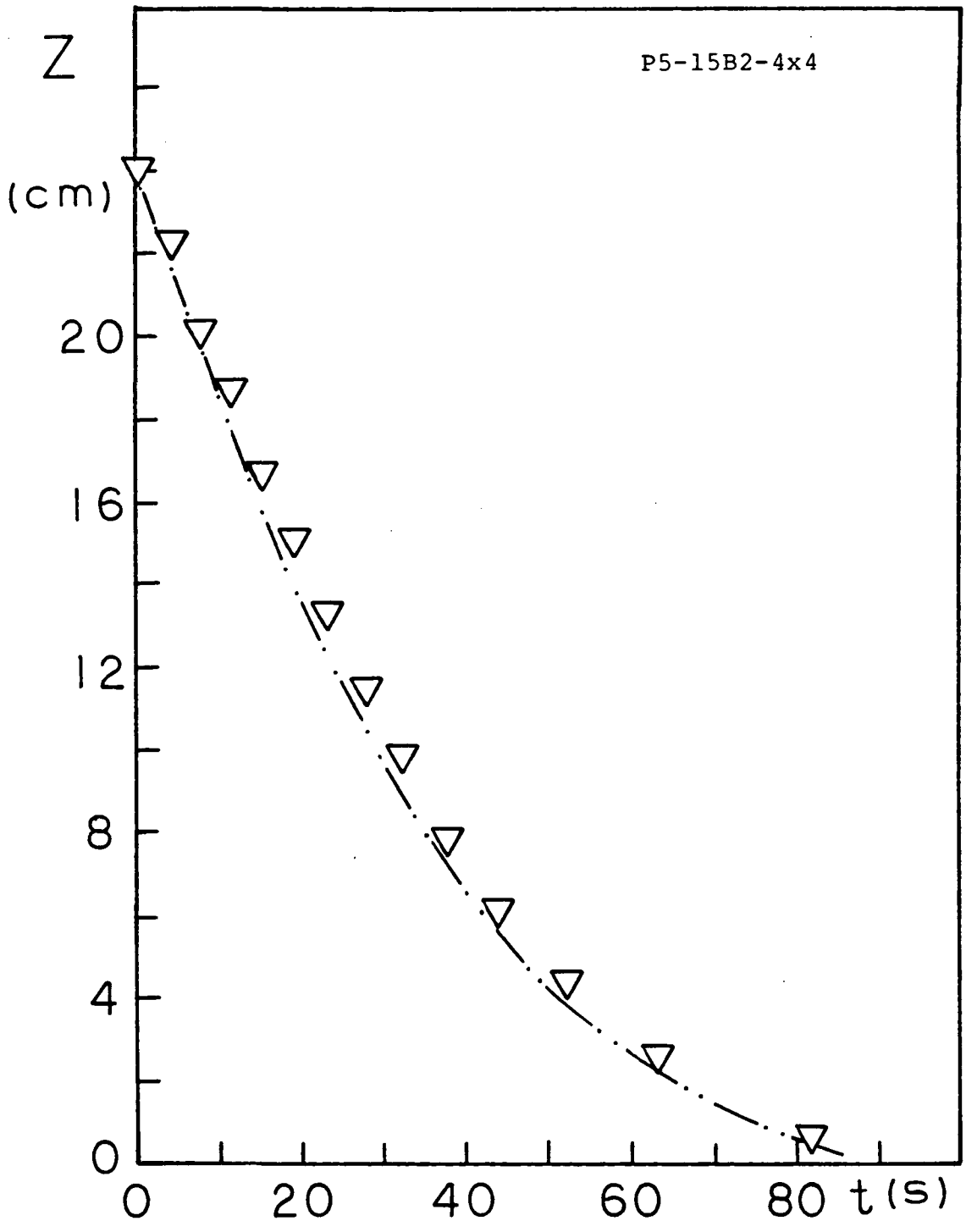

Figure 5.8. Results of the liquid He I outflow experiment, run # 4.

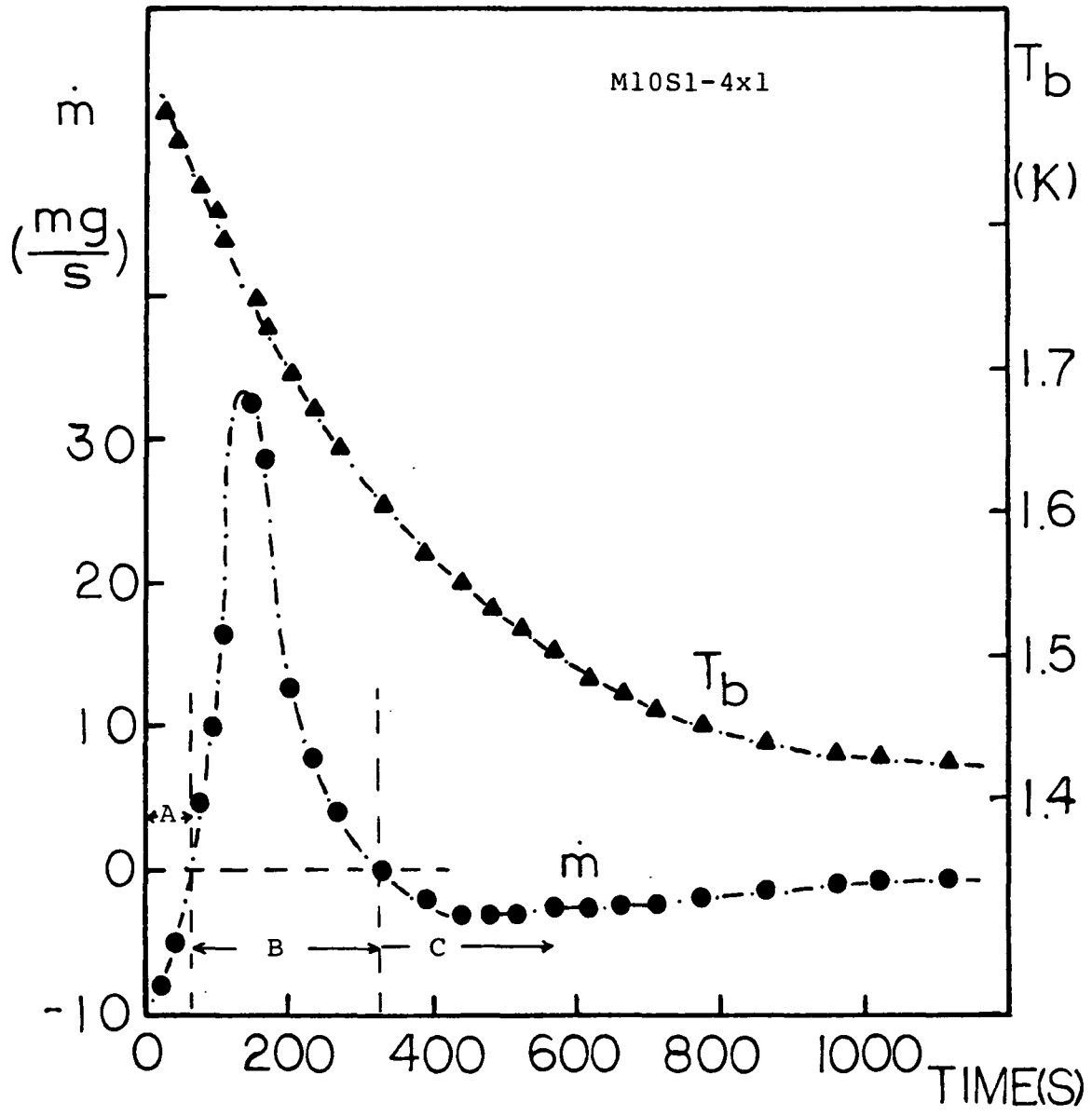

Figure 5.9. Typical data of the vapor-liquid phase separation experiment, mass flow and bath temperature as a function of time.

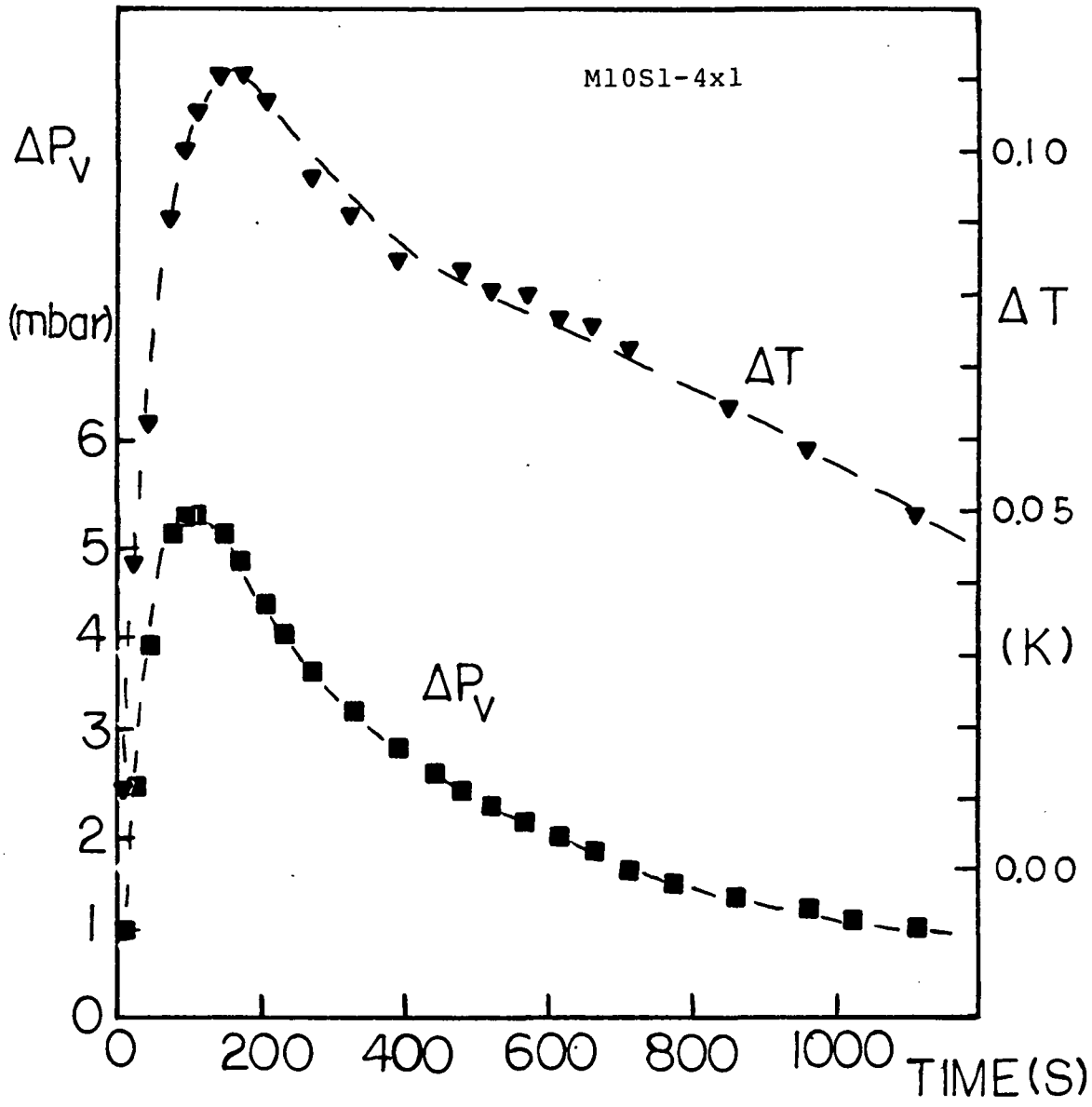

Figure 5.10. Typical data of the vapor-liquid phase separation experiment, temperature difference and vapor pressure difference as a function of time.

A and Figure 5.11a), liquid He II was forced through the plug as the valve was first opened because

$$\Delta P_T < \Delta P_v + \rho g(Z_o - Z_i) \tag{5.5}$$

where $\rho g(Z_o - Z_i)$ is the net hydrostatic pressure, with Z_i and Z_o the liquid level inside the vent pipe and the Kovar beaker respectively. As the thermo-osmotic pressure increased (due to the increase of temperature difference, Figure 5.10) and the liquid level at the downstream rose, the right hand side of Equation 5.5 finally surpassed the vapor pressure difference

$$\Delta P_T > \Delta P_v + \rho g(Z_o - Z_i) \tag{5.6}$$

This section is represented by region B in Figure 5.9 (also Figure 5.11b). At this stage, liquid flowed back into the upstream region. This is indicated by a positive mass flow rate in Figure 5.10.

When the liquid at the downstream side was emptied out (Figure 5.11c), the true VLPS mode was achieved (region C), thus

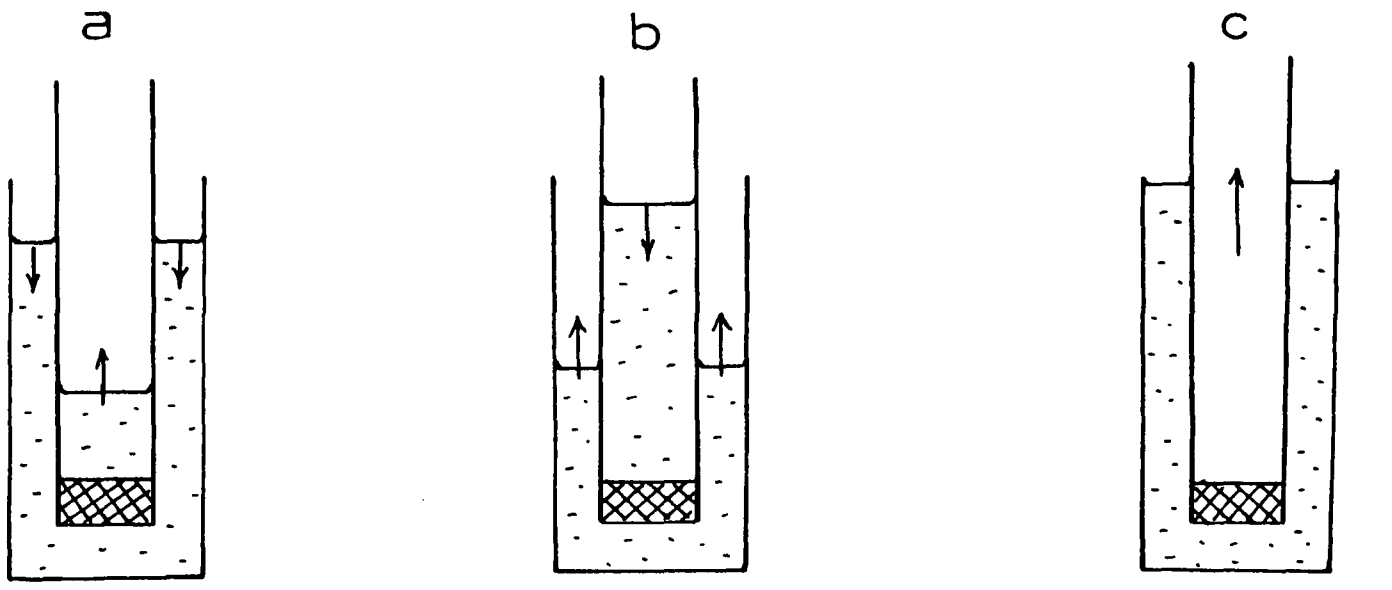

Figure 5.11. Various transport modes encountered during the vapor-liquid phase separation experiment.

$$\Delta P_T = \Delta P_v + \rho g(Z_o - Z_i) \qquad (5.7)$$

Note that the above thermodynamic equation is only valid for ideal transport where the dissipation effect is ignored. In the actual VLPS mode, the thermo-osmotic pressure was found to be much larger than the sum of the hydrostatic pressure and the vapor pressure difference. The VLPS data of a 2 μm and 10 μm Mott plug and a 5-15 μm PSM plug are presented in Figure 5.12. The thermo-osmotic pressure is plotted as a function of the sum of vapor pressure and hydrostatic pressure across the plug. As expected, ΔP_T is found to be much larger than ΔP_v and ρgZ. Thus the dissipation effect of He II in porous media used for VLPS is significant, and the ideal laminar transport is difficult to achieve. This is especially true for zero-gravity space operations where the hydrostatic term in Equation 5.7 is negligible. Since the thermo-osmotic pressure is always an order of magnitude larger than the vapor pressure difference, a large dissipation term must be present such that

$$\Delta P_T = \Delta P_v + \Delta P_{dissipation} \qquad (5.8)$$

Therefore, for VLPS in space, only the turbulent regime seems to be feasible (as described in the preceeding section on the thermodynamics of VLPS at zero gravity).

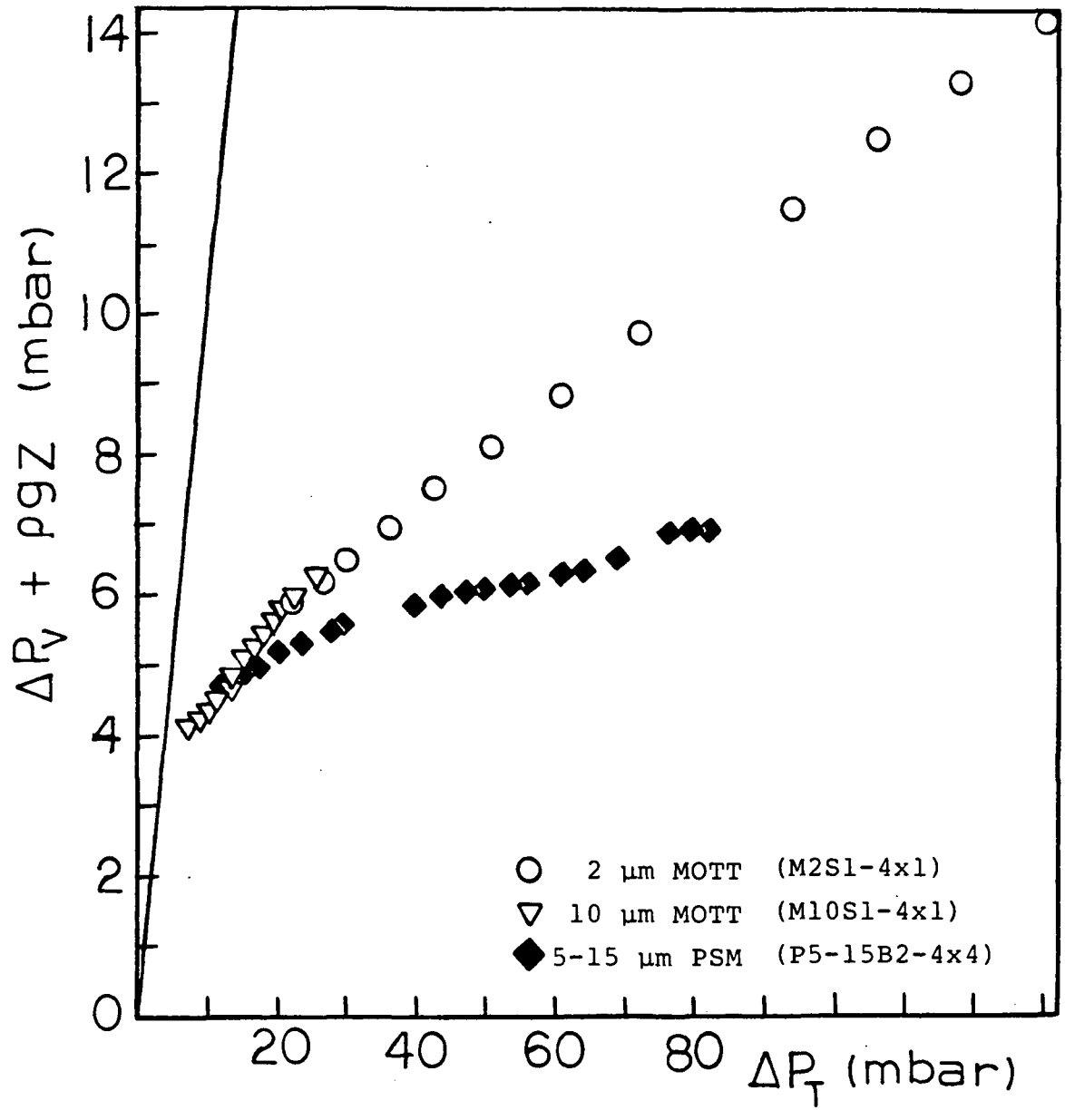

Figure 5.12. Comparison of the thermo-osmotic pressure to the sum of vapor pressure and hydrostatic pressure across the phase separator.

Using the ΔT measured from a section of the porous media (close to the upstream side), Murakami (1984) was able to fit his VLPS data by a modified Blake-Kozeny equation, as shown in Figure 5.13

$$f_M = 150 \; / \; Re_M \tag{5.9}$$

where

$$Re_M = (150K_p/\epsilon^3)^{\frac{1}{2}} \; \rho_n \vec{v}_n \; / \; \eta_n \tag{5.10}$$

and

$$f_M = (150K_p\epsilon^3)^{\frac{1}{2}} \rho S \nabla T \; / \; \rho_n \vec{v}_n^2 \tag{5.11}$$

Note that the modified Blake-Kozeny equation is same as the thermo-osmotic Darcy equation (Equation 3.15) based on the near-spherical particle assembly model. Please refer to derivation in Appendix G. Included in Figure 5.13 is the modified Ergun equation (by analogy with the Darcy law, see Appendix B) for normal fluid flow at various temperatures

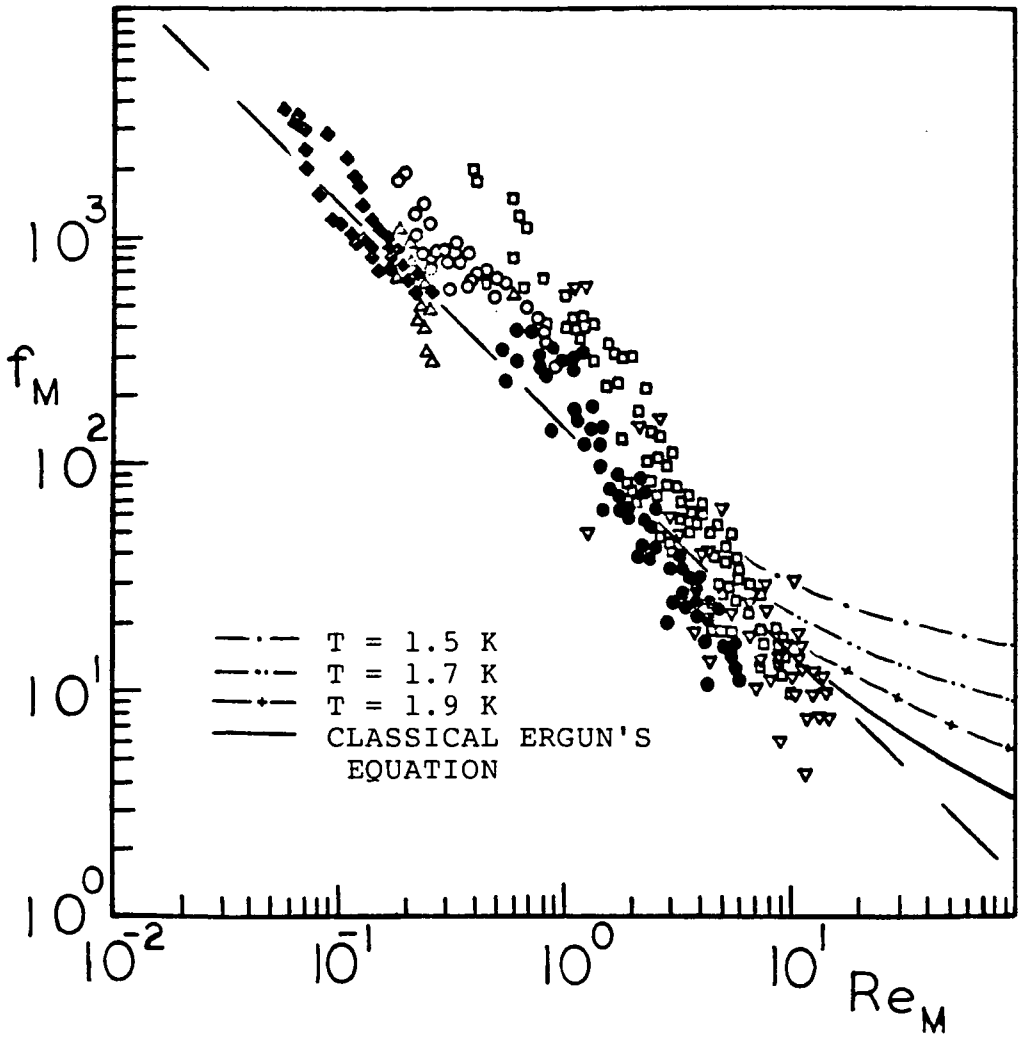

Figure 5.13. Comparison of Murakami's data to the modified Ergun equation for normal fluid flow (Equation 5.12).

$$\nabla P_T = \frac{\vec{v}_n \eta_n}{K_p} + \frac{1.75\ \vec{v}_n^2\ \rho}{\eta_n (150 K_p \varepsilon^3)^{\frac{1}{2}}} \qquad (5.12)$$

For the classical Ergun equation, the data starts to deviate from the laminar regime at a Reynolds number of about 10. However, for the modified Ergun equation for normal fluid flow, the data should turn turbulent with Re less than 10. In Figure 5.13, Murakami's data show no tendency to deviate from the Blake-Kozeny equation for Re > 10. Moreover, Murakami's data tend to curve concave down instead of concave up as predicted by Ergun's equation. It is possible that by measuring the temperature difference across a section of the porous media, the data do not represent the true VLPS mode. Moreover, the downstream thermometer might not be measuring the temperature right at the vapor-liquid interface.

Figures 5.14 to 5.17 are results of VLPS runs of this research for Mott 2 μm and 10 μm stainless steel plugs and PSM 5-15 μm bronze plug. The data were collected by the transient cool down technique as discussed in Section 4.1.4.1.. Figure 5.14 is a plot of the liquid level (inside the Kovar beaker) as a function of time. During the VLPS run, a finite amount of He II penetrated through the plug to the downstream vent line, resulting in a decrease in the liquid level at the upstream side. From the conservation of mass, the flow rate through the porous medium can be obtained.

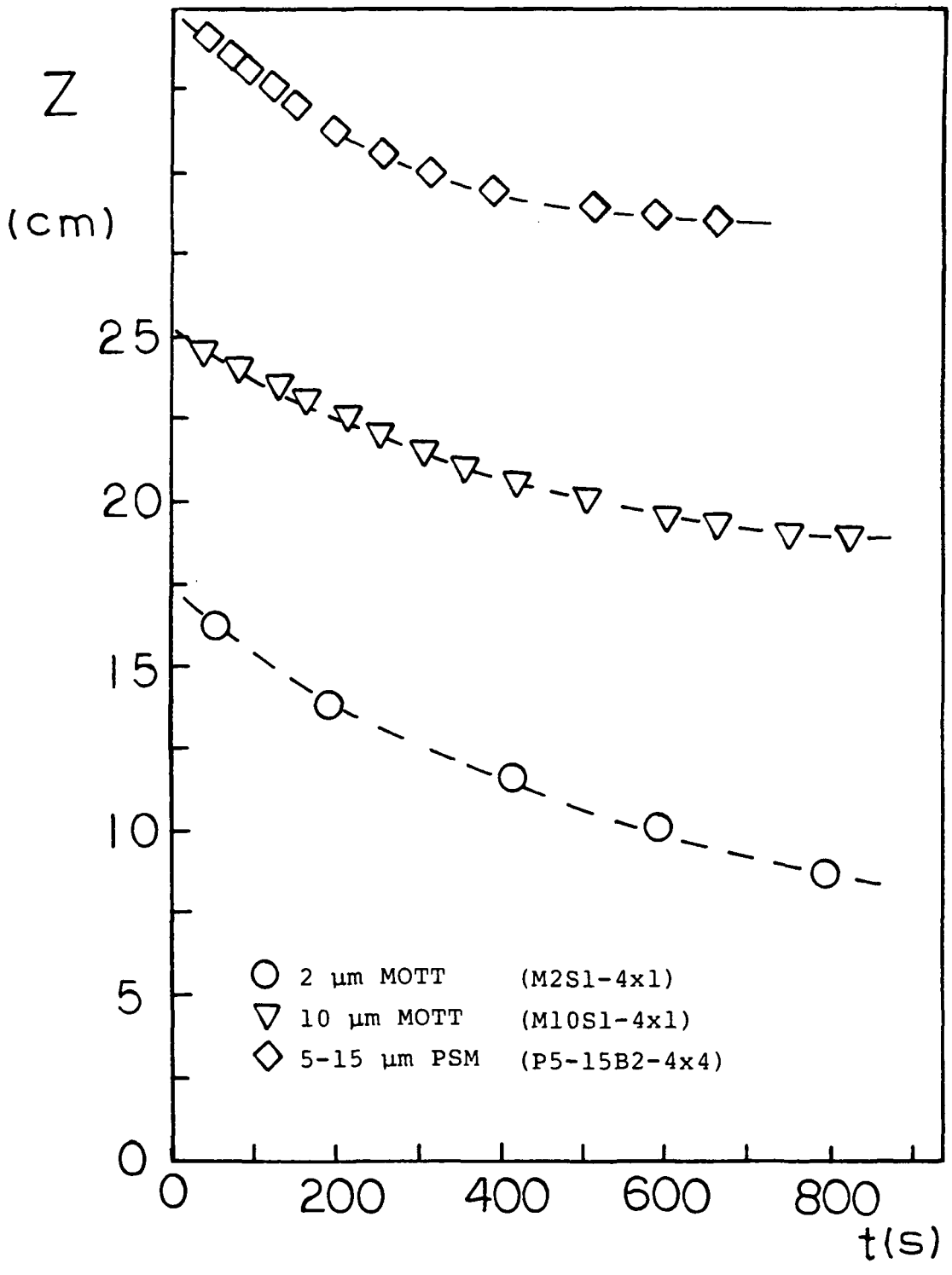

Figure 5.14. Liquid level as a function of time (VLPS data).

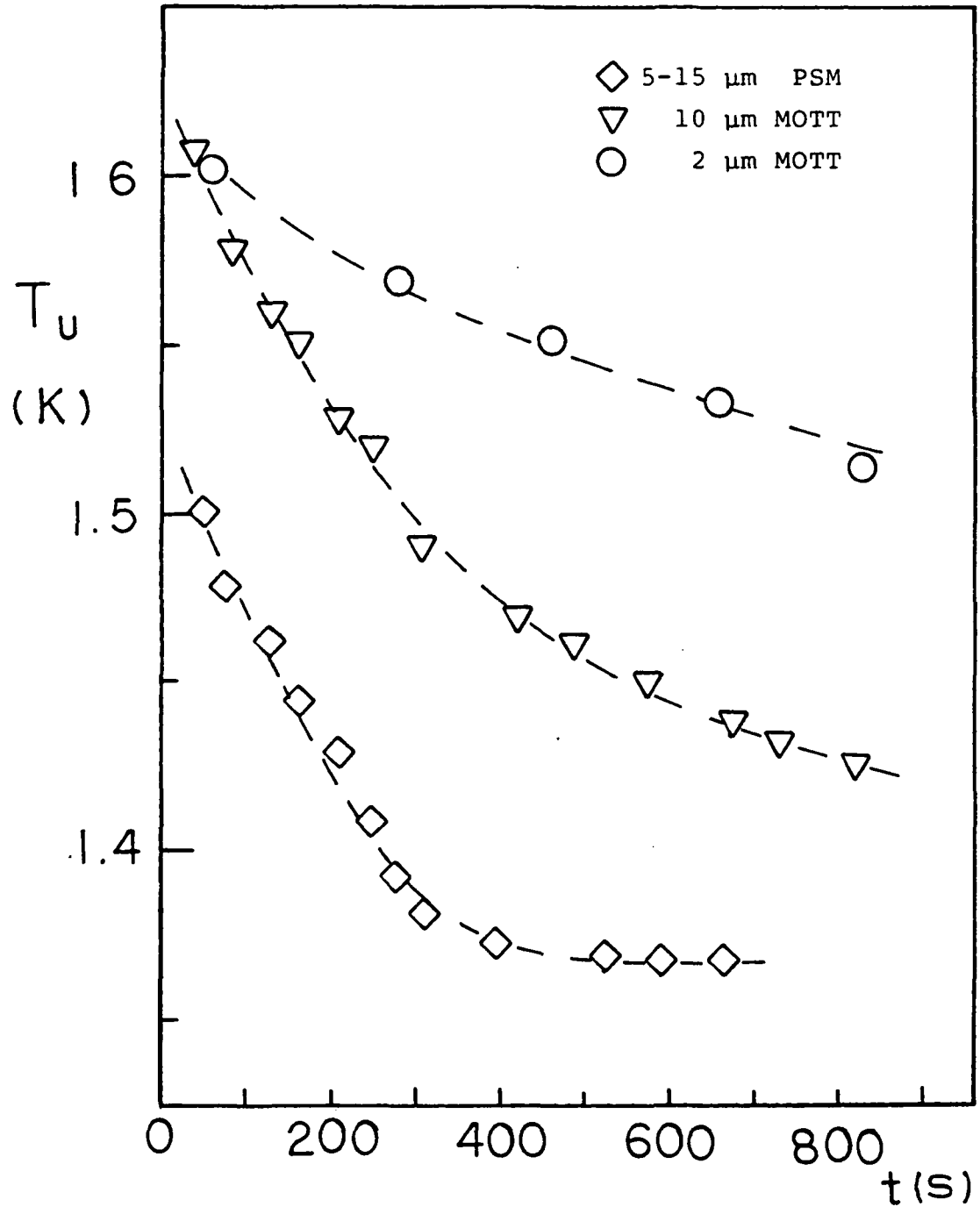

Figure 5.15. Upstream temperature as a function of time (VLPS data).

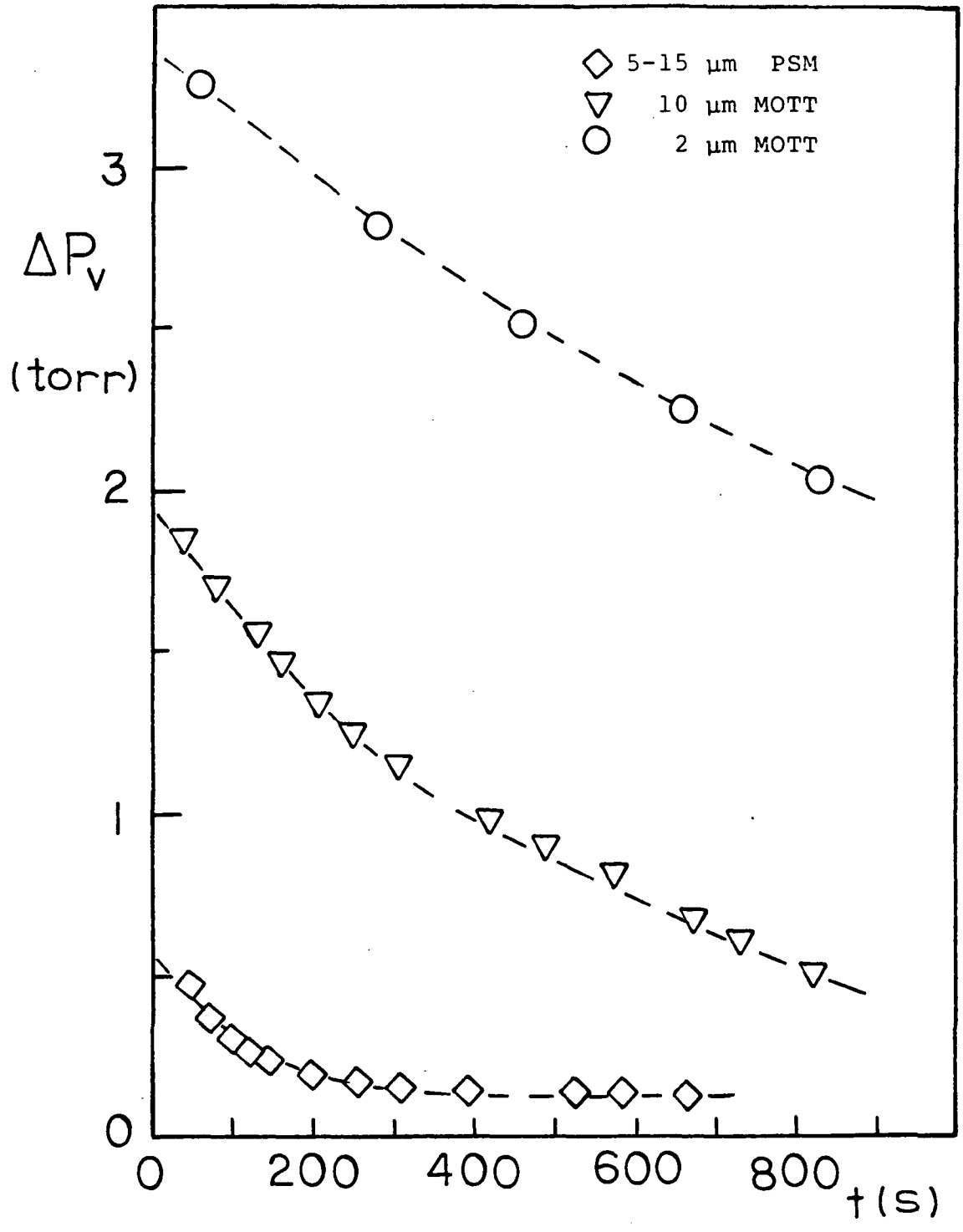

Figure 5.16. Vapor pressure difference as a function of time (VLPS data).

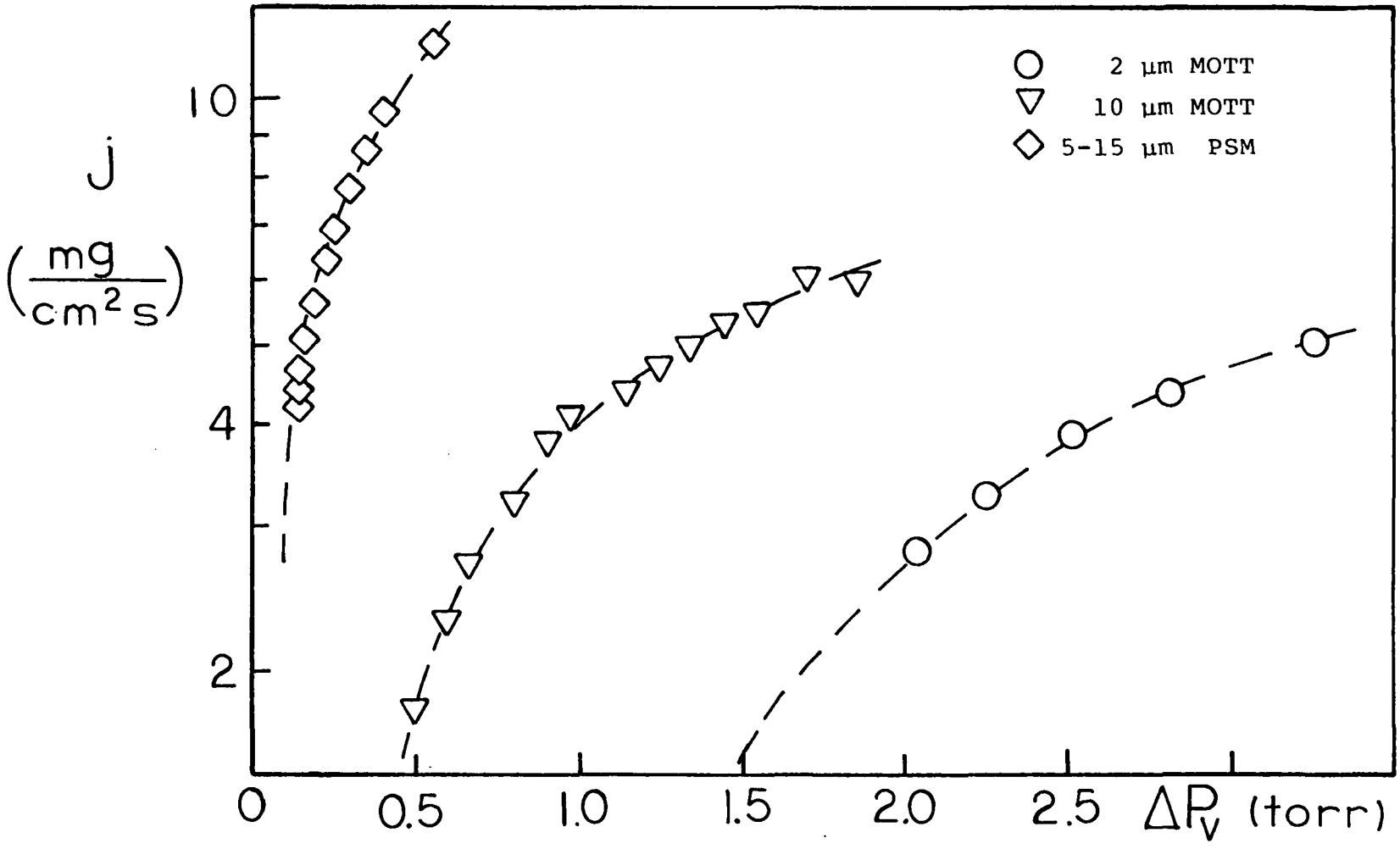

Figure 5.17. Mass flux density as a function of the vapor pressure difference across the porous plug (VLPS data).

The upstream (or bath) temperature and vapor pressure difference across the plug are shown in Figures 5.15 and 5.16 respectively. During the cool down process, both the T_u and ΔP_v decreased monotonically. From the liquid level change, the mass flux density can be calculated and is presented in Figure 5.17 versus ΔP_v.

A number of investigators have tried to characterize porous media used for VLPS. For example, Hendrick and Karr (1982) used the capillary model (Equation 1.5) and Petrac and Mason (1978) used the proportionality constant F (Equation 1.6). As was mentioned earlier, the room temperature permeability is retained at low temperatures. Thus, the Darcy permeability is a very useful parameter for the characterization of porous plugs used for VLPS.

Yet another method of measuring permeability at low temperatures is possible by utilizing the VLPS data. Looking at Equation 3.63, it is easy to see that

$$\vec{q}_{VLPS} \longrightarrow \vec{q}_{ZNMF} \qquad \begin{matrix}(\text{At low T and} \\ \text{small flow rate})\end{matrix} \qquad (5.13)$$

because $\lambda/(\lambda+ST)\sim 1$. Therefore, for VLPS data with small ΔT at low temperatures, the zero net mass flow laminar equation should be observed (Equations 3.16 & 3.17). The VLPS data

of a 5-15 μm PSM bronze plug (P5-15B1-4x4) is plotted in dimensionless form of N_q versus N_{VT} in Figure 5.18. These data were taken by the transient cool down technique. As the temperature difference across the plug and the bath temperature decreased, the ZNMF laminar equation of $N_q = N_{VT}$ was approached asymptotically. Also included in Figure 5.18 are the VLPS data of Petrac and Mason (1978) with a stainless steel collimated hole plug and Klipping's (Denner et al. 1977) 10 μm glass plug. Both sets of data show the asymptotic behavior.

The same data are replotted in a different form in Figure 5.19. The ratio of the normal fluid permeability (K_{pn}) over the room temperature or Darcy permeability ($K_{p,room}$) is presented as a function of the mean temperature across the porous media. The K_{pn}'s were calculated by Equation 3.16. If the VLPS results do indeed follow the ZNMF laminar equation, then $K_{pn}/K_{p,room} = 1$. From Figure 5.19, one can see that the room temperature permeability was approached for small flow rates (small ΔT and low temperatures).

Figure 5.20 is a plot of mass flux density versus temperature difference across the porous media for the 2 μm, 10 μm (Mott) and 5-15 μm (PSM) plugs. Due to the extreme sensitivity of Equation 3.64 to temperature, the 1/3 power law of j on ΔT cannot be observed for transient data. Even for constant bath temperature results in the literature, the

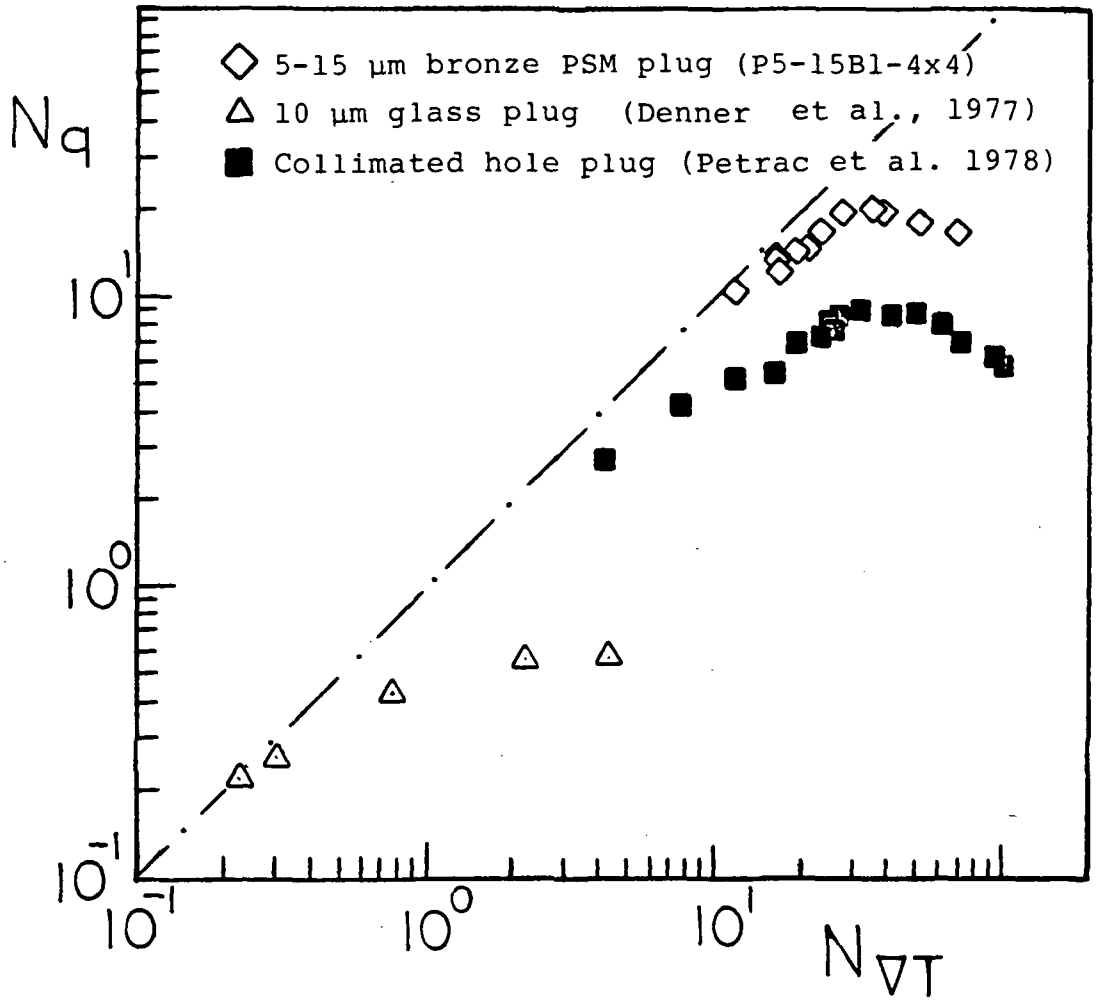

Figure 5.18. Data showing the zero net mass flow asymptotic limit of the vapor-liquid phase separation mode.

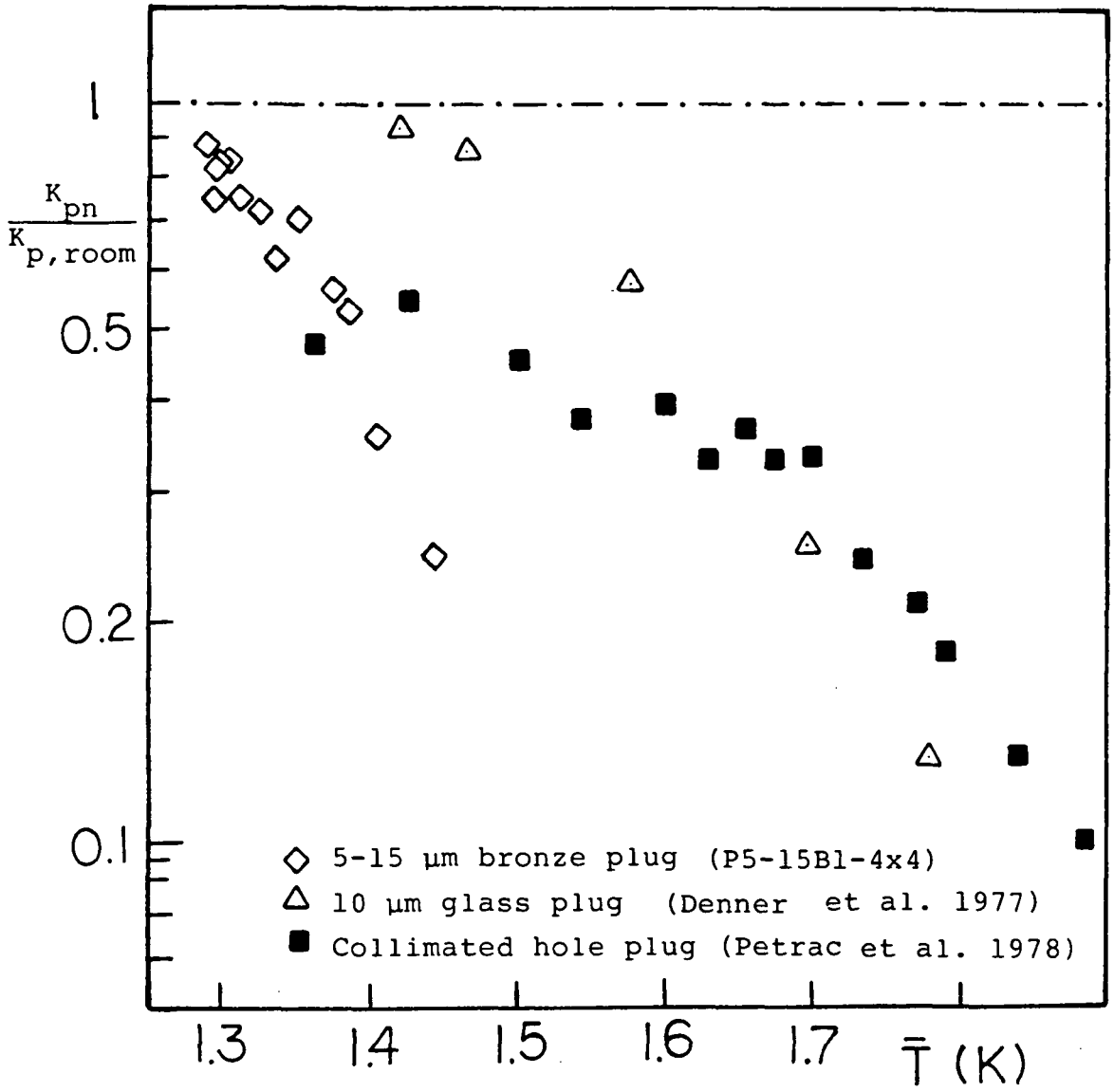

Figure 5.19. Ratio of the normal fluid permeability as a function of the mean temperature across the phase separator.

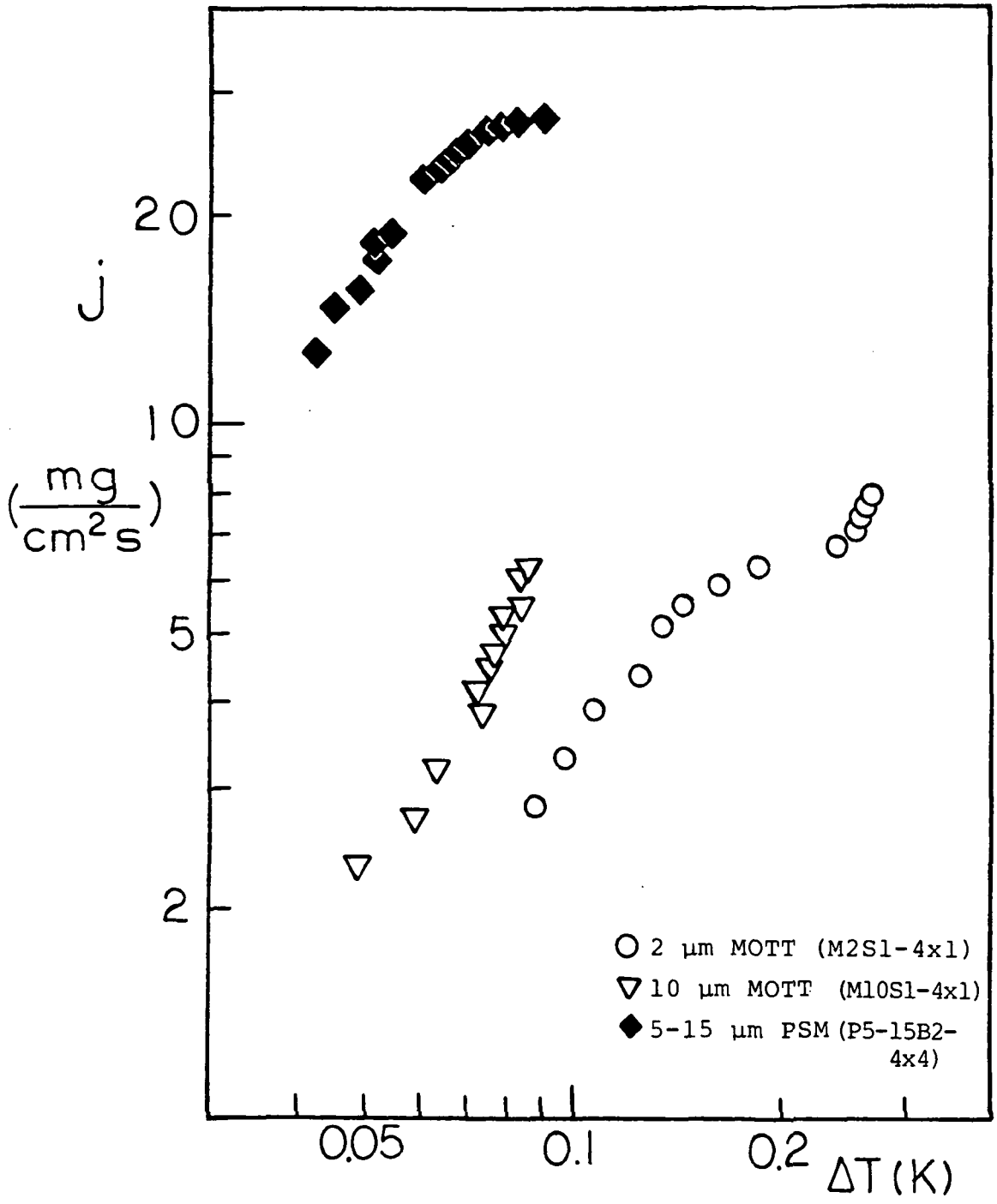

Figure 5.20. Mass flux density versus the temperature difference across the phase separator.

"1/3" law of Gorter-Mellink might be hidden if the temperature across the plug is large. In order to compare with the experimental data, Equation 3.64 is integrated by Simpson's rule from T_d to T_u (Appendix C)

$$\dot{q}_{VLPS} = [\int_{T_d}^{T_u} (K^*_{GM}\eta_n ST \frac{\lambda}{\lambda+ST} \frac{\rho_s}{\rho})^3 \frac{\rho^2\rho_s S}{L\rho_n\eta_n^2} dT]^{1/3} \quad (5.14)$$

For the sake of simplicity, Equation 5.14 can either be integrated up with constant T_d or integrated down with constant T_u. This way, smooth curves like that of Figures 3.15 and 3.16 can be generated. In Figures 5.21 and 5.22 the present experimental data are compared with the integrated Gorter-Mellink equation. The mass flux density is plotted against the bath (or upstream) temperature. The results of the 5-15 μm bronze plug are presented in Figure 5.21. The open symbols represent data taken by the transient cool down technique where a bath temperature of 1.3 K was approached. The full symbols are data collected by the transient warm up method as mentioned in section 4.1.4.2.. Both sets of data were fitted by integrating Equation 5.14 with constant T_d of 1.3 K and 1.5 K, using a K^*_{GM} value of 1.4. Results of the two Mott plugs are shown in Figure 5.22. Gorter-Mellink

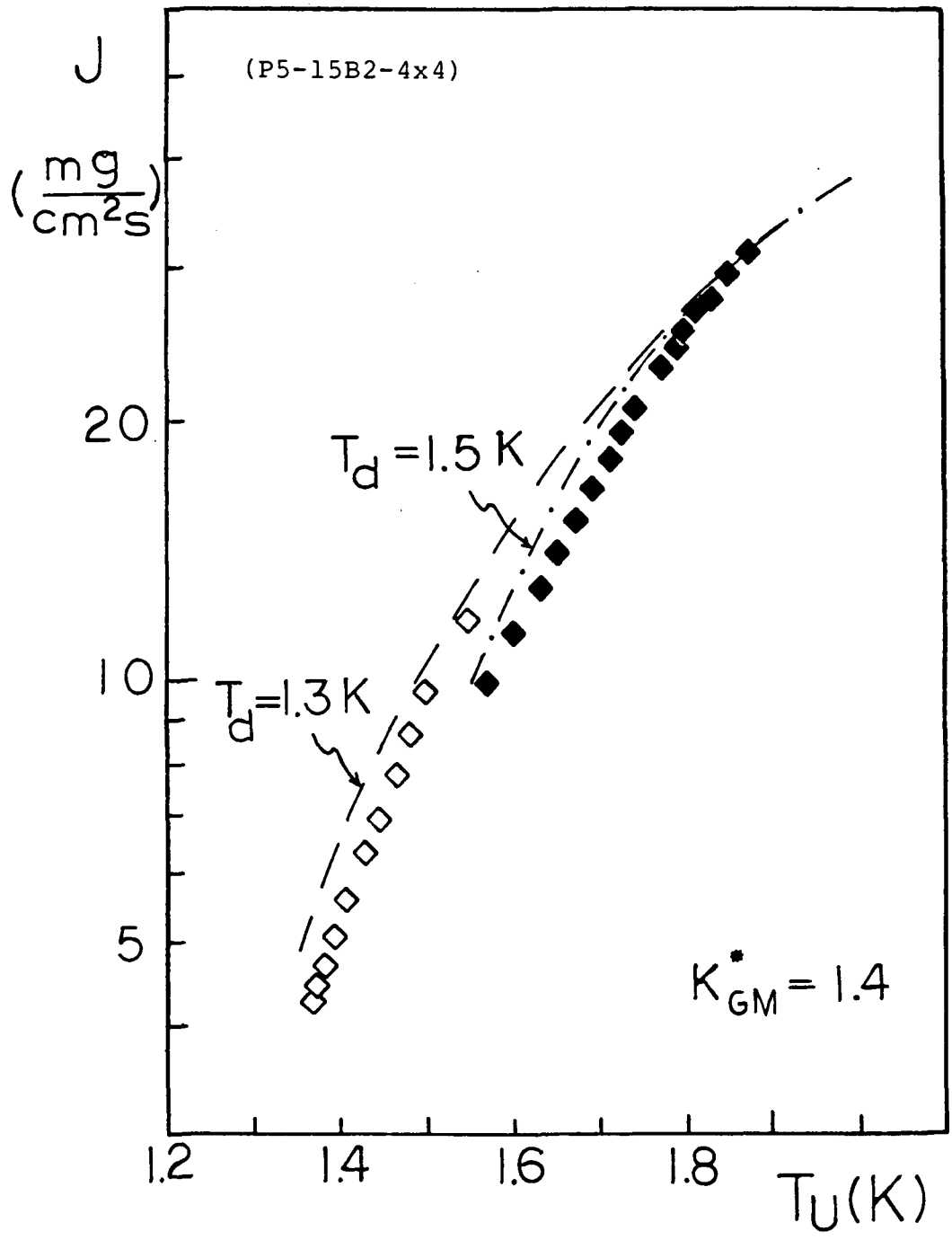

Figure 5.21. Comparison of the integrated modified Gorter-Mellink equation to the phase separation data of a 5-15 μm bronze PSM plug.

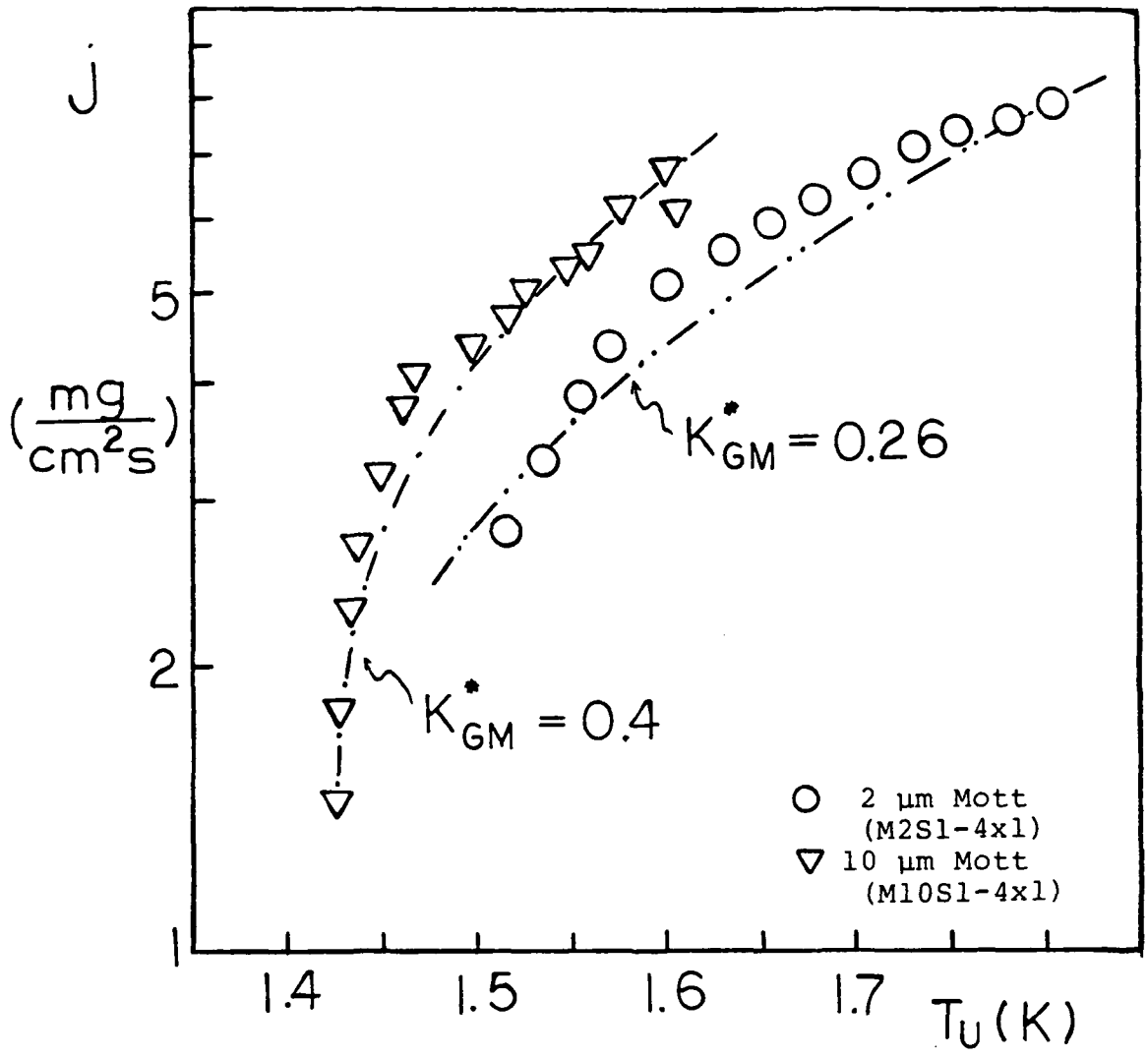

Figure 5.22. Comparison of the modified Gorter-Mellink equation to a 2 μm and a 10 μm Mott plug used for vapor-liquid phase separation of He II (T_d = 1.4 K).

constants of 0.0081 and 0.171 were used to fit the 2 μm and 10 μm plugs respectively, with T_d = 1.4 K. Good agreement is found between the theory and the experiments.

The modified Gorter-Mellink equation is also compared to other VLPS data reported in the literature. Results of Klipping (Denner et al. 1977) are presented in Figure 5.23. Data are presented for a 1 μm ceramic plug and a 10 μm glass plug. Besides an excellent agreement with Klipping's results, Equation 5.14 can also predict the leveling of mass flux density for the 1 μm ceramic plug at T > 2.0 K. Looking at Figure 3.14, one realizes that the property function in Equation 5.14 drops drastically for T > 2.0 K. Therefore, in integrating Equation 5.14 from T_d to T > 2.0 K, the increase in area under the curve beyond 2.0 K is small and the flow rate levels off. The mass flux data of the in-flight IRAS porous plug (Petrac 1979) is recreated in Figure 5.24 as a function of the vapor pressure difference. The result is rearranged by plotting j versus T_d in Figure 5.25. These data were taken at constant bath (or upstream) temperature. In this case, Equation 5.14 is integrated at constant T_u with T_d varied. Note that for T_u = 1.69 K and 1.8 K, the data are slightly below the theoretical curve. Looking at Figure 5.24, one realizes that these data were pretty close to the laminar region. Since these data might be in the transition regime (between laminar and fully developed

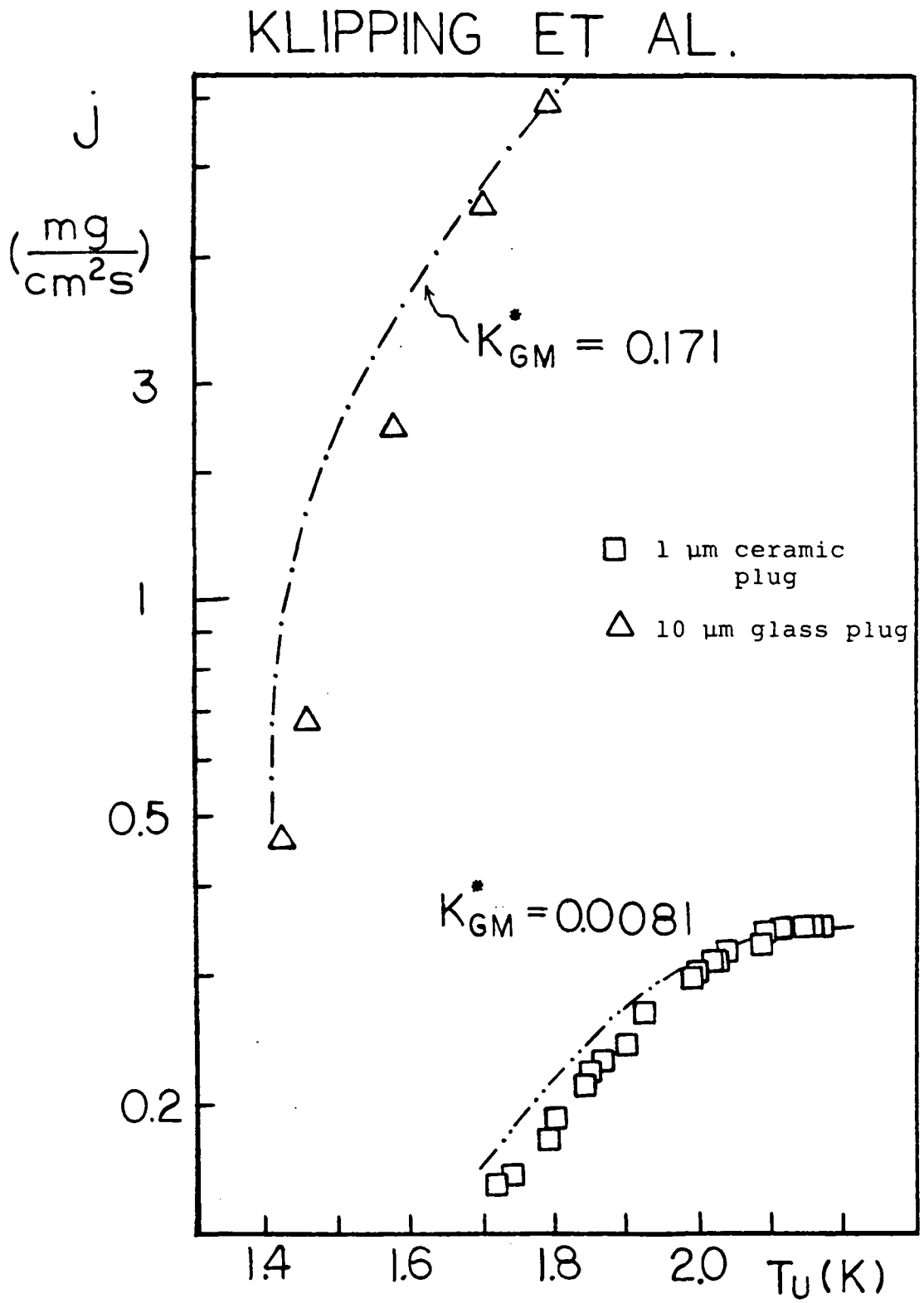

Figure 5.23. Comparison of the modified Gorter-Mellink equation to data of Klipping et al.

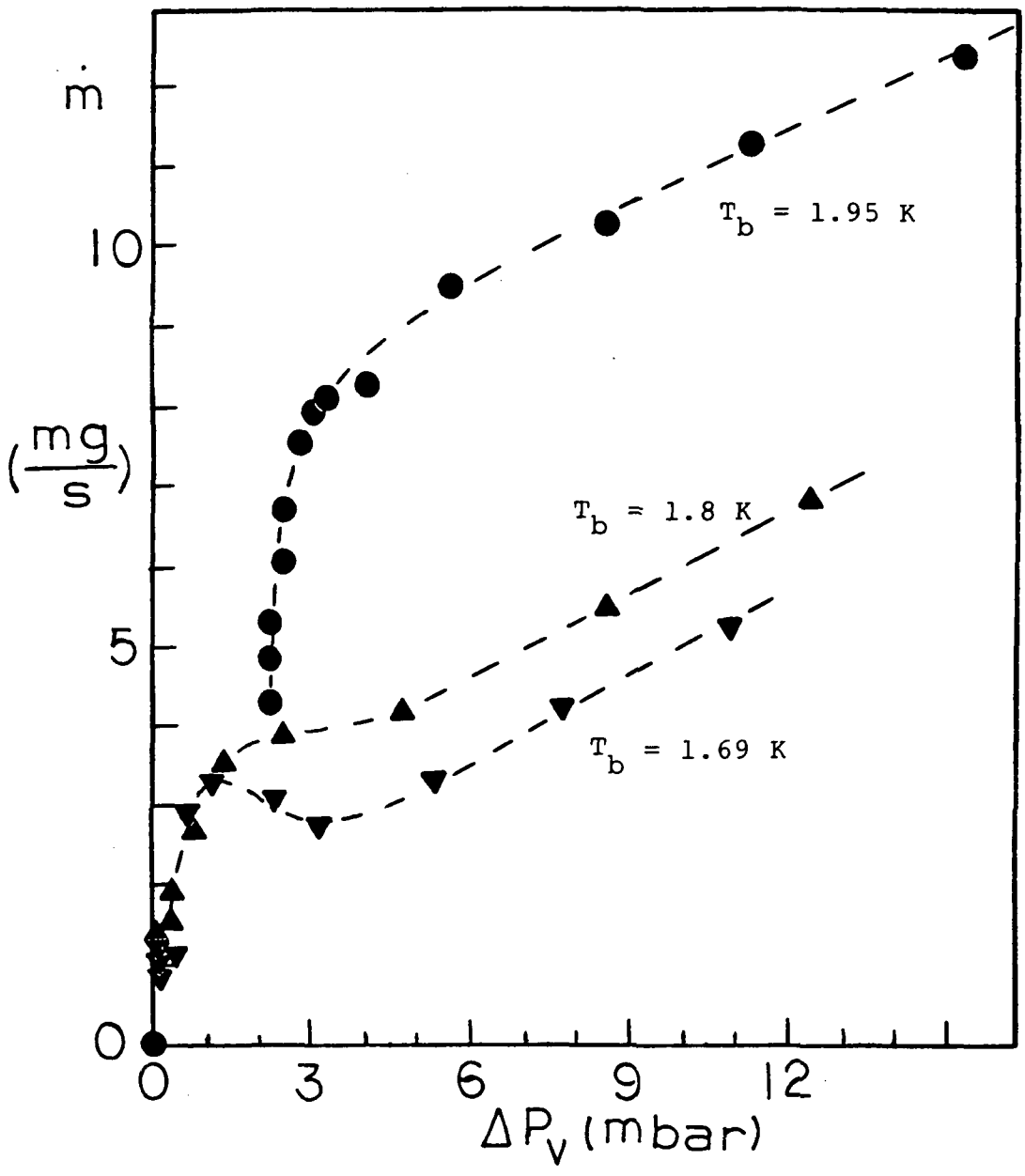

Figure 5.24. $\dot{m}$ versus ΔP_V for the phase separation of the in-flight IRAS porous plug (Petrac 1979).

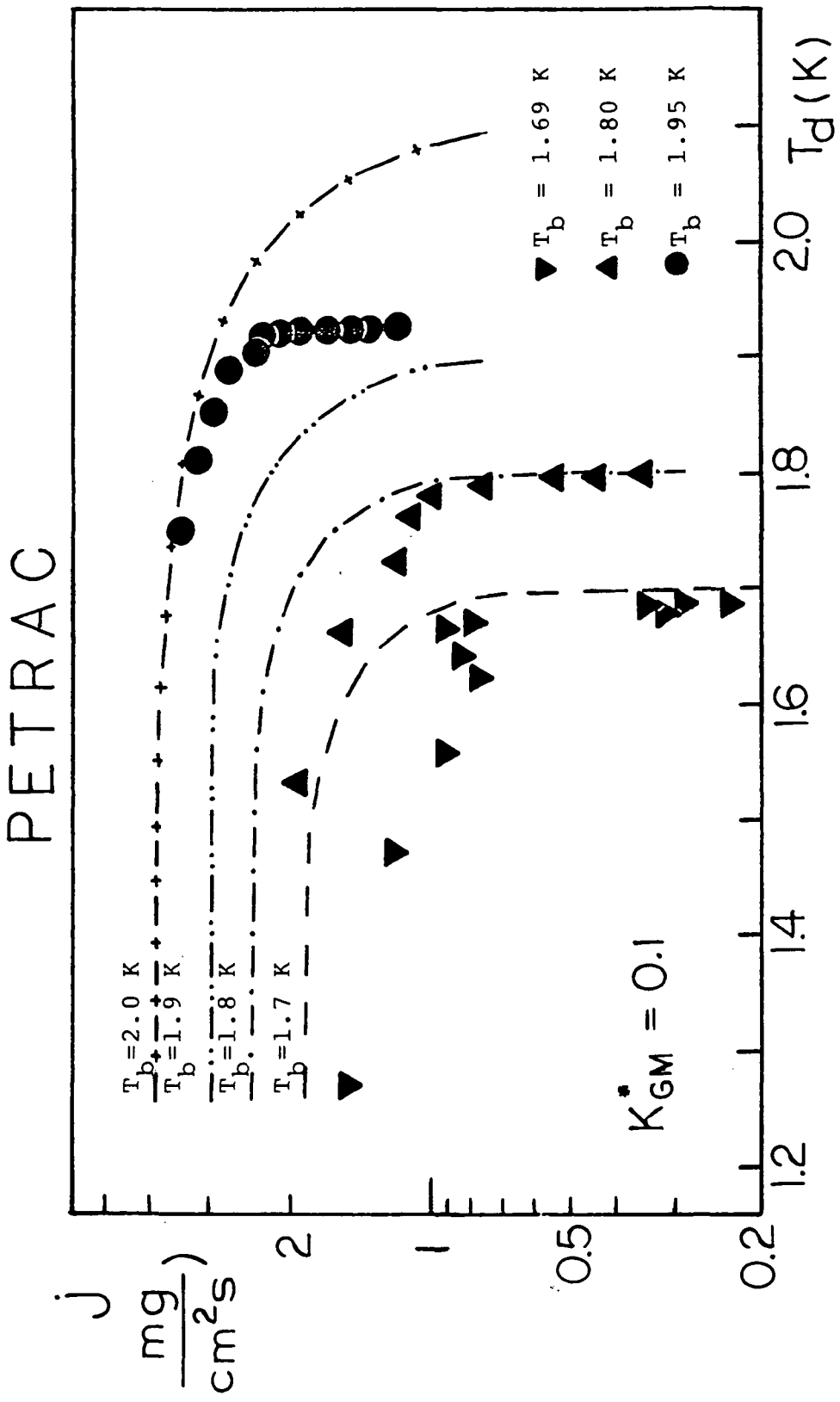

Figure 5.25. Comparison of the modified Gorter-Mellink equation to the in-flight IRAS porous plug VLPS data (D. Petrac 1979).

Gorter-Mellink transport), the use of Equation 5.14 might predict a higher flow rate. Figures 5.26 to 5.28 represent VLPS data of Murakami et al. (1984). Again, the experiments were performed with constant bath temperature. Data of ceramic plugs (No.s 3 and 4 in Murakami 1984) are plotted in Figures 5.26 and 5.27 respectively. The results of a sintered stainless steel plug are shown in Figure 5.28 (No. 6 in Murakami 1984). It is noted that for plug No.s 4 and 6, the modified Gorter-Mellink equation (Equation 5.14) tends to give a high prediction at low temperature and a low prediction at high temperature. As discussed before, the laminar linear regime is more easily accessible at low temperature (asymptotic region). Therefore, the fact that the data might be in the transition regime results in a lower mass flux density value than the fully developed Gorter-Mellink prediction. For the high temperature case ($T > 2.05$ K), the mass flow rate of Murakami's data is found to be much larger than Equation 5.14. In a number of Murakami's ceramic plugs, he noticed a radical increase in the flow rate as the temperature gradient was increased at $T_b > 2.05$ K. Murakami considered this behavior as a typical flow feature of some porous plugs, and plug No. 4 was one of them. As for the stainless steel plug (No. 6), leakage was observed by Murakami for $T_b > 2.06$ K. The breakthrough resulted in a much larger flow rate. In either case, for plug No.s 4 and 6, the flow at high temperature was not governed by the Gorter-

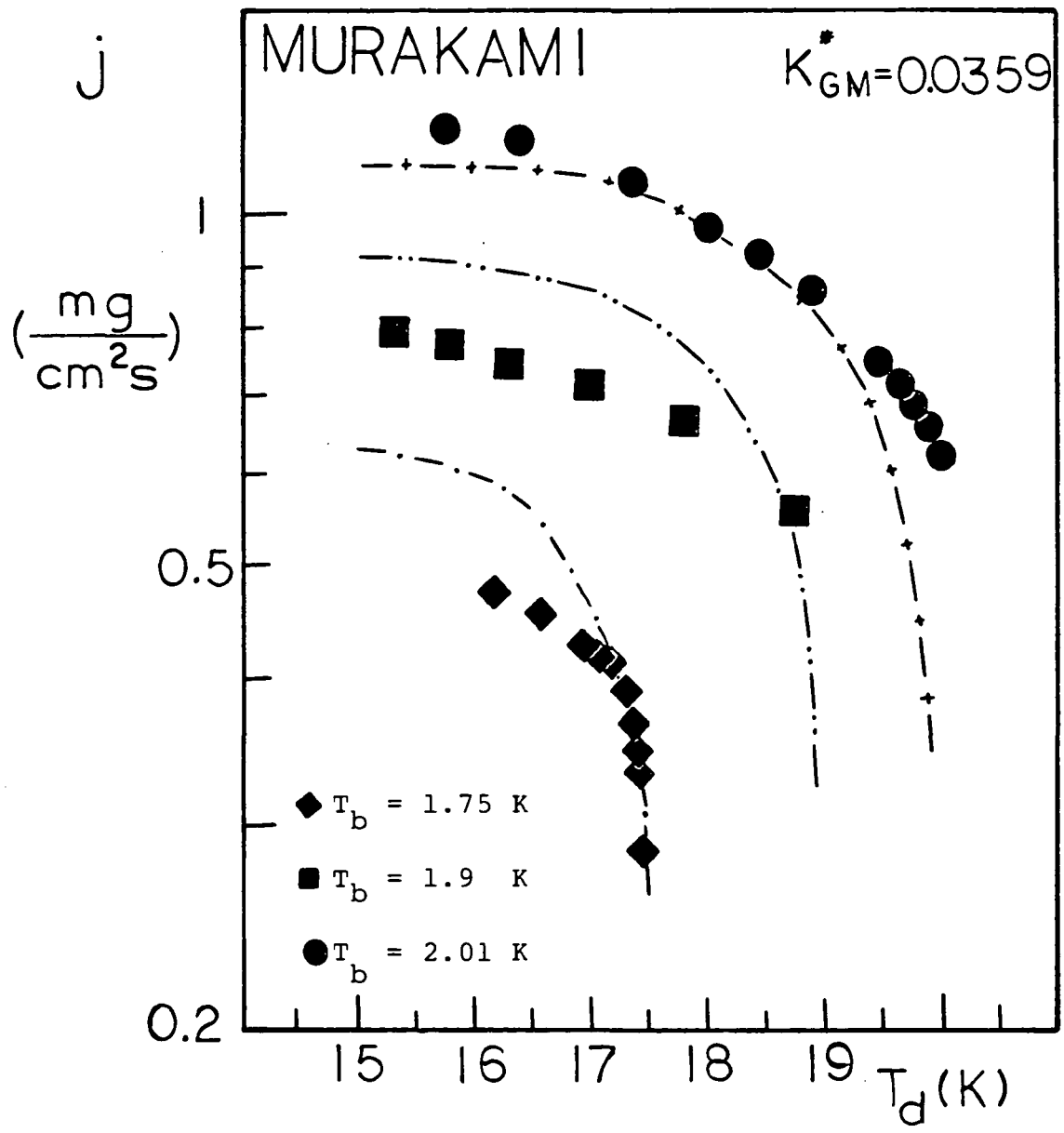

Figure 5.26. Comparison of the modified Gorter-Mellink equation to the VLPS data of Murakami's No. 3 ceramic plug (Murakami 1984).

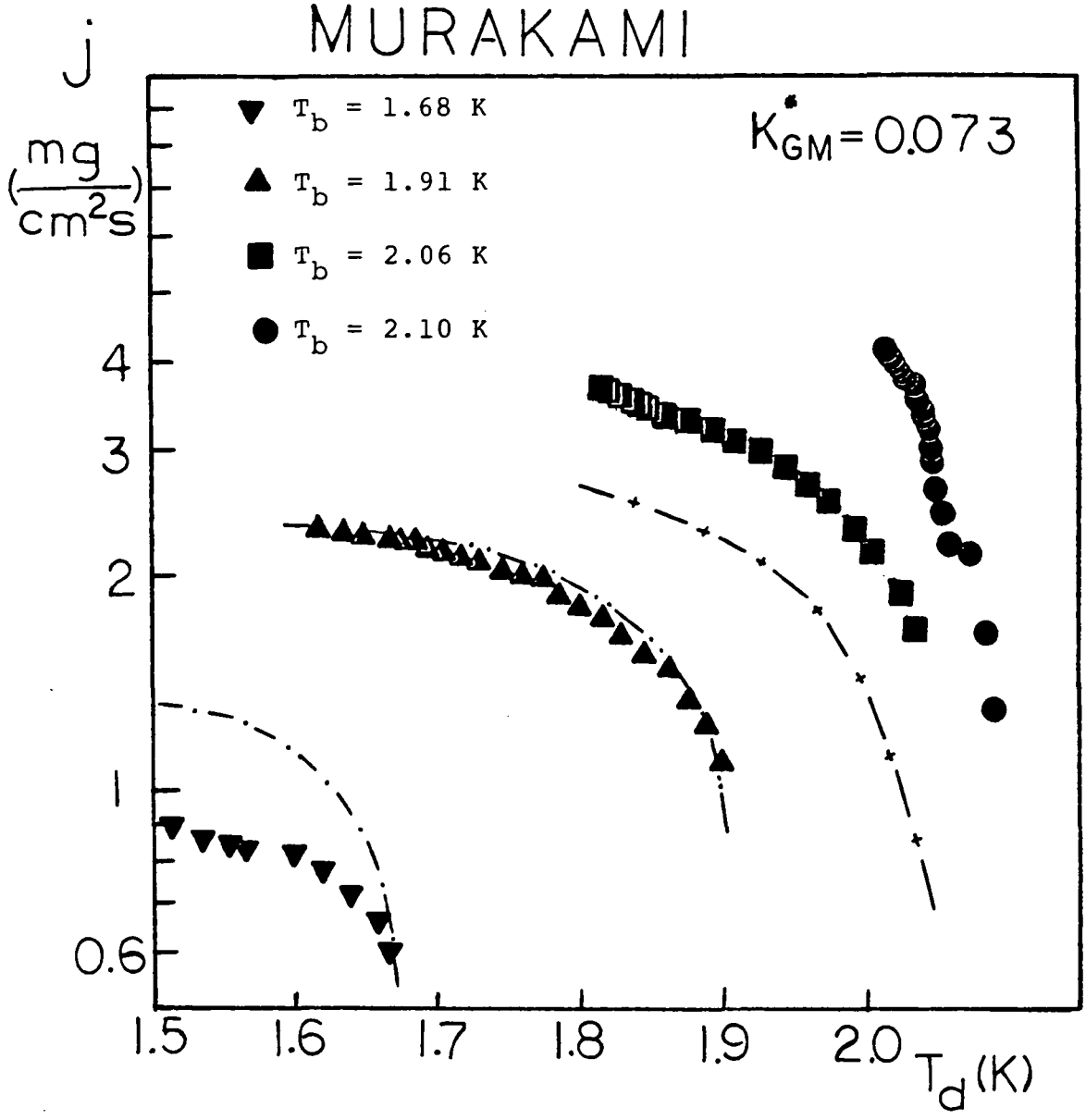

Figure 5.27. Comparison of the modified Gorter-Mellink equation to the VLPS data of Murakami's No. 4 ceramic plug (Murakami 1984).

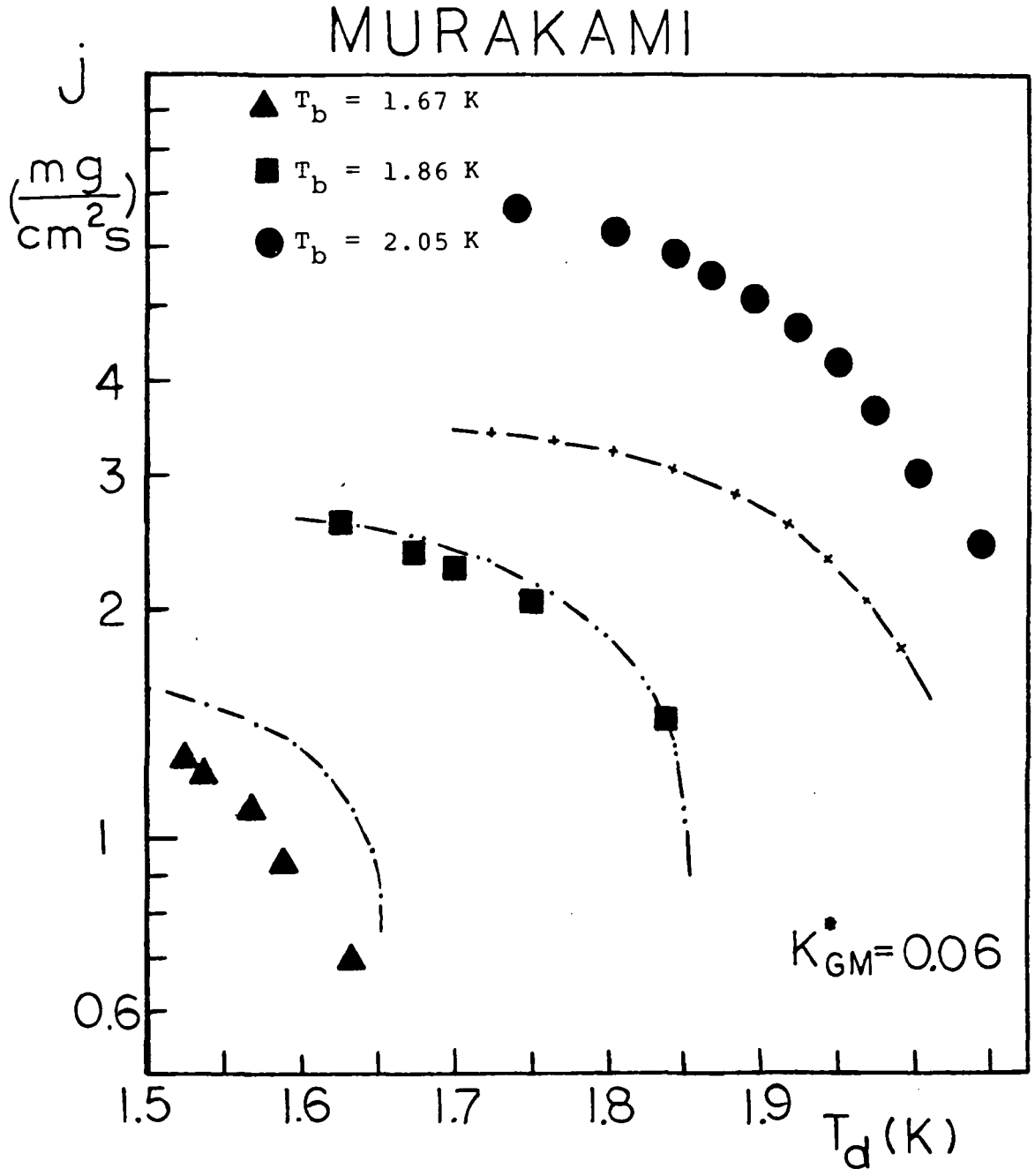

Figure 5.28. Comparison of the modified Gorter-Mellink equation to the VLPS data of Murakami's No. 6 stainless steel plug (Murakami 1984).

Mellink transport and is not expected to follow Equation 5.14.

The only adjustable parameter in the present modified Gorter-Mellink equation is K^*_{GM}. For each porous medium, a single K^*_{GM} is used to fit the data. It is found that every plug is characterized by a unique K^*_{GM}. In Figure 5.29, the room temperature permeability is compared against K^*_{GM}. The following result is found

$$K^*_{GM} \propto (K_p)^{\frac{1}{2}} \tag{5.15}$$

Lets look at the possible physical meaning behind the above relation. At steady state, the annihilation and growth of the vortex lines in Vinen's model should be balanced. Thus, Equation 3.31 becomes

$$\frac{\vec{w}}{L_{vo}^{\frac{1}{2}}} = \frac{\rho}{\rho_n} \frac{h}{2\pi m B} \frac{\chi_2}{\chi_1} \tag{5.16}$$

Substituting Equations 3.26 and 3.32 into 5.16, one can eliminate χ_1, χ_2 and the Gorter-Mellink coefficient A_{GM} to get

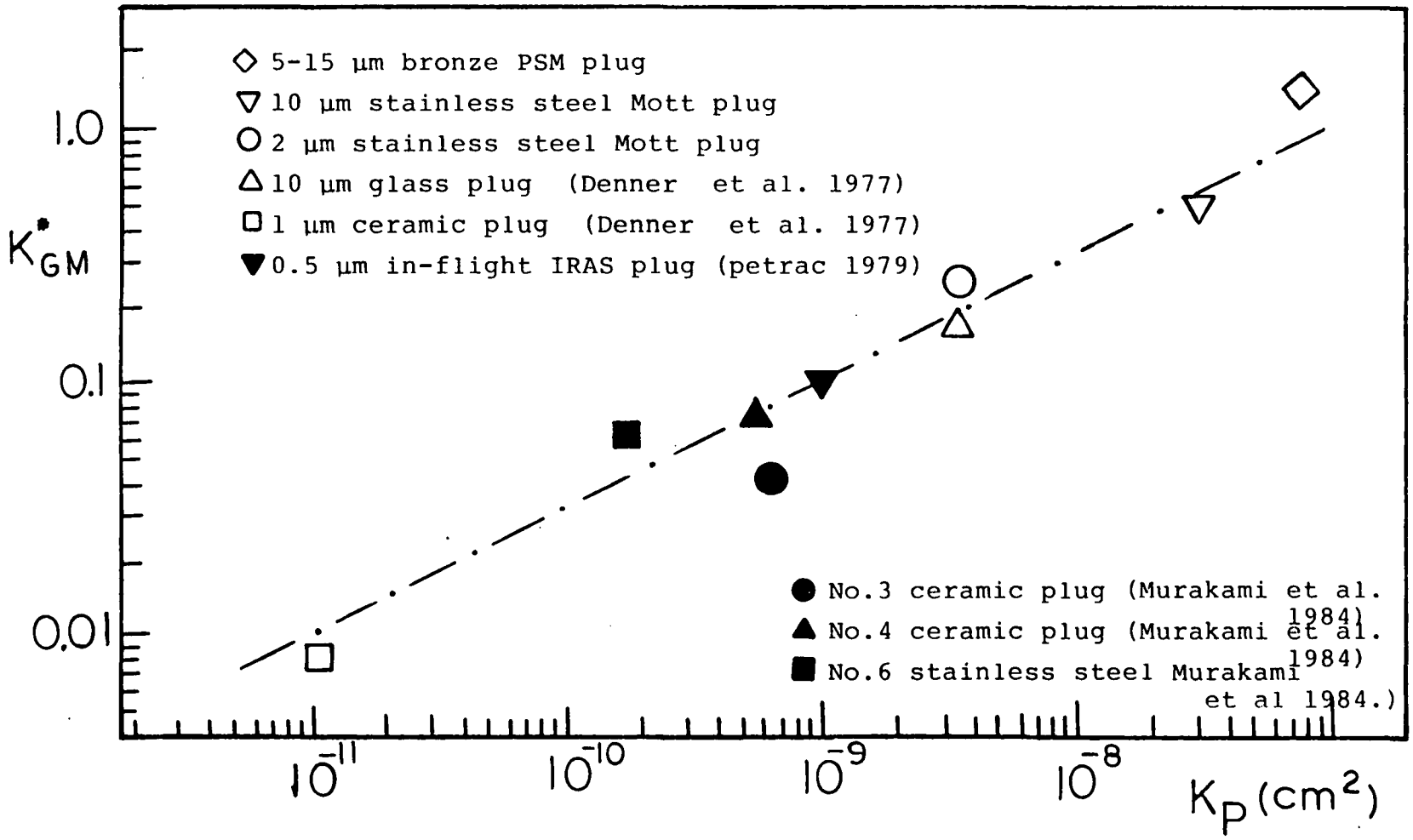

Figure 5.29. Gorter-Mellink constant as a function of the room temperature permeability.

$$K_{GM}^3 = \frac{3}{2\pi} \frac{\rho^2}{\rho_s \eta_n} \frac{2\pi m}{hB} \frac{w^2}{L_{vo}} \tag{5.17}$$

The above equation shows the relationship between K_{GM} and w/L. For unbound liquid helium, L_{vo} is the length of the vortex line per unit volume at equilibrium. Let's say that for the transport of He II in restricted geometries

$$L_{vo} = \xi/\text{volume} = \xi/L_c^3 \tag{5.18}$$

where ξ is the total length of the vortex line in the restricted volume. For the transport in porous media, a useful characteristic length is $L_c = K_p^{\frac{1}{2}}$. Thus, Equation 5.17 can be rewritten as

$$K_{GM}^* = \left(\frac{3}{2\pi} \frac{\rho^2}{\rho_s \eta_n} \frac{2\pi m w^2}{hB\xi}\right)^{1/3} (K_p)^{1/2} \tag{5.19}$$

Note that K^*_{GM} is introduced to distinguish the Gorter-Mellink constant in porous media. Therefore, if Vinen's vortex model can be extended to transport of He II in porous media,

then the Gorter-Mellink constant should be a linear function of L_c or $K_p^{\frac{1}{2}}$. This linear behavior indicates that the influence of pore size on the vortex tangle is more than a simple decay of lines at the walls (as predicted by Equation 3.33). Equation 5.19 suggests that as the pore size is reduced the vortex tangle is pinched. This results in a larger mutual friction and A_{GM} increases whereas K^*_{GM} decreases accordingly (Equation 3.26).

So far, the Gorter-Mellink constant K_{GM} has not received the attention that it deserves. If the Gorter-Mellink coefficient A_{GM} is a measure of the mutual friction between the normal fluid and the superfluid, then K_{GM} is the measure of the throughput of the normal fluid. For the transport of He II in wide ducts, Soloski (1977) found that K_{GM} equals to 11.3. In Figure 5.30, A_{GM} values from various authors are compared with Equation 3.26, with K_{GM} = 11.3. Schwartz's theory (1978) is also included in Figure 5.30. Reasonable agreement is found between Equation 3.26 and the literature values. Note that a different definition of the 'Gorter-Mellink regime' has been adopted by the Klipping group (Schotte 1980) which departs significantly from the common usage adopted in the present work.

In a recent article, Ladner (1983) pointed out that the Gorter-Mellink coefficient is "strongly geometry- and temp-

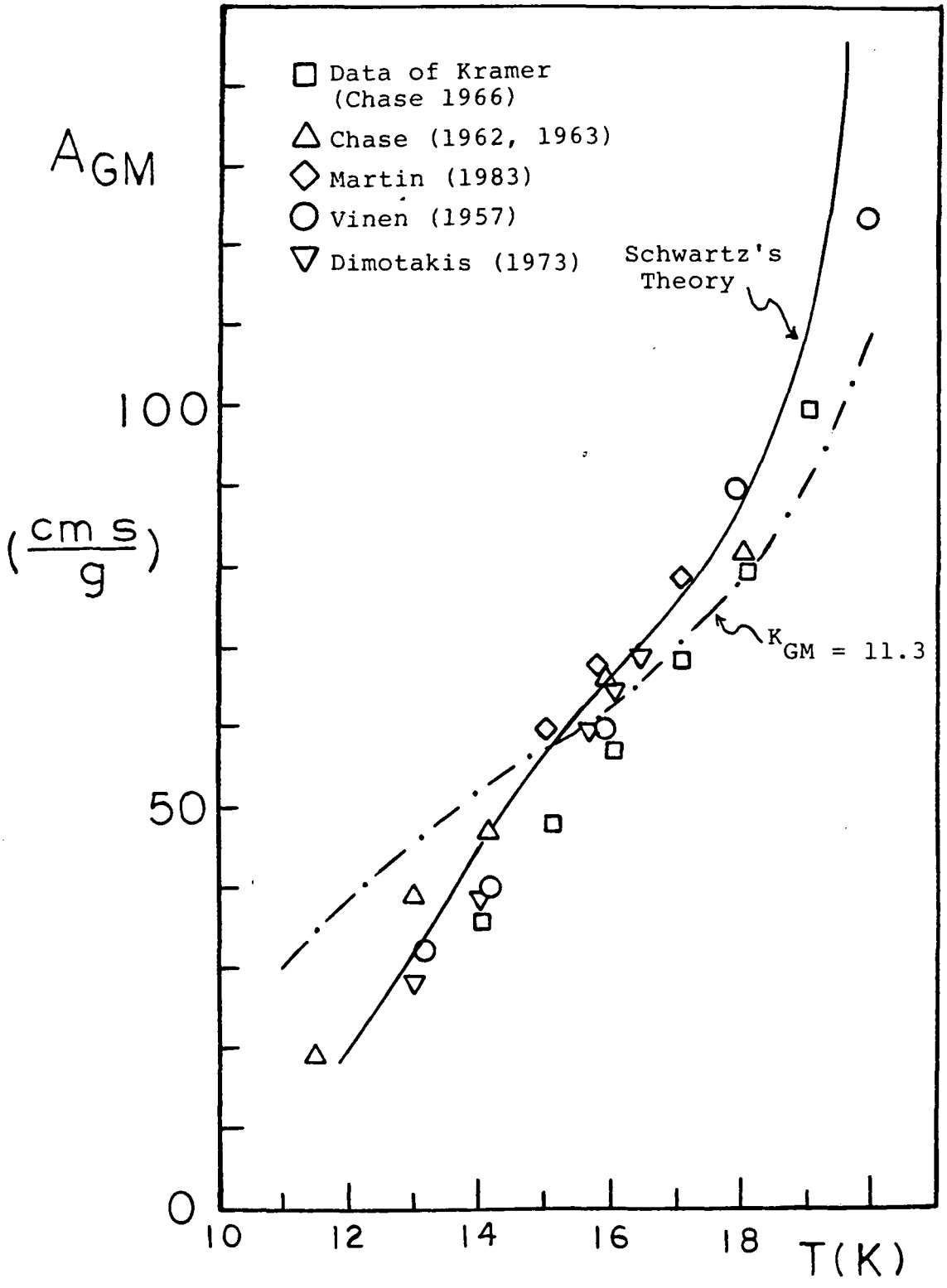

Figure 5.30. Gorter-Mellink coefficient as a function of temperature.

erature-dependent and that the often-quoted average value of 50 cm-s/g is inadequate for most meaningful calculations involving A_{GM}". Since K_{GM} is not a function of temperature, using Equation 3.26 is much more accurate and convenient than the rough estimation of A_{GM} = 50 cm-s/g.

From Figure 5.29 one realizes that for the same nominal pore size, the ceramic or glass plugs tend to give a smaller throughput (K^*_{GM} or K_p) than the corresponding sintered metal plugs.

The results of Klipping's group (Denner et al. 1977) for a 1 μm ceramic plug are plotted in Figure 5.31 together with some typical active phase separation data (Schotte et al. 1980). Since it was shown that Klipping's data follow the modified Gorter-Mellink equation, the much steeper slope of $\dot{m}$ versus ΔP_v of the slit data seems to indicate that the active phase separation system was actually operating in the breakthrough regime at high flow rates.

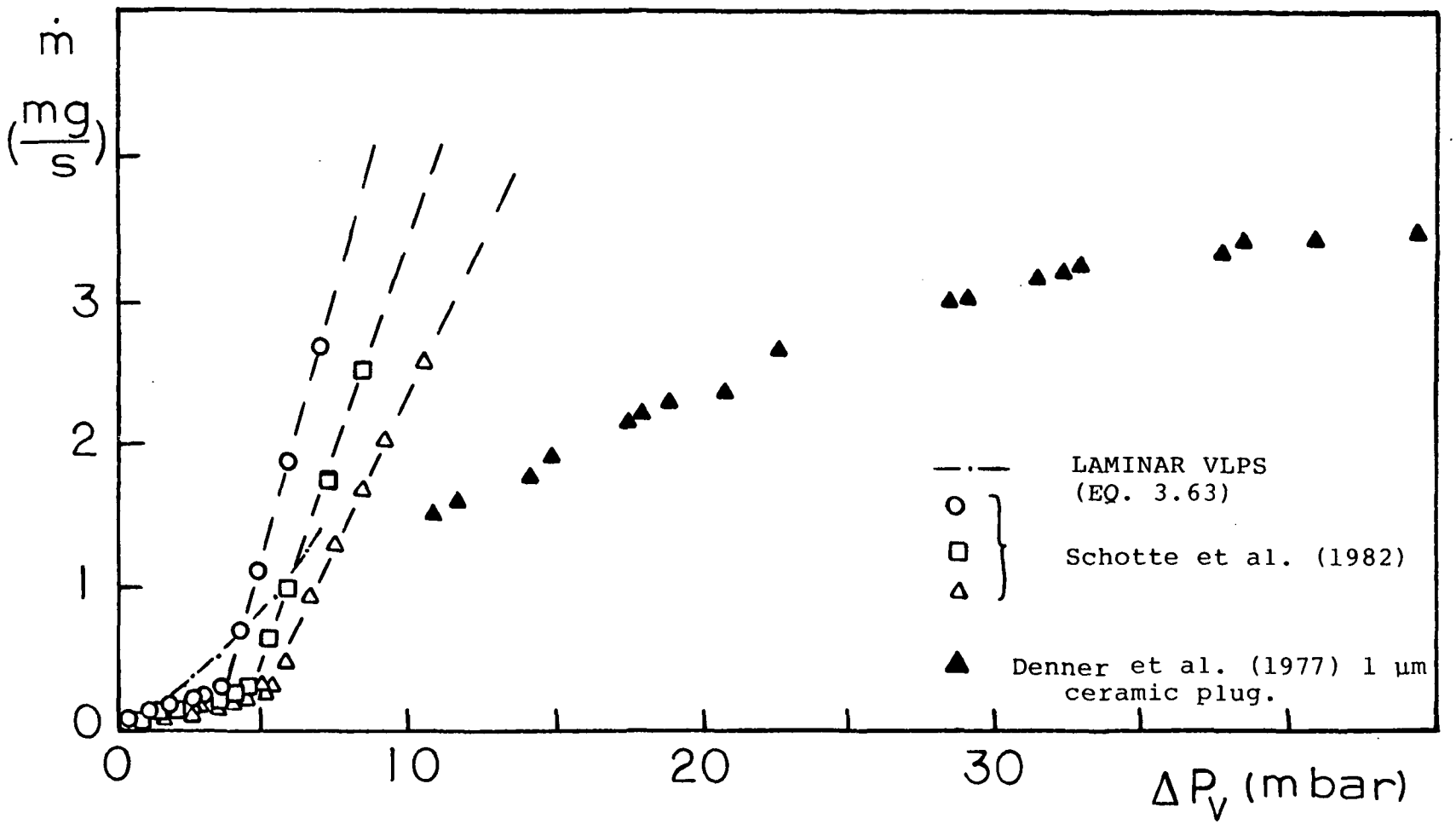

Figure 5.31. Comparison of active phase separation data to the porous plug phase separation data.

Chapter VI

CONCLUSIONS

The major conclusions of this research can be summarized as follows.

1) Newtonian Flow Results

2) He II Flow Results

6.1 NEWTONIAN FLOW RESULTS

A number of porous plug characterizing parameters were investigated, for examples, the Darcy permeability K_p, the equivalent Ergun diameter D_E and the nominal pore size S_o. Among the three characteristic lengths, the equivalent Ergun diameter has the largest value. It is related to the Darcy permeability via the following equation

$$D_E = (1 - \varepsilon)(150K_p / \varepsilon^3)^{\frac{1}{2}} \qquad (6.1)$$

For each nominal pore size of the porous media, a range of permeability was found due to the manufacturing tolerances (e.g. the presence of "dead zones"). The range of K_p in-

creased with decrease in pore size, because as the particle diameter becomes smaller, the possible configuration within the plug becomes more unpredictable. For commercially available sintered plugs, modification of the plug compression is expected to improve predictability.

The room temperature permeability of various plugs with different pore size (ranges from 0.5 to about 10 μm) has been measured and good reproducibility was found, especially for the large grain size plugs. It is recommended to measure the plug permeability at low temperature, so that one would be more confident to apply the Darcy permeability (K_p) to the VLPS mode.

In the present investigation, three different methods have been used to determine the low temperature permeability, namely, the cold vapor K_p measurement, the zero net mass flow asymptotic limit and the liquid He I outflow experiment. These experiments are readily carried out using the VLPS apparatus for which the cold vapor method is the most convenient. The room temperature K_p was found to be reproducible at low temperatures, departing not more than 10% (by using the cold vapor technique). It is concluded that one should use the Darcy permeability to characterize the porous plugs used for VLPS.

6.2 HE II RESULTS

A major conclusion of the present VLPS investigation is the dominance of thermal transport which controls the plug's transport rate of the two-fluid system. The externally applied temperature difference, necessary for thermo-osmotic liquid retention, causes heat flow, i.e. normal fluid flow. Aside from a small deviation of the VLPS transport from the ZNMF, known ZNMF functions serve as a useful basis for quantification.

The modified Gorter-Mellink equation derived in the present turbulent model (based on ZNMF)

$$\vec{q}_{VLPS} = \left[\int_{T_d}^{T_u} \left(K^*_{GM}\eta_n ST \frac{\lambda}{\lambda+ST}\frac{\rho_s}{\rho}\right)^3 \frac{\rho^2\rho_s S}{L\rho_n\eta_n^2}\, dT\right]^{1/3} \qquad (6.2)$$

is very successful in predicting most of the phase separation data in the literature and the present work. This suggests that the normal operating condition for VLPS is in the turbulent regime. For data taken close to the transition region between the laminar and the turbulent flow, Equation 6.2 predicts a higher mass flow rate due to the fact that the turbulent transport is not fully developed. On the other hand, for breakthrough data, a much higher mass flow (than the one predicted by Equation 6.2) is found.

At low temperature and small flow rates, the laminar zero net mass flow equation

$$\vec{q}_{ZNMF} = K_p \rho^2 S^2 |\nabla T| / \eta_n \qquad (6.3)$$

is approached asymptotically by the VLPS data. There is a factor of $\lambda/(\lambda+ST)$ causing a small difference between Equation 6.3 and the laminar VLPS equation proposed in this dissertation (Equation 6.4),

$$\vec{q}_{VLPS=K_p}[\lambda/(\lambda+ST)]\rho^2 S^2 |\nabla T|/\eta_n \qquad (6.4)$$

Within the scatter of the VLPS data, the ZNMF mode gives a very good approximation for the VLPS of He II ($\lambda/(\lambda+ST)$ ranges from 0.999 at 1 K to about 0.872 at T_λ).

From the preceeding findings, the possible operation conditions for the VLPS mode can be mapped as shown in Figure 6.1. At small flow rates, the data follow the laminar VLPS equation (Equation 6.4). As the ΔP_v increases, the flow turns into the transition regime and finally into the turbu-

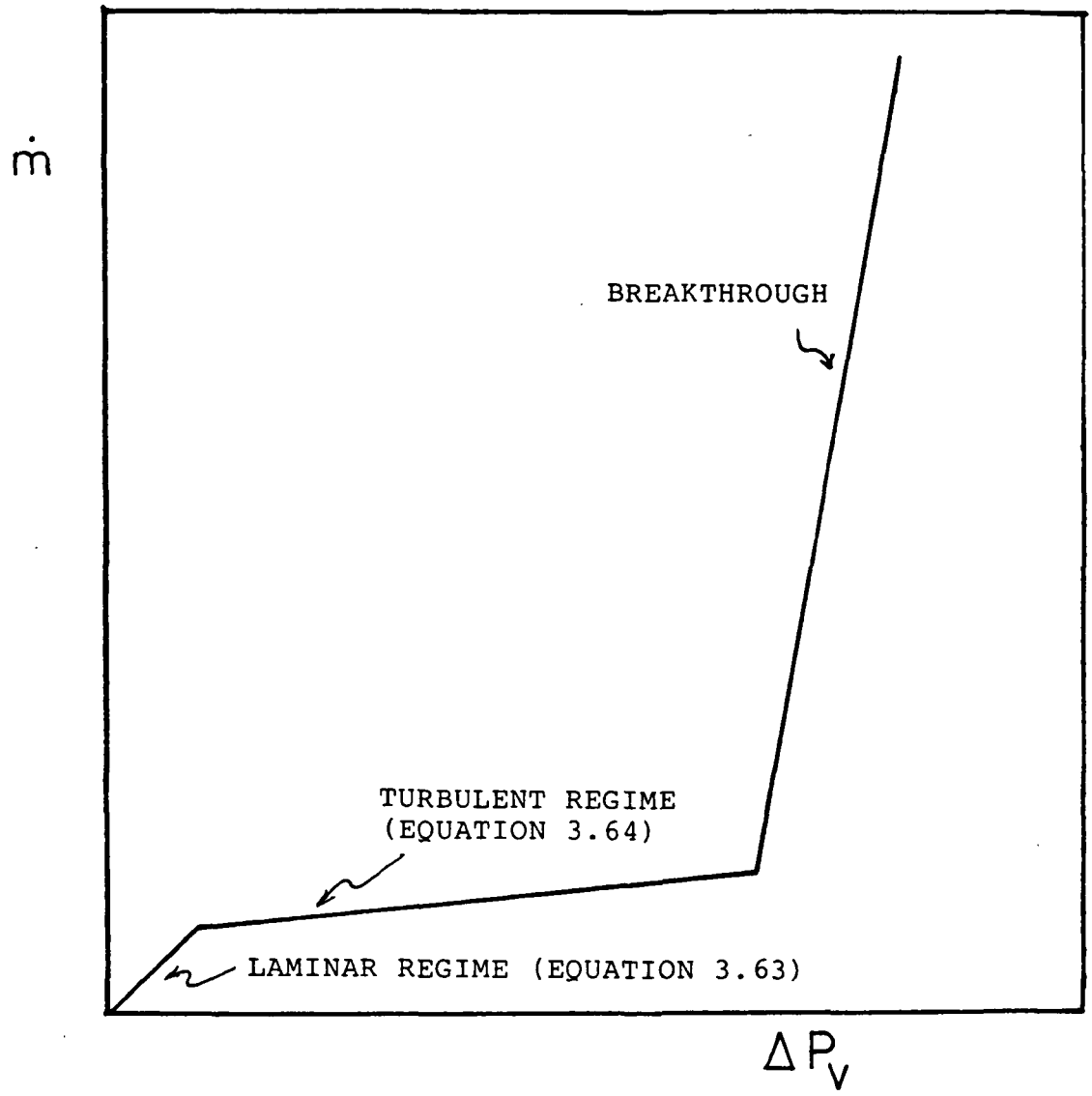

Figure 6.1. Schematic diagram showing the possible operating conditions for the vapor-liquid phase separation of He II.

lent range. When the pressure difference is very high, the onset of breakthrough occurs. Breakthrough is characterized by a sharp increase in the flow rate. This regime is not recommended for VLPS, because of the large amount of liquid loss, and the radical change of $\dot{m}$ with ΔP_v makes the system extremely unstable. After the completion of breakthrough, the flow turns into the classical Newtonian flow.

As mentioned earlier, there are secondary effects in VLPS. The fact that the modified Gorter-Mellink equation was able to describe most of the VLPS data of the present work and the literature indicates that for the porous media investigated, the surface tension effect and the thermal conductance of the plug materials have a secondary influence. However, for pore sizes < 0.5 μm, the surface tension effect within the plugs cannot be ignored. Also for very small pore size plugs, made of highly conductive metals, the clamping of the normal fluid results in the transport of heat through conduction within the solid grains. In this case, the Fairbank model is very useful. It is also found that for the same nominal pore size, the ceramic or glass plugs tend to give a smaller throughput value (K^*_{GM} or K_p) than the corresponding sintered metal plugs.

In fitting various VLPS data to the modified Gorter-Mellink equation, a unique correlation is found between the permeability and the Gorter-Mellink constant

$$K^*_{GM} = (10^7 K_p)^{\frac{1}{2}} \tag{6.5}$$

K^*_{GM} is plotted as a function of the room temperature permeability in Figure 6.2. For large permeabilities, the wide duct value of $K_{GM} = 11.3$ is approached. Interpolating between the two limits, the following equation is proposed

$$K^*_{GM} = [(1/K_{GM})^2 + (10^{-7}/K_p)^2]^{-\frac{1}{2}} \tag{6.6}$$

The data in Figure 6.2 are interpreted as providing the first evidence of the dependence of vortex tangle (or mutual friction) on the pore size. As the pore size is reduced, the vortex lines are pinched together and the throughput of the normal fluid is decreased as the mutual friction (or A_{GM}) increases. In extending Vinen's vortex model to the transport of He II in porous media, K^*_{GM} is found to be proportional to the square root of K_p. This agrees with the findings of the present model.

Within data scatter, Equation 6.6 is very valuable for the design of VLPS systems. Knowing the desired heat load and operating conditions (e.g. bath temperature) one can

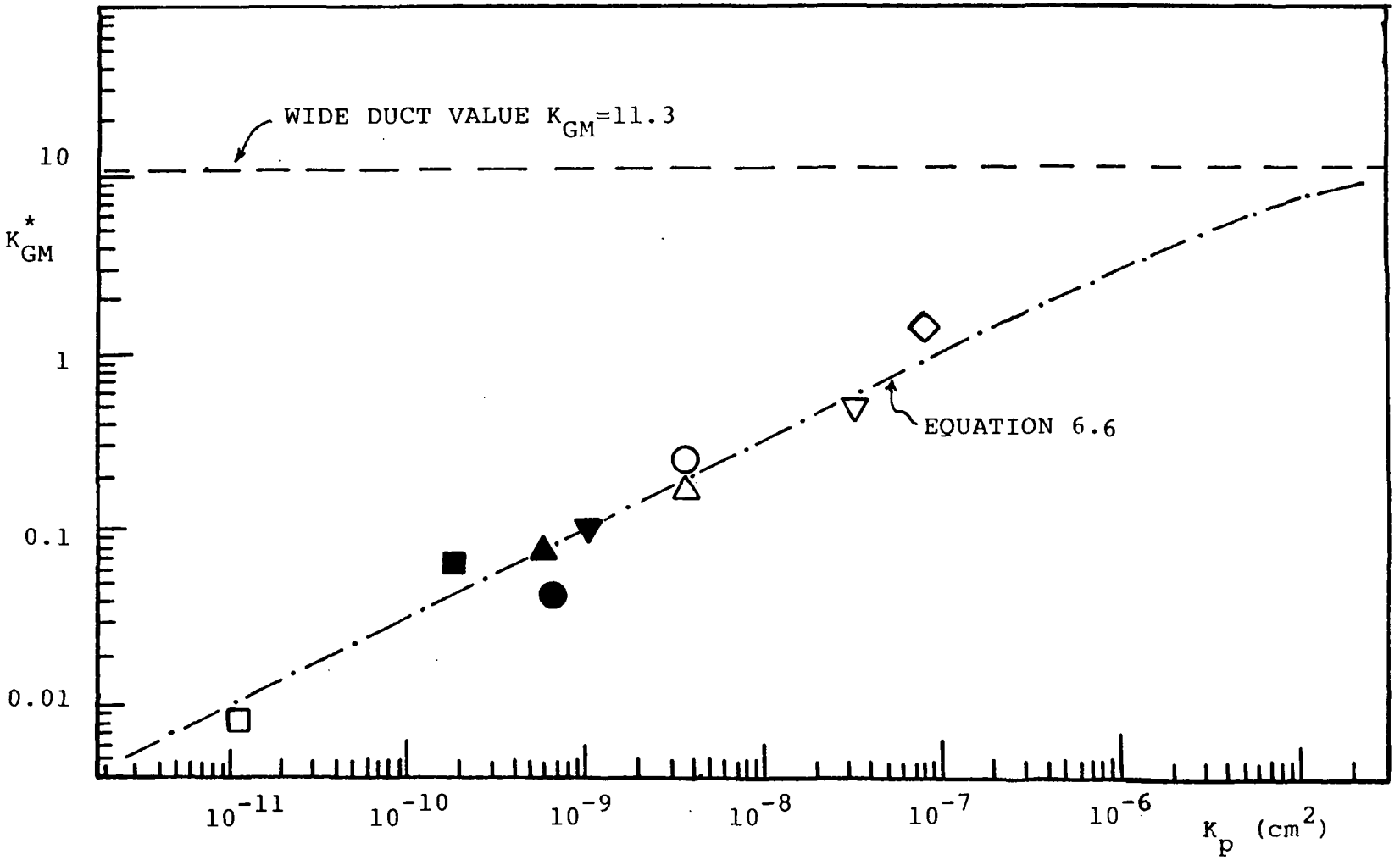

Figure 6.2. Gorter-Mellink constant K^*_{GM} as a function of room temperature permeability (the symbols used in this figure are same as those in Figure 5.29).

obtain the corresponding K^*_{GM} value via the modified Gorter-Mellink equation (Equation 6.2). The porous plug with the reguired permeability can thus be found by Equation 6.6 or Figure 6.2. In cases where the VLPS design requires a wide range of heat load (the heat load during launching can be guite different from that of the normal operation), a combination of porous plugs with different permeability is recommended.

On the basis of local thermodynamic equilibrium, it is found that zero-gravity operations of the present plugs and most of the literature plugs take place in the turbulent regime.

Concerning future work, it is noted that there are very few plug results for the ZNMF mode in the turbulent regime of fine porous media. On the other hand, concerning wide pore systems of VLPS, there are very few data in the laminar range.

A major improvement of VLPS understanding resulting from the present work, with respect to previous attempts, is the recognition that the constant K^*_{GM} is a function of the pore size. Also, the temperature dependence of the properties requires the integral of Equation 6.2.

BIBLIOGRAPHY

Allen,J.F. and A.D.Misener, Nature, 141, 75, (1938); Proc. Roy. Soc. (London), A 172, 467, (1939).

Barenghi,C.F., R.J.Donnelly and W.F.Vinen, Journal of Low Temperature Physics, vol. 52, no. 3/4, 189, (1983).

Biskeborn,R. and R.W.Guernsey,Jr., Phys. Rev. Letters, 34, 455, (1975).

Borelius,G., Cryogenics, 3, 96, (1963).

Brickwedde,F.G. and others, National Bureau of Standards, Monograph 10, June 17, (1960).

Brooks,J.S. and R.J.Donnelly, Journal of Physical Chemistry Reference Data, 6, 51, (1977).

Bruschi,L., G.Mazzi, M.Santini and G.Torzo, Journal of Low Temperature Physics, 18, 487, (1975).

Chase,C.E., Physical Review 131, 1898, (1963); Physical Review 127, 361, (1962).

Chase,C.E., in Superfluid Helium, edited by J.F.Allen, Academic Press, New York, 215, (1966).

Childers,R.K. and J.T.Tough, Physical Review B, vol. 13, no. 3, 1040, (1976).

Daunt,J.G. and K.Mendelssohn, Proc. Roy. Soc. (London) A 170, 423 & 439, (1939).

Denner,H.D., G.Klipping, I,Klipping, Menzel Ruppert, Research and Techanical Notes (1977).

Dimotakis,P.E. and J.E.Broadwell, Phys. Fluids 16, 1787, (1973).

Dimotakis,P.E., Phys. Rev. A10, 1721, (1974).

Dipirro,M., F.Fash and D.McHugh, in the Proceedings of the Space Helium Dewar Conference, Huntsville, Alabama, 121, August (1983).

Forstat,H., Physical Review 3, 1450, 1958.

Frederking,T.H.K., H.Van Kampen, M.A.Weenen and P.Wyder, Physical 108 B, 1129, (1981).

German,R.M., Powder Technology 30, 81, (1981).

Gorter,C.J. and J.H.Mellink, Physica 15, 285, (1949).

Guyon,E. and P.Pieranski, Physica 73, 184, (1974).

Heijden,G.V., W.J.P.De Voogt and H.C.Kramers, Physica 59, 473, (1972).

Hendricks,J.G. and G.R.Karr, in the Proceedings of the 9th International Cryogenic Engineering Conference, Kobe, Japan, 190, (1982).

Hendricks,J.G. and G.R.Karr, Space Worshop, Boulder, Colorado, August (1985).

Hussey,R.G. , B.J.Good and J.M.Reynolds, Physics of Fluids, 10, 89, (1967).

Kapitza,P., Nature 141, 74, (1938).

Keesom,W.H. and Wolfke, Leiden Comm. 190 b, (paper E-2 p65), (1927).

Keesom,W.H. and G.E.MacWood, Physica 5, 737, (1938).

Ladner,D.R., in the Proceedings of Space Helium Dewar Conference, Huntsville, Alabama, 231, August (1983).

Landau,L.D., Phys. Review 60, 356, (1941).

Lee,J.M., Master Thesis in Engineering, University of California, Los Angeles, (1982).

Martin,K.P. and J.T.Tough, Phys. Rev. B 27, 2788, (1983).

Maynard,J., Physical Review B, vol. 14, no. 9, 3868, (1976).

Murakami,M., in the Proceedings of the Space Cryogenics Workshop, West Berlin, Germany (F.R.), August (1984).

Murakami,M., N.Nakaniwa, H.Nakai and K.Uyama, Inst. Space and Astro. Rept. No. 612, 1984.

NBS Circular 561, Reference Tables for Thermocouples (1955).

Omega Engineering, Inc., Temperature Measurement Handbook, (1979).

Petrac,D. and P.Mason, in the Proceedings of the 7th International Cryogenic Engineering Conference, London, 120, July (1978).

Petrac,D., Report on Development Tests and Analysis Performed at JPL in July-Sep, (1979).

Putterman,S.J., Superfluid Hydrodynamics, North-Holland Publishing Co., Amsterdam London, 11, (1974).

Rorschach, Jr.H.E., Physical Review, 105, 785, (1957).

Schmidt,R. and Wiechert, Z.Physik B, 36, 1, (1979).

Schwartz,K.W., Physical Review B, 18, 245, (1978).

Selzer,P.M., W.M.Fairbank and C.W.F.Everitt, in the Proceedings of the Advances in Cryogenic Engineering 16, 277, (1970).

Schotte,U. and H.D.Denner, in the Proceedings of the 8th International Cryogenic Engineering Conference, Genova, 27, (1980).

Schotte,U. and H.D.Denner, Z.Phys. B, 41, 139, (1981).

Schotte,U., Z.Phys. B, 48, 183, (1982).

Soloski,S.C., Ph.D. Dissertation in Engineering, University of California, Los Angeles, (1977).

Tisza,L., J. Phys. Radium 1, 164, (1940); J. Phys. Radium 1, 350, (1940).

Van den Meijdenberg,C.J.N., K.W.Taconis and R.De Bruyn Oubotor, Physica, 27, 197, (1961).

Van Dijk and M.Durieux, Physica, 24, 1, (1958).

Vinen,W.F., Proc. Roy. Soc. (London) A240, 114 & 128, (1957); Proc. Roy. Soc. (London) A 242, 493, (1957); Proc. Roy. Soc. (London) A 243, 400, (1958).

Vote,F.C., J.E.Myers, H.B.Chu and T.H.K.Frederking, in the Proceedings of the Advances in Cryogenic Engineering, 16, 393, (1971).

Webeler,R.W.H. and D.C.Hammer, Physics Letters, vol. 15, no. 3, 233, (1965).

Yuan,S.W.K. and T.H.K.Frederking, in the Proceedings of the ASME-JSME Thermal Engineering Conference, Honolulu, Hawaii, 191, (1983).

Yuan,S.W.K., T.H.K.Frederking and R.M.Carandang, in the Proceedings of the 10th International Cryogenic Engineering Conference, Otaniemi, Finland, 301, (1984).

Zemansky,M.W., Heat and Thermodynamics, 5th ed., McGraw-Hill, New York, 512, (1968).

APPENDIX A

Landau's Equations for the Two Fluid Model

The hydrodynamic equations of the two fluid model arise as follows. For pure superfluid flow at absolute zero with velocity $\vec{v}_s$, it is convenient to consider the liquid being at rest and the wall of the tube is moving at a speed of $\vec{v}_s$. The interaction between the wall and the liquid excites the phonons and rotons in the He II.

Landau has shown that the energy of liquid helium in such coordinate system is

$$E = E_o + p\vec{v}_s + m\vec{v}_s^2/2 \qquad (A.1)$$

where m is the mass of the liquid, $E_o = cp$ is the energy of the phonons, p is the momentum of the phonons and c is the velocity of sound.

The mass flux density of the liquid helium equals to the momentum density of the fluid since all of the atoms have the same mass

$$\vec{j} = \rho_o \vec{v}_s + \langle p \rangle \qquad (A.2)$$

where ρ_o is the density of He II, $\langle p \rangle$ is the mean momentum of the excitations per unit volume.

To minimize the energy E, the momentum tends to align

opposite to the superfluid velocity $\vec{v}_s$.

Lets say

$$\langle P \rangle = -\rho_n(\vec{v}_s - \vec{u}) \qquad (A.3)$$

This defines ρ_n. The excitations have a drift velocity of $\vec{u}$.

Combine Equation A.2 and A.3

$$\vec{j} = \rho_o\vec{v}_s - \rho_n(\vec{v}_s - \vec{u})$$

If ρ_s is defined as $\rho_o - \rho_n$ and we write $\vec{u} = \vec{v}_n$, then,

$$\vec{j} = \rho_s\vec{v}_s + \rho_n\vec{v}_n \qquad (A.4)$$

Thus, ρ_n and $\vec{v}_n$ are associated with the excitations in the fluid. Since ρ_n is a derived concept, it does not appear to represent the density of anything which has microscopic meaning. However, one can interprete macroscopically as saying that the current of He II is like that of a mixture of two fluids, one of density ρ_s moving at velocity $\vec{v}_s$, the other of density ρ_n and velocity $\vec{v}_n$.

The flow rate $\vec{j}$ is also related to the density by the equation of continuity

$$\partial\rho/\partial t + \nabla\cdot\vec{j} = 0 \qquad (A.5)$$

(t = time). Superfluid motion is characterized by irrotational phenomena of an Euler fluid

$$\nabla \times \vec{v}_s = 0 \qquad (A.6)$$

The Landau conservation statements lead to a set of macroscopic equations for the He II hydrodynamics:
Entropy conservation (ideal case):

$$\partial \rho S/\partial t + \nabla \cdot \rho S \vec{v}_n = 0 \qquad (A.7)$$

Momentum conservation:

$$\partial \vec{j}_i/\partial t + \partial \pi_{ik}/\partial x_k = 0 \qquad (A.8)$$

Mass conservation:

$$\partial \rho/\partial t + \nabla \cdot \vec{j} = 0 \qquad (A.9)$$

Superfluid conservation statement:

$$\partial \vec{v}_s/\partial t + (\vec{v}_s \cdot \nabla)\vec{v}_s = -\nabla \mu \qquad (A.10)$$

(P = pressure, μ chemical potential, π_{ik} momentum density tenser:

$$\pi_{ik} = P\delta_{ik} + \rho_s \vec{v}_{si}\vec{v}_{sk} + \rho_n \vec{v}_{ni}\vec{v}_{nk} - \eta_n(\partial\vec{v}_{ni}/\partial x_k + \partial\vec{v}_{nk}/\partial x_i) \quad (A.11)$$

The thermodynamic identity for $d\mu$ may be expressed as

$$d\mu = -SdT + dP/\rho - (1/2)(\rho_n/\rho)d(\vec{v}_n - \vec{v}_s)^2 \quad (A.12)$$

The relative velocity is $\vec{w} = \vec{v}_n - \vec{v}_s$. After substitution of Equation A.12 into A.10, and mulitplication of both sides of the equation by ρ_s, one obtains

$$\rho_s \partial\vec{v}_s/\partial t + \rho_s(\vec{v}_s\cdot\nabla)\vec{v}_s = -(\rho_s/\rho)\nabla P + \rho_s S\nabla T + (1/2)(\rho_n\rho_s/\rho)\vec{w}^2 \quad (A.13)$$

Assume that $\partial\rho/\partial t = \partial\rho_s/\partial t = \partial\rho_n/\partial t = 0$, and $\partial S/\partial t = 0$, we have from Equation A.8 and A.9

$$\text{div } \vec{v}_n = \text{div } \vec{v}_s = 0 \quad (A.14)$$

Substituting Equation A.11 in A.9 and using A.14 we find

$$\rho_s \partial\vec{v}_s/\partial t + \rho_n \partial\vec{v}_n/\partial t + \rho_s(\vec{v}_s\cdot\nabla)\vec{v}_s + \rho_n(\vec{v}_n\cdot\nabla)\vec{v}_n = -\nabla P + \eta_n\nabla^2\vec{v}_n \quad (A.15)$$

By substitution of Equation A.15 in A.13, we get

$$\rho_n \partial \vec{v}_n/\partial t + \rho_n (\vec{v}_n \cdot \nabla)\vec{v}_n = -(\rho_n/\rho)\nabla P$$
$$-\rho_s S \nabla T - (1/2)(\rho_n \rho_s/\rho)\vec{w}^2 + \eta_n \nabla^2 \vec{v}_n \qquad \text{(A.16)}$$

Equation A.16 and A.13 are Landau's equations of motion for normal and superfluid.

APPENDIX B

Dimensionless Numbers Used In This Research

Most of the dimensionless numbers used in this thesis are analogs of the general classical dimensionless numbers.

a) The dimensionless heat flux number, N_q versus the dimensionless driving force number, $N_{\nabla T}$: (Figure B.1)

Lets start with the classical Ergun's equation,

$$\nabla P = \frac{150 V \eta (1-\varepsilon)^2}{D_p^2 \ \varepsilon^3} + \frac{\rho V^2 (1-\varepsilon)}{\eta \ D_p \ \varepsilon^3} \qquad (B.1)$$

For He II, one can substitute the pressure gradient by the thermo-osmotic pressure and the velocity & viscosity by the normal fluid value. Together with Equation 5.2, one gets,

$$\nabla P_T = \frac{v_n \eta_n}{K_p} + 1.75 \frac{\rho v_n^2 \ / \ \eta_n}{(150 K_p \varepsilon^3)^{1/2}} \qquad (B.2)$$

Multiplying both sides by $\rho K_p^{3/2} \ / \ \eta_n^2$

$$\frac{\rho \nabla P_T K_p^{3/2}}{\eta_n^2} = \frac{\rho v_n K_p^{1/2}}{\eta_n} + \frac{1.75}{(150\varepsilon^3)^{\frac{1}{2}}} \frac{\rho^2 v_n^2 K_p}{\eta_n^2} \qquad (B.3)$$

Together with the definitions of N_q and $N_{\nabla T}$,

$$N_q = \frac{q\ K_p^{1/2}}{\eta_n\ S\nabla T} = \frac{\rho v_n\ K_p^{1/2}}{\eta_n} \qquad (B.4)$$

$$N_{\nabla T} = \frac{\rho \nabla P_T\ K_p^{3/2}}{\eta_n^2} = \frac{\rho^2 S \nabla T\ K_p^{3/2}}{\eta_n^2} \qquad (B.5)$$

Equation B.3 can be written as

$$N_{\nabla T} = N_q + 1.75 N_q^2/(150\varepsilon^3)^{\frac{1}{2}} \qquad (B.6)$$

Note that $\rho v_n K_p^{1/2}/\eta_n$ is the Reynolds number for the normal fluid. For small Re or N_q, Equation B.6 reduces to Equation 3.17,

$$N_q = N_{\nabla T} \qquad (B.7)$$

b) Resistance ratio: (Figure B.1)

For packed bed data, the results are usually presented as resistance ratio

$$R/R_N = 1 + 1.75 Re_k/150 \qquad (B.8)$$

where

$$Re_k = D_p v \rho/\eta(1-\varepsilon) \qquad (B.9)$$

C - 3

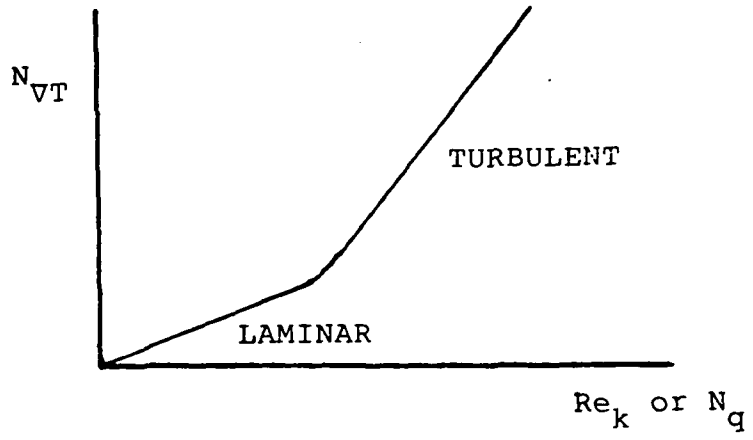

Figure B.1. N_q versus $N_{\nabla T}$.

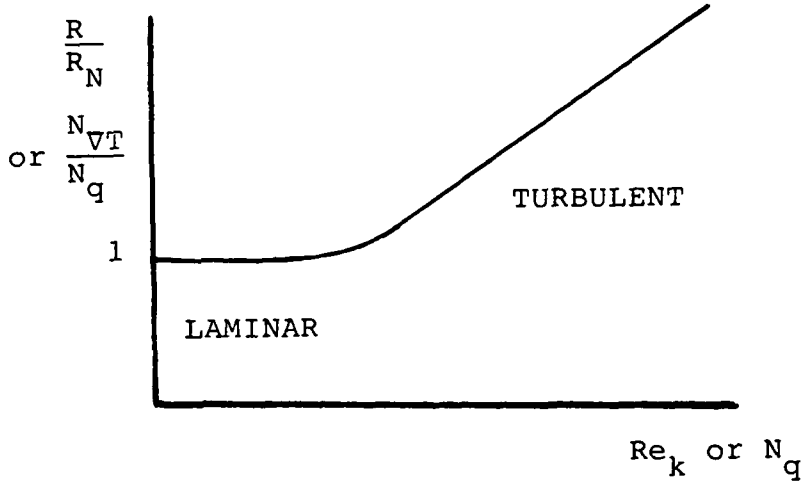

Figure B.2. Resistance ratio vs. Renolds number.

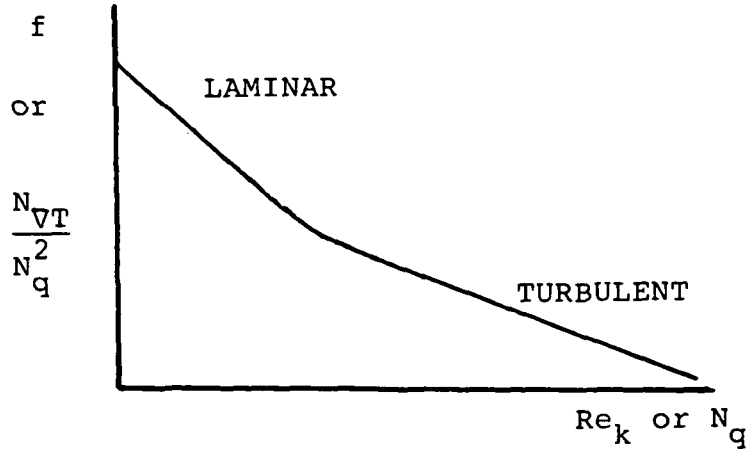

Figure B.3. Friction factor vs. Reynolds number.

For He II,

$$R/R_N = N_{\nabla T}/N_q = 1 + 1.75N_q/(150\epsilon^3)^{\frac{1}{2}} \qquad (B.10)$$

Equation B.9 and B.10 are essentially the same if one substitutes D_p by K_p.

c) Friction factor: (Figure B.3)

Another way of presenting packed bed data is by the friction factor. For the classical Ergun equation, we have

$$f = (150 / Re_k) + 1.75 \qquad (B.11)$$

For He II,

$$f' = N_{\nabla T}/N_q^2 = (1/N_q) + 1.75/(150\epsilon^3)^{\frac{1}{2}} \qquad (B.12)$$

Note that for Equation B.12, the definition of friction factor f' is slightly different from that of the classical case.

APPENDIX C

Computer Program Of Simpson's Rule Used To
Integrate The Modified Gorter-Mellink Equation

The function in Figure 3.14 is first fitted by a spline fit program. The coefficients generated are then substituted into the following program for integration:

```
      *JOB
      C       THIS PROGRAM EVALUATES THE TRAPEZOIDAL AND SIMPSON'S RULE
      C       APPROXIMATIONS OF INTEGRALS.  THE FUNCTION TO BE INTEGRATED
      C       IS PLACED IN THE FUNCTION F(X) SUBPROGRAM.
      C
            1 IMPLICIT REAL*8 (A-H,O-Z)
            2 LOGICAL*1 FLAG1,FLAG2,FLAG3
            3 COMMON C1,C2,C3,C4
            4 PRINT 100
            5 RESULT=TRAP=0.D00
            6 10  CONTINUE
            7 READ (5,*) A,B,C1,C2,N,C3,C4
            8   AT END DO
            9     PRINT 600
           10     STOP
           11   END AT END
           12 IF (A.GT.B) THEN DO
           13   FLAG1=.TRUE.
           14   SAVE=A
           15   A=B
           16   B=SAVE
           17  ELSE DO
           18   FLAG1=.FALSE.
           19 END IF
           20   FLAG2=FLAG3=.FALSE.
           21   H=DABS(B-A)/DFLOAT(N)
           22   IF (FLAG2) GOTO 30
           23   IF (MOD(N,2).EQ.1) THEN DO
           24     FLAG3=.TRUE.
           25     J=N-3
           26     RESULT=(F(B-3.D00*H)+3.D00*F(B-2.D00*H)+3.D00*F(B-H)
      *              +F(B))*9.D00/8.D00
```

```
      ELSE DO
        J=N-1
      END IF
      IF (J.LE.0) GOTO 30
      DO 20 I=1,J,2
        RESULT=RESULT+F(A+H*DFLOAT(I-1))+4.D00*F(A+H*DFLOAT(I))
     *    +F(A+H*DFLOAT(I+1))
        IF (MOD(I+1,10).EQ.0) THEN DO
          PRINT 700,A+H*DFLOAT(I+1),RESULT*H/3.D00
        END IF
20    CONTINUE
30    CONTINUE
      DO 40 I=1,N
        TRAP=TRAP+F(A+H*DFLOAT(I-1))+F(A+H*DFLOAT(I))
C       IF (MOD(I,10).EQ.0) THEN DO
C         PRINT 700,A+H*DFLOAT(I),TRAP*H/2.D00
C       END IF
40    CONTINUE
      IF (FLAG1) THEN DO
        TRAP=-TRAP
        RESULT=-RESULT
      END IF
      PRINT 250,N,TRAP*H/2.D00
      IF (FLAG2) THEN DO
        PRINT 400
       ELSE DO
        PRINT 350,RESULT*H/3.D00
        IF(FLAG3) PRINT 500
      END IF
     GOTO 10
100   FORMAT ('1',T3,'NUMBER',4X,'TRAPEZOID',7X,'SIMPSON''S',/,T5,
     *'OF',/T3,'PANELS',6X,'METHOD',10X,'RULE',/,'+ _____',4X,
     *'__________',7X,'__________')
250   FORMAT('0',I2,1P,T10,D14.7)
350   FORMAT('+',T27,1PD14.7)
400   FORMAT('+',T50,'SIMPSON''S RULE CANNOT BE USED WITHOUT ',
     *'HALVING THE INTERVAL')
500   FORMAT('+',T87,'3/8 RULE USED ON LAST 3 PANELS')
600   FORMAT('1')
700   FORMAT(G15.4,G15.6)
      END

      FUNCTION F(X)
      IMPLICIT REAL*8 (A-H,O-Z)
      COMMON C1,C2,C3,C4
      F=DEXP(((C1*X)+C2)*X+C3)*X+C4)
      RETURN
      END
```

APPENDIX D

Error Analysis

D.1 Experimental Accuracy of the Classical Permeability Measurement

The accuracy of the experiment depends on the stability and accuracy of measuring the following properties.

1) Thermometer calibration
2) Differential pressure across the porous plug
3) Volumetric flow rate of helium gas

Thermometer Calibration

The temperature in this experiment was measured by chromel/constantan thermocouples. The thermocouples were calibrated against temperature at fixed points (see Appendix E) and was found to agree within 2 K with the NBS Circular # 561 (1955) and Omega Temperature Measurement Handbook (1979).

Differential Pressure Across the Porous Plug

The pressure difference at low range was measured by Validyne's pressure transducer. It had a linearity of $\pm\frac{1}{2}\%$ of the full scale. ΔP at high pressure range was measured by a Pennwalt differential pressure gauge. It had an uncertainty in accuracy of 0.33% of the full scale.

Volumetric Flow Rate of Helium Gas

The flow rate of helium gas was measured by both a wet

test meter (Precision Scientific Co.) and a floating sphere rotameter (Brooks Instruments Co.). The rotameter had a linearity of $\pm$0.5%. Accounting for temperature effect, the total uncertainty was within 5%.

D.1.1. Random Error Analysis for the Room Temperature Permeability Measurement.

A random error analysis was performed using the least squares method to calculate the error in the room temperature measurement.

For the data of a 2 μm stainless steel Mott plug (M2S1-4x1), with an area of 5.06 cm^2 and 1/8 in thickness,

$$\Delta P = 25.75 \text{ torr}$$
$$\dot{v} = 15.99 \text{ cm}^3/\text{s}$$
$$\eta = 204.3 \times 10^{-6} \text{ g/cm s}$$

$$K_p = \dot{v}\eta L / \Delta P A = 5.73 \times 10^{-9} \text{ cm}^2$$

$$\omega_{K_p}^2 = (\omega_{\dot{v}})^2 (\partial K_p/\partial \dot{v})^2 + (\omega_{\Delta P})^2 (\partial K_p/\partial \Delta P)^2$$
$$= (\omega_{\dot{v}})^2 (L\eta/\Delta P A)^2 + (\omega_{\Delta P})^2 (\dot{v}L\eta/\Delta P^2 A)^2$$

where $\omega_{\dot{v}}$ is the uncertainty in measuring the flow rate ($\pm$ 1 cc/s) and $\omega_{\Delta P}$ is the uncertainty in the differential pressure ($\pm$ 0.34 torr).

$$\omega_{K_p} = \pm 3.73 \times 10^{-10} \text{ cm}^2$$
$$K_p = (5.73 \pm 0.37) \times 10^{-9} \text{ cm}^2$$

The random error in the room temperature permeability measurement was about 6.5 %.

D.2. Experimental Accuracy of the Thermo-Osmotic Experiment

The accuracy of the thermo-osmotic experiment depends on the stability and accuracy of measuring the following properties.

1) Thermometer calibration
2) Differential pressure across the plug
3) Liquid level of He II from which the mass flow rate was calculated
4) The bath temperature

Thermometer Calibration

Carbon resistor thermometers were used to measure the upstream and downstream temperatures. Because of the reduction of sensitivity with increasing temperature in the carbon thermometers, the uncertainty at 5 K was about 0.2 K and approximately 1 K at 20 K. The uncertainty in temperature below 2 K should not exceed 2mK.

Differential Pressure Across the Porous Plug

The uncertainty in differential pressure was discussed in section D.1.

Liquid Level of He II

The mass flow rate of He II was calculated from the conservation of mass by measuring the change in liquid level. The uncertainty in recording the liquid level corresponded to a heat flow of $Q = \pm 5$ mW.

Bath Temperature

The accuracy of the bath temperature was directly related to the accuracy of the pressure gauges used to measure the vapor pressure above the helium bath. In the He II temperature range a Wallace and Tiernan pressure gauge calibrated to the 1958 International Vapor Scale. Below 2 K, the overall uncertainty was less than 2 mK. Bath stability in this temperature range was around 1 mK.

D.2.1. Random Error Analysis for the Vapor-Liquid Phase Separation Experiment

For the VLPS data of a 5-15 bronze PSM plug (P5-15B1-4x4), with a cross sectional area of 1.27 cm^2 and 1.27 cm thickness, we have (for T = 1.3 K),

$$Q = 78.33 \text{ mW}$$
$$\Delta T = 0.00882 \text{ K}$$

$$K_{pn} = Q\eta_n L/\rho^2 S^2 T\Delta T A = 6.87 \times 10^{-8} \text{ cm}^2$$

$$\omega^2_{K_{pn}} = (\omega_Q)^2(\partial K_{pn}/\partial Q)^2 + (\omega_{\Delta T})^2(\partial K_{pn}/\partial \Delta T)^2$$

$$= (7.737 \times 10^{-12})^2[\omega_Q^2(1/\Delta T)^2+\omega^2_{\Delta T}(-Q/\Delta T^2)]$$

$$\omega_{K_{pn}} = \pm 1.62 \times 10^{-8} \text{cm}^2$$

$$K_{pn} = (6.87 \pm 1.62) \times 10^{-8} \text{ cm}^2$$

The uncertainty in the normal fluid permeability measurement is about $\pm$ 24 %.

The errors in the dimensionless heat flux number and the dimensionless driving force number are 6.4 % and 22.5 % respectively.

The accuracy of the determination of the Gorter-Mellink constant is presented in the following section

$$K_{GM} = [(\rho/\rho_s)(\rho_s/\rho_n)^{1/3}]^2 N_q/N_{\nabla T}$$

$$\omega^2_{K_{GM}} = (\rho/\rho_s)^2(\rho_n/\rho_s)^{2/3}[W^2_{N_q}(1/N^{1/3}_{\nabla T})^2 + W^2_{N_{\nabla T}}(N_q/3N^{4/3}_{\nabla T})^2]$$

$$\omega_{K_{GM}} = \pm 0.16$$

For the same data discussed in the previous section, we have

$$K_{GM} = 1.89 \pm 0.16$$

The random error is about 8.5 %.

APPENDIX E

Calibration Curves

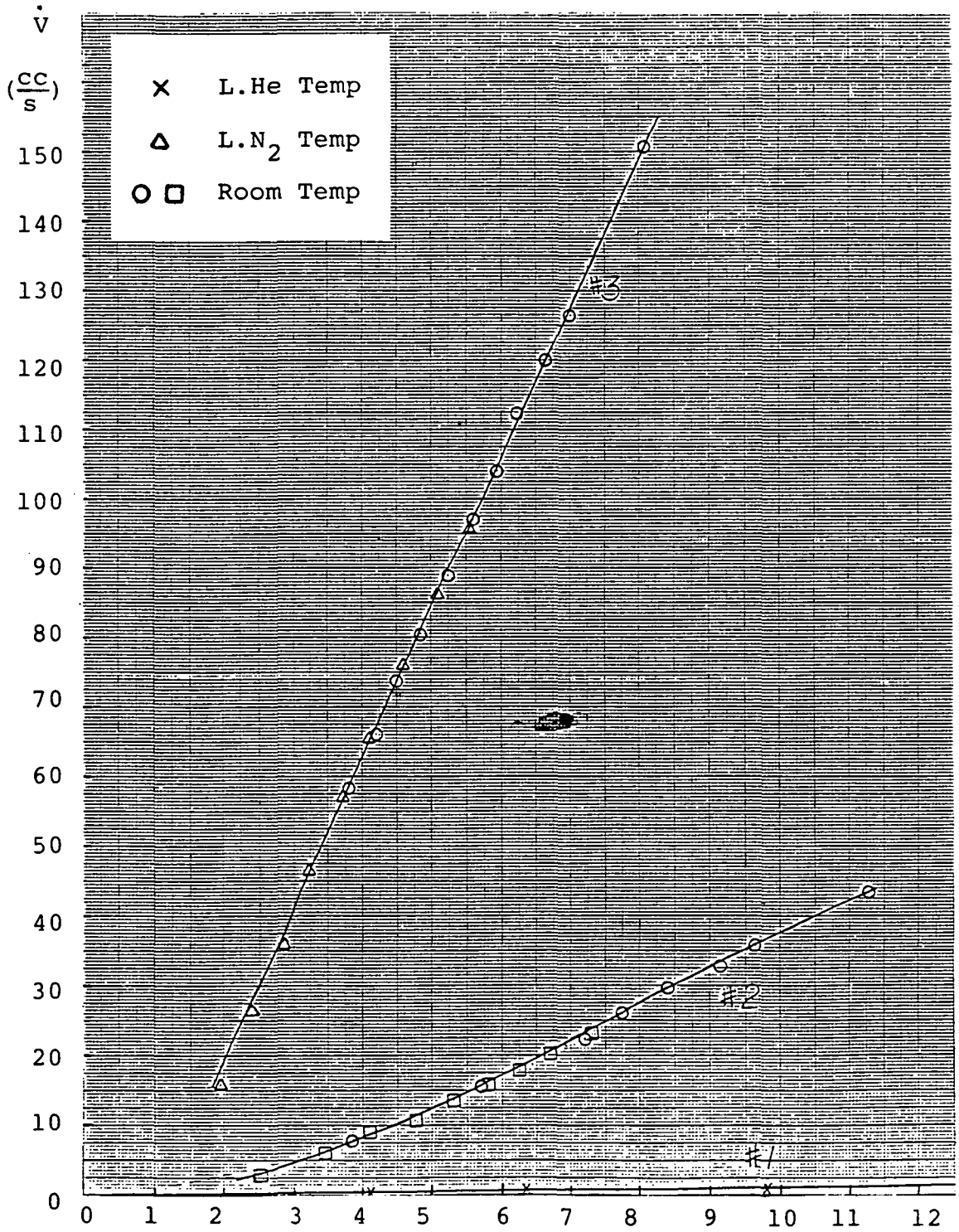

Figure E.1. Calibration curves for the rotameters.

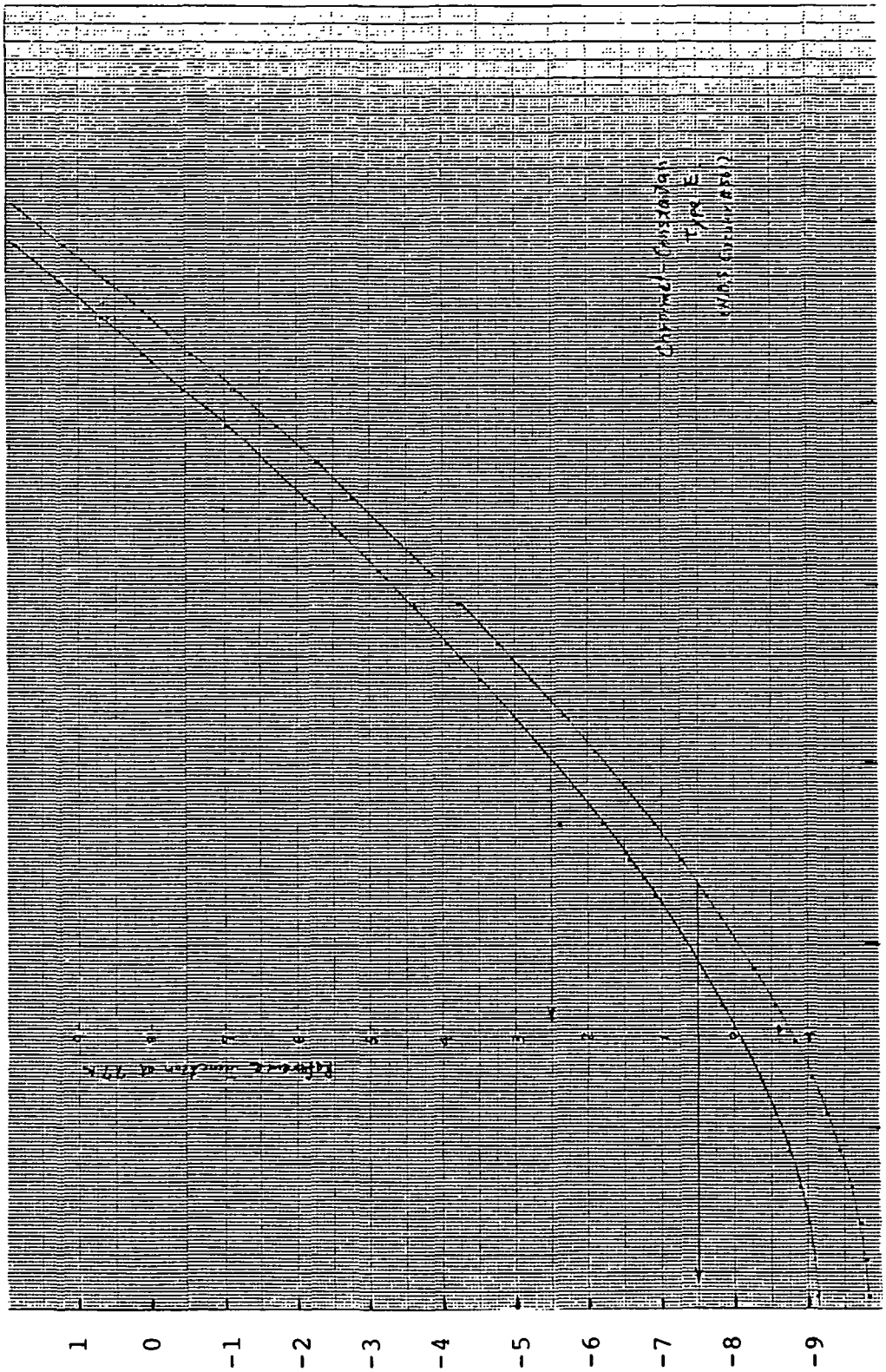

Figure E.2. Calibration curve for the chromel-constantan thermocouple (Type E).

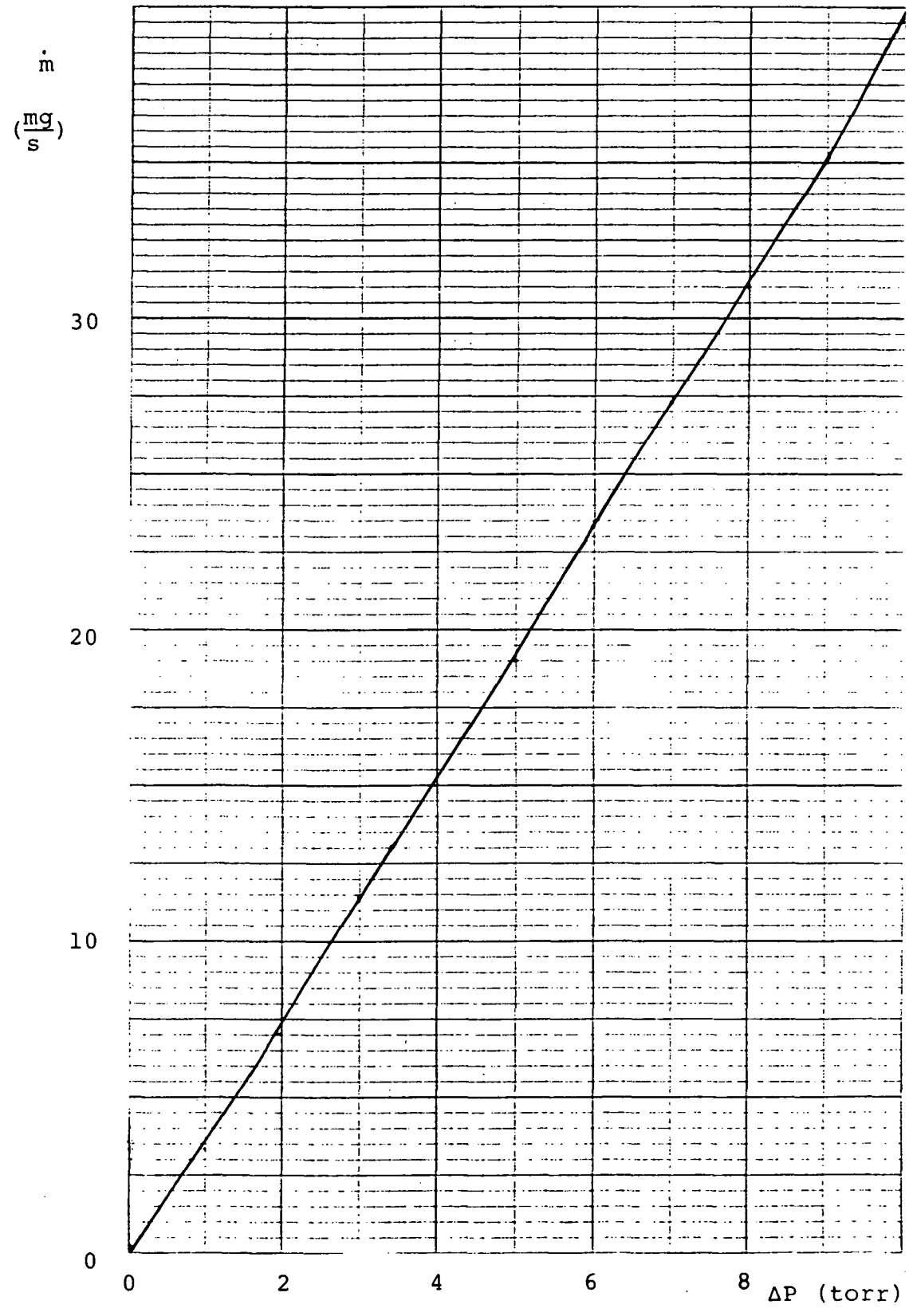

Figure E.3. Calibration curve for the ΔP-mass flow meter.

APPENDIX F

Computer Program Of Runge-Kutta-Fehlberg Used To Fit The Liquid Outflow Data Of He I

```
      *JCB
 1          EXTERNAL F
 2          DIMENSION Y(1),YP(1)
 3          REAL KP
 4          COMMON/CON/B, C,D
 5          Y(1) = 24.28
 6          A=0.0
 7          H=0.2
 8          HMX=1.0
 9          KP = 7.36E-8
10          VSC = 30.E-6
11          PRS= 0.4236
12          RL= 2.0
13          RHO= 0.146
14          AO = 1.26
15          AD = 5.06
16          B =(1.75*RHO / SQRT(150.*KP*(PRS**3)))*(AD**2/AC**2)
17          C = (VSC/KP)*(AC/AO)
18          D=RHO*980.0*RL/2.54
19          DO 1 I=1,150
20          CALL RKF (A,Y,1,F,1.0,H,HMX,1.E-6,0.0,IFLAG)
21          GO TO (1,2,2,2),IFLAG
22        1 PRINT 100, A, Y(1), YP(1), H
23      100 FORMAT (10X,F11.6,1P3E15.7)
24          STOP
25        2 PRINT 101,A,IFLAG
26      101 FORMAT (10X,F11.6,I15)
27          STOP
28          END

29          SUBROUTINE F(X,Y,YP)
30          DIMENSION Y(1), YP(1)
31          COMMON/CON/B, C,D
32          YP(1) =-(-C + SQRT(C**2 + 4*B*D*Y(1))) / (2*B)
33          RETURN
34          END
```

```
35        SUBROUTINE RKF(A,Y,N,F,DA,H,HMX,AESERR,RELERR,IFLAG)                  360
C
C  THE CODE INTEGRATES A SYSTEM OF FIRST ORDER ORDINARY DIFFERENTIAL
C  EQUATIONS BY RUNGE-KUTTA-FEHLBERG METHOD WITH AUTOMATIC ESTIMATION
C  OF LOCAL ERROR AND STEP SIZE ADJUSTMENT.
C
C        A - ON INPUT THE INITIAL VALUE OF THE INDEPENDENT VARIABLE.
C            ON OUTPUT THE LAST VALUE AT WHICH A SOLUTION WAS
C            SUCCESSFULLY COMPUTED. NORMAL OUTPUT HAS INPUT VALUE
C            OF A INCREASED BY DA.
C        Y - ON INPUT THE VECTOR OF INITIAL VALUES OF THE DEPENDENT
C            VARIABLES. ON OUTPUT THE VECTOR OF COMPUTED SOLUTIONS
C            AT OUTPUT VALUE OF A.
C        N - NUMBER OF EQUATIONS TO BE INTEGRATED.
C        F - SUBROUTINE OF THE FORM F(A,Y,YP) WHICH ACCEPTS INDEPEN-
C            DENT VARIABLE A AND A VECTOR OF DEPENDENT VARIABLES
C            Y AND FURNISHES A VECTOR OF VALUES OF THE DERIVATIVES
C            YP. USE DIMENSIONS Y(1), YP(1). IN VECTOR FORM THE
C            DIFFERENTIAL EQUATIONS SOLVED ARE
C
C                 DY/DX=YP, Y(A)=Y.
C
C       DA - INTEGRATION IS TO PROCEED FROM A TO A + DA. DA CAN BE
C            NEGATIVE.
C      HMX - UPPER BOUND ON STEP SIZE TO BE. MUST BE POSITIVE.
C      AESERR,RELERR - BOUNDS ON LOCAL ERROR PERMITTED. RELATIVE TO A
C            UNIT CHANGE IN THE INDEPENDENT VARIABLE. EACH COMPONENT
C            OF THE COMPUTED SOLUTION Y(1) OBTAINED IN A STEP OF LENGTH
C            ABS(H) MUST PASS THE TEST
C
C                    ABS(ESTIMATED LOCAL ERROR).LE.
C                    ABS(H)*(RELERR*ABS(Y(1))+ABSERR)
C
C  A FLAG, IFLAG, IS PROVIDED AS AN OUTPUT QUANTITY. IT MAY ASSUME
C  THE VALUES 1-4 WHERE
C
C       IFLAG = 1 FOR NORMAL RETURN--REACHED A+DA.
C
C             = 2 IF MORE THAN 3000 FUNCTION EVALUATIONS ARE NEEDED.
C
C             = 3 FOR ILLEGAL INPUT VALUES.
C
C             = 4 IF CODE NEEDS TO TAKE TOO SMALL A STEP FOR
C                 COMPUTER WORD LENGTH.
```

```
C
C  A, Y, AND H MUST BE VARIABLES IN THE CALLING PROGRAM SINCE THEY
C  ARE ALSO USED FOR OUTPUT.  Y MUST BE DIMENSIONED IN THE CALLING
C  PROGRAM.
C
      DIMENSION Y(N)                                                    361
C
C  THE CODE IS SET UP TO SOLVE SYSTEMS OF UP TO 10 DIFFERENTIAL
C  EQUATIONS.  IF MORE EQUATIONS ARE DESIRED, ONLY THE NEXT TWO
C  STATEMENTS NEED BE CHANGED.
C
      DIMENSION YTEMP(10),TEMP(10),R(10)                                362
      REAL K1(10),K2(10),K3(10),K4(10),K5(10),K6(10)                    363
C
C  SET U TO APPROXIMATELY THE UNIT ROUNDOFF OF SPECIFIC MACHINE.
C  (HERE IBM 360/67)
C
      U=9.0D-7                                                          364
C
C  TEST INPUT DATA AND INITIALIZE.
C
      IF(RELERR.LT.0.0.OR.ABSERR.LT.0.0)GO TO 18                        365
      IF(RELERR+ABSERR.EQ.0.0)GO TO 18                                  366
      IF(HMX.LE.0.0)GO TO 18                                            367
      B=A+DA                                                            368
      IF(ABS(DA).LE.13.0*U*AMAX1(ABS(A),ABS(B)))GO TO 19                369
      HMAX=AMIN1(HMX,ABS(DA))                                           370
      IF(ABS(H).LE.13.0*U*ABS(A))H=HMAX                                 371
      KOUNT=0                                                           372
      IADJUS=0                                                          373
C
C  LIMIT H TO HMX   AND ADJUST STEP SIZE TO MAKE OUTPUT POINT IF
C  APPROPRIATE.
C
    3 H=SIGN(AMIN1(ABS(H),HMAX),DA)                                     374
      IF(ABS(B-A).GT.1.25*ABS(H))GO TO 4                                375
      HKEEP=H                                                           376
C
C  CODE REALIZES IT HAS REACHED OUTPUT POINT WHEN IT TAKES A
C  SUCCESSFUL STEP WITH VARIABLE IADJUS=1.
C
      IADJUS=1                                                          377
      H=B-A                                                             378
C
```

```
      C
      C  BEGIN COMPUTATION OF STEP.
54      4    CALL F(A,Y,K1)                                                  379
55           KOUNT=KOUNT+1                                                   380
56      5    CONTINUE                                                        381
57           DO 6 I=1,N                                                      382
58      6    YTEMP(I)=Y(I)+0.25*H*K1(I)                                      383
59           ARG=A+0.25*H                                                    384
60           CALL F(ARG,YTEMP,K2)                                            385
61           DO 7 I=1,N                                                      386
62      7    YTEMP(I)=Y(I)+H*(K1(I)*(3.0/32.0)+K2(I)*(9.0/32.0))             387
63           ARG=A+H*(3.0/8.0)                                               388
64           CALL F(ARG,YTEMP,K3)                                            389
65           DO 8 I=1,N                                                      390
66      8    YTEMP(I)=Y(I)+H*(K1(I)*(1932.0/2197.0)-K2(I)*(7200.0/2197.0)    391
            1   +K3(I)*(7296.0/2197.0))                                      392
67           ARG=A+H*(12.0/13.0)                                             393
68           CALL F(ARG,YTEMP,K4)                                            394
69           DO 9 I=1,N                                                      395
70      9    YTEMP(I)=Y(I)+H*(K1(I)*(439.0/216.0)-8.0*K2(I)                  396
            1   +K3(I)*(3680.0/513.0)-K4(I)*(845.0/4104.0))                  397
71           ARG=A+H                                                         398
72           CALL F(ARG,YTEMP,K5)                                            399
73           DO 10 I=1,N                                                     400
74     10    YTEMP(I)=Y(I)+H*(-K1(I)*(8.0/27.0)+2.0*K2(I)-K3(I)*             401
            1   (3544.0/2565.0)+K4(I)*(1859.0/4104.0)-K5(I)*(11.0/40.0))     402
75           ARG=A+0.5*H                                                     403
76           CALL F(ARG,YTEMP,K6)                                            404
77           DO 11 I=1,N                                                     405
78           TEMP(I)=K1(I)*(25.0/216.0)+K3(I)*(1408.0/2565.0)+K4(I)*         406
            1   (2197.0/4104.0)-0.2*K5(I)                                    407
79     11    YTEMP(I)=Y(I)+H*TEMP(I)                                         408
      C
      C  NOW YTEMP(U) IS TENTATIVE RESULT OF THE STEP. COMPUTE R(I).
      C  THE ESTIMATED LOCAL ERROR RELATIVE TO A UNIT CHANGE IN THE
      C  INDEPENDENT VARIABLE.
      C
80           DO 12 I=1,N                                                     409
81     12    R(I)=K1(I)/360.0-K3(I)*(128.0/4275.0)-K4(I)*(2197.0/75240.0)+   410
            1   K5(I)/50.0+K6(I)*(2.0/55.0)                                  411
      C
      C  TEST FOR ACCURACY.
      C
82           RATIO=0.0                                                       412
83           DO 13 I=1,N                                                     413
84           TR=ABS(R(I))/(RELERR*ABS(YTEMP(I))+ABSERR)                      414
85     13    RATIO=AMAX1(RATIO,TR)                                           415
```

```
C
C RATIO.GT.1.0 MEANS REJECT STEP AND REPEAT. RATIO IS USED IN EITHER
C EVENT FOR STEP ADJUSTMENT.
C
      IF(RATIO.GT.1.0)GO TO 15                                          416
C ACCEPT RESULT OF STEP.
C
C
      DO 14 I=1,N                                                       417
   14 Y(I)=YTEMP(I)                                                     418
      A=A+H                                                             419
C
C IF WE HAVE REACHED A+DA, RETURN.
C
   15 RATIO=AMIN1(RATIO,4096.0)                                         422
C
      IF(IADJUS.EQ.1)GO TO 16                                           420
C SO THAT THE INCREASE IS LIMITED TO A FACTOR OF 5 AND THE DECREASE
C REFINE OR CHOOSE THE NEXT STEP. RATIO IS ALTERED IF NECESSARY
C TO A FACTOR OF 1/10.
C
      RATIO=AMAX1(RATIO,6.5536E-4)                                      421
      H=0.8*H/SQRT(SQRT(RATIO))                                         423
      IF(ABS(H).LE.13.0*U*ABS(A))GO TO 19                               424
      KOUNT=KOUNT+5                                                     425
      IF(KOUNT.GE.2995)GO TO 17                                         426
C
C IF RATIO.LE.1.0, THE STEP WAS SUCCESSFUL SO WE START ANOTHER
C
C STEP. OTHERWISE WE ARE REPEATING WITH A SMALLER H.
      IF(RATIO.LE.1.0)GO TO 3                                           427
      IADJUS=0                                                          428
      GO TO 5                                                           429
   16 IFLAG=1                                                           430
      H=HKEEP                                                           431
      RETURN                                                            432
   17 IFLAG=2                                                           433
      RETURN                                                            434
   18 IFLAG=3                                                           435
      RETURN                                                            436
   19 IFLAG=4                                                           437
      RETURN                                                            438
      END                                                               439
```

APPENDIX G

The Blake-Kozeny Equation and the Thermo-Osmotic Darcy Equation

Murakami proposed the Blake-Kozeny equation for He II as follows:

$$f_M = 150 / Re_M \qquad (G.1)$$

where

$$f_M = (150K_p\varepsilon^3)^{\frac{1}{2}}\nabla P_T / \rho_n v_n^2 \qquad (G.2)$$

and

$$Re_M = (150K_p\varepsilon^{-3})^{\frac{1}{2}}\rho_n v_n/\eta_n \qquad (G.3)$$

Substituting Equation G.2 and G.3 into G.1 and after re-arranging, one gets,

$$v_n = K_p\nabla P_T / \eta_n \qquad (G.4)$$

The preceeding equation is the thermo-osmotic Darcy equation (Eq. 3.15). It is noted that f_M and Re_M used by Murakami are not the same as f and Re_k of Equation B.11.

APPENDIX H

Thermal Properties of He II Used in This Research

The property data of He II used in this research are summarized in Table H.1. These data were taken from the following sources:

1) Vapor Pressure

   T-58 Scale (Brickwedde et al. 1960)

2) Density and Density Ratio

   Least squares fit of data from Brooks and Donnelly (1977), Maynard (1976) and McCarty.

3) Viscosity

   Spline fit of the data from Brooks and Donnelly (1977), Hussey et al. (1967), Webeler et al. (1965), Biskeborn et al. (1975) and Bruschi et al. (1975).

4) Entropy

   Calculated from the 5.6 power law

$$S_\lambda = S\ (T/T_\lambda)^{5.6} \qquad (H.1)$$

   where $S_\lambda = 1.538$ was obtained by the least squares fit of the data from Brooks and Donnelly (1977), Maynard (1976), Borelius (1963) and Van den Meijdenberg et al. (1961).

Table H.1. Property Data of He II

T (K)	V.P. (torr)	ρ (g/cm³)	ρn/ρ	ρs/ρ	ηn (μP)	S (J/gk)	λ (J/g)
1.00	0.1200	0.14510	0.00643	0.99357	38.100	0.0200	20.05
1.05	0.1907	0.14510	0.00997	0.99003	29.941	0.0263	20.30
1.10	0.2922	0.14510	0.01559	0.98441	23.475	0.0341	20.55
1.15	0.4334	0.14510	0.02046	0.97954	19.858	0.0437	20.80
1.20	0.6250	0.14510	0.02878	0.97122	18.095	0.0554	21.04
1.25	0.8789	0.14511	0.03687	0.96313	16.897	0.0697	21.27
1.30	1.2085	0.14511	0.04762	0.95238	15.957	0.0868	21.50
1.35	1.6286	0.14512	0.06026	0.93974	15.213	0.1072	21.71
1.40	2.1554	0.14513	0.07472	0.92528	14.601	0.1315	21.93
1.45	2.8060	0.14514	0.09415	0.90585	14.071	0.1600	22.12
1.50	3.5990	0.14515	0.11260	0.88740	13.616	0.1935	22.32
1.55	4.5536	0.14517	0.13905	0.86095	13.241	0.2325	22.50
1.60	5.6899	0.14519	0.16333	0.83667	12.950	0.2777	22.67
1.65	7.0285	0.14522	0.19682	0.80319	12.748	0.3299	22.82
1.70	8.5902	0.14525	0.23052	0.76948	12.648	0.3899	22.95
1.75	10.3959	0.14529	0.27424	0.72576	12.661	0.4587	23.04
1.80	12.4661	0.14534	0.31721	0.68279	12.799	0.5370	23.16
1.85	14.8207	0.14540	0.37235	0.62766	13.062	0.6261	23.23
1.90	17.4782	0.14547	0.42776	0.57224	13.400	0.7269	23.28

T (K)	V.P. (torr)	ρ (g/cm³)	ρ_n/ρ	ρ_s/ρ	η_n (μP)	S (J/gk)	λ (J/g)
1.95	20.4559	0.14556	0.49563	0.50437	13.802	0.8408	23.30
2.00	23.7674	0.14566	0.56661	0.43339	14.450	0.9688	23.27
2.05	27.4233	0.14576	0.66044	0.33957	15.527	1.1125	23.18
2.10	31.4281	0.14590	0.75629	0.24371	17.000	1.2732	23.07
2.15	35.7803	0.14604	0.88988	0.11012	21.617	1.4526	22.85
2.17	37.6143	0.14609	0.97512	0.02488	26.816	1.5299	22.70
2.172	37.8006	0.14610	1.00000	0.00000	27.389	1.5378	22.68

APPENDIX I

Raw Data

I.1 Data of vapor-liquid phase separation:

Table I.1 Data of the 2 μm stainless steel Mott plug (M2S1-4x1) VLPS results.

No.	T_u (K)	T_d (K)	ΔP_v(mbar)	j(mg/cm^{2}s)
1	1.8035	1.5342	10.20	7.9
2	1.7814	1.5159	9.53	7.6
3	1.7551	1.4939	8.72	7.4
4	1.7313	1.4755	7.91	7.1
5	1.7054	1.4668	7.13	6.7
6	1.6775	1.4930	6.27	6.3
7	1.6548	1.4930	5.67	5.9
8	1.6279	1.4826	4.96	5.5
9	1.6013	1.4668	4.35	5.1
10	1.5690	1.4444	3.76	4.4
11	1.5518	1.4444	3.36	3.9
12	1.5342	1.4369	3.00	3.3
13	1.5147	1.4265	2.71	2.8

Table I.2. Data of the 10 μm stainless steel Mott plug (M10S1-4x4) VLPS results.

No.	T_u (K)	T_d (K)	ΔP_v (mbar)	j ($mg/cm^2 s$)
1	1.6068	1.5226	2.47	6.0
2	1.5757	1.4897	2.25	6.2
3	1.5583	1.4747	2.07	5.5
4	1.5490	1.4687	1.93	5.3
5	1.5271	1.4470	1.77	5.0
6	1.5179	1.4410	1.65	4.7
7	1.4987	1.4227	1.52	4.4
8	1.4677	1.3951	1.29	4.1
9	1.4608	1.3868	1.20	3.8
10	1.4494	1.3851	1.08	3.2
11	1.4378	1.3785	0.89	2.7
12	1.4327	1.3833	0.80	2.3
13	1.4265	1.3850	.67	1.8

Table I.3. Data of the 5-15 μm bronze PSM plug (P5-15B2-4x4), using transient warm up technique (VLPS results).

No.	T_u (K)	T_d (K)	ΔP_v (mbar)	j (mg/cm^{2}s)
1	1.6741	1.6252	1.88	15.29
2	1.6938	1.6471	1.92	16.75
3	1.7118	1.6593	2.25	18.14
4	1.7258	1.6732	2.36	19.27
5	1.7375	1.6826	2.53	20.16
6	1.7756	1.7148	3.09	22.95
7	1.7911	1.7267	3.41	24.23
8	1.8049	1.7384	3.64	25.42
9	1.8167	1.7487	3.84	26.69
10	1.8265	1.7557	4.08	27.75
11	1.8364	1.7638	4.28	28.72
12	1.8466	1.7701	4.61	29.51
13	1.8531	1.7739	4.84	30.09
14	1.8611	1.7776	5.17	30.64
15	1.8705	1.7795	5.72	31.09

Table I.4. Data of the 5-15 μm bronze PSM plug (P5-15B2-4x4) using transient cool down technique (VLPS results).

No.	T_u (K)	T_d (K)	ΔP_v(mbar)	j(mg/cm^{2}s)
1	1.5453	1.5023	0.73	11.69
2	1.5000	1.4635	0.55	9.64
3	1.4783	1.4429	0.47	8.61
4	1.4621	1.4263	0.40	7.76
5	1.4441	1.4100	0.34	6.90
6	1.4228	1.3965	0.31	6.35
7	1.4083	1.3761	0.26	5.58
8	1.3916	1.3603	0.22	5.03
9	1.3814	1.3499	0.20	4.65
10	1.3729	1.3428	0.19	4.44
11	1.3691	1.3379	0.18	4.31
12	1.3684	1.3379	0.18	4.28
13	1.3684	1.3379	0.17	4.28

Table I.5. Data of the 5-15 μm bronze PSM plug (P5-15B1-4x4), taken from the asymptotic limit experiment.

No.	$\bar{T}$(K)	ΔT(K)	Q(mW)	N_q	$N_{\nabla T}$
1	1.44186	0.02161	239.4	14.48	44.37
2	1.40647	0.01985	227.2	15.99	33.42
3	1.38514	0.01645	224.8	17.18	24.74
4	1.37511	0.01641	218.72	17.34	23.41
5	1.35256	0.01436	195.81	16.94	18.17
6	1.33600	0.01522	155.31	14.41	17.50
7	1.32523	0.01270	134.17	13.06	13.68
8	1.31364	0.01248	121.31	12.47	12.53
9	1.30695	0.01139	115.45	12.28	10.95
10	1.30051	0.01178	110.43	12.14	10.87
11	1.29752	0.01168	104.49	11.62	10.57
12	1.29492	0.01221	96.20	10.81	10.88
13	1.29032	0.00882	78.33	8.96	7.65
14	1.28926	0.00948	72.75	8.35	8.17
15	1.28907	0.00911	63.34	7.28	7.84
16	1.28888	0.00874	58.64	6.75	7.52
17	1.28870	0.00837	57.29	6.59	7.19

I.2. Data of room temperature permeability measurements:

Table I.6. Room Temperature Permeability Measurement Results

Plug * Designation	Porosity	Permeability (cm^2)	Equivalent Ergun Diameter (μm)
+ M0.5S1-4x1	0.3127	7.836×10^{-10}	13.48
○ M2S1-8x1	0.3115	4.88×10^{-9}	33.88
M2S2-8x1	0.3089	----------	-----
□ M2S3-8x1	0.3138	5.94×10^{-9}	36.85
△ M2S4-8x1	0.3277	5.79×10^{-9}	33.40
▽ M2S7-8x1	0.3113	6.40×10^{-9}	38.85
M2S11-8x1	0.3100	----------	-----
○ M2S1-4x1	0.2582	3.43×10^{-9}	40.56
◒ M5S1-8x1	0.3462	1.02×10^{-8}	39.70
◆ M5S2-8x1	0.3283	8.86×10^{-9}	41.17
▬ M5S1-4x1	0.3716	1.28×10^{-8}	38.44
● M10S1-8x1	0.3881	3.25×10^{-8}	55.88
▼ M10S2-8x1	0.3890	3.384×10^{-8}	56.74
■ M10S1-4x1	0.3899	2.99×10^{-8}	53.07
◇ P2S1-8x1	0.3661	3.74×10^{-9}	21.43
P2S2-8x1	0.3655	4.452×10^{-9}	23.47
◆ P5-15B1-8x2	0.4508	1.135×10^{-7}	74.87
● P5-15B1-4x4	0.4223	8.64×10^{-8}	75.78
▲ P5-15B2-4x4	0.4236	7.364×10^{-8}	69.49

*The designation of the plugs is explained in the following page.

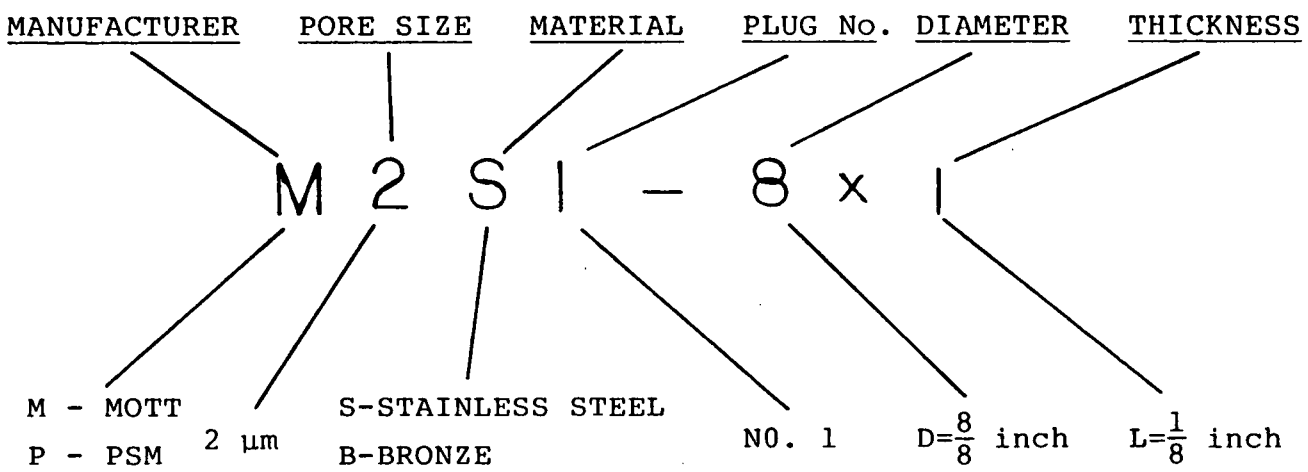
MANUFACTURER
PORE SIZE
MATERIAL
PLUG No.
DIAMETER
THICKNESS
M 2 S 1 - 8 x 1
M - MOTT
P - PSM
2 µm
S-STAINLESS STEEL
B-BRONZE
NO. 1
D=8/8 inch
L=1/8 inch